ABSTRACT

Title of Dissertation: A High-Order, Linear Time-Invariant Model for Application to Higher Harmonic Control and Flight Control System Interaction

Rendy P. Cheng, Doctor of Philosophy, 2003

Dissertation directed by: Professor Roberto Celi
Department of Aerospace Engineering

Helicopters can experience high vibration levels, which reduce passenger comfort and cause progressive damage to the aircraft structure and on-board equipment. Because the primary source of excitation is typically the main rotor, special rotor control systems have been proposed to reduce these vibrations at the source. This dissertation addresses one such system, generally known as "Higher Harmonic Control" (HHC) because it consists of superimposing high frequency rotor inputs to the conventional low frequency ones used to control and maneuver the helicopter. Because both the primary flight control system and the HHC system act on the main rotor, the risk of adverse interactions between the two systems exists. This dissertation focuses on these interactions, which have never been studied before for the lack of suitable mathematical models.

The key ingredient is an accurate linearized model of the helicopter, which includes the higher harmonic rotor response, and both the Automatic Flight Control System (AFCS) and the HHC system. Traditional linearization techniques lead to a system with periodic coefficients. Although Floquet theory can be used to study such periodic systems, there are far more control system design theories and software tools that are available for linear time-invariant systems than for periodic systems. Additionally, the theoretical evaluation of the handling qualities of the helicopter requires linear time-invariant systems.

This research describes a new methodology for the extraction of a high-order, linear time invariant model, which allows the periodicity of the helicopter response to be accurately captured. This model provides the needed level of dynamic fidelity to permit an analysis and optimization of the AFCS and HHC algorithms.

The key results of this study indicate that the closed-loop HHC system has little influence on the AFCS or on the vehicle handling qualities, which indicates that the AFCS does not need modification to work with the HHC system. On the other hand, the results show that the vibration response to maneuvers must be considered during the HHC design process, and this leads to much higher required HHC loop crossover frequencies. This research also demonstrates that the transient vibration responses during maneuvers can be reduced by optimizing the closed-loop higher harmonic control algorithm using conventional control system analyses.

A High-Order, Linear Time-Invariant Model for Application to Higher Harmonic Control and Flight Control System Interaction

by

Rendy P. Cheng

Dissertation submitted to the Faculty of the Graduate School of the
University of Maryland, College Park in partial fulfillment
of the requirements for the degree of
Doctor of Philosophy
2003

Advisory Committee:

Professor Roberto Celi, Chairman/Advisor
Professor Inderjit Chopra
Professor J. Gordon Leishman
Associate Professor Robert M. Sanner
Professor G. W. Stewart

DEDICATION

To my parents and my sister for all their love and understanding

ACKNOWLEDGEMENTS

This research was supported by the U. S. Army Aeroflightdynamics Directorate, Ames Research Center, Moffett Field, California, under grant NAG 2-1231. I would like to thank Dr. Mark Tischler for many useful comments and discussions.

I would also like to thank the members of my dissertation committee for their valuable feedback: Drs. Inderjit Chopra, J. Gordon Leishman, Robert M. Sanner, and G. W. Stewart. I especially would like to thank Dr. Roberto Celi, my dissertation director, for his guidance and support during my graduate studies.

I would like to thank Jinwei Shen and Mao Yang at the Alfred Gessow Rotorcraft Center, who provided me many helpful discussions on helicopter dynamics. In particular, I would like to thank Colin Theodore for his help and invaluable assistance while I was writing this dissertation.

Finally, I would like to thank Dr. Wayne Johnson for helping me gain a better understanding of helicopter analysis.

TABLE OF CONTENTS

LIST OF TABLES

LIST OF FIGURES

Chapter 1

Introduction

1.1 Motivation

Excessive vibration levels can reduce mission effectiveness on military aircraft and decrease passenger comfort and acceptance on commercial aircraft. Even moderate fuselage vibrations reduce the reliability of on board equipment, such as avionics [1]. Maintenance costs can be significantly reduced if airframe vibrations are reduced. It has been estimated [2] that by reducing the fuselage vibrations in the Sikorsky UH-60 helicopter from 0.2g to 0.1g, $80,000 per aircraft per year can be saved in direct maintenance costs. This is a saving of $160 million/year for a fleet of 2,000 aircraft! These savings are achieved primary from reduced component failures due to vibration. Consequently, vibration reduction is a high priority for helicopter designers and manufacturers.

The major source of vibration is the unsteady aerodynamic environment experienced by the rotor blades including blade/vortex interaction, retreating blade stall, and blade/fuselage aerodynamics interaction. These blade loads are then transmitted through the hub, resulting in vibration of the elastic fuselage. The traditional approaches for reducing helicopter vibration are generally passive meth-

ods. They attack the vibration problem by increasing the number of blades, isolating the transmission system, applying hub absorbers, installing bifilars, or adding dynamic absorbers. These systems are heavy and have narrow frequency effectiveness ranges. Over the past two decades, the helicopter industry, government and academia have demonstrated that Higher Harmonic Control (HHC) is a very effective method for vibration reduction. HHC technology may be able to achieve greater vibration reduction with less weight than the traditional approaches by suppressing the vibration at the source. Typically, the HHC input frequency has been n/rev, where n is the number of rotor blades, but other frequencies have also been utilized. A detailed survey of the extensive work in the area has been presented by Friedmann [3] and Teves et al. [4].

The active rotor control system for vibration suppression is shown in Figure 1.1. The helicopter control system generally consists of two control systems: Automatic Flight Control System (AFCS) and HHC system. In Figure 1.1, the AFCS manages the helicopter stability and controls, and the HHC system suppresses the helicopter vibration. The HHC loop consists of three basic components. First, the data acquisition system (A/D, analog-to-digital converter) receives the helicopter hub loads $Z(t)$ and converts them to the digital signal $Z(k)$. Next, the harmonic analyzer extracts the n/rev harmonic components of the hub loads and forward them to the HHC controller. Last, the HHC controller computes the ideal HHC inputs $\theta(k)$ for vibration suppression.

The rotor control system does not receive the new HHC input from HHC controller at every time step. The HHC input update rate (number of HHC input update per rotor revolution) depends on the time required to complete the data acquisition and post data processing, and it has strong influence on the HHC loop

stability margin. HHC update rates from 0.5 to 16 times per rotor revolution have been implemented on several wind tunnel and flight tests [5–10]; however, the once-per-revolution (or 1/rev) HHC update is most commonly implemented. To date,

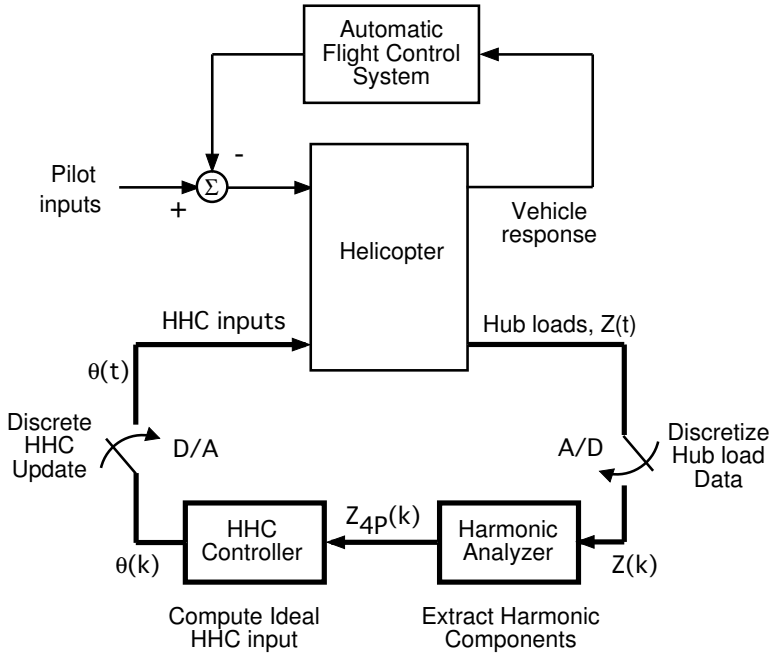

Figure 1.1: Typical active rotor control system for vibration suppression.

very little information is available on potential interactions between the HHC and AFCS. The published literature describe results from flight tests, wind tunnel tests, and numerical simulations with either a closed-loop HHC or a closed-loop AFCS, but not with both types of loops simultaneously closed. Because periodic nature of the helicopter, HHC is a control system application that has developed without the benefit of the standard control system analysis techniques. Wereley and Hall [11] have studied the stability of the closed-loop HHC system, but the plant model was assumed to be quasi-static, and it does not include periodic behavior of the rotor system. Therefore, the achievable bandwidth of HHC algorithms was

limited by the quasi-static assumption on the plant model. The HHC performance improvement could only be achieved by including the periodic behavior of the rotor system in the plant model and developing a control algorithm for the periodic time-varying plant model. Although Floquet theory can be used to study the periodic time-varying system, there are far more control system design methods and software tools that are available for linear time invariant systems than for periodic systems.

Furthermore, the effects of the HHC system on vehicle handling-qualities and maneuverability are also remained unknown. There are several important analyses that are important for evaluating the handling-qualities of the helicopter system that cannot be currently carried out. These include the calculations of gain and phase margins with the closed-loop HHC and/or AFCS, the crossover frequency of the HHC loops and the closed-loop stability of helicopter dynamics with closed-loop HHC. These quantities can be easily obtained from a linear time-invariant system

Therefore, there is a need for linear time-invariant approximations that accurately model the coupled rotor-fuselage dynamics, including the higher harmonic response of the rotor. Such time-invariant linearized approximation methods are not currently available.

1.2 Literature review

1.2.1 Higher harmonic control technology

In 1952, Stewart [12] showed the potential effectiveness of HHC in alleviating retreating blade stall. The usage of second harmonic control (2/rev) was shown to

redistribute the rotor disk loads and suppress retreating blade stall. By delaying the retreating blade stall to a higher forward speed, the speed limitation of a helicopter could be raised. Based on his analysis, the advance ratio could be increased by 0.1. However, the analysis was based on a rigid flapping blade and the airloads were calculated with quasi-static aerodynamics and uniform inflow distribution. The transonic effects, separated flow conditions, unsteady aerodynamics, blade flexibility, and non-uniform inflow distribution were all neglected.

In 1961, Arcidiacono [13] extended Stewart's research by including both 2/rev and higher harmonic blade pitch control. The analyses showed that a combination of 2 and 3/rev HHC inputs could be used to delay retreating blade stall to an even higher advance ratio than that reported by Stewart. Neither Steward nor Arcidiacono considered the effects of HHC input on vibratory hub loads.

In 1961, the first HHC flight test was carried out to investigate the feasibility of using HHC for vibration suppression on an UH-1A 2-bladed helicopter [14]. A series of flight tests was conducted by Bell Helicopter Company to determine the effects of HHC on rotor performance, blade airloads, blade loads, control loads, hub loads, and airframe vibration. The investigators noted that no reduction in shaft torque was observed. The investigation also showed that the drag reduction in the retreating side of rotor was accompanied by an increase in profile drag in the fore and aft portion of the rotor disk. These results confirmed Stewart's finding, and indicated that 2/rev HHC input could be used to change the rotor disk loading.

In 1972, McCloud [15,16] reported the first full-scale wind tunnel investigation on HHC. The rotor model was a two-bladed teetering rotor with propulsive jet flaps. A large jet flow was expelled from the blade trailing edge to propel the rotor and the HHC was applied through the angular deflection of the jet flow.

The experiments showed that the vibratory hub load reduction was accompanied by an increase in the blade bending moments. The HHC inputs required for the vibration suppression were found to vary with rotor forward speed.

In 1975, McHugh and Shaw [17, 18] conducted a series of wind tunnel experiments on a four-bladed soft-inplane hingeless rotor model. The HHC was implemented in the non-rotating frame, and HHC inputs were applied by oscillating the swashplate with servo-actuators. Results from the experiments indicated that the vibratory hub moments could be suppressed effectively without a significant increase in blade stresses. The experiments also indicated that all five components of the 4/rev hub loads (lateral, longitudinal, vertical forces; pitching and rolling moments) could be reduced simultaneously with three HHC inputs.

In 1979, a wind tunnel investigation of HHC on a four-bladed hingeless rotor model was conducted by Shaw and Albion [19, 20] in the Boeing V/STOL Wind Tunnel. The rotor model was Mach scaled and operated at full-scale tip speed. The HHC inputs were applied through swashplate excitation. The closed-loop HHC controller simultaneously reduced the 4/rev vertical hub shear, hub pitching and rolling moments up to 90%. The closed-loop transient behaviors were studied by introducing a step disturbance in the swashplate command. The results showed that the disturbance was suppressed within two rotor revolutions, which confirmed the quasi-static assumption made on the HHC model.

In 1980, Shaw [21] presented the results of a comprehensive analytical investigation of HHC. He compared the potential benefits of servo-flap versus conventional blade root feathering and studied the automatic in-flight adaptive algorithm. The investigation was based on a coupled modal analysis and included a vortex wake induced flow calculation. An approximation to the Theodorsen lift deficiency func-

tion was used to include the effect of the shed wake. A transfer matrix (T-matrix) approach was implemented to relate the higher harmonic hub loads to the HHC inputs. The analytical results showed that the nonlinearities in the HHC input-output model were small. The results also indicated that the vibration suppression was caused by the mutual cancellation between the aerodynamic and the inertial components of the transmitted vibratory loads at the blade roots. With the HHC inputs, the control loads were increased by roughly 30%, and the change in rotor performance was negligible. For changing flight conditions, the closed-loop HHC controller with fixed gain performed satisfactorily over an advance ratio range of 0.2. An adaptive gain controller was used for the cases when the fixed gain controller performed poorly. For the adaptive gain controller, the model parameters were estimated using a Kalman filter. Simulation results showed that the adaptive controller performed well for varying flight conditions.

In 1981, Molusis, Hammond and Cline [22] studied several HHC algorithms for vibration suppression, and the algorithm performance was evaluated in wind tunnel testing. The rotor model was a Mach-scaled four-bladed articulated rotor. The HHC controllers were configured to suppress the 4/rev vertical, longitudinal, and lateral signals from a triaxial accelerometer mounted beneath the rotor in the non-rotating frame. The advance ratio was varied between 0.2 to 0.4. The HHC system was modeled using T-matrix approach. The HHC algorithms studied were separated into two groups: the adaptive controllers and the gain-scheduled controllers. Each type of controller was further classified. The adaptive controllers were classified into deterministic controllers and cautious controllers. The gain-scheduled controllers were classified into perturbation controllers and proportional controllers. The wind tunnel results showed that the gain-scheduled controllers per-

formed poorly. The cause might be the nonlinear behavior of the HHC model. The deterministic (adaptive) controller was shown to significantly reduce the steady-state vibration levels, but there were large transient responses that occurred before the vibration converged to the steady-state value. The authors noted that the cautious controller offered the best performance among the four controllers.

In 1981, the performance of four different feedback controllers or regulators were investigated by Chopra and McCloud [8] for the multicyclic control of helicopter vibration. These controllers were open-loop and closed-loop with off-line and on-line identification. The off-line identification of model characteristics was made using the least-squared-error method and used a succession of input and output measurements. The on-line identification of model characteristics was computed using a Kalman-filter solution. The optimal controls were calculated by minimizing the quadratic performance function based on response and control inputs. Both global (linear) and local (piecewise linear) models were simulated. The results showed that the closed-loop controller with a local model using on-line identification technique performed the best. For the cases with large initial errors in the transfer matrix, large overshoots were found in the transient response using this controller.

In 1982, Wood et al. [23,24] conducted a HHC flight test on a modified Hughes OH-6A helicopter with a gross weight of about 3,000 lb. The HHC input was achieved by blade root feathering through the 4/rev swashplate oscillations. A triaxial accelerometer was mounted beneath the pilot seat to sense and feed back the 4/rev vibrations to the HHC controller. The aircraft was flown from hover to 100 kts with the HHC system operated in open-loop (manually) and closed-loop (computer controlled). For the closed-loop controller, the cautious controller presented in Ref. 22 was used. The test results indicated that up to 90% reduction

in vibration could be obtained with HHC amplitude less than 1°.

During 1980's, extensive research on the use of HHC implemented in the form of Individual Blade Control (IBC) was carried out by Ham and his coworkers [25,26]. The potential applications of IBC were proposed that included reducing the severe effects of atmospheric turbulence, retreating blade stall, blade-vortex interaction, blade-fuselage interference, and blade instabilities, while providing improved fly qualities and automatic blade tracking. The theoretical analysis showed that the rotor blade flapping, inplane, and torsional motion could be reduced by feedback control of the effective inertia, damping, and stiffness of the appropriate modes.

In 1985, Shaw et al. [6] described wind tunnel tests on a dynamically scaled three-bladed CH-47D Chinook rotor in the Boeing V/STOL Wind Tunnel. The 2, 3, and 4/rev HHC inputs were applied to suppress the 3/rev vertical hub force and the 2 and 4/rev rotating inplane hub shears throughout a wide test envelope which included trimmed flight up to 188 kts The open-loop tests were conducted to obtain transfer matrices under several flight conditions. These transfer matrices were used with fixed- or gain-scheduled controllers. The wind tunnel results showed that a fixed-gain controller with a local model can suppress more than 90% in all three vibratory hub shears components. The wind tunnel results indicated that the gain-scheduled controller performed as well as the fixed-gain controller. The adaptive controllers, similar to those in Ref. 22, were either unstable or ineffective in suppressing the vibratory loads.

In 1986, Polychroniadis and Achache [27,28] discussed the application of HHC on an Aerospatiale SA-349 Gazelle helicopter (4,500 lb) for vibration reduction and noise reduction, and included a performance analysis based on both theoretical studies and wind tunnel testing. The HHC input was achieved by blade root

feathering through the 4/rev swashplate oscillations. The HHC controller was a self-adaptive controller that used the vibration sensors placed at pre-selected locations in the aircraft. The test results showed a 70 to 90% reduction in vibration was achieved at forward speeds up to 135 kts

In 1994 and 1995, Jacklin et al. [29, 30] described two wind tunnel tests that evaluated the effects of IBC at various frequencies on rotor performance, vibrations, and acoustics using a full-scaled BO-105 helicopter rotor. The IBC system, developed by ZF Luftfahrttechnik, was tested on the NASA/Army Rotor Test Apparatus in the NASA Ames 40- by 80-Foot Wind Tunnel. Test results indicated that a single-frequency IBC input of 2-4/rev could simultaneously reduce all 4/rev rotor balance forces and moments up to 70% at 43 kts

In 2002, U. T. P. Arnold [10] described the certification, ground and flight testing of an experimental IBC system for a Sikorsky CH-53G helicopter with a gross weight of about 68,000 lb The primary goal of the IBC system was to extend the service life of the CH-53 by reducing the component fatigue and failure induced by high vibratory stresses. The IBC system was designed, built, installed, and certified by ZF Luftfahrttechnik, GmbH. The IBC system, weighing less than 1% of the helicopter maximum take-off weight, completely integrated all mechanical and hydraulic components into the rotating frame. The IBC controller was based on a second order T-matrix model. Initial test results showed a high effectiveness of IBC in reducing vibration with a relatively small single harmonic input of $\pm 0.15^{\circ}$.

Most of the active vibration control algorithms discussed above were implemented in frequency domain. In 1980, Du Val and Gupta [31] proposed a time domain approach for the active control of helicopter vibration. The controller was designed by optimizing a cost function, which placed a large penalty on fuse-

lage vibration at n/rev frequency. The fuselage accelerations were passed through an undamped second-order system tuned to the n/rev frequency. At the resonant frequency, the regulator locked onto the magnitude and phase of the fuselage accelerations without the need for harmonic analysis. By placing an infinite weighting on the n/rev response, a controller is guaranteed to drive the n/rev response to zero. Because the dynamics of the rotor and fuselage were included in the plant model, the quasi-static assumption was no longer necessary. Also, because the state feedback was used, on-line identification of the model parameters were not necessary. This method assumed the system was linear time-invariant (LTI), not linear time-periodic (LTP). The standard linear analysis techniques and software tools could therefore be applied.

In 1989, Wereley and Hall [11,32] presented a framework to provide the evaluation of active vibration control algorithms performance in terms of classical control theory. They showed that HHC was fundamentally similar to the sinusoidal disturbance rejection techniques of classical control. By treating the periodic disturbance as a stochastic rather than a deterministic phenomenon, the methods of Shaw et al. [6] and Du Val and Gupta [31] could be compared quantitatively. The authors indicated that the achievable bandwidth of HHC algorithms was limited by the quasi-static and linear time-invariant assumptions on the plant model. The HHC performance improvement could only be achieved by including the periodic behavior of the rotor system in the plant model and developing a control algorithm for the periodic time-varying plant model.

In 2000, Spencer [33] presented the open and closed-loop wind tunnel testing of a Mach-scaled active rotor system with piezoelectric bender actuated trailing-edge flaps for active vibration control. The closed-loop vibration suppression tests were

conducted at several advance ratios and collective setting. The controller design is based on a radial basis neural network which is used to approximate the command input to the active rotor. The controller is implemented in discrete time by sampling the hub loads and control input at 1/rev frequency. The optimum set of network weights is determined by minimizing the cost function which is based on the vibration response and command input. One of the advantage of the neural network controller is that it simultaneously learns while it commands the on-blade actuator thus adaptively suppressing the blade or hub vibrations. No off-line training of the network is required. These test successfully reduced the 4/rev oscillatory fixed frame thrust, pitching moment, and rolling moment levels up to 90%. Transient vibration control test was also conducted by varying the rotor speed, wind speed, and the collective pitch angle to simulate maneuvering flight. For all three individual perturbations, the neural-controller was unable to compensate vibration response fluctuation. The authors indicated the controller was not able to react fast enough to the perturbations because of hardware limitations.

1.2.2 Linear models

In 1981, Howlett [34] presented a nonlinear mathematical model known as GenHel, based on the Sikorsky UH-60A Black Hawk helicopter, for performance and handling-qualities evaluations. The rotor was modeled with a rigid blade flap and rigid blade lag degree of freedom. The torsional dynamics were modeled using a simple dynamic twist model. The aerodynamic forces on the rotor were computed using blade element theory and quasi-static aerodynamics. Aerodynamics coefficients of the blade were provided by the look-up tables as function of the angle of attack and Mach number. The fuselage was modeled as a rigid body with aerody-

namic coefficients of the fuselage and empennage provided by the look-up tables as a function of angle of attack.

GenHel simulation model could provide a linear model, but it was limited to the six fuselage degrees of freedom. The linearization was performed numerically by perturbing each of the states and controls, and using finite difference approximations. Because of the unusual flight dynamic model implementation in GenHel, the perturbation scheme was not straightforward. For instance, the fuselage states and control inputs were perturbed one at a time about the trim condition to produce a 9-state rigid body linear model from the nonlinear GenHel mathematical model. The rotor equations of motion continued to be integrated while all rigid body acceleration integrations were suppressed. The change in the state derivatives was calculated when the rotor response had reached a steady-state condition. This method produced a six fuselage degree of freedom linear model with a quasi-static rotor; i.e., the dynamics of the rotor system was not modeled.

In 1982, Zhao and Curtiss [35] developed the first linear model of helicopter including blade dynamics for forward flight. This linear model had 24 or 27 states depending on whether dynamic inflow was included. Flap and lag degrees of freedom were modeled by transforming the rotor equations of motion into the non-rotating frame using multi-blade coordinate transformation. Only the collective and the first two cyclic modes for each rotor degree of freedom were retained. Unsteady aerodynamic effects were introduced through the dynamic inflow model. A flat vortex wake model was used to approximate the effects of the main rotor wake interference on the tail surfaces and tail rotor. The linearized model was derived using symbolic mathematic manipulation program to obtain an analytical solution. The linearization process consisted of expressing the time dependent variables in

the equations of motion as the sum of the trim value and time dependent perturbation about the trim value. A linearized model could be obtained by applying order reduction and setting the remaining perturbation quantities to zero.

In 1986, Chen and Tischler [36] discussed the method of developing the simplified analytical linearized model from the flight test data by using modern system or parameter identification techniques. The simplified analytical model could be used for handling-qualities evaluation, design of stability and control augmentation systems, and ground simulator validation. Authors stated that the importance of recognizing that each lower-order model used for rotorcraft parameter identification had a limited range of applicability. They also discussed the benefits and limitations of using frequency sweeps as flight test input signals for identification of frequency response for rotorcraft and for the subsequent fitting of parametric transfer function models. The authors concluded that analytical modeling and understanding the limitation of lower-order models could be more important than merely relying on the identification algorithms.

In 1987, Miller and White [37] presented an algorithm called Exponential Basis Function (EBF) which allowed computer generation of a comprehensive coupled rotor-fuselage nonlinear model. EBF represented the position vector of a generic mass element of the helicopter exponentially, and was used to simplify the differentiation of the position vector. EBF was used to write the time dependent coordinate transformation as the product of constant matrices and matrix exponentials. Since the multiplication of exponentials is equivalent to addition of exponential arguments, multiplication of the transformation matrices could be accomplished by adding matrix exponentials. The transformation matrices written in EBF could also be differentiated easily. The equations of motion were formu-

lated using Lagrange's equation. The rotor degrees of freedom were transformed to a non-rotating frame using the multi-blade coordinate transformation. The rotor dynamics included rigid body flap and lag degrees of freedom. Engine rotor speed, fuselage rigid body degrees of freedom, and the inflow dynamics were also modeled. Authors stated that the linear model obtained through EBF could be used to analyze handling-qualities phenomena for highly augmented helicopters when realistic trim conditions and high-order dynamics were considered.

In 1990, Kim, Celi, and Tischler [38] developed a high-order linearized model of helicopter flight dynamics extracted from a nonlinear time domain simulation. The model had 29 states that described the fuselage rigid body degrees of freedom, the flap and lag dynamics in non-rotating frame, the inflow dynamics, and the delayed entry of the horizontal tail into the main rotor wake. The blade torsional degree of freedom was approximated using a pseudo-modal approach. In GenHel, the calculation of forces and moments acting on the helicopter at a given instant in time was solved sequentially; the rotor equations of motion were solved first, and the fuselage equations of motion were solved next. Because of this separation, the equations of motion were not perturbed simultaneously, which could cause inaccuracies in the solution at higher frequencies. The perturbation process was also complicated by this splitting solution process. Therefore, GenHel could only produce a six fuselage degree of freedom linear model with a quasi-static rotor.

To carry out a theoretically rigorous linearization and retain the rotor dynamics within the linear model, the mathematical model of the helicopter as implemented in GenHel was extensively modified to a first-order, state variable form. This required several modifications including solving both the rotor and the fuselage equations of motion simultaneously. The linear model was validated against the

nonlinear model, and the results showed a good agreement between these two models for small amplitude control inputs. In case of large amplitude inputs, which violated the small perturbation assumption inherently contained in the linear model, the agreement deteriorated greatly.

1.3 Objectives of study

The objectives of this study are as follows:

- Develop a methodology for the derivation of linearized, time-invariant, state-space models of coupled rotor-fuselage dynamics that include the effects of higher harmonic response of rotor and fuselage to both higher harmonic pitch control and pilot inputs.
- Apply the new linear state-space models for a study of the potential interactions between a higher harmonic control system and an automatic flight control system, including any impact on handling-qualities.

It should be pointed out that this research does not focus on the method to improve the helicopter vibratory hub load predictions. A comprehensive analysis on this topic is beyond the scope of the present study. The helicopter simulation model used in this study is adequate to capture the first-order effects, but it may not be sufficient for accurate quantitative predictions of vibratory hub loads.

1.4 Principal contributions

- Implement a HHC in a flight dynamics model for a free flight condition to investigate the interaction between HHC and AFCS.

- Developed a linear time-invariant state-space approximation that accurately models the coupled rotor-fuselage dynamics including the higher harmonic response of the rotor. This coupled high-order linear model provides the needed level of dynamic fidelity to permit study of AFCS and HHC interaction.

- Provided detail analyses on the HHC/AFCS interaction, and developed a improved HHC controller to reduce the vibration transients during the maneuvering flight.

1.5 Organization of the dissertation

Chapter 2 describes the mathematical model of the helicopter and provides the solution method for the trim calculation, the linearization, the time integration, and the vibratory hub load calculation.

Chapter 3 is devoted to the HHC system for the vibration suppression. The inner working of the harmonic analyzer, the HHC controller, and the HHC update scheme are discussed in detail. The methods of obtaining the continuous-time domain equivalent for each component are also presented.

Chapter 4 presents a new linearization method that converts a nonlinear system to a linear time-invariant system while capturing the n/rev characteristic of the helicopter. The new linear model was validated by comparing the vibratory hub loads and the rotor states for both the higher harmonic inputs and piloted input at several forward speeds.

Chapter 5 presents the results of the HHC/AFCS interaction study. The effect

of HHC input on handling-qualities was tested for both open-loop and closed-loop HHC systems. This chapter also discusses the effect of the HHC on the vibration transients during maneuvers, and develops a new HHC algorithm to overcome the problem.

Chapter 6 presents conclusions of the study and recommendations for future work.

Chapter 2

Mathematical Model

This chapter contains a brief history of the helicopter mathematical model used in this study, followed by the definition and implementation method of HHC system, the methods used to calculate the helicopter trim states, a linearized model, and the time history. Next, the definition and the computation method of the vibratory hub load are discussed. Finally, the last section presents the method of extracting n/rev vibration using Fourier series approximation.

2.1 History of helicopter simulation model

The flight dynamic simulation model used in this study is originally from the helicopter simulation model GenHel [34] specialized for the Sikorsky UH-60 Black Hawk. The rotor was modeled with a rigid blade flap and rigid blade lag degrees of freedom. The torsional dynamics was modeled using a pseudo-modal approach. The fuselage was modeled as a rigid body with aerodynamic coefficients of the fuselage and empennage provided by the look-up table. The fidelity of GenHel model was improved by Ballin [39] who also implemented the engine model. Kim [40, 41] included the main rotor inflow model using the Pitt-Peters

dynamic inflow model [42]. A new trim procedure was also developed with the equations of motion presented in first-order state-space form. This allows a linear time-invariant model to be extracted using perturbation-averaging method. The model developed by Kim was named UM-GenHel. UM-GenHel continued a series of calibration based on the actual flight test data at NASA Ames Research Center. This version of UM-GenHel was renamed FORECAST, and is widely used in flight dynamics analysis at NASA Ames Research Center.

At the same time, the UM-GenHel remained at the University of Maryland as a research helicopter model. Turnour [43] extended the rotor blade modeling in UH-GenHel by including the aeroelastic rotor, which was originally developed by Celi [44] and extended by Spence [45] to included the coupled rotor/fuselage formulation. Turnour also added the finite state wake [46] and the Leishman-Nguyen [47] state-space unsteady aerodynamics model. This version of research model was renamed by Turnour as FlexUM. Theodore [48] extended the inflow flow model to included the maneuvering Free Wake model [49], which improves the off-axis response predictions. A full BO-105 helicopter configuration is also added to the FlexUM. The research model was renamed to HeliUM by Theodore.

2.2 Helicopter model

The basic formulation and solution of the equations are unchanged with respect to the previous works. The helicopter model used in this study is similar to the Sikorsky UH-60 Black Hawk with the following simplifying assumption. The helicopter equations of motion are based on a set of coupled nonlinear rotor-fuselage equations in first-order, state-space form. The rigid body dynamics of the helicopter is modeled using non-linear Euler equations. The aerodynamic coefficients

of fuselage and tail surfaces are provided in the form of look-up tables. The blade is assumed to be straight, i.e., with zero tip sweep. The blade dynamics consists of two rigid blade degrees of freedom plus first torsional degree of freedom. The aerodynamic coefficients of the blade are also provided in the form of look-up tables as a function of angle of attack and Mach number. Unless stated otherwise, the main rotor inflow is calculated using a three-state dynamic inflow model, which yields linear inflow distributions over the rotor disk. Tip losses are taken into account by assuming that the outboard 3% of the blade does not generate lift. A one-state dynamic inflow model is used for the tail rotor. Stall and compressibility effects are incorporated in a quasi-static form, and unsteady aerodynamic effects have been neglected. Two additional assumptions are that the rotor speed is constant and that there is no limitation on the power supplied by the engine. All the results presented in this dissertation were obtained from a coupled rotor-fuselage trim procedure simulating free flight conditions. All the trim calculations include the HHC input, if one is present. In all the parametric studies, the helicopter is retrimmed every time that the magnitude or phase of the n/rev input changes.

2.3 HHC implementation

The higher harmonic control inputs is implemented by varying the blade pitch at blade root. Unlike the real active pitch links system, the stiffness of the pitch link is assumed to be infinitely stiff and the dynamics of the active pitch links is ignored. The geometric pitch angle θ_G of the blade is given by:

$$\theta_G(\psi) = \theta_0 + \theta_{1c}\cos(\psi + \Delta_{SP}) + \theta_{1s}\sin(\psi + \Delta_{SP}) + \theta_n(\psi) \tag{2.1}$$

where θ_0, θ_{1c}, and θ_{1s} are respectively the collective, lateral cyclic, and longitudinal cyclic pitch, Δ_{SP} is the swashplate phasing angle, $\Delta_{SP} = -9.7°$, and $\theta_n(\psi)$ is the n/rev input, defined as:

$$\theta_n(\psi) = A_n \cos(n\psi + \phi_n) \tag{2.2}$$

where A_n and ϕ_n are the magnitude and phase of the n/rev input.

2.4 Solution methods: trim

This section presents the methods to calculate the helicopter trim states. The flight condition is assumed to be a steady coordinated helical turn. Straight level flight is then a special case with both flight path angle and turn rate equal to zero. The helicopter trim equations were originally developed by Chen [50], and later extended by Celi [51] to include the steady state response of the rotor. They are modified further by Kim [40] to consider the periodicity of both rotor and fuselage motion. The trim states are generally obtained from an algebraic trim procedure.

2.4.1 Algebraic trim

The typical trim solution is based on algebraic trim. The solution of the steady state condition is determined by converting a set of coupled ordinary differential equations to a set of coupled nonlinear algebraic equations. The periodicity of the helicopter response must be satisfied in a steady state condition. This set of algebraic equations is then solved using the Powell Hybrid algorithm. The trim solution is reached when the sum of the forces and moments at the vehicle center of gravity are zero in one rotor revolution.

Although this trim method can obtain a trim solution quickly, it does not

guarantee the rotor blades returning to the same position after one revolution of time integration. In other words, time integration starting from an algebraic trim solution without control perturbation may not respond precisely to n-multiple/rev. This does not appear to be crucial for flight dynamics analyses, but it has large effect on vibration related computations. The periodic trim procedures can fulfill this task.

2.4.2 Periodic trim

There are two methods to achieve a periodic trim solution: the shooting method, and the time marching method.

The shooting method

After algebraic trim is achieved, the state vector and control vector are adjusted such that the state vector remains the same after integration of one rotor revolution. This is a two-point nonlinear boundary value problem, and it is based on a shooting method [52]. The basic idea behind the shooting method is to convert a boundary value problem (BVP) into an initial value problem (IVP). Given an initial guess for the parameters, an iterative solver is used to find values of the parameters that produce solutions that satisfy the boundary conditions. The method will guarantee a n/rev periodic trim, but its convergence proved erratic, and at least one order of magnitude more expensive computationally, compared with the algebraic trim procedure.

The time marching method

The second method is the time marching solution. As stated earlier, the free flight response from the time integration starting from the algebraic trim solution may not have precise n-multiple/rev response. Because of the unstable Phugoid mode, the helicopter will slowly drift away from the trim. The low gain stabilization loop was added to ensure the helicopter does not become unstable as integration time increases. As the time integration continues, the n-multiple/rev response will emerge. Generally, the periodic trim solution can be reached within four rotor revolutions starting from an algebraic trim solution. At the end of time integration, the trimmed state vectors around the rotor azimuth are available. Additional information about the time integration is presented in Sec. 2.6.

2.5 Solution methods: linearization of the equation of motion

This techniques consist of perturbing each state and control about an equilibrium position. Using this approach, the individual blade pitch is introduced in terms of the harmonics in the rotating frame. This method leads to systems of rotor equations containing periodic coefficients, which are represented in the rotating frame. The transformation from the rotating frame to the fixed frame is accomplished using a Multi-blade Coordinate Transformation (MCT, Appendix C). To remove the time dependency, the linearized models are computed over one rotor revolution and then averaged to obtain a LTI system in the fixed frame. As a consequence, this averaging eliminates the periodicity of the system and all the higher harmonics in both the controls and the rotor response. Additional information about this

technique will be discussed in Chapter 4.

2.6 Solution methods: time integration

The free flight response of the helicopter is computed by integrating the equations of motion based on a given set of initial condition and control inputs. The equations of motion are represented by a system of coupled nonlinear ordinary differential equations expressed symbolically in the first-order ODE form

$$\dot{\mathbf{y}} = \mathbf{f}\left(\mathbf{y}, \mathbf{u}; t\right) \tag{2.3}$$

where $\mathbf{y}$ is the state vector and $\mathbf{u}$ is the control vector. Eq. (2.3) can be solved numerically using Adams-Bashforth method, which is a variable-step, variable-order, predictor-corrector, numerical method for solving linear first-order ordinary differential equations. It estimates the behavior of the solution curve by evaluating the derivative function at the old solution values along with the current solution and derivative function and uses the interpolation method to estimate the new solution. In other words, Adams-Bashforth methods try to squeeze information out of old solution points. For problems where the solution is smooth, these methods can be highly accurate and efficient.

In this study, the simulation is started from the trim condition, and the equations of motion are integrated with respect to time. This produces the time histories of all the state variables for prescribed control inputs. Generally, the control inputs include the time history of pilot inputs or the swashplate controls. For the HHC system, the control inputs are extended to the blade root pitch angle which can be prescribed as single or multiple harmonics in terms of the n/rev amplitude A_n and phase angle ϕ_n as stated in Eq. (2.2).

2.7 Vibration calculation

2.7.1 Hub loads calculation

The equations of motion of the helicopter can be expressed as Eq. (2.3). Because the coupled rotor-fuselage-inflow equations of motion have the state derivatives appear on the right hand side of the equations, these equations are expressed as:

$$\dot{\mathbf{y}}_c = \mathbf{f}_c\left(\dot{\mathbf{y}}, \mathbf{y}, \mathbf{u}; t\right) \tag{2.4}$$

where $\dot{\mathbf{y}}_c$ is a vector which contains all the state derivatives appear on the right hand side of Eq. (2.4). For instance, the flap equation for ith blade of a simple rotor model (rigid flap and lag modes only) is:

$$\begin{aligned}
\ddot{\beta}_i &= \frac{S_b}{I_b}\Big\langle \cos\beta_i\Big\{\dot{w} + e\left[2\Omega\left(p\cos\psi_i - q\sin\psi_i\right) + \dot{p}\sin\psi_i + \dot{q}\cos\psi_i\right]\Big\} \\
&+ \sin\beta_i\cos\zeta_i\left[\dot{v}\sin\psi_i - \dot{u}\cos\psi_i - e\left(r - \Omega\right)^2\right]\Big\rangle \\
&+ \cos^2\beta_i\Big\{\cos\zeta_i\left[\dot{p}\sin\psi_i + \dot{q}\cos\psi_i - 2\left(\dot{\zeta} + \Omega\right)\left(\dot{q}\sin\psi_i - \dot{p}\cos\psi_i\right)\right] \\
&- 2\Omega\sin\psi_i\left(p\sin\psi_i + q\cos\psi_i\right)\Big\} \\
&+ \cos\beta_i\sin\beta_i\left\{2\dot{\zeta}_i\left(r - \Omega\right) - \left(r - \Omega\right)^2 - \dot{\zeta}_i^2\right\} \\
&- \left[\left(r - \Omega\right) - \dot{\zeta}\right]^2 + \frac{\left(M_{LD\beta_i} + M_{Aero\beta_i}\right)}{I_b}
\end{aligned} \tag{2.5}$$

where S_b and I_b are the first and second blade moments of inertia about its hinge, $M_{Aero\beta}$ is the flap aerodynamic moment, and $M_{LD\beta}$ is the flap moments due to the lag damper. Since the state derivatives $\dot{u}$, $\dot{v}$, $\dot{w}$, $\dot{p}$, and $\dot{q}$ on the right hand side of Eq. (2.5) do not couple with other state derivatives, it can be rewritten as:

$$\ddot{\beta}_1 = [\mathbf{e}]\ \dot{\mathbf{y}}_c + \mathbf{F}_{\beta_1}\left(\mathbf{y}, \mathbf{u}; t\right) \tag{2.6}$$

where

$$\mathbf{e} = \begin{bmatrix} -\frac{S_b}{I_b}\sin\beta\cos\zeta\cos\psi \\ \frac{S_b}{I_b}\sin\beta\cos\zeta\sin\psi \\ \frac{S_b}{I_b}\cos\beta \\ \frac{S_b}{I_b}e\ \cos\beta\sin\psi + \ \cos^2\beta\cos\zeta\sin\psi \\ \frac{S_b}{I_b}e\ \cos\beta\cos\psi + \ \cos^2\beta\cos\zeta\cos\psi \\ \mathbf{0}_{10\times 1} \end{bmatrix}^T \tag{2.7}$$

$$\dot{\mathbf{y}}_c = [\dot{u}, \dot{v}, \dot{w}, \dot{p}, \dot{q}, \dot{r}, \dot{\Omega}, \ddot{\beta}_1, \ddot{\beta}_2, \ddot{\beta}_3, \ddot{\beta}_4, \ddot{\zeta}_1, \ddot{\zeta}_2, \ddot{\zeta}_3, \ddot{\zeta}_4]^T \tag{2.8}$$

Similar expression can also be rewritten for the remaining equations ($\dot{u}$, $\dot{v}$, $\dot{w}$, $\dot{p}$, $\dot{q}$, $\dot{r}$, ...). The resultant row vectors $\mathbf{e}$ are assembled into a coupling matrix $\mathbf{E}$, and Eq. (2.4) can be rewritten as follow:

$$\dot{\mathbf{y}}_c = [\mathbf{E}]\ \dot{\mathbf{y}}_c + \ \mathbf{F}_k(\mathbf{y}, \mathbf{u}; t) \tag{2.9}$$

By re-arranging Eq. (2.9) into first-order form, $\dot{\mathbf{y}}_c$ can be solved as

$$\dot{\mathbf{y}}_c = [I - \ \mathbf{E}]^{-1}\ \mathbf{F}_k(\mathbf{y}, \mathbf{u}; t) \tag{2.10}$$

Re-write Eq. (2.9) again and parse it as follow:

$$\underbrace{\begin{bmatrix} \dot{\mathbf{y}}_{fus} \\ \dot{\mathbf{y}}_{mr} \end{bmatrix}_c}_{\dot{\mathbf{y}}_c} = \underbrace{\begin{bmatrix} E_{11} & E_{12} \\ E_{21} & E_{22} \end{bmatrix} \begin{bmatrix} \dot{\mathbf{y}}_{fus} \\ \dot{\mathbf{y}}_{mr} \end{bmatrix}_c}_{[\mathbf{E}]\ \dot{\mathbf{y}}_c} + \underbrace{F_{mr} + F_{tr} + F_{fus}}_{F_k(\mathbf{y},\mathbf{u};t)} \tag{2.11}$$

$$\dot{\mathbf{y}}_{fus} = [\dot{u}, \dot{v}, \dot{w}, \dot{p}, \dot{q}, \dot{r}]^T \tag{2.12}$$

$$\dot{\mathbf{y}}_{mr} = \left[\dot{\Omega}, \ddot{\beta}_1, \ddot{\beta}_2, \ddot{\beta}_3, \ddot{\beta}_4, \ddot{\zeta}_1, \ddot{\zeta}_2, \ddot{\zeta}_3, \ddot{\zeta}_4\right]^T \tag{2.13}$$

where $[E_{11}\dot{\mathbf{y}}_{fus}]$ is the inertial acceleration due to the fuselage acceleration, $[E_{12}\dot{\mathbf{y}}_{mr}]$ is the inertial acceleration due to the main rotor acceleration, F_{mr} is the acceleration contributed by the main rotor excluding the inertial coupling term, F_{tr} is the acceleration contributed by the tail rotor, and F_{fus} is the acceleration contributed by the fuselage, the horizontal, and the vertical surfaces. Therefore, the vibratory hub loads are the sum of all the loads that are transmitted from the main rotor to the hub in the fixed system; i.e., $F_{mr} + [E_{12}\dot{\mathbf{y}}_{mr}]$.

2.7.2 Cockpit vibration calculation with the rigid fuselage

In the flight test, the helicopter vibration level is measured by mounting accelerometers at several key areas inside the helicopter, and one of the key areas is the pilot station. The flight dynamics model (HeliUM) used in this study also needs to produce the same pilot station acceleration in order to compare the results with the flight test data. However, this information is not directly available. Although HeliUM is based on a coupled rotor/fuselage formulation, the fuselage is actually modeled as a rigid body and does not contain any dynamics. All results from the free flight trim procedure are only available at the center of gravity (C. G.) of helicopter. Nevertheless, the pilot station acceleration can be obtained by a simple transformation. The velocity at the pilot station can be expressed as follows:

$$\mathbf{v}_{pilot} = \mathbf{v}_{cg} + \boldsymbol{\omega} \times \mathbf{R} \tag{2.14}$$

$$\mathbf{v}_{cg} = [u, v, w]^T \tag{2.15}$$

$$\boldsymbol{\omega} = [p, q, r]^T \tag{2.16}$$

$$\mathbf{R} = [x, y, z]^T \tag{2.17}$$

where $\mathbf{v}_{cg}$ is the velocity vector at the C. G., $\boldsymbol{\omega}$ is the rotational vector of the helicopter at the C. G., and $\mathbf{R}$ is the position vector from C. G. to the pilot station. The pilot station acceleration can then be calculated by differentiating Eq. (2.14) with respect to time,

$$\dot{\mathbf{v}}_{pilot} = \dot{\mathbf{v}}_{cg} + \dot{\boldsymbol{\omega}} \times \mathbf{R} + \boldsymbol{\omega} \times \dot{\mathbf{R}} \tag{2.18}$$

Because the fuselage is a rigid body, the distance between the C. G. and the pilot station is constant; i.e., $\dot{\mathbf{R}} = 0$. Expanding the cross product term, Eq. (2.18) becomes

$$\dot{\mathbf{v}}_{pilot} = \dot{\mathbf{v}}_{cg} + \dot{\boldsymbol{\omega}} \times \mathbf{R} = \begin{bmatrix} \dot{u} - \dot{r}y + \dot{q}z \\ \dot{v} + \dot{r}y - \dot{p}z \\ \dot{w} - \dot{q}x + \dot{p}y \end{bmatrix} \tag{2.19}$$

The 4/rev vibration can then be determined by collecting $\dot{\mathbf{v}}_{pilot}$ over one rotor revolution, and extracting its 4/rev components using the Fourier approximation.

Figures 2.1a and 2.1b compare the pilot and copilot station vibrations with the flight test from hover to 140 kts The flight test data represents several sets of baseline data collected over the span of the flight test program. The scatter in the data could be caused by changes in the aircraft configuration and non-ideal flight conditions during the test.

The main rotor inflow used in HeliUM is based on a linear inflow model. The blade dynamics consist of a rigid blade flap, a rigid blade lag, and first blade torsion mode. The figures also show Yang's [53] results from UMARC[1], which uses 8 blade modes, a free wake model, and a flexible fuselage model. These two figures indicate that the cockpit acceleration computed from HeliUM is under estimated through out the entire speed range. This study has also included additional blade

[1]Both the flight test data and the UMARC results are the courtesy of M. Yang and I. Chopra.

flexibility (result not shown here), but the vibration level is very similar to the one with the rigid blade model.

It was believed that this under prediction could be caused by a lack of aerodynamic interaction. Because the linear inflow model only contains 1/rev harmonics, the higher harmonic airload was not excited. Next, the linear inflow model is replaced with a free wake model, and the results are shown in Figures 2.2a and 2.2b. As expected, the cockpit vibration level has greatly improved. However, the vibration level in the higher speed range is on the low side; especially at 120 kts, which is the baseline configuration of this research. In addition, the helicopter simulation with the free wake model is computationally expensive. The computation time required is generally over one order of magnitude higher than the one with a linear inflow model.

2.7.3 Cockpit vibration calculation with the flexible fuselage

To determine the importance of the fuselage flexibility on cockpit vibration calculations, the effect of the flexible fuselage is added to HeliUM. This is achieved by feeding the hub loads from a trim condition into a separate fully elastic 3-D fuselage model. This fuselage model is built using NASTRAN [54] based on a Sikorsky SH-60B (a variant of UH-60) helicopter fuselage. It consists of structural elements such as scalar springs, rods, bars, shear panels, and triangular and quadrilateral membranes for more than 8,400 elements. NASTRAN is used to calculate fuselage mode shapes, modal mass, and stiffness. The resulting data are used to build a transformation matrix N which maps the 4/rev hub shears and moments to the

cockpit accelerations at the 4/rev frequency.

$$\begin{bmatrix} a_x \\ a_y \\ a_z \\ a_l \\ a_m \\ a_n \end{bmatrix}_{\text{cockpit, 4/rev}} = \begin{bmatrix} \underline{\mathrm{N}}_x & \underline{\mathrm{N}}_y & \cdots & \underline{\mathrm{N}}_n \end{bmatrix} \begin{bmatrix} F_x \\ F_y \\ F_z \\ M_x \\ M_y \\ M_z \end{bmatrix}_{\text{hub, 4/rev}} \tag{2.20}$$

For example, the first column vector $\underline{\mathrm{N}}_x$ is obtained by applying a unit 4/rev longitudinal force $F_{x_{4P}}$ at the NASTRAN model's hub node and measuring all six 4/rev accelerations at the cockpit station. Note that this "open-loop" method is only an approximation. The flexible fuselage dynamics are not part of the coupled rotor-fuselage free flight trim procedure. That it, the calculated hub load does not include the flexible fuselage motions.

Figures 2.4a and 2.4b show the 4/rev acceleration magnitudes at the pilot and copilot stations. Note that the result from HeliUM closely follows the UMARC result up to 90 kts Beyond 90 kts, the HeliUM result continues to rise as the forward speed increases. Overall the predictions qualitatively follow the trends of the flight test data except in the higher speed range. This over-prediction could be caused by several factors. First, the hub load calculation from HeliUM does not include the effect of the flexible fuselage dynamics. The effect of aerodynamic damping on the hub load calculation is also not considered. Second, HeliUM does not have any passive vibration damping device such as the hub absorbers, the bifilars, and the spring-mass fuselage absorbers. Third, Eq. (2.20) assumes that the 4/rev cockpit station acceleration is a linear combination of the 4/rev hub shears and moments. Because vibration is not a linear phenomenon, this assumption may not hold true

in the high-speed flight condition. The cockpit station accelerations provided here only intended to serve as a qualitative measure.

2.8 Optimization formulation

In the first attempt to formulate the optimization problem, the trim equations were included directly in the form of equality constraints $h(\mathbf{X})$ (recall that the trim problem is formulated as a set of nonlinear algebraic equations as stated in Sec. 2.4.1, and the trim unknowns $\mathbf{X}$ were included as design variables. Therefore, the optimization problem was formulated as follows: Minimize the norm of 4/rev in-plane hub shears, F_{4P}

$$F(\mathbf{X}) = \|F_{4P}\|_2 \rightarrow min$$

Subject to

$$\text{Equality Constraints, } h_j(\mathbf{X}) \leq \varepsilon$$

Of the 29 equality constraints, 11 represented the trim conditions for the entire aircraft, 4 for the inflow trim equations, and 14 for the main rotor equations. The vector $\mathbf{X}$ of design variables was composed of 31 elements, namely, the 29 trim variables, and the sine and cosine magnitudes of the HHC input. The initial solution was obtained from an algebraic trim procedure without a HHC input, and therefore it was always feasible. The optimization was carried out using a modified method of feasible directions [55], as implemented in the code DOT [56]. The numerical properties of this formulation proved to be extremely poor. Convergence was very slow, and the software often terminated the optimization for lack of progress. After unsuccessfully trying several variations of the baseline process, this formulation was abandoned.

A different approach to the optimization process proved much more successful. The problem was formulated as an *unconstrained* minimization:

$$F(\mathbf{X}) = \|F_{4P}\|_2 \rightarrow min$$

Subject to

Unconstrained optimization

with a vector $\mathbf{X}$ of design variables consisting of just 2 elements, namely the sine and cosine magnitudes of the HHC input. This way, the trim procedure was decoupled from the optimization, and it was simply executed separately for every value of $\mathbf{X}$ proposed by the optimizer. The optimization was carried out using a Broyden-Fletcher-Goldfarb-Shanno (BFGS) algorithm [55], as implemented in the code DOT.

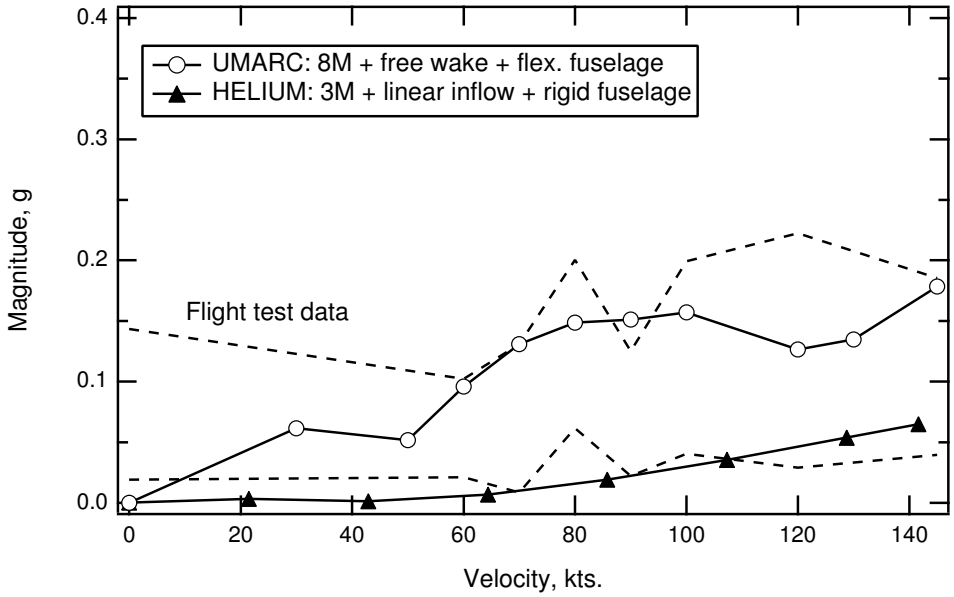

(a) Pilot station vibration level

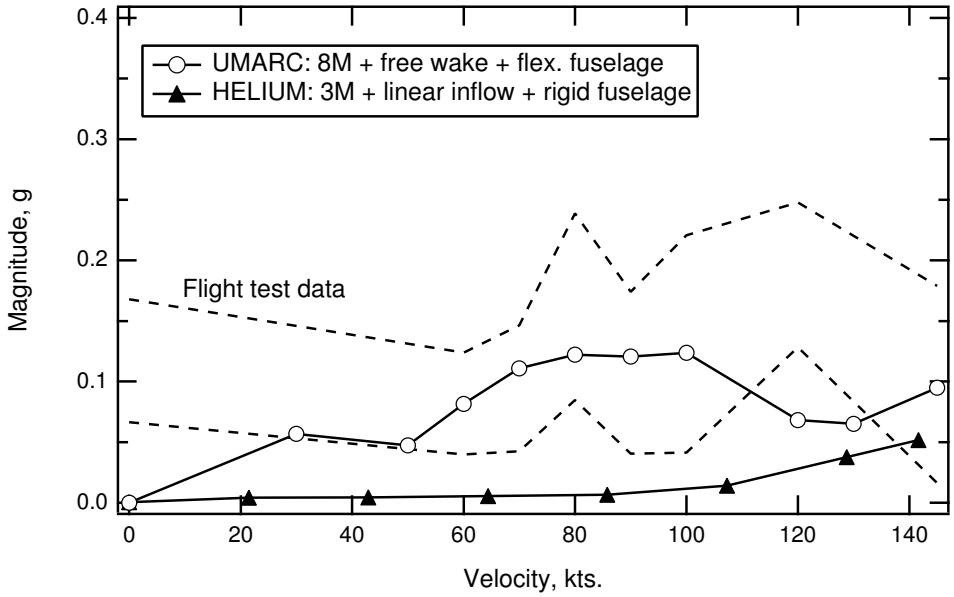

(b) Copilot station vibration level

Figure 2.1: Cockpit vibration comparison; 18,000 lb, linear inflow model, rigid fuselage

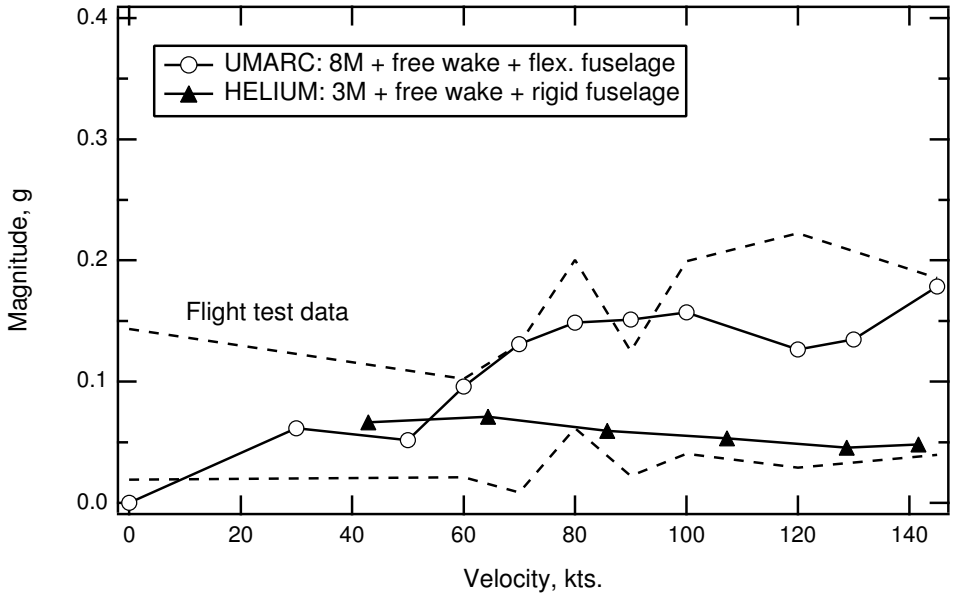

(a) Pilot station vibration level

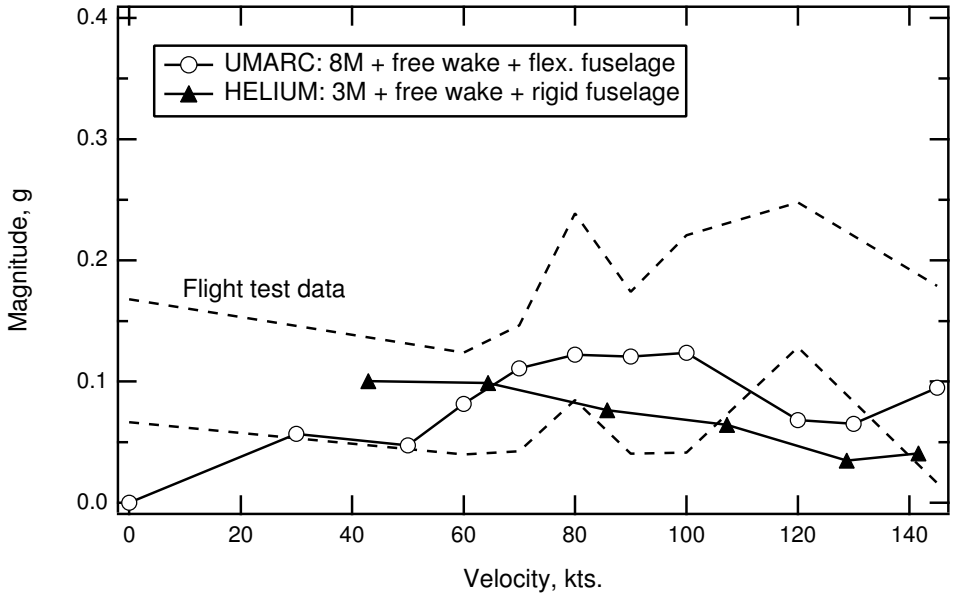

(b) Copilot station vibration level

Figure 2.2: Cockpit vibration comparison; 18,000 lb, free wake model, rigid fuselage

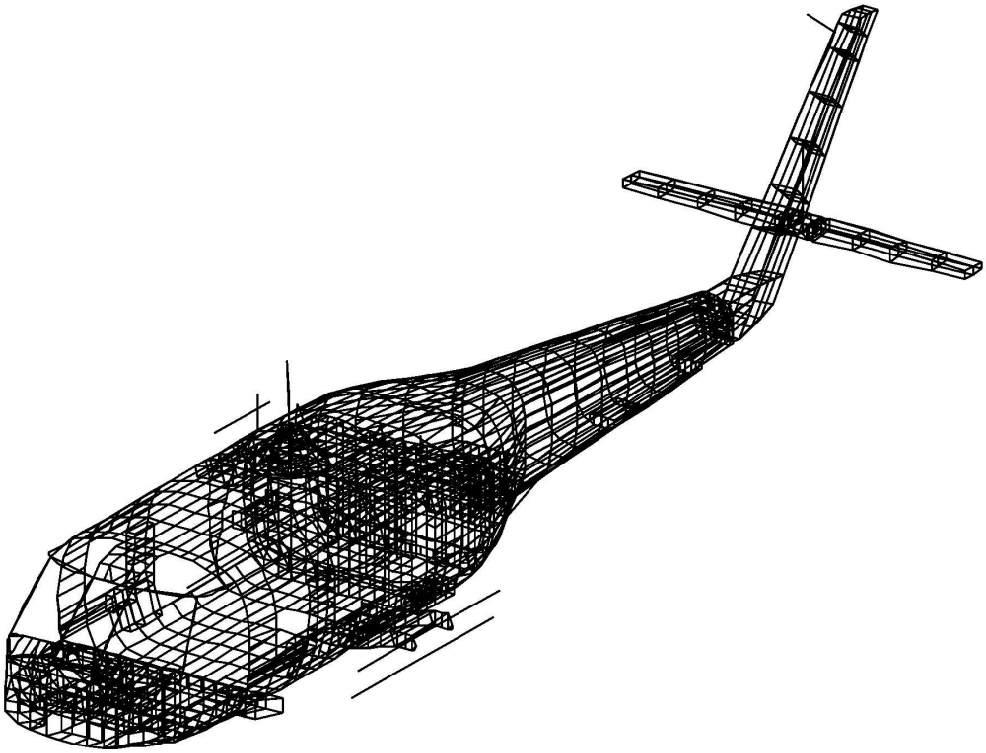

Figure 2.3: SH-60 fuselage NASTRAN model; Courtesy of M. Yang and I. Chopra

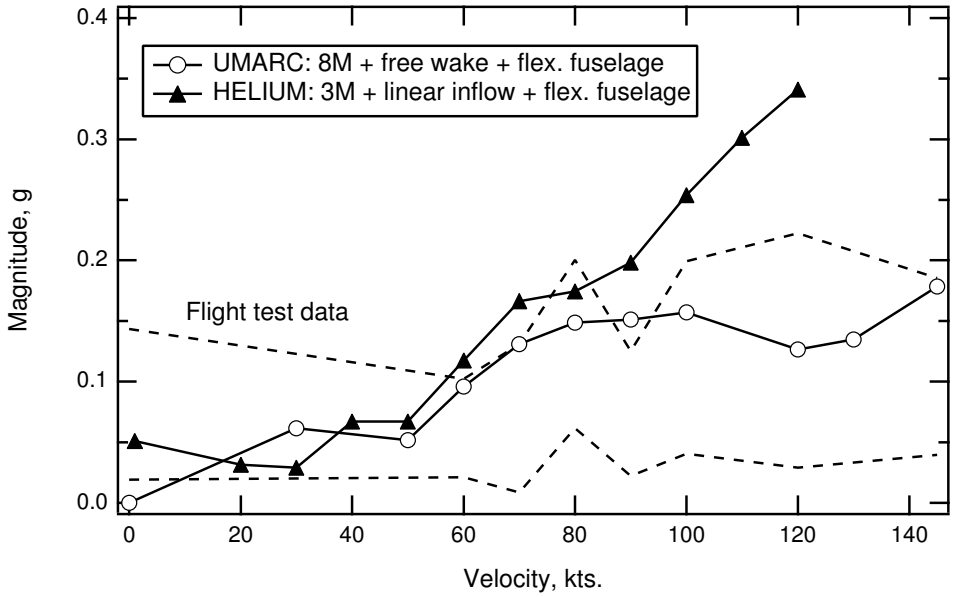

(a) Pilot station vibration level

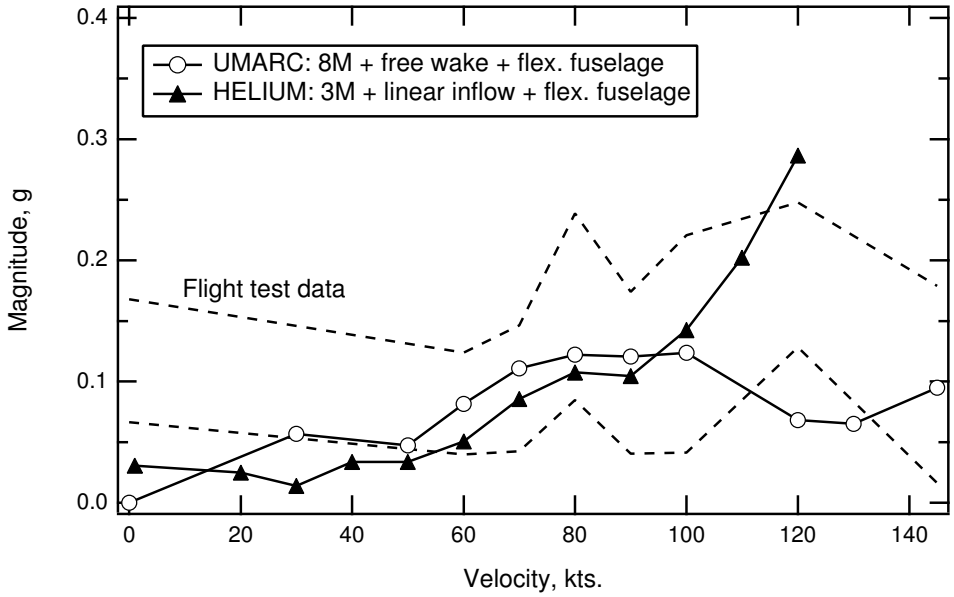

(b) Copilot station vibration level

Figure 2.4: Cockpit vibration comparison; 18,000 lb, linear model model, flexible fuselage

Chapter 3

Active Rotor Control System for Vibration Suppression

The active rotor control system is implemented in the nonlinear helicopter simulation as shown in Figure 3.1. This loop consists of three main parts: the harmonic analyzer, the HHC controller, and the discrete HHC update. Because the final higher harmonic control (HHC) and automatic flight control systems (AFCS) interaction study (Chapter 5) is performed in the continuous linear time-invariant system, each component in the feedback path is converted to an equivalent linear model.

This chapter is divided into three main parts. The first describes the function of the harmonic analyzer and its linear time-invariant equivalent model. The second describes the algorithm of a HHC controller for the steady-state vibration suppression. The third section describes the discrete HHC update and its linear time-invariant equivalent system.

3.1 Harmonic analyzer

In several research studies, the method of extracting n/rev vibration components is using the harmonic analyzer. The harmonic analyzer can be formulated by using either an analog bandpass filter [6, 9, 32] or a Fourier analyzer [7, 10, 29, 30, 57].

3.1.1 Analog bandpass filter method

This type of harmonic analyzer consists of three components: a bandpass filter, demodulator, and a lowpass filter (Figure 3.2a). An analog filter operates on continuous-time signals, and it provides a continuous sensor output without the effect of the sampling window (Sec. 3.1.3) that is typically associated with Fourier analysis.

First, the analog bandpass filter extracts the spectral band of interest from the source signal. This spectral band is centered on 4/rev frequency and has a width of ω_{BW}. The pre-filtered signal is demodulated by multiplying the exact 4/rev harmonic frequencies. The resultant signal contains all the sum and difference frequencies created by the multiplication. Last, the lowpass filter removes frequency above $\omega_{BW}/2$ with an assumption $\omega < \omega_{BW}/2$.. The following example illustrates this process. Let $Z_{4P}(t)$ be one of the spectrum band of some general non-periodic hub load signal $Z(t)$.

$$Z_{4P}(t) = A_4 \cos(4\Omega t + \omega t) \tag{3.1}$$

where A_4 is the 4/rev amplitude, Ω is the rotor speed in radian per second, and ωt is the 4/rev phase angle in radian. Although the hub loads in a trim condition are restricted to periodic waveforms, there is no such restriction during gusts and maneuvers in which the hub loads may contain significant non-periodic transients.

Therefore, the source signal $Z(t)$ is first screened through the bandpass filter to extract its components near the 4/rev frequency, i.e., more precisely, in the range of $4\Omega - \omega_{BW}/2$ and $4\Omega + \omega_{BW}/2$. This pre-filtered signal is called $Z_{4P}(t)$ and can be written in the form of Eq. (3.1). Next, the pre-filtered signal is demodulated, i.e., multiplied by $\cos 4\Omega t$ and $\sin 4\Omega t$ as follows:

$$\begin{aligned} \hat{A}_{4c} &= Z_{4P}(t)\cos 4\Omega t \\ &= \frac{1}{2}A_4[\cos(\omega t) + \cos(8\Omega t + \omega t)] \qquad (3.2) \\ \hat{A}_{4s} &= Z_{4P}(t)\sin 4\Omega t \\ &= \frac{1}{2}A_4[-\sin(\omega t) + \sin(8\Omega t + \omega t)] \qquad (3.3) \end{aligned}$$

The demodulated signals $\hat{A}_{4c}$ and $\hat{A}_{4s}$ are passed through the lowpass filter to remove all frequencies above $\omega_{BW}/2$ and doubled with an assumption $\omega < \omega_{BW}/2$. The resultant signal is given by Eq. (3.4) and (3.5).

$$A_{4c} = A_4\cos(\omega t) \qquad (3.4)$$

$$A_{4s} = -A_4\sin(\omega t) \qquad (3.5)$$

Eq. (3.1) can be rewritten, using Eq. (3.4) and Eq. (3.5), as

$$\begin{aligned} Z_{4P}(t) &= A_4\cos(4\Omega t + \omega t) \\ &= A_4\cos(\omega t)\cos(4\Omega t) - A_4\sin(\omega t)\sin(4\Omega t) \\ &= A_{4c}\cos(4\Omega t) + A_{4s}\sin(4\Omega t) \qquad (3.6) \end{aligned}$$

Using analog bandpass filter to extract the 4/rev signal adds a large time delay to the system because the method requires a high order bandpass filter with narrow passband width (small ω_{BW}) to extract the steady-state vibration value. The analog harmonic analyzer does not present a problem for steady-state vibration extraction; however, the large time delay will mask all the transient responses.

3.1.2 Fourier analyzer method

Another method of extracting the harmonic components out of the source signal is using a Fourier analyzer, which is also the one used in this study. This type of harmonic analyzer also consists of three components: a sample window, the Fourier analyzer, and a lowpass filter (Figure 3.2b). The sample window serves as the data buffer which stores the incoming data streams. Next, the Fourier analyzer identifies the harmonic contents of the source signal within the sample window. This Fourier analyzer can be either a Fourier series approximation or a Fourier transform in either the continuous-time or discrete-time domain. Last, the lowpass filter is used to removes the undesired frequency contents above n/rev frequency. Because the HHC/AFCS interaction study is performed in the continuous-time domain system, the Fourier series approximation method is chosen as the Fourier analyzer within the harmonic analyzer. Nevertheless, one can use the Fourier transform (such as FFT, Appendix B) as the Fourier analyzer for the digital version of the harmonic analyzer.

The theory of Fourier series approximation lies in the idea that most signals, and all engineering signals, can be represented as a sum of sine waves:

$$f(t) = \frac{1}{2}a_0 + \sum_{n=1}^{\infty}[a_n \cos(2\pi n f t) + b_n \sin(2\pi n f t)]$$

with

$$\begin{aligned} a_n &= \frac{2}{T}\int_0^T f(t)\cos(2\pi n f t)\ \mathrm{d}t, \qquad n = 0, 1, 2, \ldots \\ b_n &= \frac{2}{T}\int_0^T f(t)\sin(2\pi n f t)\ \mathrm{d}t, \qquad n = 1, 2, 3, \ldots \end{aligned} \tag{3.7}$$

where T is the fundamental period and $f = 1/T$ is the fundamental frequency in Hz. For example, the vertical vibratory hub load F_Z can be approximated using the

finite version of Eq. (3.7) that will pass through N data values in one fundamental period:

$$F_Z(k\Delta t) \;=\; \overline{F_Z} + \sum_{n=1}^{N/2} F_{Znc}\cos\left(\frac{2\pi nk}{N}\right) + \sum_{n=1}^{(N/2)-1} F_{Zns}\sin\left(\frac{2\pi nk}{N}\right) \tag{3.8}$$

with

$$t = k\Delta t, \quad k = 1, 2, \ldots, N, \quad \text{where} \quad \Delta t = T/N \tag{3.9}$$

$$\overline{F_Z} = \frac{1}{N}\sum_{k=1}^{N} F_Z(k\Delta t) \tag{3.10}$$

$$F_{Znc} = \frac{2}{N}\sum_{k=1}^{N} F_Z(k\Delta t)\cos\left(\frac{2\pi nk}{N}\right), \qquad n = 1, 2, \ldots, \frac{N}{2} - 1 \tag{3.11}$$

$$F_{Zns} = \frac{2}{N}\sum_{k=1}^{N} F_Z(k\Delta t)\sin\left(\frac{2\pi nk}{N}\right), \qquad n = 1, 2, \ldots, \frac{N}{2} - 1 \tag{3.12}$$

The fundamental frequency f is the rotor speed Ω in rad/sec or $\Omega/2\pi$ in Hz, and the fundamental period T is $2\pi/\Omega$ second. To extract n/rev components of F_Z, the sampling frequency must be at least twice as fast as n/rev frequency to avoid aliasing problem. In this study, a factor of 6 is chosen which leads to a sampling frequency of $(6n\Omega/2\pi)$ Hz.

For a rotor with four identical blades and zero tracking error[1], the only frequencies transmitted to the fixed system are the four multiples per revolution (4/rev, 8/rev, 12/rev ...). Therefore, the sampling frequency required to extract F_{Z4c} and F_{Z4s} of the Sikorsky UH-60 helicopter with a nominal rotor speed Ω=27 rad/sec is $f_s = 6n\Omega/2\pi = (6 * 4 * 27)/2\pi = 103Hz$ or $N = 24$ sample data per rotor revolution. Although the major vibratory hub loads interested in this study have a 4/rev frequency, the study is also monitoring the 8 and 12/rev

[1]The main rotor blades are all flying in the same tip-path-plane and maintain equidistant angular spacings during flight.

frequency, which are the second and third harmonics transmitted to the fixed system for a four-bladed helicopter. In that case, the sampling frequency required is $f_s = 6n\Omega/2\pi = (6 * 12 * 27)/2\pi = 310Hz$ or $N = 72$ sample data per rotor revolution.

The calculation of the Fourier coefficients is very time consuming since it requires N^2 number of function evaluations. To reduce the computation time, the most frequently used algorithm for real-time applications is the fast Fourier transform (FFT, Appendix B). It is a discrete Fourier transform that reduces the number function evaluation from N^2 to $N \log N$. Since the helicopter simulation program used in this study is in the continuous-time domain and it is not a real-time simulation, the simulation time does not advance to the time frame until the Fourier series calculations is finished. Therefore, the additional computation time required for the Fourier series calculations has no impact on 4/rev vibration extraction.

The lowpass filter implemented in this harmonic analyzer is a 4^{th} order Bessel lowpass filter with the break frequency ω_o at 6.5/rev. The 6.5/rev break frequency is chosen to produce a -12 dB magnitude drop between 4/rev and 8/rev signals. Additional information about Bessel filter will be discussed in Sec. 3.1.4.

Using the Fourier analyzer (either Fourier series approximation or FFT method) to extract the 4/rev signals adds delays to the system. The source of delay is from the sample window, which is discussed the next section.

3.1.3 Effect of windowing

When performing a digital harmonic analysis with a physical system, a sample window must be used, because it is necessary to truncate long data streams to a

finite size. The size of the window has a significant effect on the accuracy of the extraction of the desired frequency components. A large window; i.e., a window that extends over a long time, increases the accuracy of the low-frequency components identification but degrades the high-frequency ones. On the other hand, a small window high-frequency components identification but degrades the low-frequency. Generally, the minimum window size is one cycle of the source signal. For the 4/rev hub load study, the minimum sample window is equal to quarter revolution. However, a sample window of one revolution (4 cycles of the source signal) was used in this study. As the rotor rotates beyond its first revolution, the sample window advances continuously with it.

Figure 3.3 illustrates the time delay introduced by the sample window. The vertical hub load F_Z, shown in the second figure, starts from a trim condition without HHC input for the first two revolutions. At the end of the second revolution, a 4/rev HHC input is added (this is an arbitrary input, which will not necessarily reduce vibrations), and the helicopter reaches the new steady state condition. In the third revolution, F_Z has reached the steady state almost instantaneously. Although there is a low frequency drift, mainly 1/rev response, the third revolution is mostly dominated by the 4/rev response, and it is very close to the new steady state condition. The spectral analysis performed on third revolution also confirms this finding and the result is shown in the third figure. However, according to online Fourier analysis with a moving sample window (fourth figure), $F_{Z_{4C}}$ and $F_{Z_{4S}}$ take approximately one rotor revolution to reach the new steady state condition. This does not agree with the result stated earlier. The cause of this difference is the sample window. In other words, the sample window behaves as a lowpass filter, which adds large time delay and masks all the transient responses.

3.1.4 Equivalent lowpass filter

A window essentially behaves as a lowpass filter. The sample window used in the study is based on the rectangular or "box car" window. Figure 3.4a is the rectangular window, $h(t)$, in time domain which has a window size of $2T_0$. Its expression is given by:

$$h(t) = \begin{cases} A & |t| < T_0 \\ 0 & |t| \geq T_0 \end{cases} \tag{3.13}$$

and its Fourier transform is given by:

$$\begin{aligned} H(f) &= \int_{-T_0}^{T_0} h(t)\, e^{-2j\pi ft} dt \\ &= A\int_{-T_0}^{T_0} \cos(2\pi ft) dt - jA\int_{-T_0}^{T_0} \sin(2\pi ft) dt \\ &= 2AT_0 \frac{\sin(2\pi T_0 f)}{2\pi T_0 f} \end{aligned} \tag{3.14}$$

where f is the frequency in Hz. Figure 3.4b shows that the Fourier transformation of a rectangular waveform consists of a central lobe which contains most of the energy of the window and the side lobes which generally decay rapidly. The magnitude difference of the first two lobes is 13.4 dB (79% reduction) with a break frequency at $1/2T_0$ Hz.

Eq. (3.14) is a closed form solution, and it is a function of frequency. For the LTI system analysis, Eq. (3.14) can be approximated by an equivalent lowpass filter. The equivalent lowpass filter chosen is the Bessel filter because it has the following characteristics:

- k poles and no zeros
- DC gain = 1
- break frequency = ω_o

- ,maximally flat group delay about 0 Hz, and the phase response is approximately linear in the passband
- the linearity degrades at the higher frequencies, and the group delay drops to zero
- no overshoot around break frequency

For the Sikorsky UH-60 helicopter, the Bessel filter chosen is a 4^{th} order function with the break frequency ω_o at $1/2T_0$. $2T_0$ is the length of the sample window, which is equal to the time to complete one rotor revolution.

The frequency response comparison $H(f)$ of the rectangular window and that of the Bessel filter are compared in Figure 3.4c. The Bessel filter low-passes the signal at a break frequency ω_o of 4.3 Hz and produces a frequency drop off similar to the rectangular sample window. Note that the Bessel filter designed in this section is only implemented in an LTI system analysis to mimic the dynamics and the time delay of the actual rectangular sample window.

3.2 Higher harmonic control algorithm

3.2.1 *T*-matrix method

The closed-loop HHC algorithm implemented is based on the fixed-gain T-matrix feedback controller:

$$\mathbf{Z}_{4P}(k) = \mathbf{Z}_{4P}(k-1) + T\left[\boldsymbol{\theta}_{hhc}(k) - \boldsymbol{\theta}_{hhc}(k-1)\right] \tag{3.15}$$

Eq. (3.15) is a difference equation for discrete-time domain system. The variable k is the discrete-time index, while $\mathbf{Z}_{4P}$ is the vibration response vector consisting

of cosine and sine components of 4/rev vibratory hub loads excluding the 4/rev yawing moments:

$$\mathbf{Z}_{4P} = [F_{X_{4C}}, F_{X_{4S}}, F_{Y_{4C}}, F_{Y_{4S}}, F_{Z_{4C}}, F_{Z_{4S}}, M_{X_{4C}}, M_{X_{4S}}, M_{Y_{4C}}, M_{Y_{4S}}]^T \tag{3.16}$$

and it is a function of the state vector $\mathbf{x}$, the pilot inputs $\boldsymbol{\theta}_{pilot}$, and the HHC inputs $\boldsymbol{\theta}_{hhc}$

$$\mathbf{Z}_{4P} = \mathbf{f}(\mathbf{x}, \boldsymbol{\theta}_{pilot}, \boldsymbol{\theta}_{hhc}) \tag{3.17}$$

$$\boldsymbol{\theta}_{pilot} = [\delta_{lat}, \delta_{lon}, \delta_{col}, \delta_{ped}]^T \tag{3.18}$$

$$\boldsymbol{\theta}_{hhc} = [\theta_{3C}, \theta_{3S}, \theta_{4C}, \theta_{4S}, \theta_{5C}, \theta_{5S}]^T \tag{3.19}$$

The T-matrix is the Jacobian of function $\mathbf{f}$ computed about a reference input vector, $\boldsymbol{\theta}_{hhc_o}$:

$$T = \left.\frac{\partial \mathbf{f}}{\partial \boldsymbol{\theta}}\right|_{\boldsymbol{\theta}_{hhc_o}} \tag{3.20}$$

In other words, T is a linear approximation of the 4/rev vibration response $\mathbf{Z}_{4P}$ to the HHC inputs $\boldsymbol{\theta}_{hhc}$ at a steady-state condition. That is, Eq. (3.20) assumes that the changes in the vibration response $\Delta\mathbf{Z}_{4P}$ with respect to the changes in the HHC input $\Delta\boldsymbol{\theta}_{hhc}$ are linear over the entire range of $\boldsymbol{\theta}_{hhc}$. This relationship is can be written as

$$\Delta\mathbf{Z}_{4P} = T\ \Delta\boldsymbol{\theta}_{hhc} \tag{3.21}$$

In this study, the helicopter is trimmed without the HHC input; therefore, the reference input vector $\boldsymbol{\theta}_{hhc_o}$ is a zero vector, and the $\Delta\boldsymbol{\theta}_{hhc}$ in Eq. (3.21) is the same as $\boldsymbol{\theta}_{hhc}$. Total 4/rev vibration approximated using T-matrix method is given by

$$\mathbf{Z}_{4P} = \mathbf{Z}_{4P_0} + T\ \boldsymbol{\theta}_{hhc} \tag{3.22}$$

where $\mathbf{Z}_{4P_0}$ is the 4/rev vibrations of the nonlinear baseline (HHC-off) case.

For vibration suppression, the optimal control is obtained by minimizing the cost function J:

$$J = \frac{1}{2}\ \mathbf{Z}_{4P}^{T}(k)\ Q\ \mathbf{Z}_{4P}(k)\ +\ \frac{1}{2}\ \boldsymbol{\theta}_{hhc}^{T}(k)\ R\ \boldsymbol{\theta}_{hhc}(k) \tag{3.23}$$

where Q and R are the weighting matrices on the responses and controls:

$$Q\ =\ diag\{1,\ 1,\ 1,\ 1,\ 1,\ 1,\ q_7, \ldots,\ q_{10}\} \tag{3.24}$$

$$R\ =\ diag\{1,\ 1,\ 1,\ 1,\ 1,\ 1\} \tag{3.25}$$

and $q_7, \ldots, q_{10} = 1/\Delta z_{cg}^2$ where Δz_{cg} is the vertical displacement of the rotor hub to the center of gravity of the helicopter. The choice of the weighting $1/\Delta z_{cg}^2$ transforms the moments to the equivalent forces. The optimal control is computed by setting the first derivative of the cost function of Eq. (3.23) to zero and solving for the optimal HHC input:

$$\frac{\partial J}{\partial \boldsymbol{\theta}} = 0 \tag{3.26}$$

With this scheme, the HHC input is computed based on the current response vector:

$$\boldsymbol{\theta}(k) =\ T^{\dagger}\ T^{T}\ \boldsymbol{\theta}(k-1)\ -\ T^{\dagger}\ \mathbf{Z}_{4P}(k-1) \tag{3.27}$$

where the fixed-gain regulator is

$$T^{\dagger} =\ (T^{T}\ Q\ T\ +\ R)^{-1}\ T^{T}\ Q \tag{3.28}$$

If $R = \mathbf{0}$ or $T^T Q T \gg R$, $T^{\dagger}$ is a pseudo-inverse of T, and Eq. (3.27) becomes

$$\boldsymbol{\theta}(k)\ =\ \boldsymbol{\theta}(k-1)\ -\ T^{\dagger}\ \mathbf{Z}_{4P}(k-1) \tag{3.29}$$

3.2.2 *T*-matrix validation

As stated before, T-matrix is a linear approximation of the 4/rev vibration response $\mathbf{Z}_{4P}$ to the HHC inputs $\boldsymbol{\theta}_{hhc}$ at a steady-state condition. The total 4/rev vibration

response $\mathbf{Z}_{4P}$ of the nonlinear model and that of the T-matrix approximation are compared in Figure 3.5-3.7 for 3, 4, and 5/rev inputs to determine the accuracy of the T-matrix approximation. The total 4/rev vibration response $\mathbf{Z}_{4P}$ of the nonlinear model at the steady-state condition was computed for a HHC input, and the 4/rev vibration response was extracted from the helicopter hub loads using Fourier series approximation. The total 4/rev vibration response $\mathbf{Z}_{4P}$ of the T-matrix approximation is computed using Eq. (3.22) where $\mathbf{Z}_{4P_0}$ is the 4/rev vibrations of the baseline (HHC-off) case from the nonlinear simulation. The HHC input for the both methods has an amplitude of 1° with a phase angle varying from 0° to 360° with an increment of 30°.

The diamond symbol represents the baseline (HHC-off) 4/rev vibration responses $\mathbf{Z}_{4P_0}$ from the nonlinear model, and their values are tabulated in Table 3.1. The open circles represent the vibration responses from the nonlinear model with the HHC inputs engaged; the solid circles represent the vibration responses from T-matrix approximation based on Eq. (3.22) with $\boldsymbol{\theta}_{hhc}$ determined from Eq. (3.29). The number next to the symbol is the n/rev input phase angle.

These figures illustrate the 4/rev vibration prediction error resulting from the T-matrix approximation. For the 3/rev case (Figure 3.5), the 4/rev vibration responses from the T-matrix approximation match well with the ones from the nonlinear model. For the 4/rev and 5/rev cases, there are some differences between the two methods. The difference is from the earlier assumption that the vibration response to the HHC input is linear over the entire range of $\boldsymbol{\theta}_{hhc}$. Since the vibration responses to the HHC inputs are not necessary linear, the small differences between linear and nonlinear models are expected.

3.3 Discrete HHC update

The ideal HHC inputs computed by the T-matrix controller for vibration suppression are not returned to the rotor system at every time step. The HHC input has a discrete update rate which typically varies from 0.5 to 16 times per rotor revolution [5–10]. A typical HHC input update rate is once-per-revolution. In the discrete-time domain, the discrete HHC update is performed by the sample-and-hold operation. To implement this in a continuous-time domain system, the effect of the sample-and-hold operation must be approximated in the continuous-time domain.

Figure 3.8 illustrates the effect of a sample-and-hold operation on a continuous signal. The sampler transforms the continuous signal to an amplitude-modulated pulse signal at a sample rate ω_s. At the output of the digital controller, the digital signal must be converted to analog signal by the process called digital-to-analog conversion. The simplest device that transforms a digital input to an analog output is a zero-order-hold. The bottom of Figure 3.8 shows the relationship between the digital input and the analog output. The zero-order-hold holds the value of the sampled signal over T_s second to produce a reconstructed signal with *staircase* waveform. Notice that an approximation to the reconstructed signal is identical to the original signal with a delay of $T_s/2$ second. Therefore, a zero-order-hold operating at a sample rate ω_s is equivalent to a time delay of π/ω_s second. Similarly, the discrete HHC input operating at ω_{s2} frequency also can be approximated by a Padé function with a time delay of π/ω_{s2} second.

	4P Cos-Comp.	4P Sin-Comp.	Amplitude
F_X (lb)	151.6	87.8	175.2
F_Y (lb)	73.5	-61.3	95.7
F_Z (lb)	39.5	8.9	40.5
M_X (ft-lb)	40.1	62.6	74.3
M_Y (ft-lb)	80.0	30.2	85.5

Table 3.1: Baseline (HHC-off) Vibration Level

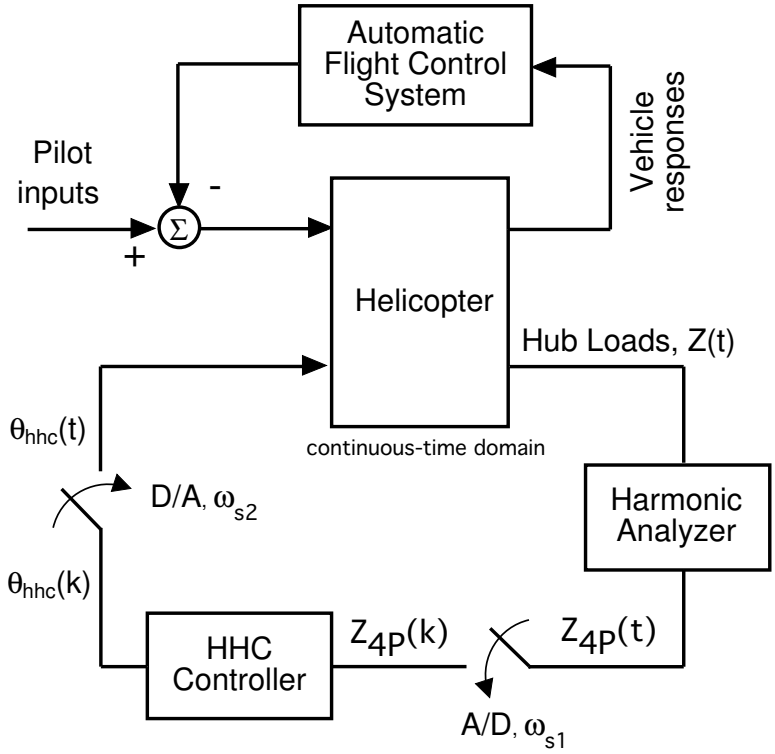

Figure 3.1: Nonlinear simulation scheme; multi-rate system.

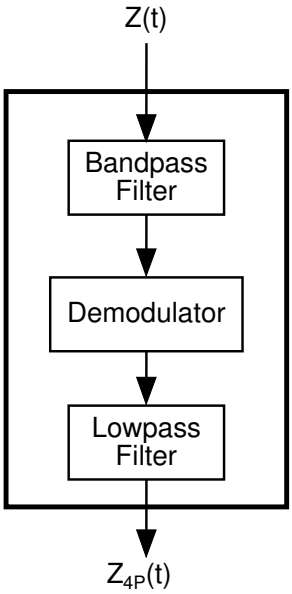

(a) Analog Bandpass Filter Method

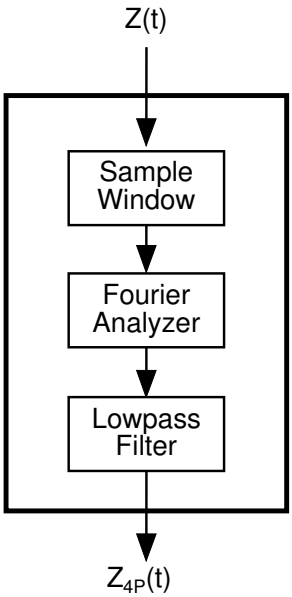

(b) Fourier Analyzer Method

Figure 3.2: Internal components of the harmonic analyzer.

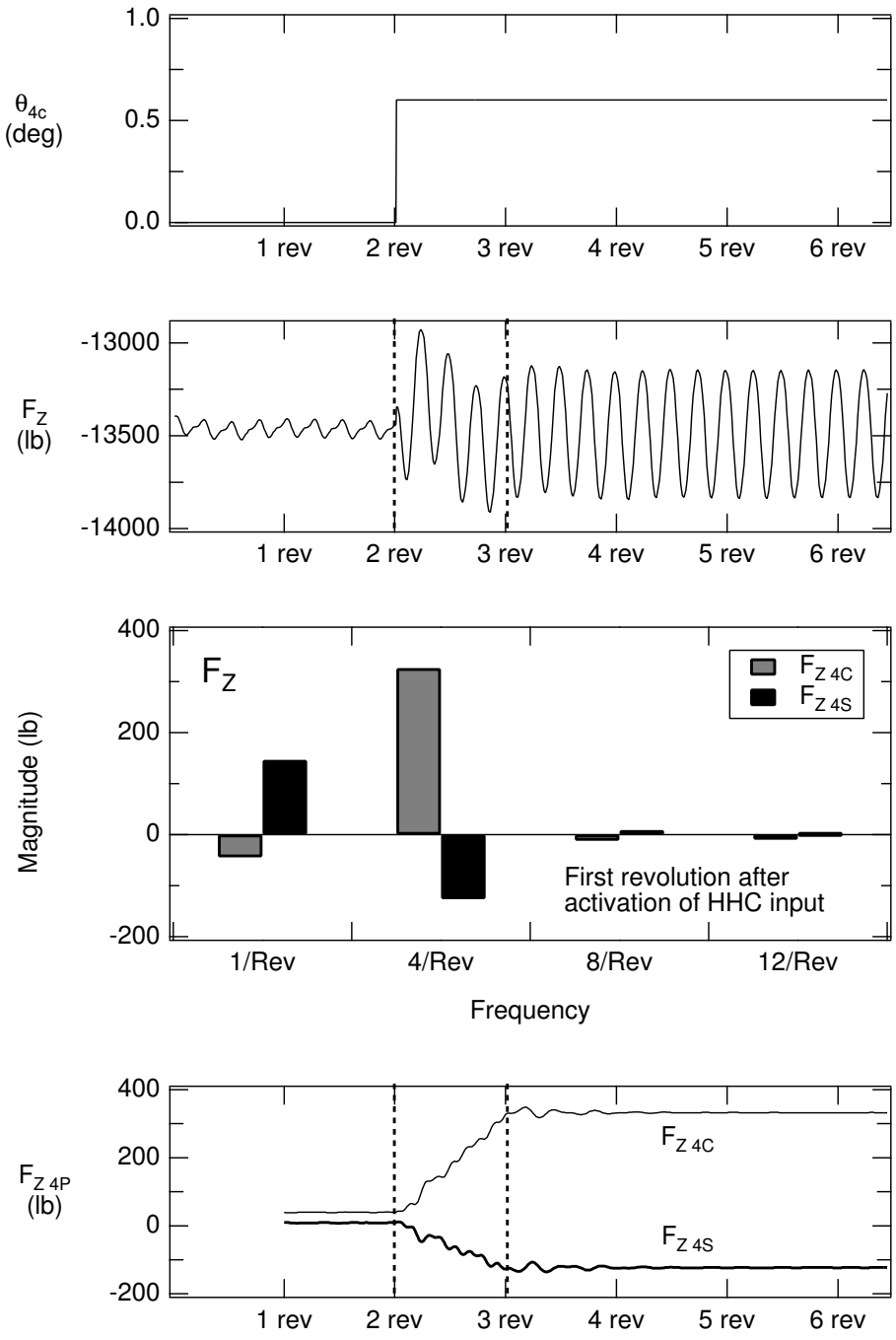

Figure 3.3: Example of the time delay induced by the sample window

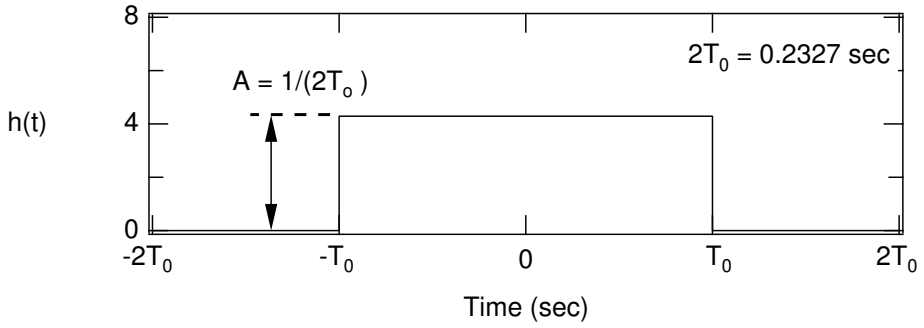

(a) Time Window

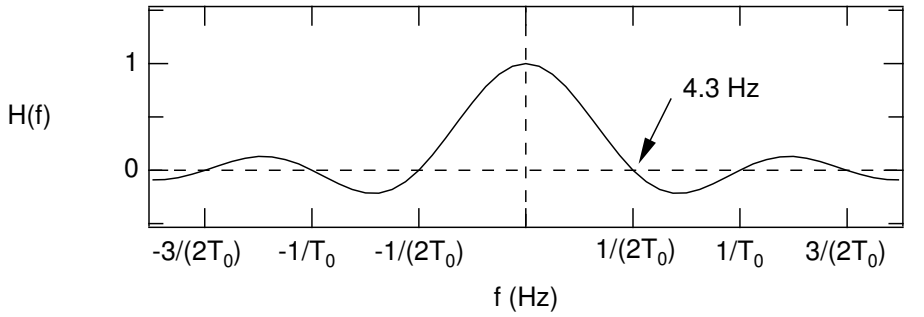

(b) Spectral Window (linear scale)

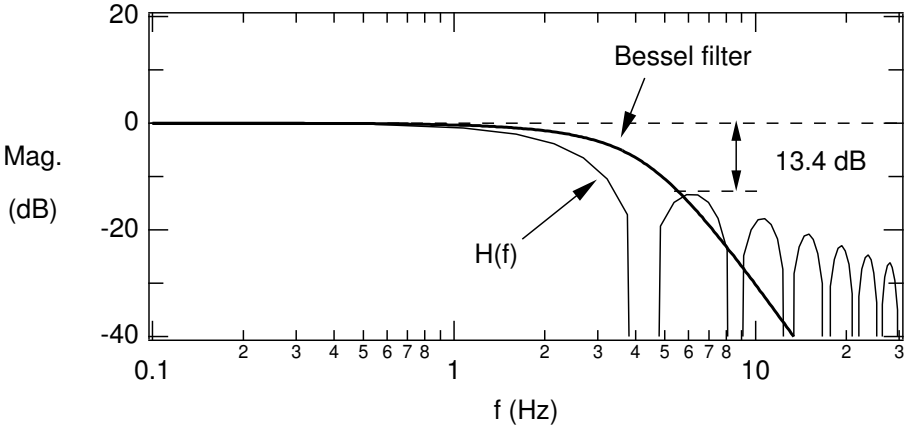

(c) Spectral Window (logarithmic scale)

Figure 3.4: Frequency response of the rectangular window.

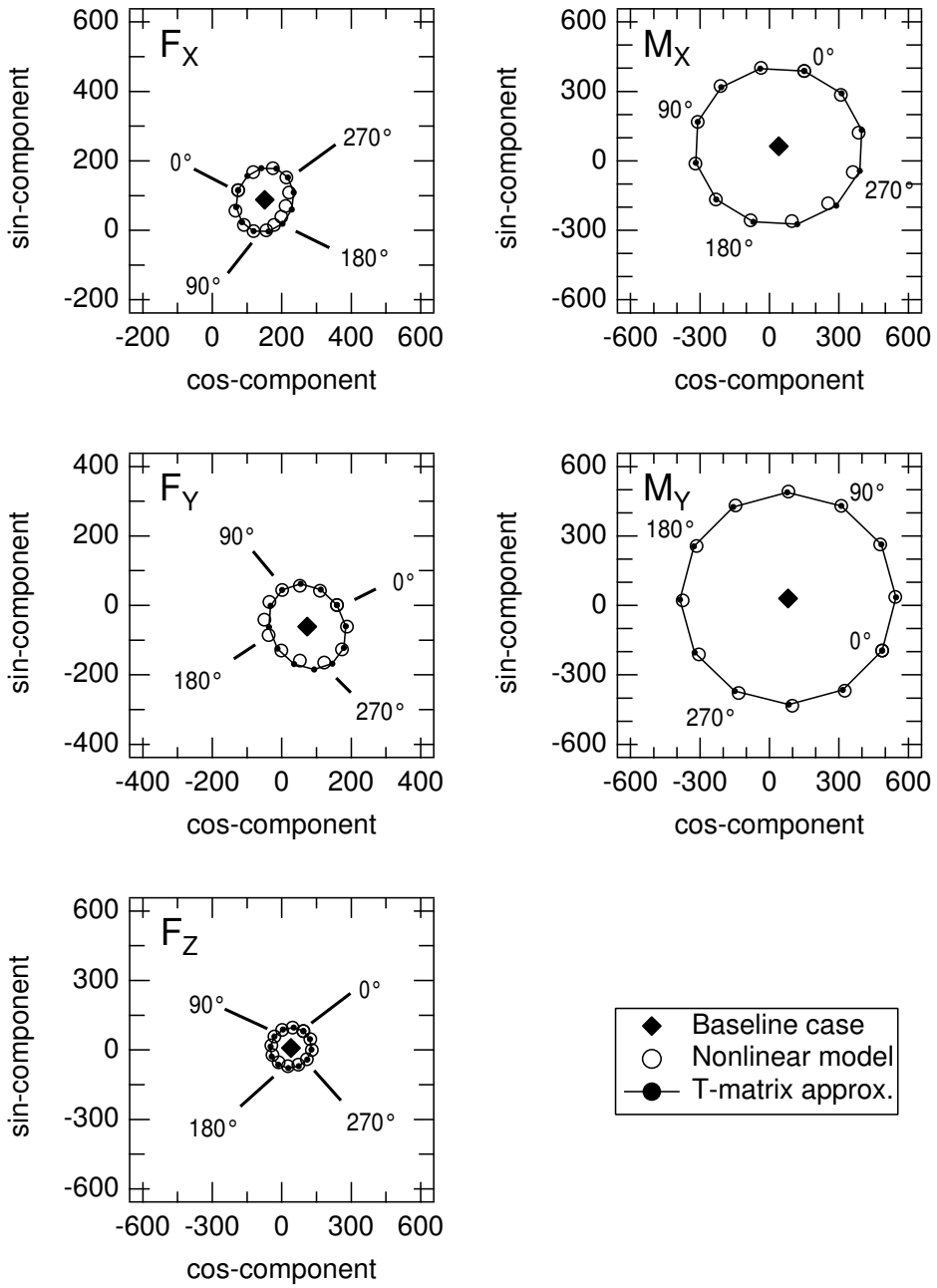

Figure 3.5: 4/rev vibration response comparison; A_3=1°; V=120 kts (μ=0.28), Weight=14,000 lb

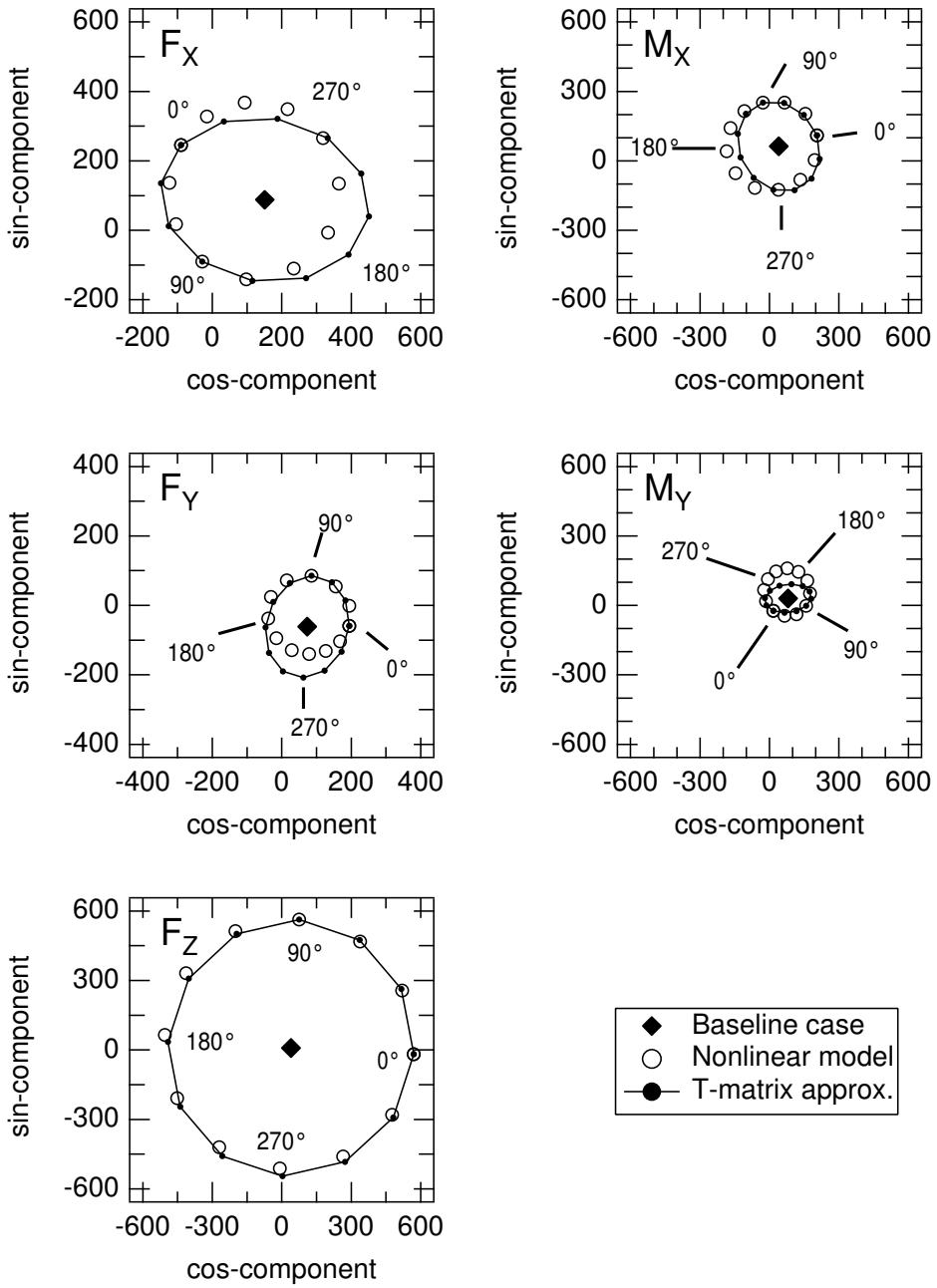

Figure 3.6: 4/rev vibration response comparison; A_4=1°; V=120 kts (μ=0.28), Weight=14,000 lb

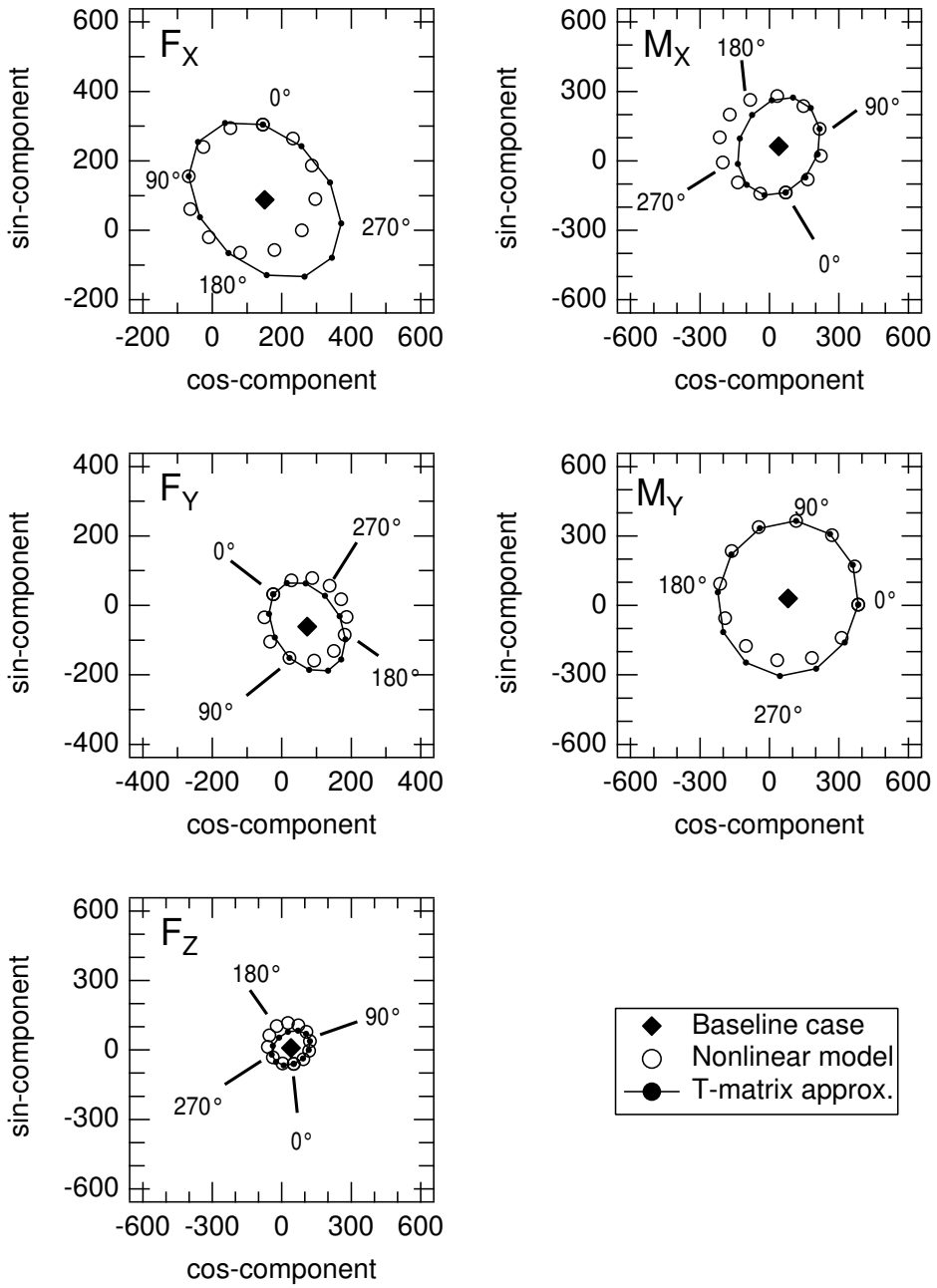

Figure 3.7: 4/rev vibration response comparison; A_5=1°; V=120 kts (μ=0.28), Weight=14,000 lb

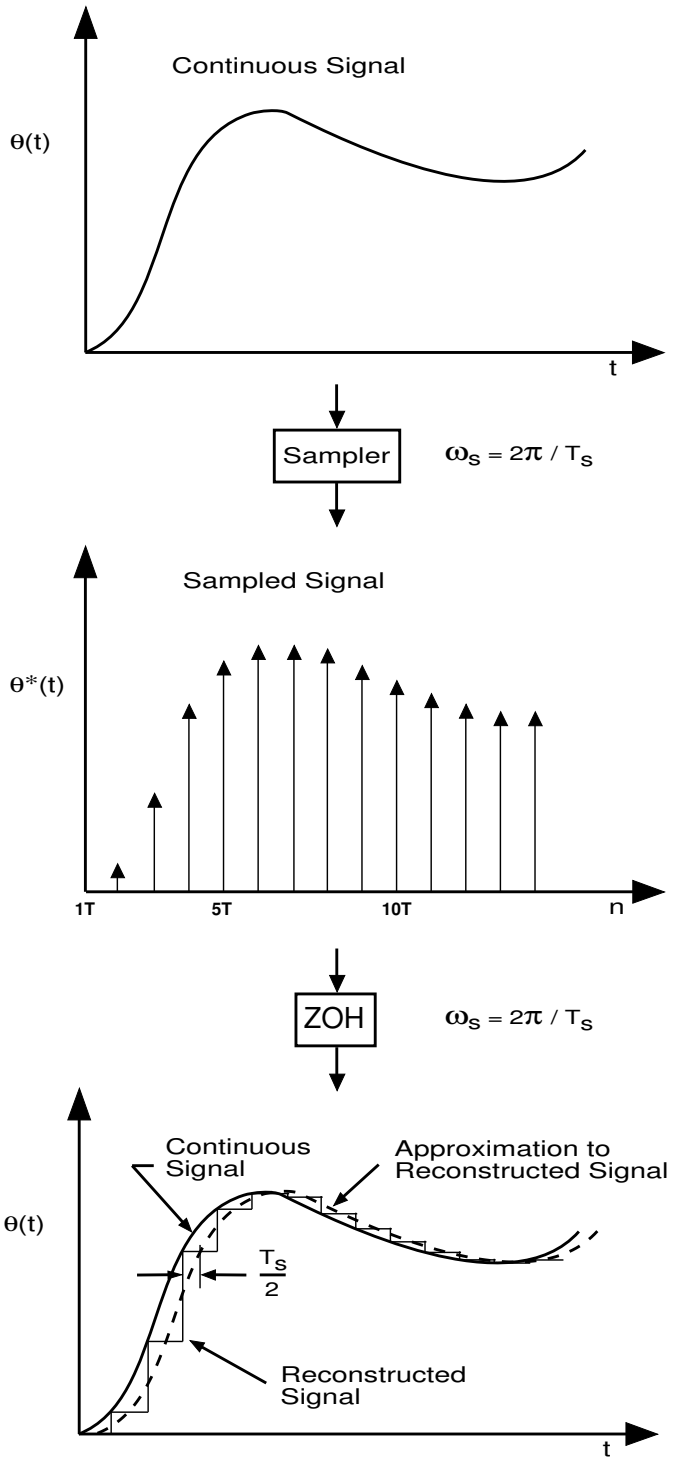

Figure 3.8: Time delay approximation for sample and hold circuit (sampler and zero-order-hold operating at a same rate, ω_s.

Chapter 4

Extraction of the Constant-Coefficient Linearized Model

A key ingredient for the study of potential interactions between HHC and flight control system is a linearized time-invariant model of the helicopter dynamics, including higher harmonic inputs and controls. This chapter contains the derivation of such a model, and is composed of three sections.

The first section summarizes the main steps of the extraction of a conventional linearized model, i.e., one without higher harmonic inputs and controls. The second section extends the derivation to include such higher harmonics, and shows that: (i) one portion of the output equation is the equivalent of the traditional T-matrix, and (ii) through an appropriate formulation of the output equation, the need for online identification and adaptation of the T-matrix in maneuvering flight is substantially reduced. The third section describes the application of the methodology to simple linear rotor equations, for which analytic expressions for the coefficients of the model can be derived.

4.1 Extraction of a linearized model without higher harmonics

Consider the equations of motion of the helicopter written in symbolic form as:

$$\mathbf{f}(\dot{\mathbf{x}}, \mathbf{x}, \mathbf{u}; \psi) = \mathbf{0} \tag{4.1}$$

and take first order differentials

$$\mathrm{d}\mathbf{f}(\dot{\mathbf{x}}, \mathbf{x}, \mathbf{u}; \psi) = \mathbf{0} \tag{4.2}$$

which can be expanded into

$$\left.\frac{\partial \mathbf{f}}{\partial \dot{\mathbf{x}}}\right|_{\dot{\mathbf{x}} = \dot{\mathbf{x}}_0} \mathrm{d}\dot{\mathbf{x}} + \left.\frac{\partial \mathbf{f}}{\partial \dot{\mathbf{x}}}\right|_{\mathbf{x} = \mathbf{x}_0} \mathrm{d}\mathbf{x} + \left.\frac{\partial \mathbf{f}}{\partial \mathbf{u}}\right|_{\mathbf{u} = \mathbf{u}_0} \mathrm{d}\mathbf{u} = \mathbf{0} \tag{4.3}$$

where the subscript $(\ldots)_0$ denotes the trim values of the respective vectors. Replace now $\mathrm{d}(\ldots)$ with $\Delta(\ldots)$ and introduce the notation

$$[E(\psi)] \stackrel{def}{=} \left.\frac{\partial \mathbf{f}}{\partial \dot{\mathbf{x}}}\right|_{\dot{\mathbf{x}} = \dot{\mathbf{x}}_0} \tag{4.4}$$

$$[A_1(\psi)] \stackrel{def}{=} \left.\frac{\partial \mathbf{f}}{\partial \dot{\mathbf{x}}}\right|_{\mathbf{x} = \mathbf{x}_0} \tag{4.5}$$

$$[B_1(\psi)] \stackrel{def}{=} \left.\frac{\partial \mathbf{f}}{\partial \mathbf{u}}\right|_{\mathbf{u} = \mathbf{u}_0} \tag{4.6}$$

Then Eq. (4.3) can be rewritten as:

$$\begin{aligned} \Delta\dot{\mathbf{x}} &= -[E(\psi)]^{-1}[A_1(\psi)]\Delta\mathbf{x} - [E(\psi)]^{-1}[B_1(\psi)]\Delta\mathbf{u} \\ &= [A(\psi)]\Delta\mathbf{x} + [B(\psi)]\Delta\mathbf{u} \end{aligned} \tag{4.7}$$

with $[A(\psi)] \stackrel{def}{=} -[E(\psi)]^{-1}[A_1(\psi)]$ and $[B(\psi)] \stackrel{def}{=} -[E(\psi)]^{-1}[B_1(\psi)]$. The linearized matrices $[E(\psi)]$, $[A_1(\psi)]$, and $[B_1(\psi)]$ can be calculate using finite difference approximations. For example, using central finite differences, the j-th columns of the

matrices $[A_1(\psi)]$, $[B_1(\psi)]$, and $[E(\psi)]$ at the azimuth ψ_i are given by, respectively:

$$\{A_1(\psi_i)\}_j = \left.\frac{\partial \mathbf{f}}{\partial x_j}\right|_{\mathbf{x}=\mathbf{x}_0} \approx \frac{\mathbf{f}(\mathbf{x}_0 + h\mathbf{e}_j; \psi_i) - \mathbf{f}(\mathbf{x}_0 - h\mathbf{e}_j; \psi_i)}{2h} \tag{4.8}$$

$$\{B_1(\psi_i)\}_j = \left.\frac{\partial \mathbf{f}}{\partial u_j}\right|_{\mathbf{u}=\mathbf{u}_0} \approx \frac{\mathbf{f}(\mathbf{u}_0 + h\mathbf{e}_j; \psi_i) - \mathbf{f}(\mathbf{u}_0 - h\mathbf{e}_j; \psi_i)}{2h} \tag{4.9}$$

$$\{E(\psi_i)\}_j = \left.\frac{\partial \mathbf{f}}{\partial \dot{x}_j}\right|_{\dot{\mathbf{x}}=\dot{\mathbf{x}}_0} \approx \frac{\mathbf{f}(\dot{\mathbf{x}}_0 + h\mathbf{e}_j; \psi_i) - \mathbf{f}(\dot{\mathbf{x}}_0 - h\mathbf{e}_j; \psi_i)}{2h} \tag{4.10}$$

where $\mathbf{e}_j$ is a vector with all its elements equal to zero except for the j-th, which is equal to one, and h is the finite difference step size. All the matrices above are periodic, with common period equal to one rotor revolution. Therefore, the state matrix $[A(\psi)]$ and the control matrix $[B(\psi)]$ are also periodic, and can be expanded in Fourier Series:

$$[A(\psi)] = [A_0] + \sum_{k=1}^{K} \left([A_{kc}] \cos k\psi + [A_{ks}] \sin k\psi\right) \tag{4.11}$$

$$[B(\psi)] = [B_0] + \sum_{k=1}^{K} \left([B_{kc}] \cos k\psi + [B_{ks}] \sin k\psi\right) \tag{4.12}$$

If the state vector $\mathbf{x}$ is defined entirely in a fixed coordinate system, then a time invariant linearized model can be obtained by retaining only the constant matrices $[A_0]$ and $[B_0]$. If, additionally, the blades are assumed to be identical, then the summations in Eqs. (4.11) and (4.12) only contain harmonics that are multiples of the number of blades. Therefore, for an N-bladed rotor, $k = N, 2N, 3N, \ldots$

4.2 Extraction of a linearized model with higher harmonics

This section presents the extension of the linearization procedure to the case in which both the state vector $\mathbf{x}$ and the control vector $\mathbf{u}$ contain higher harmonics.

The precise definitions of $\mathbf{x}$ and $\mathbf{u}$ will be introduced first, together with general expressions for the linearized system. The derivation of the control matrix $[B(\psi)]$ will be presented next, because it requires only minor modifications of the baseline procedure of the previous section. Finally, the derivation of the state matrix $[A(\psi)]$, which requires some special treatment, will be presented.

4.2.1 Definitions

The control vector $\mathbf{u}(\psi)$ used in the present study is defined as:

$$\mathbf{u}(\psi) = \begin{bmatrix} \mathbf{u}_{pilot}(\psi) \\ \mathbf{u}_{HHC}(\psi) \end{bmatrix} \tag{4.13}$$

where $\mathbf{u}_{pilot}(\psi)$ is the vector of conventional pilot controls

$$\mathbf{u}_{pilot}(\psi) = [\delta_{lat} \;\; \delta_{lon} \;\; \delta_{col} \;\; \delta_{ped}]^T \tag{4.14}$$

and $\mathbf{u}_{HHC}$ is the vector of higher harmonic controls

$$\mathbf{u}_{HHC}(\psi) = [\theta_{3c} \;\; \theta_{3s} \;\; \theta_{4c} \;\; \theta_{4s} \;\; \theta_{5c} \;\; \theta_{5s}]^T \tag{4.15}$$

The HHC is applied to the blade in the rotating system. For the 4-bladed helicopter configurations used in this research, 3/, 4/, and 5/rev control inputs in the rotating system are required to generate the desired 4/rev inputs in the fixed system. The vector $\mathbf{u}(\psi)$ should be interpreted as "perturbations from the trim values of the controls". The state vector $\mathbf{x}(\psi)$, also representing perturbations from trim values, can be written in the symbolic form:

$$\mathbf{x}(\psi) = \begin{bmatrix} \mathbf{x}_B \\ \\ \mathbf{x}_{MR} \end{bmatrix} \tag{4.16}$$

where $\mathbf{x}_B$ is the vector of states not associated with the main rotor, defined as:

$$\mathbf{x}_B = [u \;\; v \;\; w \;\; p \;\; q \;\; r \;\; \phi \;\; \theta \;\; \psi \;\; \lambda_0 \;\; \lambda_c \;\; \lambda_s \;\; \lambda_{tr} \;\; \nu_x \;\; \nu_y]^T \tag{4.17}$$

and $\mathbf{x}_{MR}$ is the vector of rotor states, defined in a fixed coordinate system. The elements of the rotor state vector are based on the assumption that each state is composed of an average and a 4/rev portion, both azimuth dependent. For example, with the longitudinal rigid body flapping $\beta_{1c}(\psi)$ written as:

$$\beta_{1c}(\psi) = \beta_{1c_{ave}}(\psi) + \beta_{1c_{4c}}(\psi)\cos 4\psi + \beta_{1c_{4s}}(\psi)\sin 4\psi \tag{4.18}$$

the quantities $\beta_{1c_{ave}}(\psi)$, $\beta_{1c_{4c}}(\psi)$, and $\beta_{1c_{4s}}(\psi)$ will be considered as states and included in the rotor portion $\mathbf{x}_{MR}$ of the state vector. The state $\beta_{1c_{ave}}(\psi)$ is equivalent to the longitudinal flap state that would appear in a traditional rotor state vector. The additional higher harmonic states $\beta_{1c_{4c}}(\psi)$ and $\beta_{1c_{4s}}(\psi)$ represent a new way of modeling the effects of higher harmonic control, introduced for the first time in the present research. Although the formulation of Eq. (4.18) appears intuitively reasonable, it will not be justified on a rigorous theoretical basis. However, its validity will be established through simulation, by comparing linearized and nonlinear responses to pilot inputs.

The assumption that each rotor state is composed of an average and a 4/rev portion leads to an expanded state vector defined as follows:

$$\mathbf{x} = \begin{bmatrix} \mathbf{x}_{ave} \\ \\ \mathbf{x}_{4P} \end{bmatrix} \tag{4.19}$$

where $\mathbf{x}_{ave}$ contains the vector $\mathbf{x}_B$ defined in Eq. (4.17) and the average rotor

states, that is:

$$\begin{aligned}\mathbf{x}_{ave} &= \Big[\mathbf{x}_B^T\ \dot{\beta}_{0_{ave}}\ \dot{\beta}_{1c_{ave}}\ \dot{\beta}_{1s_{ave}}\ \dot{\beta}_{2_{ave}}\ \beta_{0_{ave}}\ \beta_{1c_{ave}}\ \beta_{1s_{ave}}\ \beta_{2_{ave}}\ \dots \\ &\quad \dots \dot{\zeta}_{0_{ave}}\ \dot{\zeta}_{1c_{ave}}\ \dot{\zeta}_{1s_{ave}}\ \dot{\zeta}_{2_{ave}}\ \zeta_{0_{ave}}\ \zeta_{1c_{ave}}\ \zeta_{1s_{ave}}\ \zeta_{2_{ave}}\ \dots \\ &\quad \dots \dot{\phi}_{0_{ave}}\ \dot{\phi}_{1c_{ave}}\ \dot{\phi}_{1s_{ave}}\ \dot{\phi}_{2_{ave}}\ \phi_{0_{ave}}\ \phi_{1c_{ave}}\ \phi_{1s_{ave}}\ \phi_{2_{ave}}\ \Big]^T \end{aligned} \tag{4.20}$$

and $\mathbf{x}_{4P}$ contains the 4/rev components, sine and cosine, of the rotor states:

$$\begin{aligned}\mathbf{x}_{4P} &= \Big[\dot{\beta}_{0_{4c}}\ \dot{\beta}_{0_{4s}}\ \dot{\beta}_{1c_{4c}}\ \dot{\beta}_{1c_{4s}}\ \dot{\beta}_{1s_{4c}}\ \dot{\beta}_{1s_{4s}}\ \dot{\beta}_{2_{4c}}\ \dot{\beta}_{2_{4s}}\ \dots \\ &\quad \dots \beta_{0_{4c}}\ \beta_{0_{4s}}\ \beta_{1c_{4c}}\ \beta_{1c_{4s}}\ \beta_{1s_{4c}}\ \beta_{1s_{4s}}\ \beta_{2_{4c}}\ \beta_{2_{4s}}\ \dots \\ &\quad \dots \dot{\zeta}_{0_{4c}}\ \dot{\zeta}_{0_{4s}}\ \dot{\zeta}_{1c_{4c}}\ \dot{\zeta}_{1c_{4s}}\ \dot{\zeta}_{1s_{4c}}\ \dot{\zeta}_{1s_{4s}}\ \dot{\zeta}_{2_{4c}}\ \dot{\zeta}_{2_{4s}}\ \dots \\ &\quad \dots \zeta_{0_{4c}}\ \zeta_{0_{4s}}\ \zeta_{1c_{4c}}\ \zeta_{1c_{4s}}\ \zeta_{1s_{4c}}\ \zeta_{1s_{4s}}\ \zeta_{2_{4c}}\ \zeta_{2_{4s}}\ \dots \\ &\quad \dots \dot{\phi}_{0_{4c}}\ \dot{\phi}_{0_{4s}}\ \dot{\phi}_{1c_{4c}}\ \dot{\phi}_{1c_{4s}}\ \dot{\phi}_{1s_{4c}}\ \dot{\phi}_{1s_{4s}}\ \dot{\phi}_{2_{4c}}\ \dot{\phi}_{2_{4s}}\ \dots \\ &\quad \dots \phi_{0_{4c}}\ \phi_{0_{4s}}\ \phi_{1c_{4c}}\ \phi_{1c_{4s}}\ \phi_{1s_{4c}}\ \phi_{1s_{4s}}\ \phi_{2_{4c}}\ \phi_{2_{4s}}\Big]^T \end{aligned} \tag{4.21}$$

The notation in Eqs. (4.20) and (4.21) reflects the fact that in the present study the rotor blades are modeled using one rigid flap mode β, one rigid lag mode ζ, and one flexible torsion mode ϕ, but both equations can be rewritten for a generic number of rigid and flexible modes. Also note that both vectors $\mathbf{x}_{ave}$ and $\mathbf{x}_{HHC}$ are in general time dependent.

With these definitions of the state and the control vector the linearized system, Eq. (4.7), becomes

$$\left\{\begin{array}{c}\dot{\mathbf{x}}_{ave}\\ \dot{\mathbf{x}}_{4P}\end{array}\right\} = \left[\begin{array}{cc}A_{ave} & A_{12}\\ A_{21} & A_{HHC}\end{array}\right]\left\{\begin{array}{c}\mathbf{x}_{ave}\\ \mathbf{x}_{4P}\end{array}\right\} + \left[\begin{array}{cc}B_{ave} & B_{12}\\ B_{21} & B_{HHC}\end{array}\right]\left\{\begin{array}{c}\mathbf{u}_{pilot}\\ \mathbf{u}_{HHC}\end{array}\right\} \tag{4.22}$$

where now all the partitions of A and B are time-invariant. In other words, by decomposing the state vector into an average and a 4/rev component, the original linearized system with periodic coefficients has been converted into a larger linearized system, but with constant coefficients.

The linearized model also includes an output equation, which has the form:

$$\underbrace{\left\{\begin{array}{c}\mathbf{y}_{ave}\\ \mathbf{y}_{4P}\\ \mathbf{F}_{ave}\\ \mathbf{F}_{4P}\end{array}\right\}}_{\stackrel{def}{=}\mathbf{y}} = \underbrace{\left[\begin{array}{cc} I & 0\\ 0 & C_{22}\\ C_{31} & C_{32}\\ C_{41} & C_{42}\end{array}\right]}_{\stackrel{def}{=}C}\left\{\begin{array}{c}\mathbf{x}_{ave}\\ \mathbf{x}_{4P}\end{array}\right\} + \underbrace{\left[\begin{array}{cc} 0 & 0\\ 0 & 0\\ D_{31} & D_{32}\\ D_{41} & D_{42}\end{array}\right]}_{\stackrel{def}{=}D}\left\{\begin{array}{c}\mathbf{u}_{pilot}\\ \mathbf{u}_{HHC}\end{array}\right\} \tag{4.23}$$

where the C and D matrices have constant coefficients. The vectors $\mathbf{F}_{ave}$ and $\mathbf{F}_{4P}$ contain the the average and 4/rev hub loads at the hub, and are defined as:

$$\mathbf{F}_{ave} = [F_{x_{ave}}\ F_{x_{ave}}\ F_{y_{ave}}\ M_{x_{ave}}\ M_{y_{ave}}\ M_{z_{ave}}\ ]^T \tag{4.24}$$

$$\mathbf{F}_{4P} = [F_{x_{4c}}\ F_{x_{4s}}\ F_{y_{4c}}\ F_{y_{4s}}\ F_{z_{4c}}\ F_{z_{4s}}\ M_{x_{4c}}\ M_{x_{4s}}\ M_{y_{4c}}\ M_{y_{4s}}\ M_{z_{4c}}\ M_{z_{4s}}\ ]^T \tag{4.25}$$

where F_x, F_y, F_z, and M_x, M_y, M_z denote the rotor force and moment components along and about the body axes. The remaining two partitions of the output vector $\mathbf{y}$ in Eq. (4.23) are $\mathbf{y}_{ave}$ and $\mathbf{y}_{4P}$. The output subvector $\mathbf{y}_{ave}$ is identical to the average state vector $\mathbf{x}_{ave}$. The output subsector $\mathbf{y}_{4P}$ is the global 4/rev rotor state vector:

$$\begin{aligned}\mathbf{y}_{4P} = \Big[&\beta'_{0_{4c}}\ \beta'_{0_{4s}}\ \beta'_{1c_{4c}}\ \beta'_{1c_{4s}}\ \beta'_{1s_{4c}}\ \beta'_{1s_{4s}}\ \beta'_{2_{4c}}\ \beta'_{2_{4s}}\ \dots\\ &\dots\zeta'_{0_{4c}}\ \zeta'_{0_{4s}}\ \zeta'_{1c_{4c}}\ \zeta'_{1c_{4s}}\ \zeta'_{1s_{4c}}\ \zeta'_{1s_{4s}}\ \zeta'_{2_{4c}}\ \zeta'_{2_{4s}}\ \dots\\ &\dots\phi'_{0_{4c}}\ \phi'_{0_{4s}}\ \phi'_{1c_{4c}}\ \phi'_{1c_{4s}}\ \phi'_{1s_{4c}}\ \phi'_{1s_{4s}}\ \phi'_{2_{4c}}\ \phi'_{2_{4s}}\Big]^T\end{aligned} \tag{4.26}$$

The portion of the output equation corresponding to $\mathbf{y}_{ave}$ and $\mathbf{y}_{4P}$ is simply a mathematical means to indicate that the outputs are the average and global 4/rev rotor states, no physics are involved.

The submatrices C_{31} and C_{32} express a linearized relationship between the average hub loads and average and 4/rev rotor states. Similarly, the submatrices

C_{41} and C_{42} express a linearized relationship between the vibratory loads and average and 4/rev rotor states.

As for the feedforward matrix, the submatrices D_{31} and D_{32} link the average vibratory loads to, respectively, pilot and HHC inputs. The submatrices D_{41} and D_{42} link the 4/rev harmonics of the vibratory loads to, respectively, pilot and HHC inputs. Therefore, the D_{42} submatrix is the equivalent of the T-matrix in typical HHC studies. The submatrix D_{41} represents the effects of pilot maneuvers on the vibratory loads: these effects are not taken into account explicitly in typical HHC studies, instead, the maneuver effects are captured by online identification of the T-matrix and adaptation. By including the maneuver effects in the output model, the need for adaptation is substantially reduced.

4.2.2 Extraction of the control matrix B

The extraction of the control matrix B is presented first, because the procedure is more similar to that for the traditional linearization without higher harmonic components of the states. In fact, the control perturbation vector $\mathbf{u}$ is already defined in the rotating system. The control matrix B is extracted through numerical perturbation of the full nonlinear equations of motion about a trimmed equilibrium position. Each element of the matrix is obtained using central difference approximations.

The calculation proceeds as follows. For every azimuth angle ψ_i:

1. Perturb the k-th element $u_k(\psi_i)$ of the control vector $\mathbf{u}$ (pilot and HHC controls are treated in exactly the same way) by Δu_k, i.e., let the perturbed

control vector $\mathbf{u}_+(\psi_i)$ be

$$\mathbf{u}_+(\psi_i) = \left\{ \begin{array}{c} u_1 \\ u_2 \\ \vdots \\ u_k + \Delta u_k \\ \vdots \\ u_m \end{array} \right\} \tag{4.27}$$

where the subscript "+" denotes the positive perturbation in the central difference calculation.

2. Substitute the perturbed control vector $\mathbf{u}_+(\psi_i)$ into the system of equations of motion of the helicopter, to obtain the perturbed acceleration vector $\dot{\mathbf{x}}_{R+}$

$$\dot{\mathbf{x}}_{R+} = \mathbf{f}(\mathbf{x}_R, \mathbf{u}_+, \psi_i) \tag{4.28}$$

where a subscript R has been added to the state vector to indicate that the rotor portions of it are formulated in the rotating system (note that the state vector in the linearized model is entirely expressed in the fixed system). The state vector $\mathbf{x}_R$ corresponds to the desired trim condition, and is held constant during the perturbation.

3. Repeat the two previous steps with a negative perturbation of the k-th control, $u_k - \Delta u_k$, to obtain the perturbed acceleration vector $\dot{\mathbf{x}}_{R-}$.

4. Build the derivative using central difference approximations. This derivative is the k-th column of the B_R matrix (i.e., with the rotor portions still in the rotating system) at the azimuth angle ψ_i:

$$\{B_R(\psi_i)\}_k \approx \frac{1}{2\Delta u_k} \left(\dot{\mathbf{x}}_{R+} - \dot{\mathbf{x}}_{R-}\right) \tag{4.29}$$

5. Repeat the four previous steps for each of the m elements of the control vector, i.e., for $u_k, k = 1, \ldots, m$, to obtain the complete control matrix $B_R(\psi_i)$

$$B_R(\psi_i) = [\{B_R(\psi_i)\}_1 \{B_R(\psi_i)\}_2 \cdots \{B_R(\psi_i)\}_m] \tag{4.30}$$

The next step of the linearization procedure typically consists of performing a multiblade coordinate transformation, to convert the rotor states from the rotating to the fixed system, and therefore to obtain a control matrix $B(\psi_i)$ entirely in the fixed system. Then, after steps 1-5 are carried out for a sufficient number of azimuth angles ψ_i, the resulting control matrices $B(\psi_i)$ are typically averaged to obtain the final constant control matrix B. This is the traditional linearization procedure, and it is also what is done in the present study for the calculation of the rows of the B matrix corresponding to the "average" states, i.e., for the submatrices B_{ave} and B_{12} in Eq. (4.22).

Some additional manipulations are instead required for the rows corresponding to the 4/rev states, i.e., for the submatrices B_{21} and B_{HHC}. These manipulation consist of a Fourier analysis of $B(\psi_i)$ to extract the 4/rev cosine and sine harmonics. Define:

$$B_{4c} = \frac{2}{N_\psi} \sum_{i=1}^{N_\psi} B(\psi_i) \cos 4\psi_i \tag{4.31}$$

$$B_{4s} = \frac{2}{N_\psi} \sum_{i=1}^{N_\psi} B(\psi_i) \sin 4\psi_i \tag{4.32}$$

where N_ψ is number of azimuth angle ψ_i in one rotor revolution. Then it is essentially

$$[B_{21}\ B_{HHC}] = \begin{bmatrix} B_{4c} \\ B_{4s} \end{bmatrix} \tag{4.33}$$

except that the rows of B_{4c} and B_{4s} must be appropriately permutated because

the state subvector $\mathbf{x}_{4P}$, Eq. (4.21), is arranged with the 4/rev cosine and sine components interlaced rather than grouped together.

4.2.3 Extraction of the state matrix A

The general procedure to extract the state matrix A is similar to that of the control matrix B, except that the state vector is defined in the fixed system, both for the average and the 4/rev components.

Rows corresponding to the average states $\mathbf{x}_{ave}$

The rows of the A matrix corresponding to the average states $\mathbf{x}_{ave}$, i.e., the submatrices A_{ave} and A_{21} in Eq. (4.22) can be obtained with the same procedure as previously shown for the B matrix, i.e., through the following steps.

For every azimuth angle ψ_i:

1. Perturb the k-th element $x_{ave_k}(\psi_i)$ of the partition $\mathbf{x}_{ave}$ of the state vector $\mathbf{x}$ by Δx_k, i.e., let the perturbed state vector $\mathbf{x}_+(\psi_i)$ be

$$\mathbf{x}_+(\psi_i) = \left\{ \begin{array}{c} x_{ave_1} \\ x_{ave_2} \\ \vdots \\ x_{ave_k} + \Delta x_k \\ \vdots \\ x_{ave_N} \\ \mathbf{x}_{4p} \end{array} \right\} \tag{4.34}$$

   where the subscript "+" denotes the positive perturbation in the central difference calculation.

2. Substitute the perturbed state vector $\mathbf{x}_+(\psi_i)$ into the system of equations of motion of the helicopter, to obtain the perturbed acceleration vector $\dot{\mathbf{x}}_+$. Because the rotor equations are formulated and implemented in the rotating system, $\mathbf{x}_+(\psi_i)$ must first be converted to the rotating system, using a multiblade coordinate transformation that yields the corresponding rotating state vector $\mathbf{x}_{R+}(\psi_i)$

$$\dot{\mathbf{x}}_{R+} = \mathbf{f}(\mathbf{x}_{R+}, \mathbf{u}, \psi_i) \tag{4.35}$$

where the subscript R again indicates that the rotor portions are in the rotating system. The control vector $\mathbf{u}$ corresponds to the desired trim condition, and is held constant during the perturbation.

3. Repeat the two previous steps with a negative perturbation of the k-th average state, $x_{ave_k} - \Delta x_k$, to obtain the perturbed acceleration vector $\dot{\mathbf{x}}_{R-}$.

4. Build the derivative using central difference approximations. This derivative is the k-th column of a matrix $A_R(\psi_i)$ at the azimuth angle ψ_i , that is:

$$\{A_R(\psi_i)\}_k \approx \frac{1}{2\Delta x_k} (\dot{\mathbf{x}}_{R+} - \dot{\mathbf{x}}_{R-}) \tag{4.36}$$

Position in the state matrix and dimensions of $A_R(\psi_i)$ are the same as the submatrix A_{ave} in Eq. (4.22), but A_{ave} is constant and in the fixed system, whereas $A_R(\psi_i)$ is periodic and in the rotating system.

5. Repeat the four previous steps for each of the N elements of the state vector partition $\mathbf{x}_{ave}$, i.e., for $x_{ave_k}, k = 1, \ldots, N$, to obtain the complete matrix $A_R(\psi_i)$

$$A_R(\psi_i) = [\{A_R(\psi_i)\}_1 \{A_R(\psi_i)\}_2 \cdots \{A_R(\psi_i)\}_N] \tag{4.37}$$

The next step of the linearization procedure typically consists of performing a multiblade coordinate transformation, to convert the rotor states from the rotating to the fixed system, and therefore to obtain a state matrix $A(\psi_i)$ entirely in the fixed system. Then, after steps 1-5 are carried out for a sufficient number of azimuth angles ψ_i, the resulting state matrices $A(\psi_i)$ are typically averaged to obtain the final constant state matrix A. This is the traditional linearization procedure, and it is also what is done in the present study for the calculation of the portion of the A matrix corresponding to the "average" states, i.e., for the submatrix A_{ave} in Eq. (4.22).

Some additional manipulations are required for the rows corresponding to the 4/rev derivatives $\dot{\mathbf{x}}_{4P}$, i.e., for the submatrix A_{21}. As for the B matrix case, first perform a multiblade coordinate transformation on $A_R(\psi_i)$, resulting in $A_F(\psi_i)$, and then extract the 4/rev cosine and sine harmonics through a Fourier analysis. Define:

$$A_{F_{4c}} = \frac{2}{N_\psi} \sum_{i=1}^{N_\psi} A_F(\psi_i) \cos 4\psi_i \tag{4.38}$$

$$A_{F_{4s}} = \frac{2}{N_\psi} \sum_{i=1}^{N_\psi} A_F(\psi_i) \sin 4\psi_i \tag{4.39}$$

Then it is essentially

$$A_{21} = \begin{bmatrix} A_{F_{4c}} \\ A_{F_{4s}} \end{bmatrix} \tag{4.40}$$

except that the rows $A_{F_{4c}}$ and $A_{F_{4s}}$ must be appropriately permutated because the state derivative subvector $\dot{\mathbf{x}}_{4P}$, Eq. (4.21), is arranged with the 4/rev cosine and sine components interlaced rather than grouped together.

Rows corresponding to the 4/rev states $\mathbf{x}_{4P}$

The rows of the A matrix corresponding to the 4/rev state vector $\mathbf{x}_{4P}$, i.e., the submatrices A_{12} and A_{HHC} in Eq. (4.22) can be obtained with the same procedure as previously shown for the A_{ave} and A_{21} matrices with two special treatments: 4/rev perturbation and kinematic relationship.

Unlike the conventional linearization method which has a constant perturbation, the submatrices A_{12} and A_{HHC} are obtained by perturbing $\mathbf{x}_{4P}$ in 4/rev frequency in both sine and cosine direction. The 4/rev frequency is chosen to excite the 4/rev response. Because the equations of motion of the helicopter are not expressed in terms of 4/rev states, they cannot be perturbed directly. The alternative solution is to perturb each main rotor states x_{MR} of the partition $\mathbf{x}_{ave}$ by $\pm\Delta x_{MR}\cos 4\psi_i$ and $\pm\Delta x_{MR}\sin 4\psi_i$. This is the same as perturbing $x_{MR_{4c}}$ and $x_{MR_{4s}}$ by $\pm\Delta x_{MR}$, respectively.

Another important aspect regarding the 4/rev perturbation is the kinematic relationship between the rotor states. There are several types of kinematic relationships, and one of them is the integral relationship such as

$$\frac{\mathrm{d}}{dt}(\beta_{1c}) = \dot{\beta}_{1c} \tag{4.41}$$

$$\frac{\mathrm{d}}{dt}(\dot{\beta}_{1c}) = \ddot{\beta}_{1c} \tag{4.42}$$

Because the periodic nature of the 4/rev states, the kinematic relationships are maintained in a different way. Continuing with the previous example, the first and

second derivatives of Eq. (4.18) with respect to time are given by:

$$\begin{aligned}
\beta_{1c}(\psi) &= \beta_{1c_{ave}}(\psi) + \beta_{1c_{4c}}(\psi)\cos\psi + \beta_{1c_{4s}}(\psi)\sin\psi \qquad \text{(4.18) repeated} \\
\dot{\beta}_{1c}(\psi) &= \dot{\beta}_{1c_{ave}} + \underbrace{(\dot{\beta}_{1c_{4c}} + 4\Omega\beta_{1c_{4s}})}_{\beta'_{1c_{4c}}}\cos 4\psi + \underbrace{(\dot{\beta}_{1c_{4s}} - 4\Omega\beta_{1c_{4c}})}_{\beta'_{1c_{4s}}}\sin 4\psi \qquad (4.43) \\
\ddot{\beta}_{1c}(\psi) &= \ddot{\beta}_{1c_{ave}} + \underbrace{(\ddot{\beta}_{1c_{4c}} + 8\Omega\dot{\beta}_{1c_{4s}} - 16\Omega^2\beta_{1c_{4c}})}_{\beta''_{1c_{4c}}}\cos 4\psi \\
&\quad + \underbrace{(\ddot{\beta}_{1c_{4s}} - 8\Omega\dot{\beta}_{1c_{4c}} - 16\Omega^2\beta_{1c_{4s}})}_{\beta''_{1c_{4s}}}\sin 4\psi \qquad (4.44)
\end{aligned}$$

Although β_{1c}, $\dot{\beta}_{1c}$, and $\ddot{\beta}_{1c}$ on the left-hand side of Eqs. (4.18), (4.43), and (4.44) correspond to the integral relationships, the primed and dotted variables on right-hand side of Eqs. (4.18), (4.43), and (4.44) do not maintain the same integral relationships. For example,

$$\begin{aligned}
\frac{\mathrm{d}}{\mathrm{d}t}(\beta_{1c_{4c}}) &\neq \beta'_{c_{4c}} \qquad (4.45) \\
\frac{\mathrm{d}}{\mathrm{d}t}(\beta_{1c_{4s}}) &\neq \beta'_{c_{4s}} \qquad (4.46) \\
\frac{\mathrm{d}}{\mathrm{d}t}(\beta'_{1c_{4c}}) &\neq \beta''_{1c_{4c}} \qquad (4.47) \\
\frac{\mathrm{d}}{\mathrm{d}t}(\beta'_{1c_{4s}}) &\neq \beta''_{1c_{4s}} \qquad (4.48) \\
& \qquad (4.49)
\end{aligned}$$

Define all the dotted and non-dotted variables such as $\beta_{1c_{4c}}$, $\beta_{1c_{4s}}$, $\dot{\beta}_{1c_{4c}}$, and $\dot{\beta}_{1c_{4c}}$ on the right-hand side of Eqs. (4.18) and (4.43) be the *4/rev rotor states*, and the primed variables such as $\beta'_{1c_{4c}}$ and $\beta'_{1c_{4s}}$ be the *global 4/rev rotor states* (for this simple example). Then, the kinematic relationships between the 4/rev rotor states

and global 4/rev rotor states are as follows:

$$\beta'_{1c_{4c}} = \dot{\beta}_{1c_{4c}} + 4\Omega\beta_{1c_{4s}} \tag{4.50}$$

$$\beta'_{1c_{4s}} = \dot{\beta}_{1c_{4s}} - 4\Omega\beta_{1c_{4c}} \tag{4.51}$$

$$\beta''_{1c_{4c}} = \ddot{\beta}_{1c_{4c}} + 8\Omega\dot{\beta}_{1c_{4s}} - 16\Omega^2\beta_{1c_{4c}} \tag{4.52}$$

$$\beta''_{1c_{4s}} = \ddot{\beta}_{1c_{4s}} - 8\Omega\dot{\beta}_{1c_{4c}} - 16\Omega^2\beta_{1c_{4s}} \tag{4.53}$$

For this research, the 4/rev rotor state vector and the global 4/rev rotor state vector are shown in Eqs. (4.21) and (4.26), respectively.

The kinematic relationship must always be maintained through out the linearization process. For instance, if the β_{1c} was perturbed by a constant $\Delta\beta_{1c}$, the $\dot{\beta}_{1c}$ must also be perturbed by $\frac{\mathrm{d}}{\mathrm{d}t}(\Delta\beta_{1c})$ at the same time to maintain kinematic consistency. Because the time derivative of a constant perturbation is zero, the traditional linearization method only perturbs one state at a time while the rest of the states remain fixed.

For a 4/rev perturbation, if β_{1c} is perturbed by $\Delta\beta_{1c}\cos 4\psi$, $\dot{\beta}_{1c}$ must also be perturbed by $\frac{\mathrm{d}}{\mathrm{d}t}(\Delta\beta_{1c}\cos 4\psi)$ at the same time. Conversely, if β_{1c} is perturbed by $\Delta\beta_{1c}\sin 4\psi$, $\dot{\beta}_{1c}$ must also be perturbed by $\frac{\mathrm{d}}{\mathrm{d}t}(\Delta\beta_{1c}\sin 4\psi)$. It is important to remember that the equations of motion of the helicopter are not expressed in terms of 4/rev rotor state, $\mathbf{x}_{4P}$ cannot be perturbed directly. The procedure described below perturbs each main rotor state with $\mathbf{x}_{MR}$ in both sine and cosine direction at a 4/rev frequency.

The calculation of submatrices A_{12} and A_{HHC} proceeds as follow:

For every azimuth angle ψ_i:

1. Perturbation of the 4/rev cosine component

(a) Perturb the j^{th} main rotor state $x_{MR_j}(\psi_i)$ of partition $\mathbf{x}_{MR}(\psi_i)$ in the state vector $\mathbf{x}_{ave}(\psi_i)$ by $\Delta x_{MR_j} \cos 4\psi_i$, i.e., let the perturbed state vector $\mathbf{x}_{4c+}(\psi_i)$ be

$$\mathbf{x}_{4c+}(\psi_i) = \left\{ \begin{array}{c} \mathbf{x}_B \\ x_{MR_1} \\ \vdots \\ x_{MR_{j-4}} + [-4\Omega\Delta x_{MR_j} \sin 4\psi_i] \\ \vdots \\ x_{MR_j} + \Delta x_{MR_j} \cos 4\psi_i \\ \vdots \\ x_{MR_L} \end{array} \right\} \tag{4.54}$$

where the subscript "4c+" denotes the positive 4/rev cosine perturbation in the central difference calculation.

(b) Substitute the perturbed state vector $\mathbf{x}_{4c+}(\psi_i)$ into the system of equations of motion of the helicopter, to obtain the perturbed state vector derivative $\dot{\mathbf{x}}_{4c+}(\psi_i)$. Because the rotor equations are formulated and implemented in the rotating system, $\mathbf{x}_{4c+}(\psi_i)$ must first be converted to the rotating system, using a multi-blade coordinate transformation that yields the corresponding rotating state vector $\mathbf{x}_{R4c+}(\psi_i)$

$$\dot{\mathbf{x}}_{R4c+}(\psi_i) = \mathbf{f}(\mathbf{x}_{R4c+}(\psi_i), \mathbf{u}(\psi_i), \psi_i) \tag{4.55}$$

The control vector $\mathbf{u}(\psi_i)$ corresponds to the desired trim condition, and is held constant during the perturbation.

If and only if x_{MR_j} is one of the displacement states (β_0, β_{1c}, β_{1s}, β_2, ζ_0, ζ_{1c}, ζ_{1s}, ζ_2, ϕ_0, ϕ_{1c}, ϕ_{1s}, ϕ_2), its derivative state $x_{MR_{j-4}}$ ($\dot{\beta}_0$, $\dot{\beta}_{1c}$,

$\dot{\beta}_{1s}$, $\dot{\beta}_2$, $\dot{\zeta}_0$, $\dot{\zeta}_{1c}$, $\dot{\zeta}_{1s}$, $\dot{\zeta}_2$, $\dot{\phi}_0$, $\dot{\phi}_{1c}$, $\dot{\phi}_{1s}$, $\dot{\phi}_2$) also needs to be perturbed by $-4\Omega\Delta x_{MR_j} \sin 4\psi_i$ at the same time. This additional perturbation is represented by [...] in Eq. (4.54).

(c) Repeat the two previous steps with a negative perturbation of the j^{th} main rotor state, $x_{MR_j} - \Delta x_{MR_j} \cos 4\psi_i$, and build the derivative using central difference approximations. This derivative is the j^{th} column of an interim matrix $P_R(\psi_i)$ at the azimuth angle ψ_i , that is:

$$\{P_R(\psi_i)\}_j \approx \frac{1}{2\Delta x_{MR_j}} \left(\dot{\mathbf{x}}_{R4c+}(\psi_i) - \dot{\mathbf{x}}_{R4c-}(\psi_i)\right) \tag{4.56}$$

(d) Repeat the three previous steps for each of the L elements of the main rotor state vector partition $\mathbf{x}_{MR}$, i.e., for the main rotor state in x_{MR_j}, $j = 1, \ldots, L$, to obtain the first half of the interim matrix $P_R(\psi_i)$

$$P_R(\psi_i) = \left[\{P_R(\psi_i)\}_1 \{P_R(\psi_i)\}_2 \cdots \{P_R(\psi_i)\}_L\right]_{n\times L} \tag{4.57}$$

2. Perturbation of the 4/rev sine component

(a) Perturb the j^{th} main rotor state $x_{MR_j}(\psi_i)$ of partition $\mathbf{x}_{MR}(\psi_i)$ in the state vector $\mathbf{x}_{ave}(\psi_i)$ by $\Delta x_{MR_j} \sin 4\psi_i$, i.e., let the perturbed state vector $\mathbf{x}_{4s+}(\psi_i)$ be

$$\mathbf{x}_{4s+}(\psi_i) = \left\{ \begin{array}{c} \mathbf{x}_B \\ x_{MR_1} \\ \vdots \\ x_{MR_{j-4}} + [4\Omega\Delta x_{MR_j} \cos 4\psi_i] \\ \vdots \\ x_{MR_j} + \Delta x_{MR_j} \sin 4\psi_i \\ \vdots \\ x_{MR_L} \end{array} \right\} \tag{4.58}$$

where the subscript "4s+" denotes the positive 4/rev sine perturbation in the central difference calculation.

(b) Substitute the perturbed state vector $\mathbf{x}_{4s+}(\psi_i)$ into the system of equations of motion of the helicopter, to obtain the perturbed state vector derivative $\dot{\mathbf{x}}_{4s+}(\psi_i)$. Because the rotor equations are formulated and implemented in the rotating system, $\mathbf{x}_{4s+}(\psi_i)$ must first be converted to the rotating system, using a multi-blade coordinate transformation that yields the corresponding rotating state vector $\mathbf{x}_{R4s+}(\psi_i)$

$$\dot{\mathbf{x}}_{R4s+}(\psi_i) = \mathbf{f}(\mathbf{x}_{R4s+}(\psi_i), \mathbf{u}(\psi_i), \psi_i) \tag{4.59}$$

The control vector $\mathbf{u}(\psi_i)$ corresponds to the desired trim condition, and is held constant during the perturbation.

If and only if x_{MR_j} is one of the displacement states, its derivative $x_{MR_{j-4}}$ also needs to be perturbed by $+4\Omega\Delta x_{MR_j}\cos 4\psi_i$ at the same time. This additional perturbation is represented by [...] in Eq. (4.58).

(c) Repeat the two previous steps with a negative perturbation of the j^{th} main rotor state, $x_{MR_j} - \Delta x_{MR_j}\sin 4\psi_i$, and build the derivative using central difference approximations. This derivative is the $(L+j)^{th}$ column of the interim matrix $P_R(\psi_i)$ at the azimuth angle ψ_i , that is:

$$\{P_R(\psi_i)\}_{L+j} \approx \frac{1}{2\Delta x_{MR_j}}\left(\dot{\mathbf{x}}_{R4s+}(\psi_i) - \dot{\mathbf{x}}_{R4s-}(\psi_i)\right) \tag{4.60}$$

(d) Repeat the three previous steps for each of the L elements of the main rotor state vector partition $\mathbf{x}_{MR}$, i.e., for the main rotor state in x_{MR_j}, $j = 1, \ldots, L$, to complete the second half of the interim matrix $P_R(\psi_i)$

$$P_R(\psi_i) = \Big[\{P_R(\psi_i)\}_1 \cdots \{P_R(\psi_i)\}_L \;\; \{P_R(\psi_i)\}_{L+1} \cdots \{P_R(\psi_i)\}_{2L}\Big]_{n\times 2L} \tag{4.61}$$

The next step is to perform a multi-blade coordinate transformation to obtain a interim matrix $P_F(\psi_i)$ entirely in the fixed system. Then, after steps 1-2 are carried out for one rotor revolution, the resulting interim matrices $P_F(\psi_i)$ are averaged to obtain the state matrix A_{12}. Next, the columns of A_{12} must be appropriately permutated because the state subvector $\mathbf{x}_{4P}$, Eq. (4.21), is arranged with the 4/rev cosine and sine components interlaced rather than grouped together.

The state matrix A_{HHC} can be obtained by extracting the 4/rev cosine and sine harmonics from $P_F(\psi_i)$ using Fourier analysis. Define:

$$A_{F_{4c}} = \frac{2}{N_\psi} \sum_{i=1}^{N_\psi} P_F(\psi_i) \cos 4\psi_i \tag{4.62}$$

$$A_{F_{4s}} = \frac{2}{N_\psi} \sum_{i=1}^{N_\psi} P_F(\psi_i) \sin 4\psi_i \tag{4.63}$$

Then it is essentially

$$A_{HHC} = \begin{bmatrix} A_{F_{4c}} \\ A_{F_{4s}} \end{bmatrix} \tag{4.64}$$

except that the rows and columns of $A_{F_{4c}}$ and $A_{F_{4s}}$ must be appropriately permutated because the state subvector $\mathbf{x}_{4P}$, Eq. (4.21), is arranged with the 4/rev cosine and sine components interlaced rather than grouped together.

There is one last special treatment related to state matrix A_{HHC}. Both submatrices $A_{F_{4c}}$ and $A_{F_{4s}}$ do not contain the 4/rev state derivatives $\dot{\mathbf{x}}_{4P}$. Recall that the interim matrix $P_F(\psi_i)$ contains the perturbed state vector derivative which has elements such as $\ddot{\beta}_{1c}$. The Fourier analysis only extracts the global 4/rev rotor states ($\beta''_{1c_{4c}}$ and $\beta''_{1c_{4s}}$) not the 4/rev rotor states ($\ddot{\beta}_{1c_{4c}}$ or $\ddot{\beta}_{1c_{4s}}$). To conform with standard state-space representation $\dot{\mathbf{x}} = A\mathbf{x} + B\mathbf{u}$, the global 4/rev rotor states in $A_{F_{4c}}$ and $A_{F_{4s}}$ are converted to the 4/rev rotor states using the kinematic relationship as shown in Eqs. (4.50)-(4.53).

4.2.4 Extraction of the feedforward matrix D

Consider the hub loads at hub in body axes can be written in symbolic form as:

$$\mathbf{F} \;=\; \mathbf{g}(\dot{\mathbf{x}}, \mathbf{x}, \mathbf{u}; \psi) \tag{4.65}$$

The extraction procedure for the feedforward matrix D is the same as the one for the control matrix B except the subject of the interest is the hub loads $\mathbf{F}$ instead of the state vector derivatives $\dot{\mathbf{x}}$.

The calculation proceeds as follows. For every azimuth angle ψ_i:

1. Perturb the k-th element $u_k(\psi_i)$ of the control vector $\mathbf{u}$ (pilot and HHC controls are treated in exactly the same way) by Δu_k, i.e., let the perturbed control vector $\mathbf{u}_+(\psi_i)$ be

$$\mathbf{u}_+(\psi_i) = \left\{ \begin{array}{c} u_1 \\ u_2 \\ \vdots \\ u_k + \Delta u_k \\ \vdots \\ u_m \end{array} \right\} \tag{4.66}$$

   where the subscript "+" denotes the positive perturbation in the central difference calculation.

2. Substitute the perturbed control vector $\mathbf{u}_+(\psi_i)$ into the Eq. (4.65), to obtain the perturbed hub loads $\mathbf{F}_+$

$$\mathbf{F}_+ = \mathbf{g}(\mathbf{x}, \mathbf{u}_+, \psi_i) \tag{4.67}$$

   The state vector $\mathbf{x}$ corresponds to the desired trim condition, and is held constant during the perturbation.

3. Repeat the two previous steps with a negative perturbation of the k-th control, $u_k - \Delta u_k$, to obtain the perturbed acceleration vector $\mathbf{F}_-$.

4. Build the derivative using central difference approximations. This derivative is the k-th column of the D matrix at the azimuth angle ψ_i:

$$\{D(\psi_i)\}_k \approx \frac{1}{2\Delta u_k} (\mathbf{F}_+ - \mathbf{F}_-) \tag{4.68}$$

5. Repeat the four previous steps for each of the m elements of the control vector, i.e., for $u_k, k = 1, \ldots, m$, to obtain the complete control matrix $D(\psi_i)$

$$D(\psi_i) = [\{D(\psi_i)\}_1 \{D(\psi_i)\}_2 \cdots \{D(\psi_i)\}_m] \tag{4.69}$$

6. Repeat steps 1-5 for N_ψ azimuth angles ψ_i for one rotor revolution.

7. Extract the average, 4/rev cosine, and 4/rev sine harmonics of $D(\psi_i)$ using Fourier analysis.

   Define:

$$D_{ave} = \frac{1}{N_\psi} \sum_{i=1}^{N_\psi} D(\psi_i) \tag{4.70}$$

$$D_{4c} = \frac{2}{N_\psi} \sum_{i=1}^{N_\psi} D(\psi_i) \cos 4\psi_i \tag{4.71}$$

$$D_{4s} = \frac{2}{N_\psi} \sum_{i=1}^{N_\psi} D(\psi_i) \sin 4\psi_i \tag{4.72}$$

   Then it is essentially

$$[D_{31}\ D_{32}] = D_{ave} \tag{4.73}$$

$$[D_{41}\ D_{42}] = \begin{bmatrix} D_{4c} \\ D_{4s} \end{bmatrix} \tag{4.74}$$

   except that the rows of D_{4c} and D_{4s} must be appropriately permutated because the output subvector $\mathbf{F}_{4P}$, Eq. (4.25), is arranged with the 4/rev cosine and sine components interlaced rather than grouped together.

4.2.5 Extraction of the output matrix C

The general procedure to extract the state matrix C is similar to that of the control matrix A.

Submatrix C_{22}

The submatrix C_{22} relates the 4/rev rotor states $\mathbf{x}_{4P}$ to the global 4/rev rotor state vector $\mathbf{y}_{4P}$; i.e., C_{22} is a kinematic matrix. Using $\beta'_{1c_{4c}}$ and $\beta'_{1c_{4s}}$ as an example, the kinematic equations for β_{1c} are

$$\begin{aligned} \beta'_{1c_{4c}} &= \dot{\beta}_{1c_{4c}} + 4\Omega\beta_{1c_{4s}} && \text{(4.50) repeated} \\ \beta'_{1c_{4s}} &= \dot{\beta}_{1c_{4s}} - 4\Omega\beta_{1c_{4c}} && \text{(4.51) repeated} \end{aligned} \tag{4.75}$$

Re-write the above equations in matrix form:

$$\begin{bmatrix} \beta'_{1c_{4c}} \\ \beta'_{1c_{4s}} \end{bmatrix} = \begin{bmatrix} 1 & 0 & 0 & 4\Omega \\ 0 & 1 & -4\Omega & 0 \end{bmatrix} \begin{bmatrix} \dot{\beta}_{1c_{4c}} \\ \dot{\beta}_{1c_{4s}} \\ \beta_{1c_{4c}} \\ \beta_{1c_{4s}} \end{bmatrix} \tag{4.76}$$

Likewise, the C_{22} can be structured as follows:

$$\mathbf{y}_{4P} = \begin{bmatrix} H & 0 & 0 \\ 0 & H & 0 \\ 0 & 0 & H \end{bmatrix} \mathbf{x}_{4p} \tag{4.77}$$

$$H = \begin{bmatrix} I & 0 & 0 & 0 & W & 0 & 0 & 0 \\ 0 & I & 0 & 0 & 0 & W & 0 & 0 \\ 0 & 0 & I & 0 & 0 & 0 & W & 0 \\ 0 & 0 & 0 & I & 0 & 0 & 0 & W \end{bmatrix} \quad W = \begin{bmatrix} 0 & 4\Omega \\ -4\Omega & 0 \end{bmatrix} \tag{4.78}$$

Submatrices C_{31} and C_{41}

The rows of the C matrix corresponding to the average states $\mathbf{x}_{ave}$, i.e., the submatrices C_{31} and C_{41} in Eq. (4.23) can be obtained with the same procedure as previously shown for the A_{ave} and A_{21} matrices, i.e., through the following steps.

For every azimuth angle ψ_i:

1. Perturb the k-th element $x_{ave_k}(\psi_i)$ of the partition $\mathbf{x}_{ave}$ of the state vector $\mathbf{x}$ by Δx_k, i.e., let the perturbed state vector $\mathbf{x}_+(\psi_i)$ be

$$\mathbf{x}_+(\psi_i) = \left\{ \begin{array}{c} x_{ave_1} \\ x_{ave_2} \\ \vdots \\ x_{ave_k} + \Delta x_k \\ \vdots \\ x_{ave_N} \\ \mathbf{x}_{4p} \end{array} \right\} \tag{4.79}$$

   where the subscript "+" denotes the positive perturbation in the central difference calculation.

2. Substitute the perturbed state vector $\mathbf{x}_+(\psi_i)$ into Eq. (4.65) to obtain the perturbed hub loads $\mathbf{F}_+$.

$$\mathbf{F}_+ = \mathbf{g}(\mathbf{x}_+, \mathbf{u}, \psi_i) \tag{4.80}$$

   The control vector $\mathbf{u}$ corresponds to the desired trim condition, and is held constant during the perturbation.

3. Repeat the two previous steps with a negative perturbation of the k-th average state, $x_{ave_k} - \Delta x_k$, to obtain the perturbed hub loads $\mathbf{F}_-$.

4. Build the derivative using central difference approximations. This derivative is the k-th column of a interim matrix $P(\psi_i)$ at the azimuth angle ψ_i , that is:

$$\{P(\psi_i)\}_k \approx \frac{1}{2\Delta x_k}\left(\mathbf{F}_+ - \mathbf{F}_-\right) \tag{4.81}$$

5. Repeat the four previous steps for each of the N elements of the state vector partition $\mathbf{x}_{ave}$, i.e., for $x_{ave_k}, k = 1, \ldots, N$, to obtain the complete matrix $P(\psi_i)$

$$P(\psi_i) = \left[\{P(\psi_i)\}_1 \{P(\psi_i)\}_2 \cdots \{P(\psi_i)\}_N\right] \tag{4.82}$$

6. Repeat steps 1-5 for N_ψ azimuth angles ψ_i for one rotor revolution.

7. Extract the average, 4/rev cosine, and 4/rev sine harmonics of $P(\psi_i)$ using Fourier analysis.

   Define:

$$C_{ave} = \frac{1}{N_\psi}\sum_{i=1}^{N_\psi} P(\psi_i) \tag{4.83}$$

$$C_{4c} = \frac{2}{N_\psi}\sum_{i=1}^{N_\psi} P(\psi_i)\cos 4\psi_i \tag{4.84}$$

$$C_{4s} = \frac{2}{N_\psi}\sum_{i=1}^{N_\psi} P(\psi_i)\sin 4\psi_i \tag{4.85}$$

   Then it is essentially

$$C_{31} = C_{ave} \tag{4.86}$$

$$C_{41} = \begin{bmatrix} C_{4c} \\ C_{4s} \end{bmatrix} \tag{4.87}$$

   except that the rows C_{4c} and C_{4s} must be appropriately permutated because the output subvector $\mathbf{F}_{4P}$, Eq. (4.25), is arranged with the 4/rev cosine and sine components interlaced rather than grouped together.

Submatrices C_{32} and C_{42}

The submatrices C_{32} and C_{42} can be obtained with the same procedure as previously shown for the A_{12} and A_{HHC} matrices which proceeds as follow:

For every azimuth angle ψ_i:

1. Perturbation of the 4/rev cosine component

   (a) Perturb the j^{th} main rotor state $x_{MR_j}(\psi_i)$ of partition $\mathbf{x}_{MR}(\psi_i)$ in the state vector $\mathbf{x}_{ave}(\psi_i)$ by $\Delta x_{MR_j} \cos 4\psi_i$, i.e., let the perturbed state vector $\mathbf{x}_{4c+}(\psi_i)$ be

$$\mathbf{x}_{4c+}(\psi_i) = \left\{ \begin{array}{c} \mathbf{x}_B \\ x_{MR_1} \\ \vdots \\ x_{MR_{j-4}} + [-4\Omega\Delta x_{MR_j} \sin 4\psi_i] \\ \vdots \\ x_{MR_j} + \Delta x_{MR_j} \cos 4\psi_i \\ \vdots \\ x_{MR_L} \end{array} \right\} \tag{4.88}$$

   where the subscript "4c+" denotes the positive 4/rev cosine perturbation in the central difference calculation.

   (b) Substitute the perturbed state vector $\mathbf{x}_{4c+}(\psi_i)$ into Eq. (4.65) to obtain the perturbed hub loads $\mathbf{F}_{4c+}(\psi_i)$.

$$\mathbf{F}_{4c+}(\psi_i) = \mathbf{g}(\mathbf{x}_{4c+}(\psi_i), \mathbf{u}(\psi_i), \psi_i) \tag{4.89}$$

   The control vector $\mathbf{u}(\psi_i)$ corresponds to the desired trim condition, and is held constant during the perturbation.

If and only if x_{MR_j} is one of the displacement states (β_0, β_{1c}, β_{1s}, β_2, ζ_0, ζ_{1c}, ζ_{1s}, ζ_2, ϕ_0, ϕ_{1c}, ϕ_{1s}, ϕ_2), its derivative state $x_{MR_{j-4}}$ ($\dot{\beta}_0$, $\dot{\beta}_{1c}$, $\dot{\beta}_{1s}$, $\dot{\beta}_2$, $\dot{\zeta}_0$, $\dot{\zeta}_{1c}$, $\dot{\zeta}_{1s}$, $\dot{\zeta}_2$, $\dot{\phi}_0$, $\dot{\phi}_{1c}$, $\dot{\phi}_{1s}$, $\dot{\phi}_2$) also needs to be perturbed by $-4\Omega\Delta x_{MR_j} \sin 4\psi_i$ at the same time. This additional perturbation is represented by [...] in Eq. (4.88).

(c) Repeat the two previous steps with a negative perturbation of the j^{th} main rotor state, $x_{MR_j} - \Delta x_{MR_j} \cos 4\psi_i$, and build the derivative using central difference approximations. This derivative is the j^{th} column of an interim matrix $P(\psi_i)$ at the azimuth angle ψ_i , that is:

$$\{P(\psi_i)\}_j \approx \frac{1}{2\Delta x_j} \left(\mathbf{F}_{4c+}(\psi_i) - \mathbf{F}_{4c-}(\psi_i)\right) \tag{4.90}$$

(d) Repeat the three previous steps for each of the L elements of the main rotor state vector partition $\mathbf{x}_{MR}$, i.e., for the main rotor state in x_{MR_j}, $j = 1, \ldots, L$, to obtain the first half of the interim matrix $P(\psi_i)$

$$P(\psi_i) = \left[\{P(\psi_i)\}_1 \{P(\psi_i)\}_2 \cdots \{P(\psi_i)\}_L\right]_{n \times L} \tag{4.91}$$

2. Perturbation of the 4/rev sine component

(a) Perturb the j^{th} main rotor state $x_{MR_j}(\psi_i)$ of partition $\mathbf{x}_{MR}(\psi_i)$ in the state vector $\mathbf{x}_{ave}(\psi_i)$ by $\Delta x_{MR_j} \sin 4\psi_i$, i.e., let the perturbed state vec-

tor $\mathbf{x}_{4s+}(\psi_i)$ be

$$\mathbf{x}_{4s+}(\psi_i) = \left\{ \begin{array}{c} \mathbf{x}_B \\ x_{MR_1} \\ \vdots \\ x_{MR_{j-4}} + [4\Omega\Delta x_{MR_j} \cos 4\psi_i] \\ \vdots \\ x_{MR_j} + \Delta x_{MR_j} \sin 4\psi_i \\ \vdots \\ x_{MR_L} \end{array} \right\} \tag{4.92}$$

where the subscript "4s+" denotes the positive 4/rev sine perturbation in the central difference calculation.

(b) Substitute the perturbed state vector $\mathbf{x}_{4s+}(\psi_i)$ into Eq. (4.65) to obtain the perturbed hub loads $\mathbf{F}_{4s+}(\psi_i)$.

$$\mathbf{F}_{4s+}(\psi_i) = \mathbf{g}(\mathbf{x}_{4s+}(\psi_i), \mathbf{u}(\psi_i), \psi_i) \tag{4.93}$$

The control vector $\mathbf{u}(\psi_i)$ corresponds to the desired trim condition, and is held constant during the perturbation.

If and only if x_{MR_j} is one of the displacement states, its derivative $x_{MR_{j-4}}$ also needs to be perturbed by $+4\Omega\Delta x_{MR_j} \cos 4\psi_i$ at the same time. This additional perturbation is represented by [...] in Eq. (4.92).

(c) Repeat the two previous steps with a negative perturbation of the j^{th} main rotor state, $x_{MR_j} - \Delta x_{MR_j} \sin 4\psi_i$, and build the derivative using central difference approximations. This derivative is the $(L+j)^{th}$ column of the interim matrix $P(\psi_i)$ at the azimuth angle ψ_i , that is:

$$\{P(\psi_i)\}_{L+j} \approx \frac{1}{2\Delta x_j} \left(\mathbf{F}_{4s+}(\psi_i) - \mathbf{F}_{4s-}(\psi_i)\right) \tag{4.94}$$

(d) Repeat the three previous steps for each of the L elements of the main rotor state vector partition $\mathbf{x}_{MR}$, i.e., for the main rotor state in x_{MR_j}, $j = 1, \ldots, L$, to complete the second half of the interim matrix $P(\psi_i)$

$$P(\psi_i) = \Big[\{P(\psi_i)\}_1 \cdots \{P(\psi_i)\}_L \ \{P(\psi_i)\}_{L+1} \cdots \{P(\psi_i)\}_{2L}\Big]_{n\times 2L} \tag{4.95}$$

3. Repeat steps 1-2 for N_ψ azimuth angles ψ_i for one rotor revolution.

4. Extract the average, 4/rev cosine, and 4/rev sine harmonics of $P(\psi_i)$ using Fourier analysis.

   Define:

$$C_{ave} = \frac{\Delta\psi}{N_\psi}\sum_{i=1}^{N_\psi} P(\psi_i) \tag{4.96}$$

$$C_{4c} = \frac{2}{N_\psi}\sum_{i=1}^{N_\psi} P(\psi_i)\cos 4\psi_i \tag{4.97}$$

$$C_{4s} = \frac{2}{N_\psi}\sum_{i=1}^{N_\psi} P(\psi_i)\sin 4\psi_i \tag{4.98}$$

   Then it is essentially

$$C_{32} = C_{ave} \tag{4.99}$$

$$C_{42} = \begin{bmatrix} C_{4c} \\ C_{4s} \end{bmatrix} \tag{4.100}$$

   except that the rows and columns of C_{4c} and C_{4s} must be appropriately permutated because the state subvector $\mathbf{x}_{4P}$, Eq. (4.21) and the output subvector $\mathbf{F}_{4P}$, Eq. (4.25) are arranged with the 4/rev cosine and sine components interlaced rather than grouped together.

4.3 Application to simple rotor equations

In this section, the perturbation technique described in the previous section is applied to a simple example, namely the flap equation of motion of a 4-bladed isolated rotor written in fixed-system coordinates. The blades are assumed to be rigid and hinged at the axis of rotation. This simplified model represents a useful test case because states and harmonics appear explicitly in the equation of motion, and therefore can be manipulated directly, rather than being hidden in the much more complicated numerics of the model used in the rest of this research.

The flapping equations of motion in the rotating system for a 4-bladed rotor with rigid blades hinged on the axis of rotation, and flapping degrees of freedom only can be expressed as

$$\begin{aligned}\ddot{\beta}_i + \nu^2\beta_i &= \gamma\Big[-\mu\cos\psi_i(\frac{1}{6}+\frac{\mu}{4}\sin\psi_i)\beta_i - (\frac{1}{8}+\frac{1}{6}\mu\sin\psi_i)\dot{\beta}_i \\ &+ (\frac{1}{8}+\frac{1}{3}\mu\sin\psi_i+\frac{1}{4}\mu^2\sin^2\psi_i)\theta_i \\ &- (\frac{1}{6}+\frac{1}{4}\mu\sin\psi_i)\lambda\Big] \end{aligned} \tag{4.101}$$

where λ, θ_i are the main rotor inflow and the blade pitch angle, respectively. After performing the multi-blade coordinate transformation, the equations of motion are:

$$\begin{bmatrix}\ddot{\beta}_0\\ \ddot{\beta}_{1c}\\ \ddot{\beta}_{1s}\\ \ddot{\beta}_2\end{bmatrix} + C\begin{bmatrix}\dot{\beta}_0\\ \dot{\beta}_{1c}\\ \dot{\beta}_{1s}\\ \dot{\beta}_2\end{bmatrix} + K\begin{bmatrix}\beta_0\\ \beta_{1c}\\ \beta_{1s}\\ \beta_2\end{bmatrix} = \begin{bmatrix}F_1\\ F_2\\ F_3\\ F_4\end{bmatrix} \tag{4.102}$$

where

$$C = \begin{bmatrix} \frac{\gamma}{8} & 0 & \frac{\gamma}{12}\mu & 0 \\ 0 & \frac{\gamma}{8} & 2 & -\frac{\gamma}{6}\mu\sin 2\psi \\ \frac{\gamma}{6}\mu & -2 & \frac{\gamma}{8} & \frac{\gamma}{6}\mu\cos 2\psi \\ 0 & -\frac{\gamma}{12}\mu\sin 2\psi & \frac{\gamma}{12}\mu\cos 2\psi & \frac{\gamma}{8} \end{bmatrix} \tag{4.103}$$

$$K = \begin{bmatrix} \nu^2 & 0 & 0 & -\frac{\gamma}{8}\mu^2 \sin 2\psi \\ \frac{\gamma}{6}\mu & -1+\nu^2+\frac{\gamma}{16}\mu^2 \sin 4\psi & \frac{\gamma}{8}-\frac{\gamma}{16}\mu^2 \cos 4\psi + \frac{\gamma}{16}\mu^2 & -\frac{\gamma}{6}\mu \cos 2\psi \\ 0 & -\frac{\gamma}{8}-\frac{\gamma}{16}\mu^2 \cos 4\psi + \frac{\gamma}{16}\mu^2 & -1+\nu^2-\frac{\gamma}{16}\mu^2 \sin 4\psi & -\frac{\gamma}{6}\mu \sin 2\psi \\ -\frac{\gamma}{8}\mu^2 \sin 2\psi & -\frac{\gamma}{6}\mu \cos 2\psi & -\frac{\gamma}{6}\mu \sin 2\psi & \nu^2 \end{bmatrix} \tag{4.104}$$

$$\begin{aligned} F_1 &= \frac{\gamma}{8}(1+\mu^2)\theta_0 \\ &+ \frac{\gamma}{6}\mu\theta_{1s} - \frac{\gamma}{6}\lambda + \left[\frac{\gamma}{8}(1+\mu^2)\theta_{4c} + \frac{\gamma}{6}\mu\theta_{5s} - \frac{\gamma}{6}\mu\theta_{3s}\right]\cos 4\psi \\ &+ \left[\frac{\gamma}{8}(1+\mu^2)\theta_{4s} + \frac{\gamma}{6}\mu\theta_{3c} - \frac{\gamma}{6}\mu\theta_{5c}\right]\sin 4\psi \end{aligned} \tag{4.105}$$

$$\begin{aligned} F_2 &= \frac{\gamma}{8}(1+\frac{1}{2}\mu^2)\theta_{1c} - \frac{\gamma}{16}\mu^2\theta_{3c} \\ &+ \left[-\frac{\gamma}{16}\mu^2\theta_{1c} + \frac{\gamma}{8}(1+\frac{1}{2}\mu^2)\theta_{5c} + \frac{\gamma}{8}(1+\frac{1}{2}\mu^2)\theta_{3c}\right]\cos 4\psi \\ &+ \left[\frac{\gamma}{8}(1+\frac{1}{2}\mu^2)\theta_{5s} + \frac{\gamma}{8}(1+\frac{1}{2}\mu^2)\theta_{3s} - \frac{\gamma}{16}\mu^2\theta_{1s}\right]\sin 4\psi \\ &- \frac{\gamma}{16}\mu^2\theta_{5s}\sin 8\psi - \frac{\gamma}{16}\mu^2\theta_{5c}\cos 8\psi \end{aligned} \tag{4.106}$$

$$\begin{aligned} F_3 &= -\frac{\gamma}{4}\lambda\mu + \frac{\gamma}{8}(1+\frac{3}{2}\mu^2)\theta_{1s} + \frac{\gamma}{3}\mu\theta_0 - \frac{\gamma}{16}\mu^2\theta_{3s} \\ &+ \left[-\frac{\gamma}{8}(1+\frac{3}{2}\mu^2)\theta_{3s} + \frac{\gamma}{8}(1+\frac{3}{2}\mu^2)\theta_{5s} + \frac{\gamma}{16}\mu^2\theta_{1s} + \frac{\gamma}{3}\mu\theta_{4c}\right]\cos 4\psi \\ &+ \left[\frac{\gamma}{3}\mu\theta_{4s} - \frac{\gamma}{16}\mu^2\theta_{1c} - \frac{\gamma}{8}(1+\frac{3}{2}\mu^2)\theta_{5c} + \frac{\gamma}{8}(1+\frac{3}{2}\mu^2)\theta_{3c}\right]\sin 4\psi \\ &- \frac{\gamma}{16}\mu^2\theta_{5c}\sin 8\psi + \frac{\gamma}{16}\mu^2\theta_{5s}\cos 8\psi \end{aligned} \tag{4.107}$$

$$
\begin{aligned}
F_4 &= (-\frac{\gamma}{6}\mu\theta_{3s} + \frac{\gamma}{6}\mu\theta_{1s} + \frac{\gamma}{8}\mu^2\theta_0 + \frac{\gamma}{16}\mu^2\theta_{4c})\cos 2\psi \\
&+ (\frac{\gamma}{16}\mu^2\theta_{4s} - \frac{\gamma}{6}\mu\theta_{1c} + \frac{\gamma}{6}\mu\theta_{3c})\sin 2\psi \\
&+ (\frac{\gamma}{16}\mu^2\theta_{4s} - \frac{\gamma}{6}\mu\theta_{5c})\sin 6\psi + (\frac{\gamma}{16}\mu^2\theta_{4c} + \frac{\gamma}{6}\mu\theta_{5s})\cos 6\psi \qquad (4.108)
\end{aligned}
$$

To illustrate the technique for the extraction of a linear model that included 4/rev characteristics, the longitudinal flapping equation of motion in the fixed system is:

$$
\begin{aligned}
\ddot{\beta}_{1c} + 2\dot{\beta}_{1s} &+ (\nu^2 - 1)\beta_{1c} \\
&= -\frac{\gamma}{16}\mu^2 \sin 4\psi\beta_{1c} + \frac{\gamma}{6}\mu \sin 2\psi\dot{\beta}_2 - \frac{\gamma}{6}\mu\beta_0 - \frac{\gamma}{8}\dot{\beta}_{1c} \\
&+ (\frac{\gamma}{6}\mu\cos 2\psi)\beta_2 - (\frac{\gamma}{8} - \frac{\gamma}{16}\mu^2\cos 4\psi + \frac{\gamma}{16}\mu^2)\beta_{1s} \\
&+ \frac{\gamma}{8}(1 + \frac{1}{2}\mu^2)\theta_{1c} - \frac{\gamma}{16}\mu^2\theta_{3c} \\
&+ \left[-\frac{\gamma}{16}\mu^2\theta_{1c} + \frac{\gamma}{8}(1 + \frac{1}{2}\mu^2)\theta_{5c} + \frac{\gamma}{8}(1 + \frac{1}{2}\mu^2)\theta_{3c}\right]\cos 4\psi \\
&+ \left[\frac{\gamma}{8}(1 + \frac{1}{2}\mu^2)\theta_{5s} + \frac{\gamma}{8}(1 + \frac{1}{2}\mu^2)\theta_{3s} - \frac{\gamma}{16}\mu^2\theta_{1s}\right]\sin 4\psi \\
&- \frac{\gamma}{16}\mu^2\theta_{5s}\sin 8\psi - \frac{\gamma}{16}\mu^2\theta_{5c}\cos 8\psi \qquad (4.109)
\end{aligned}
$$

For simplicity, only the $-\frac{\gamma}{16}\mu^2 \sin 4\psi\beta_{1c}$ term from aerodynamics and $\frac{\gamma}{8}(1+\frac{\mu^2}{2})(\theta_{3c}\cos 4\psi + \theta_{3s}\sin 4\psi)$ terms from the 3/rev input, and $-\frac{\gamma}{16}\mu^2\theta_{1s}\sin 4\psi$ term from the longitudinal cyclic pitch angle are retained. The rest of the variables are represented by M_θ and M_β terms. Equation (4.109) can therefore be rewritten as:

$$
\begin{aligned}
\ddot{\beta}_{1c} &= -\frac{\gamma}{8}\dot{\beta}_{1c} + (\nu^2 - \frac{\gamma\mu^2}{16}\sin 4\psi - 1)\ \beta_{1c} \\
&+ \frac{\gamma}{8}(1 + \frac{1}{2}\mu^2)(\theta_{3c}\cos 4\psi + \theta_{3s}\sin 4\psi) - \frac{\gamma}{16}\mu^2\theta_{1s}\sin 4\psi + M_\theta + M_\beta \\
&\qquad (4.110)
\end{aligned}
$$

4.3.1 Prescribed solution form

The assumed solution for Eq. (4.110) has an average plus 4/rev cosine and sine components as shown in Eq. (4.18). Substituting Eqs. (4.18) and (4.43) into Eq. (4.110), the longitudinal flapping equation of motion becomes:

$$\begin{aligned}\ddot{\beta}_{1c} = \quad &- \quad \frac{\gamma}{8}\Big[\dot{\beta}_{1c_{ave}} + (\dot{\beta}_{1c_{4c}} + 4\Omega\beta_{1c_{4s}})\cos 4\psi + (\dot{\beta}_{1c_{4s}} - 4\Omega\beta_{1c_{4c}})\sin 4\psi\Big] \\ &+ \quad (\nu^2 - \frac{\gamma\mu^2}{16}\sin 4\psi - 1)(\beta_{1c_{ave}} + \beta_{1c_{4c}}\cos 4\psi + \beta_{1c_{4s}}\sin 4\psi) \\ &+ \quad \frac{\gamma}{8}(1 + \frac{\mu^2}{2})(\theta_{3c}\cos 4\psi + \theta_{3s}\sin 4\psi) - \frac{\gamma}{16}\mu^2\theta_{1s}\sin 4\psi + M_\theta + M_\beta\end{aligned} \tag{4.111}$$

Note that Eqs. (4.43) and (4.44) contain an average value and harmonics at only 4/rev, which results from the original assumed solution defined in Eq. (4.18). However, the equation of motion shown in Eq. (4.111) also has 8/rev frequency components that result from the aerodynamic term in Eq. (4.110).

$$\begin{aligned}-\frac{\gamma\mu^2}{16}\ \sin 4\psi\ \beta_{1c} \quad &= \quad -\frac{\gamma\mu^2}{16}\ \sin 4\psi\Big(\beta_{1c_{ave}} + \beta_{1c_{4c}}\cos 4\psi + \beta_{1c_{4s}}\sin 4\psi\Big) \\ &= \quad -\frac{\gamma\mu^2}{16}\Big(\beta_{1c_{ave}}\sin 4\psi + \frac{1}{2}\beta_{1c_{4s}} + \frac{1}{2}\beta_{1c_{4c}}\sin 8\psi - \frac{1}{2}\beta_{1c_{4s}}\cos 8\psi\Big)\end{aligned} \tag{4.112}$$

Therefore, Eq. (4.111) can also be written as follows:

$$\begin{aligned}\ddot{\beta}_{1c} = \quad &- \quad \frac{\gamma}{8}\Big[\dot{\beta}_{1c_{ave}} + (\dot{\beta}_{1c_{4c}} + 4\Omega\beta_{1c_{4s}})\cos 4\psi + (\dot{\beta}_{1c_{4s}} - 4\Omega\beta_{1c_{4c}})\sin 4\psi\Big] \\ &+ \quad (\nu^2 - 1)(\beta_{1c_{ave}} + \beta_{1c_{4c}}\cos 4\psi + \beta_{1c_{4s}}\sin 4\psi) \\ &- \quad \frac{\gamma\mu^2}{16}(\beta_{1c_{ave}}\sin 4\psi + \frac{1}{2}\beta_{1c_{4s}}) \\ &- \quad \frac{\gamma\mu^2}{16}(\frac{1}{2}\beta_{1c_{4c}}\sin 8\psi - \frac{1}{2}\beta_{1c_{4s}}\cos 8\psi) \\ &+ \quad \frac{\gamma}{8}(1 + \frac{\mu^2}{2})\ (\theta_{3c}\cos 4\psi + \theta_{3s}\sin 4\psi) \\ &- \quad \frac{\gamma}{16}\mu^2\theta_{1s}\sin 4\psi + M_\theta + M_\beta\end{aligned} \tag{4.113}$$

4.3.2 Perturbation of the equations of motion

To simplified the expression, the perturbations of the M_θ and M_β terms in Eq. (4.111) are not shown here, but they are not eliminated from Eq. (4.111).

Perturbing $\boldsymbol{\beta_{1c}}$ by $\pm\,\boldsymbol{\Delta\beta_{1c}}$ at $\boldsymbol{\psi_i}$

$$\begin{aligned}
\ddot{\beta}_{1c}(\psi_i)\Big|^{\pm}_{\beta_{1c_{ave}}} = \; & - \; \frac{\gamma}{8}\Big\{\dot{\beta}_{1c_{ave}} + \Big[\dot{\beta}_{1c_{4c}} + 4\Omega\beta_{1c_{4s}}\Big]\cos 4\psi \\
& + \; \Big[\dot{\beta}_{1c_{4s}} - 4\Omega\beta_{1c_{4c}}\Big]\sin 4\psi\Big\} + (\nu^2 - \frac{\gamma\mu^2}{16}\sin 4\psi - 1) \\
& \times \; \Big[(\beta_{1c_{ave}} \pm \Delta\beta_{1c}) + \beta_{1c_{4c}}\cos 4\psi + \beta_{1c_{4s}}\sin 4\psi\Big] \\
& + \; \frac{\gamma}{8}(\frac{\mu^2}{2} + 1)(\theta_{3c}\cos 4\psi + \theta_{3s}\sin 4\psi) \\
& - \; \frac{\gamma}{16}\mu^2\theta_{1s}\sin 4\psi
\end{aligned} \tag{4.114}$$

where the superscript $\pm$ represents the direction of the perturbation, and the subscript $\beta_{1c_{ave}}$ represents the perturbed state variable.

Perturbing $\boldsymbol{\beta_{1c}}$ by $\pm\,\boldsymbol{\Delta\beta_{1c}\cos 4\psi}$ at $\boldsymbol{\psi_i}$

$$\begin{aligned}
\ddot{\beta}_{1c}(\psi_i)\Big|^{\pm}_{\beta_{1c_{4c}}} = \; & - \; \frac{\gamma}{8}\Big\{\dot{\beta}_{1c_{ave}} + (\dot{\beta}_{1c_{4c}} + 4\Omega\beta_{1c_{4s}})\cos 4\psi \\
& + \; \Big[\dot{\beta}_{1c_{4s}} - 4\Omega(\beta_{1c_{4c}} \pm \Delta\beta_{1c})\Big]\sin 4\psi\Big\} + (\nu^2 - \frac{\gamma\mu^2}{16}\sin 4\psi - 1) \\
& \times \; \Big[\beta_{1c_{ave}} + (\beta_{1c_{4c}} \pm \Delta\beta_{1c})\cos 4\psi + \beta_{1c_{4s}}\sin 4\psi\Big] \\
& + \; \frac{\gamma}{8}(\frac{\mu^2}{2} + 1)(\theta_{3c}\cos 4\psi + \theta_{3s}\sin 4\psi) \\
& - \; \frac{\gamma}{16}\mu^2\theta_{1s}\sin 4\psi
\end{aligned} \tag{4.115}$$

Perturbing $\boldsymbol{\beta_{1c}}$ by $\pm\,\boldsymbol{\Delta\beta_{1c}}\sin 4\boldsymbol{\psi}$ at $\boldsymbol{\psi_i}$

$$\begin{aligned}
\ddot{\beta}_{1c}(\psi_i)\Big|^{\pm}_{\beta_{1c_{4s}}} = & - \frac{\gamma}{8}\Big\{\dot{\beta}_{1c_{ave}} + \Big[\dot{\beta}_{1c_{4c}} + 4\Omega(\beta_{1c_{4s}} \pm \Delta\beta_{1c})\Big]\cos 4\psi \\
& + \Big[\dot{\beta}_{1c_{4s}} - 4\Omega\beta_{1c_{4c}}\Big]\sin 4\psi\Big\} + (\nu^2 - \frac{\gamma\mu^2}{16}\sin 4\psi - 1) \\
& \times \Big[\beta_{1c_{ave}} + \beta_{1c_{4c}}\cos 4\psi + (\beta_{1c_{4s}} \pm \Delta\beta_{1c})\sin 4\psi\Big] \\
& + \frac{\gamma}{8}(\frac{\mu^2}{2} + 1)(\theta_{3c}\cos 4\psi + \theta_{3s}\sin 4\psi) \\
& - \frac{\gamma}{16}\mu^2\theta_{1s}\sin 4\psi
\end{aligned} \tag{4.116}$$

Perturbing $\dot{\boldsymbol{\beta}}_{\mathbf{1c}}$ by $\pm\,\boldsymbol{\Delta\dot{\beta}_{1c}}$ at $\boldsymbol{\psi_i}$

$$\begin{aligned}
\ddot{\beta}_{1c}(\psi_i)\Big|^{\pm}_{\dot{\beta}_{1c_{ave}}} = & - \frac{\gamma}{8}\Big\{(\dot{\beta}_{1c_{ave}} \pm \Delta\dot{\beta}_{1c}) + \Big[\dot{\beta}_{1c_{4c}} + 4\Omega\beta_{1c_{4s}}\Big]\cos 4\psi \\
& + \Big[\dot{\beta}_{1c_{4s}} - 4\Omega\beta_{1c_{4c}}\Big]\sin 4\psi\Big\} + (\nu^2 - \frac{\gamma\mu^2}{16}\sin 4\psi - 1) \\
& \times \Big[\beta_{1c_{ave}} + \beta_{1c_{4c}}\cos 4\psi + \beta_{1c_{4s}}\sin 4\psi\Big] \\
& + \frac{\gamma}{8}(\frac{\mu^2}{2} + 1)(\theta_{3c}\cos 4\psi + \theta_{3s}\sin 4\psi) \\
& - \frac{\gamma}{16}\mu^2\theta_{1s}\sin 4\psi
\end{aligned} \tag{4.117}$$

Perturbing $\dot{\boldsymbol{\beta}}_{\mathbf{1c}}$ by $\pm\,\boldsymbol{\Delta\dot{\beta}_{1c}}\cos 4\boldsymbol{\psi}$ at $\boldsymbol{\psi_i}$

$$\begin{aligned}
\ddot{\beta}_{1c}(\psi_i)\Big|^{\pm}_{\dot{\beta}_{1c_{4c}}} = & - \frac{\gamma}{8}\Big\{\dot{\beta}_{1c_{ave}} + \Big[(\dot{\beta}_{1c_{4c}} \pm \Delta\dot{\beta}_{1c}) + 4\Omega\beta_{1c_{4s}}\Big]\cos 4\psi \\
& + \Big[\dot{\beta}_{1c_{4s}} - 4\Omega\beta_{1c_{4c}}\Big]\sin 4\psi\Big\} + (\nu^2 - \frac{\gamma\mu^2}{16}\sin 4\psi - 1) \\
& \times \Big[\beta_{1c_{ave}} + \beta_{1c_{4c}}\cos 4\psi + \beta_{1c_{4s}}\sin 4\psi\Big] \\
& + \frac{\gamma}{8}(\frac{\mu^2}{2} + 1)(\theta_{3c}\cos 4\psi + \theta_{3s}\sin 4\psi) \\
& - \frac{\gamma}{16}\mu^2\theta_{1s}\sin 4\psi
\end{aligned} \tag{4.118}$$

Perturbing $\dot{\beta}_{1c}$ by $\pm\,\Delta\dot{\beta}_{1c}\sin 4\psi$ at ψ_i

$$\begin{aligned}
\ddot{\beta}_{1c}(\psi_i)\Big|^{\pm}_{\dot{\beta}_{1c_{4s}}} = & - \frac{\gamma}{8}\Big\{\dot{\beta}_{1c_{ave}} + \Big[\dot{\beta}_{1c_{4c}} + 4\Omega\beta_{1c_{4s}}\Big]\cos 4\psi \\
& + \Big[(\dot{\beta}_{1c_{4s}} \pm \Delta\dot{\beta}_{1c}) - 4\Omega\beta_{1c_{4c}}\Big]\sin 4\psi\Big\} + (\nu^2 - \frac{\gamma\mu^2}{16}\sin 4\psi - 1) \\
& \times \Big[\beta_{1c_{ave}} + \beta_{1c_{4c}}\cos 4\psi + \beta_{1c_{4s}}\sin 4\psi\Big] \\
& + \frac{\gamma}{8}(\frac{\mu^2}{2} + 1)(\theta_{3c}\cos 4\psi + \theta_{3s}\sin 4\psi) \\
& - \frac{\gamma}{16}\mu^2\theta_{1s}\sin 4\psi
\end{aligned} \tag{4.119}$$

Perturbing θ_{1s} by $\pm\,\Delta\theta_{1s}$ at ψ_i

$$\begin{aligned}
\ddot{\beta}_{1c}(\psi_i)\Big|^{\pm}_{\theta_{3c}} = & - \frac{\gamma}{8}\Big\{\dot{\beta}_{1c_{ave}} + \Big[\dot{\beta}_{1c_{4c}} + 4\Omega\beta_{1c_{4s}}\Big]\cos 4\psi \\
& + \Big[\dot{\beta}_{1c_{4s}} - 4\Omega\beta_{1c_{4c}}\Big]\sin 4\psi\Big\} + (\nu^2 - \frac{\gamma\mu^2}{16}\sin 4\psi - 1) \\
& \times \Big[\beta_{1c_{ave}} + \beta_{1c_{4c}}\cos 4\psi + \beta_{1c_{4s}}\sin 4\psi\Big] \\
& + \frac{\gamma}{8}(\frac{\mu^2}{2} + 1)\Big[\theta_{3c}\cos 4\psi + \theta_{3s}\sin 4\psi\Big] \\
& - \frac{\gamma}{16}\mu^2(\theta_{1s} \pm \Delta\theta_{1s})\sin 4\psi
\end{aligned} \tag{4.120}$$

Perturbing θ_{3c} by $\pm\,\Delta\theta_{3c}$ at ψ_i

$$\begin{aligned}
\ddot{\beta}_{1c}(\psi_i)\Big|^{\pm}_{\theta_{3c}} = & - \frac{\gamma}{8}\Big\{\dot{\beta}_{1c_{ave}} + \Big[\dot{\beta}_{1c_{4c}} + 4\Omega\beta_{1c_{4s}}\Big]\cos 4\psi \\
& + \Big[\dot{\beta}_{1c_{4s}} - 4\Omega\beta_{1c_{4c}}\Big]\sin 4\psi\Big\} + (\nu^2 - \frac{\gamma\mu^2}{16}\sin 4\psi - 1) \\
& \times \Big[\beta_{1c_{ave}} + \beta_{1c_{4c}}\cos 4\psi + \beta_{1c_{4s}}\sin 4\psi\Big] \\
& + \frac{\gamma}{8}(\frac{\mu^2}{2} + 1)\Big[(\theta_{3c} \pm \Delta\theta_{3c})\cos 4\psi + \theta_{3s}\sin 4\psi\Big] \\
& - \frac{\gamma}{16}\mu^2\theta_{1s}\sin 4\psi
\end{aligned} \tag{4.121}$$

Perturbing θ_{3s} by $\pm\,\Delta\theta_{3s}$ at ψ_i

$$\begin{aligned}
\ddot{\beta}_{1c}(\psi_i)\Big|_{\theta_{3s}}^{\pm} = \; & - \frac{\gamma}{8}\Big\{\dot{\beta}_{1c_{ave}} + \Big[\dot{\beta}_{1c_{4c}} + 4\Omega\beta_{1c_{4s}}\Big]\cos 4\psi \\
& + \Big[\dot{\beta}_{1c_{4s}} - 4\Omega\beta_{1c_{4c}}\Big]\sin 4\psi\Big\} + (\nu^2 - \frac{\gamma\mu^2}{16}\sin 4\psi - 1) \\
& \times \Big[\beta_{1c_{ave}} + \beta_{1c_{4c}}\cos 4\psi + \beta_{1c_{4s}}\sin 4\psi\Big] \\
& + \frac{\gamma}{8}(\frac{\mu^2}{2} + 1)\Big[\theta_{3c}\cos 4\psi + (\theta_{3s} \pm \Delta\theta_{3s})\sin 4\psi\Big] \\
& - \frac{\gamma}{16}\mu^2\theta_{1s}\sin 4\psi
\end{aligned} \tag{4.122}$$

4.3.3 Extract four/rev harmonic components

The average value and the 4/rev harmonic components of the perturbed equations Eqs. (4.114)-(4.122) can be obtained by applying the Fourier series approximation over one sample window. The length of the sample window used in this study is one rotor revolution or $\psi = 0 \sim 2\pi$.

Extract $\frac{\partial\ddot{\beta}_{1c_{ave}}}{\partial\beta_{1c_{ave}}}$, $\frac{\partial\beta''_{1c_{4c}}}{\partial\beta_{1c_{ave}}}$, $\frac{\partial\beta''_{1c_{4s}}}{\partial\beta_{1c_{ave}}}$ from $\ddot{\beta}_{1c}(\psi_i)\Big|_{\beta_{1c_{ave}}}^{\pm}$

$$\begin{aligned}
\ddot{\beta}^{+}_{1c_{ave}} &= \frac{1}{2\pi}\int_0^{2\pi} \ddot{\beta}_{1c}(\psi_i)\Big|_{\beta_{1c_{ave}}}^{+} \mathrm{d}\psi \\
&= \frac{1}{2\pi}\int_0^{2\pi}\Big[-\frac{\gamma}{8}\dot{\beta}_{1c_{ave}} + (\nu^2-1)(\beta_{1c_{ave}} + \Delta\beta_{1c_{ave}}) - \frac{\gamma\mu^2}{16}\sin^2 4\psi\Big]\mathrm{d}\psi \\
&= \frac{1}{2\pi}\Big[-\frac{\gamma}{8}\dot{\beta}_{1c_{ave}}\psi + (\nu^2-1)(\beta_{1c_{ave}} + \Delta\beta_{1c_{ave}})\psi - \frac{\gamma\mu^2}{16}(\frac{\psi}{2})\Big]_0^{2\pi} \\
&= -\frac{\gamma}{8}\dot{\beta}_{1c_{ave}} + (\nu^2-1)(\beta_{1c_{ave}} + \Delta\beta_{1c_{ave}}) - \frac{\gamma\mu^2}{32}
\end{aligned}$$

$$
\begin{aligned}
\ddot{\beta}^{-}_{1c_{ave}} &= \frac{1}{2\pi}\int_0^{2\pi} \ddot{\beta}_{1c}(\psi_i)\Big|^{-}_{\beta_{1c_{ave}}} \mathrm{d}\psi \\
&= \frac{1}{2\pi}\int_0^{2\pi} \Big[-\frac{\gamma}{8}\dot{\beta}_{1c_{ave}} + (\nu^2-1)(\beta_{1c_{ave}} - \Delta\beta_{1c_{ave}}) - \frac{\gamma\mu^2}{16}\sin^2 4\psi\Big]\mathrm{d}\psi \\
&= -\frac{\gamma}{8}\dot{\beta}_{1c_{ave}} + (\nu^2-1)(\beta_{1c_{ave}} - \Delta\beta_{1c_{ave}}) - \frac{\gamma\mu^2}{32}
\end{aligned}
$$

The elements of the state matrix can be calculated using central difference approximation.

$$
\frac{\partial\ddot{\beta}_{1c_{ave}}}{\partial\beta_{1c_{ave}}} = \frac{\ddot{\beta}^{+}_{1c_{ave}} - \ddot{\beta}^{-}_{1c_{ave}}}{2\Delta\beta_{1c_{ave}}} = \frac{(\nu^2-1)(2\Delta\beta_{1c_{ave}})}{2\Delta\beta_{1c_{ave}}} = (\nu^2-1) \tag{4.123}
$$

$$
\begin{aligned}
{\beta''_{1c_{4c}}}^{+} &= \frac{1}{\pi}\int_0^{2\pi} \ddot{\beta}_{1c}(\psi_i)\Big|^{+}_{\beta_{1c_{ave}}} \cos 4\psi \ \mathrm{d}\psi \\
&= \frac{1}{\pi}\int_0^{2\pi} \Big\{\Big[-\frac{\gamma}{8}(\dot{\beta}_{1c_{4c}} + 4\Omega\beta_{1c_{4s}})\cos^2 4\psi + (\nu^2-1)\beta_{1c_{4c}}\cos^2 4\psi\Big] \\
&+ \frac{\gamma}{8}(\frac{\mu^2}{2}+1)(\theta_{3c}\cos^2 4\psi + \theta_{3s}\sin 4\psi\cos 4\psi)\Big\}\mathrm{d}\psi \\
&= \frac{1}{\pi}\Big[-\frac{\gamma}{8}(\dot{\beta}_{1c_{4c}} + 4\Omega\beta_{1c_{4s}}) + (\nu^2-1)\beta_{1c_{4c}} + \frac{\gamma}{8}(\frac{\mu^2}{2}+1)\theta_{3c}\Big](\frac{\psi}{2})\Big|_0^{2\pi} \\
&- \frac{\gamma}{8}(\dot{\beta}_{1c_{4c}} + 4\Omega\beta_{1c_{4s}}) + (\nu^2-1)\beta_{1c_{4c}} + \frac{\gamma}{8}(\frac{\mu^2}{2}+1)\theta_{3c}
\end{aligned}
$$

$$
\begin{aligned}
{\beta''_{1c_{4c}}}^{-} &= \frac{1}{\pi}\int_0^{2\pi} \ddot{\beta}_{1c}(\psi_i)\Big|^{-}_{\beta_{1c_{ave}}} \cos 4\psi \ \mathrm{d}\psi \\
&= \frac{1}{\pi}\int_0^{2\pi} \Big\{\Big[-\frac{\gamma}{8}(\dot{\beta}_{1c_{4c}} + 4\Omega\beta_{1c_{4s}})\cos^2 4\psi + (\nu^2-1)\beta_{1c_{4c}}\cos^2 4\psi\Big] \\
&+ \frac{\gamma}{8}(\frac{\mu^2}{2}+1)(\theta_{3c}\cos^2 4\psi + \theta_{3s}\sin 4\psi\cos 4\psi)\Big\}\mathrm{d}\psi \\
&- \frac{\gamma}{8}(\dot{\beta}_{1c_{4c}} + 4\Omega\beta_{1c_{4s}}) + (\nu^2-1)\beta_{1c_{4c}} + \frac{\gamma}{8}(\frac{\mu^2}{2}+1)\theta_{3c}
\end{aligned}
$$

$$
\frac{\partial\beta''_{1c_{4c}}}{\partial\beta_{1c_{ave}}} = \frac{{\beta''_{1c_{4c}}}^{+} - {\beta''_{1c_{4c}}}^{-}}{2\Delta\beta_{1c_{ave}}} = 0 \tag{4.124}
$$

$$
\begin{aligned}
{\beta''_{1c_{4s}}}^{+} &= \frac{1}{\pi}\int_0^{2\pi} \ddot{\beta}_{1c}(\psi_i)\Big|^{+}_{\beta_{1c_{ave}}} \sin 4\psi \mathrm{d}\psi \\
&= \frac{1}{\pi}\int_0^{2\pi} \Big\{\Big[-\frac{\gamma}{8}(\dot{\beta}_{1c_{4s}} - 4\Omega\beta_{1c_{4c}})\sin^2 4\psi + (\nu^2-1)\beta_{1c_{4s}}\sin^2 4\psi \\
&- \frac{\gamma\mu^2}{16}(\beta_{1c_{ave}} + \Delta\beta_{1c_{ave}})\sin^2 4\psi\Big] + \frac{\gamma}{8}(\frac{\mu^2}{2}+1)(\theta_{3c}\cos 4\psi \sin 4\psi \\
&+ \theta_{3s}\sin^2 4\psi) - \frac{\gamma}{16}\mu^2\theta_{1s}\sin^2 4\psi\Big\}\mathrm{d}\psi \\
&= \frac{1}{\pi}\Big[-\frac{\gamma}{8}(\dot{\beta}_{1c_{4s}} - 4\Omega\beta_{1c_{4c}}) + (\nu^2-1)\beta_{1c_{4s}} - \frac{\gamma\mu^2}{16}(\beta_{1c_{ave}} + \Delta\beta_{1c_{ave}}) \\
&+ \frac{\gamma}{8}(\frac{\mu^2}{2}+1)\theta_{3s} - \frac{\gamma}{16}\mu^2\theta_{1s}\Big](\frac{\psi}{2})\Big|_0^{2\pi} \\
&= -\frac{\gamma}{8}(\dot{\beta}_{1c_{4s}} - 4\Omega\beta_{1c_{4c}}) + (\nu^2-1)\beta_{1c_{4s}} - \frac{\gamma\mu^2}{16}(\beta_{1c_{ave}} + \Delta\beta_{1c_{ave}}) \\
&+ \frac{\gamma}{8}(\frac{\mu^2}{2}+1)\theta_{3s} - \frac{\gamma}{16}\mu^2\theta_{1s}
\end{aligned}
$$

$$
\begin{aligned}
{\beta''_{1c_{4s}}}^{-} &= \frac{1}{\pi}\int_0^{2\pi} \ddot{\beta}_{1c}(\psi_i)\Big|^{-}_{\beta_{1c_{ave}}} \sin 4\psi \mathrm{d}\psi \\
&= \frac{1}{\pi}\int_0^{2\pi} \Big\{\Big[-\frac{\gamma}{8}(\dot{\beta}_{1c_{4s}} - 4\Omega\beta_{1c_{4c}})\sin^2 4\psi + (\nu^2-1)\beta_{1c_{4s}}\sin^2 4\psi \\
&- \frac{\gamma\mu^2}{16}(\beta_{1c_{ave}} - \Delta\beta_{1c_{ave}})\sin^2 4\psi\Big] + \frac{\gamma}{8}(\frac{\mu^2}{2}+1)(\theta_{3c}\cos 4\psi \sin 4\psi \\
&+ \theta_{3s}\sin^2 4\psi) - \frac{\gamma}{16}\mu^2\theta_{1s}\sin^2 4\psi\Big\}\mathrm{d}\psi \\
&= -\frac{\gamma}{8}(\dot{\beta}_{1c_{4s}} - 4\Omega\beta_{1c_{4c}}) + (\nu^2-1)\beta_{1c_{4s}} - \frac{\gamma\mu^2}{16}(\beta_{1c_{ave}} - \Delta\beta_{1c_{ave}}) \\
&+ \frac{\gamma}{8}(\frac{\mu^2}{2}+1)\theta_{3s} - \frac{\gamma}{16}\mu^2\theta_{1s}
\end{aligned}
$$

$$
\frac{\partial\beta''_{1c_{4s}}}{\partial\beta_{1c_{ave}}} = \frac{{\beta''_{1c_{4s}}}^{+} - {\beta''_{1c_{4s}}}^{-}}{2\Delta\beta_{1c_{ave}}} = \frac{-\frac{\gamma\mu^2}{16}(2\Delta\beta_{1c_{ave}})}{2\Delta\beta_{1c_{ave}}} = -\frac{\gamma\mu^2}{16} \tag{4.125}
$$

Extract $\frac{\partial \ddot{\beta}_{1c_{ave}}}{\partial \beta_{1c_{4c}}}$, $\frac{\partial \beta''_{1c_{4c}}}{\partial \beta_{1c_{4c}}}$, $\frac{\partial \beta''_{1c_{4s}}}{\partial \beta_{1c_{4c}}}$ **from** $\ddot{\boldsymbol{\beta}}_{\mathbf{1c}}(\boldsymbol{\psi}_i)\Big|^{\pm}_{\boldsymbol{\beta}_{\mathbf{1c_{4c}}}}$

$$\frac{\partial \ddot{\beta}_{1c_{ave}}}{\partial \beta_{1c_{4c}}} = 0 \tag{4.126}$$

$$\frac{\partial \beta''_{1c_{4c}}}{\partial \beta_{1c_{4c}}} = (\nu^2 - 1) \tag{4.127}$$

$$\frac{\partial \beta''_{1c_{4s}}}{\partial \beta_{1c_{4c}}} = \frac{\gamma\mu^2}{16} \tag{4.128}$$

Extract $\frac{\partial \ddot{\beta}_{1c_{ave}}}{\partial \beta_{1c_{4s}}}$, $\frac{\partial \beta''_{1c_{4c}}}{\partial \beta_{1c_{4s}}}$, $\frac{\partial \beta''_{1c_{4s}}}{\partial \beta_{1c_{4s}}}$ **from** $\ddot{\boldsymbol{\beta}}_{\mathbf{1c}}(\boldsymbol{\psi}_i)\Big|^{\pm}_{\boldsymbol{\beta}_{\mathbf{1c_{4s}}}}$

$$\frac{\partial \ddot{\beta}_{1c_{ave}}}{\partial \beta_{1c_{4s}}} = -\frac{\gamma\mu^2}{32} \tag{4.129}$$

$$\frac{\partial \beta''_{1c_{4c}}}{\partial \beta_{1c_{4s}}} = -\frac{\gamma\Omega}{2} \tag{4.130}$$

$$\frac{\partial \beta''_{1c_{4s}}}{\partial \beta_{1c_{4s}}} = (\nu^2 - 1) \tag{4.131}$$

Extract $\frac{\partial \ddot{\beta}_{1c_{ave}}}{\partial \dot{\beta}_{1c_{ave}}}$, $\frac{\partial \beta''_{1c_{4c}}}{\partial \dot{\beta}_{1c_{ave}}}$, $\frac{\partial \beta''_{1c_{4s}}}{\partial \dot{\beta}_{1c_{ave}}}$ **from** $\ddot{\boldsymbol{\beta}}_{\mathbf{1c}}(\boldsymbol{\psi}_i)\Big|^{\pm}_{\dot{\boldsymbol{\beta}}_{\mathbf{1c_{ave}}}}$

$$\frac{\partial \ddot{\beta}_{1c_{ave}}}{\partial \dot{\beta}_{1c_{ave}}} = -\frac{\gamma}{8} \tag{4.132}$$

$$\frac{\partial \beta''_{1c_{4c}}}{\partial \dot{\beta}_{1c_{ave}}} = 0 \tag{4.133}$$

$$\frac{\partial \beta''_{1c_{4s}}}{\partial \dot{\beta}_{1c_{ave}}} = 0 \tag{4.134}$$

Extract $\frac{\partial \ddot{\beta}_{1c_{ave}}}{\partial \dot{\beta}_{1c_{4c}}}$, $\frac{\partial \beta''_{1c_{4c}}}{\partial \dot{\beta}_{1c_{4c}}}$, $\frac{\partial \beta''_{1c_{4s}}}{\partial \dot{\beta}_{1c_{4c}}}$ **from** $\ddot{\boldsymbol{\beta}}_{\mathbf{1c}}(\boldsymbol{\psi}_i)\Big|^{\pm}_{\dot{\boldsymbol{\beta}}_{\mathbf{1c_{4c}}}}$

$$\frac{\partial \ddot{\beta}_{1c_{ave}}}{\partial \dot{\beta}_{1c_{4c}}} = 0 \tag{4.135}$$

$$\frac{\partial \beta''_{1c_{4c}}}{\partial \dot{\beta}_{1c_{4c}}} = -\frac{\gamma}{8} \tag{4.136}$$

$$\frac{\partial \beta''_{1c_{4s}}}{\partial \dot{\beta}_{1c_{4c}}} = 0 \tag{4.137}$$

Extract $\frac{\partial \ddot{\beta}_{1c_{ave}}}{\partial \dot{\beta}_{1c_{4s}}}$, $\frac{\partial \beta''_{1c_{4c}}}{\partial \dot{\beta}_{1c_{4s}}}$, $\frac{\partial \beta''_{1c_{4s}}}{\partial \dot{\beta}_{1c_{4s}}}$ from $\ddot{\boldsymbol{\beta}}_{\mathbf{1c}}(\boldsymbol{\psi}_i)\Big|^{\pm}_{\dot{\boldsymbol{\beta}}_{\mathbf{1c_{4s}}}}$

$$\frac{\partial \ddot{\beta}_{1c_{ave}}}{\partial \dot{\beta}_{1c_{4s}}} = 0 \tag{4.138}$$

$$\frac{\partial \beta''_{1c_{4c}}}{\partial \dot{\beta}_{1c_{4s}}} = 0 \tag{4.139}$$

$$\frac{\partial \beta''_{1c_{4s}}}{\partial \dot{\beta}_{1c_{4s}}} = -\frac{\gamma}{8} \tag{4.140}$$

Extract $\frac{\partial \ddot{\beta}_{1c_{ave}}}{\partial \theta_{1s}}$, $\frac{\partial \beta''_{1c_{4c}}}{\partial \theta_{1s}}$, $\frac{\partial \beta''_{1c_{4s}}}{\partial \theta_{1s}}$ from $\ddot{\boldsymbol{\beta}}_{\mathbf{1c}}(\boldsymbol{\psi}_i)\Big|^{\pm}_{\boldsymbol{\theta}_{\mathbf{1s}}}$

$$\frac{\partial \ddot{\beta}_{1c_{ave}}}{\partial \theta_{1s}} = 0 \tag{4.141}$$

$$\frac{\partial \beta''_{1c_{4c}}}{\partial \theta_{1s}} = 0 \tag{4.142}$$

$$\frac{\partial \beta''_{1c_{4s}}}{\partial \theta_{1s}} = -\frac{\gamma}{16}\mu^2 \tag{4.143}$$

Extract $\frac{\partial \ddot{\beta}_{1c_{ave}}}{\partial \theta_{3c}}$, $\frac{\partial \beta''_{1c_{4c}}}{\partial \theta_{3c}}$, $\frac{\partial \beta''_{1c_{4s}}}{\partial \theta_{3c}}$ from $\ddot{\boldsymbol{\beta}}_{\mathbf{1c}}(\boldsymbol{\psi}_i)\Big|^{\pm}_{\boldsymbol{\theta}_{\mathbf{3c}}}$

$$\frac{\partial \ddot{\beta}_{1c_{ave}}}{\partial \theta_{3c}} = 0 \tag{4.144}$$

$$\frac{\partial \beta''_{1c_{4c}}}{\partial \theta_{3c}} = \frac{\gamma}{8}(\frac{\mu^2}{2} + 1) \tag{4.145}$$

$$\frac{\partial \beta''_{1c_{4s}}}{\partial \theta_{3c}} = 0 \tag{4.146}$$

Extract $\frac{\partial \ddot{\beta}_{1c_{ave}}}{\partial \theta_{3s}}$, $\frac{\partial \beta''_{1c_{4c}}}{\partial \theta_{3s}}$, $\frac{\partial \beta''_{1c_{4s}}}{\partial \theta_{3s}}$ from $\ddot{\boldsymbol{\beta}}_{\mathbf{1c}}(\boldsymbol{\psi}_i)\Big|^{\pm}_{\boldsymbol{\theta}_{\mathbf{3s}}}$

$$\frac{\partial \ddot{\beta}_{1c_{ave}}}{\partial \theta_{3s}} = 0 \tag{4.147}$$

$$\frac{\partial \beta''_{1c_{4c}}}{\partial \theta_{3s}} = 0 \tag{4.148}$$

$$\frac{\partial \beta''_{1c_{4s}}}{\partial \theta_{3s}} = \frac{\gamma}{8}(\frac{\mu^2}{2} + 1) \tag{4.149}$$

4.3.4 Construction of the state equation

Combining Eqs. (4.123)-(4.149) and Eqs. (4.50)-(4.51), the state equation of the 4/rev LTI-HHC model can be constructed as follows:

$$\begin{Bmatrix} \ddot{\beta}_{1c_{ave}} \\ \dot{\beta}_{1c_{ave}} \\ \beta''_{1c_{4c}} \\ \beta''_{1c_{4s}} \\ \beta'_{1c_{4c}} \\ \beta'_{1c_{4s}} \end{Bmatrix} = \begin{bmatrix} -\gamma/8 & (\nu^2-1) & 0 & 0 & 0 & -\gamma\mu^2/32 \\ 1 & 0 & 0 & 0 & 0 & 0 \\ 0 & 0 & -\gamma/8 & 0 & (\nu^2-1) & -\gamma\Omega/2 \\ 0 & -\gamma\mu^2/16 & 0 & -\gamma/8 & \gamma\mu^2/16 & (\nu^2-1) \\ 0 & 0 & 1 & 0 & 0 & 4\Omega \\ 0 & 0 & 0 & 1 & -4\Omega & 0 \end{bmatrix} \begin{Bmatrix} \dot{\beta}_{1c_{ave}} \\ \beta_{1c_{ave}} \\ \dot{\beta}_{1c_{4c}} \\ \dot{\beta}_{1c_{4s}} \\ \beta_{1c_{4c}} \\ \beta_{1c_{4s}} \end{Bmatrix}$$

$$+ \begin{bmatrix} 0 & 0 & 0 \\ 0 & 0 & 0 \\ 0 & \frac{\gamma}{8}(\frac{\mu^2}{2}+1) & 0 \\ -\frac{\gamma}{16}\mu^2 & 0 & \frac{\gamma}{8}(\frac{\mu^2}{2}+1) \\ 0 & 0 & 0 \\ 0 & 0 & 0 \end{bmatrix} \begin{Bmatrix} \theta_{1s} \\ \theta_{3c} \\ \theta_{3s} \end{Bmatrix} + M_\theta + M_\beta \qquad (4.150)$$

The vector on the left-hand side of Eq. (4.150) consists of primed variables. To conform with the standard state-space representation, $\dot{\mathbf{x}} = \mathbf{A}\mathbf{x} + \mathbf{B}\mathbf{u}$, the primed variables are replaced with the dotted variables using Eqs. (4.50)-(4.53) as follows:

$$\begin{Bmatrix} \ddot{\beta}_{1c_{ave}} \\ \dot{\beta}_{1c_{ave}} \\ \beta''_{1c_{4c}} \\ \beta''_{1c_{4s}} \\ \beta'_{1c_{4c}} \\ \beta'_{1c_{4s}} \end{Bmatrix} = \begin{Bmatrix} \ddot{\beta}_{1c_{ave}} \\ \dot{\beta}_{1c_{ave}} \\ \ddot{\beta}_{1c_{4c}} \\ \ddot{\beta}_{1c_{4s}} \\ \dot{\beta}_{1c_{4c}} \\ \dot{\beta}_{1c_{4s}} \end{Bmatrix} + \begin{Bmatrix} 0 \\ 0 \\ 8\Omega\dot{\beta}_{1c_{4s}} - 16\Omega^2\beta_{1c_{4c}} \\ -8\Omega\dot{\beta}_{1c_{4c}} - 16\Omega^2\beta_{1c_{4s}} \\ 4\Omega\beta_{1c_{4s}} \\ -4\Omega\beta_{1c_{4c}} \end{Bmatrix} \qquad (4.151)$$

Substitute Eq. (4.151) in Eq. (4.150), and re-arrange the equation. The 4/rev LTI-HHC model is given by:

$$\begin{Bmatrix} \ddot{\beta}_{1c_{ave}} \\ \dot{\beta}_{1c_{ave}} \\ \ddot{\beta}_{1c_{4c}} \\ \ddot{\beta}_{1c_{4s}} \\ \dot{\beta}_{1c_{4c}} \\ \dot{\beta}_{1c_{4s}} \end{Bmatrix} = \mathbf{A} \begin{Bmatrix} \dot{\beta}_{1c_{ave}} \\ \beta_{1c_{ave}} \\ \dot{\beta}_{1c_{4c}} \\ \dot{\beta}_{1c_{4s}} \\ \beta_{1c_{4c}} \\ \beta_{1c_{4s}} \end{Bmatrix} + \mathbf{B} \begin{Bmatrix} \theta_{1s} \\ \theta_{3c} \\ \theta_{3s} \end{Bmatrix} + M_\theta + M_\beta \tag{4.152}$$

where

$$\mathbf{A} = \begin{bmatrix} -\gamma/8 & (\nu^2-1) & 0 & 0 & 0 & -\gamma\mu^2/32 \\ 1 & 0 & 0 & 0 & 0 & 0 \\ 0 & 0 & -\gamma/8 & -8\Omega & (\nu^2-1+16\Omega^2) & -\gamma\Omega/2 \\ 0 & -\gamma\mu^2/16 & 8\Omega & -\gamma/8 & \gamma\mu^2/16 & (\nu^2-1+16\Omega^2) \\ 0 & 0 & 1 & 0 & 0 & 0 \\ 0 & 0 & 0 & 1 & 0 & 0 \end{bmatrix} \tag{4.153}$$

$$\mathbf{B} = \begin{bmatrix} 0 & 0 & 0 \\ 0 & 0 & 0 \\ 0 & \frac{\gamma}{8}(\frac{\mu^2}{2}+1) & 0 \\ -\frac{\gamma}{16}\mu^2 & 0 & \frac{\gamma}{8}(\frac{\mu^2}{2}+1) \\ 0 & 0 & 0 \\ 0 & 0 & 0 \end{bmatrix} \tag{4.154}$$

4.3.5 Analytical model validation

From Eq. (4.152), $\ddot{\beta}_{1c_{ave}}$, $\ddot{\beta}_{1c_{4c}}$, and $\ddot{\beta}_{1c_{4s}}$ can be expressed as follows:

$$\ddot{\beta}_{1c_{ave}} = -\frac{\gamma}{8}\dot{\beta}_{1c_{ave}} + (\nu^2-1)\beta_{1c_{ave}} - \frac{\gamma\mu^2}{32}\beta_{1c_{4s}} \tag{4.155}$$

$$\begin{aligned}\ddot{\beta}_{1c_{4c}} &= -\frac{\gamma}{8}\dot{\beta}_{1c_{4c}} - 8\Omega\dot{\beta}_{1c_{4s}} + (\nu^2-1+16\Omega^2)\beta_{1c_{4c}} - \frac{\gamma\Omega}{2}\beta_{1c_{4s}} \\ &+ \frac{\gamma}{8}(\frac{\mu^2}{2}+1)\theta_{3c}\end{aligned} \tag{4.156}$$

$$\begin{aligned}\ddot{\beta}_{1c_{4s}} &= -\frac{\gamma}{8}\dot{\beta}_{1c_{4s}} + 8\Omega\dot{\beta}_{1c_{4c}} - \frac{\gamma\mu^2}{16}\beta_{1c_{ave}} + \frac{\gamma\Omega}{2}\beta_{1c_{4c}} + (\nu^2-1+16\Omega^2)\beta_{1c_{4s}} \\ &+ \frac{\gamma}{8}(\frac{\mu^2}{2}+1)\theta_{3s} - \frac{\gamma}{16}\mu^2\theta_{1s}\end{aligned} \tag{4.157}$$

Substitute Eqs. (4.155 and 4.157) in Eq. (4.44),

$$\begin{aligned}\ddot{\beta}_{1c} &= -\frac{\gamma}{8}\Big[\dot{\beta}_{1c_{ave}} + (\dot{\beta}_{1c_{4c}} + 4\Omega\beta_{1c_{4s}})\cos 4\psi + (\dot{\beta}_{1c_{4s}} - 4\Omega\beta_{1c_{4c}})\sin 4\psi\Big] \\ &+ (\nu^2-1)(\beta_{1c_{ave}} + \beta_{1c_{4c}}\cos 4\psi + \beta_{1c_{4s}}\sin 4\psi) \\ &- \frac{\gamma\mu^2}{16}(\beta_{1c_{ave}}\sin 4\psi + \frac{1}{2}\beta_{1c_{4s}}) \\ &+ \frac{\gamma}{8}(\frac{\mu^2}{2}+1)(\theta_{3c}\cos 4\psi + \theta_{3s}\sin 4\psi) \\ &- \frac{\gamma}{16}\mu^2\theta_{1s}\sin 4\psi + M_\theta + M_\beta\end{aligned} \tag{4.158}$$

Compare Eq. (4.158) with the equation of motion Eq. (4.113) which is shown below:

$$\begin{aligned}\ddot{\beta}_{1c} &= -\frac{\gamma}{8}\Big[\dot{\beta}_{1c_{ave}} + (\dot{\beta}_{1c_{4c}} + 4\Omega\beta_{1c_{4s}})\cos 4\psi + (\dot{\beta}_{1c_{4s}} - 4\Omega\beta_{1c_{4c}})\sin 4\psi\Big] \\ &+ (\nu^2-1)(\beta_{1c_{ave}} + \beta_{1c_{4c}}\cos 4\psi + \beta_{1c_{4s}}\sin 4\psi) \\ &- \frac{\gamma\mu^2}{16}(\beta_{1c_{ave}}\sin 4\psi + \frac{1}{2}\beta_{1c_{4s}}) \\ &- \frac{\gamma\mu^2}{16}(\frac{1}{2}\beta_{1c_{4c}}\sin 8\psi - \frac{1}{2}\beta_{1c_{4s}}\cos 8\psi) \\ &+ \frac{\gamma}{8}(\frac{\mu^2}{2}+1)\,(\theta_{3c}\cos 4\psi + \theta_{3s}\sin 4\psi) \\ &- \frac{\gamma}{16}\mu^2\theta_{1s}\sin 4\psi + M_\theta + M_\beta\end{aligned}$$

The differences are the 8/rev frequency contents which were truncated from the linearization procedures. These 8/rev frequency contents can be retained in the linear model if the prescribed solution of Eq. (4.18) also contains 8/rev components as well as 4/rev components.

4.4 LTI-HHC model validation

In this section, the LTI-HHC model was validated against with the full-blown nonlinear helicopter model by comparing their 4/rev hub load and the rotor responses over several flight configurations.

4.4.1 4/rev hub load comparison

The validation was conducted for the forward velocity of 40, 80, and 120 kts. Each case starts from the trim condition without HHC input. After two rotor revolutions, the HHC input is engaged, and the results are shown in Figures 4.1-4.15. The HHC input is a 3/rev input with an amplitude of 0.6° at 0° phase angle.

The 4/rev hub loads calculated from the nonlinear helicopter model are the output of the harmonic analyzer which contains time delay. On the other hand, the 4/rev hub loads calculated from LTI-HHC model are obtained instantaneously. There is no time delay associated with the sample window as with the harmonic analyzer. The effect of the sample window can be approximated by an equivalent lowpass filter that must include in the output of the LTI-HHC model before it is compared to the nonlinear 4/rev results.

As illustrated in the figures, the LTI-HHC model produces the levels of 4/rev

vibrations that are very close to the nonlinear 4/rev vibration. A close match is not seen only in steady state condition but also in transients. The small ripples in the nonlinear results are the 8/rev and higher frequencies that were not modeled in the LTI-HHC model.

The effect of the pilot input on vibrations is illustrated in Figures 4.16-4.30. The input is a lateral cyclic doublet input with an amplitude of one stick inch. From the figures, the LTI-HHC model shows the capability of predicting the 4/rev hub loads. There are strong 8/rev and higher frequencies in the nonlinear results that are not modeled in the LTI-HHC model. However, the 8/rev frequency can be captured by the LTI-HHC model if the 8/rev frequency is prescribed in the assumed solution. The dimension of the LTI-HHC model matrices will increase to accommodate the addition 8/rev rotor states.

4.4.2 Rotor states comparison

Figures 4.31-4.33 compare the rotor states from both the nonlinear and the LTI-HHC model simulation for the 120 kts case. The HHC input is the same 3/rev input in the previous case. The rotor states compared in the figures are the full values, i.e., they are not the 4/rev rotor states. The rotor state data of the nonlinear helicopter model is obtained directly from the time integration of the equations of motion. Since this set of data has never passed through the harmonic analyzer to obtain its 4/rev components, the effect of the sample window is not included.

To compare with the nonlinear results, the rotor state data of the LTI-HHC model is constructed by modulating the instantaneous 4/rev rotor state data as shown in Eq. (4.18) without including the effect of the sample window. These figures illustrate that the prediction from the LTI-HHC model is very similar to

the one from the nonlinear helicopter model in both the steady-state and transient condition.

Figures 4.34-4.36 show the effect of lateral pilot input on blade rigid flap, rigid lag, and the torsion modes for both the nonlinear and the LTI-HHC models. The input is a lateral cyclic doublet input with the amplitude of one stick inch. The variation of the 4/rev rigid flap and 4/rev rigid lag modes within the nonlinear helicopter model are relatively small compared with the variation of their mean value. With the LTI-HHC model, the 4/rev characteristic of the torsion mode of the nonlinear helicopter model as shown in Figure 4.36 is predicted not only in the steady-state condition but also in the transient.

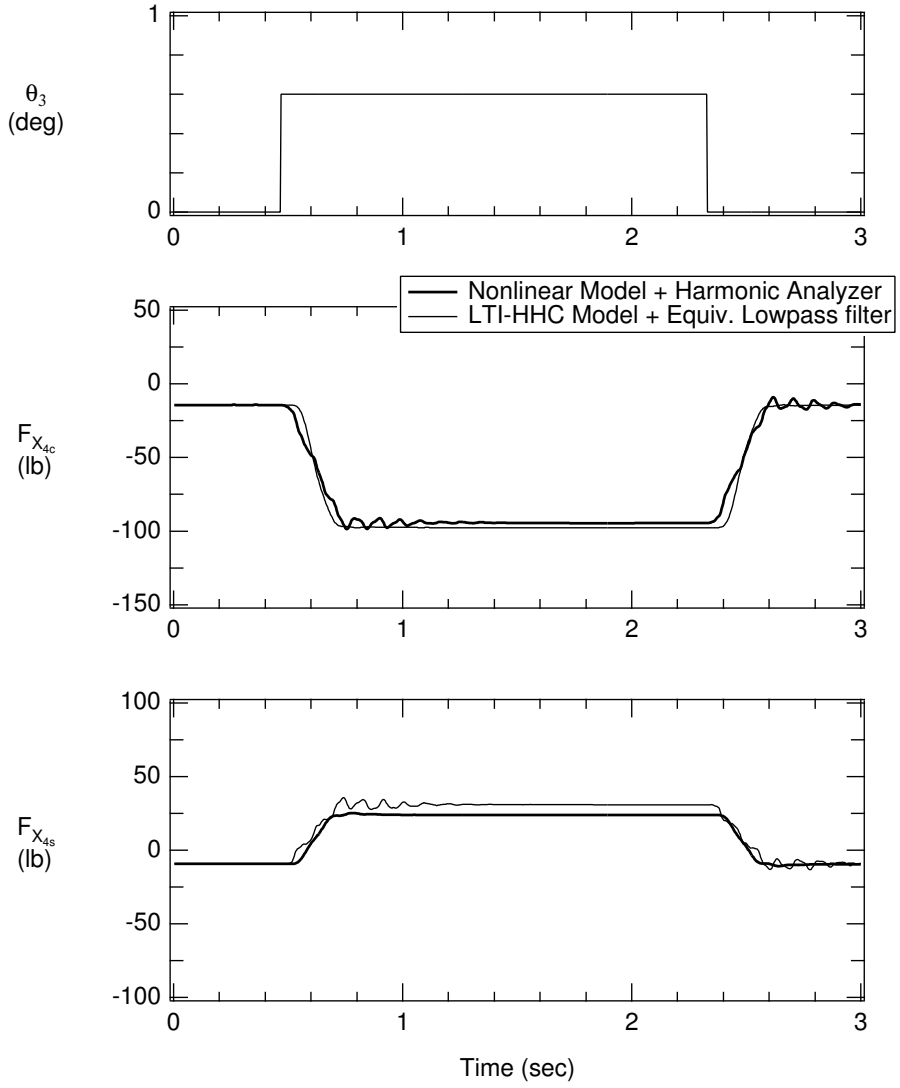

Figure 4.1: Longitudinal hub shear comparison; V= 40 kts, W=14,000 lb, $A_3 = 0.6^o$, $\phi_3 = 0^o$.

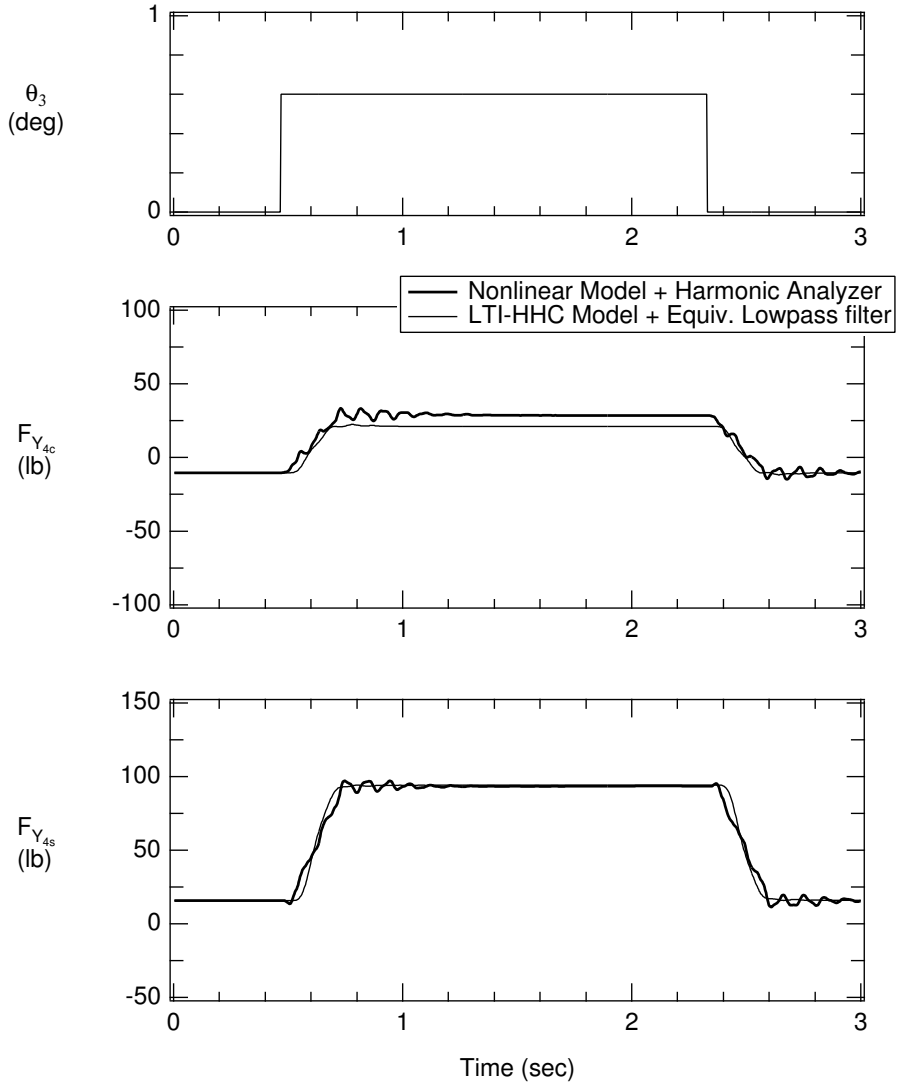

Figure 4.2: Lateral hub shear comparison; V= 40 kts, W=14,000 lb, $A_3 = 0.6^o$, $\phi_3 = 0^o$.

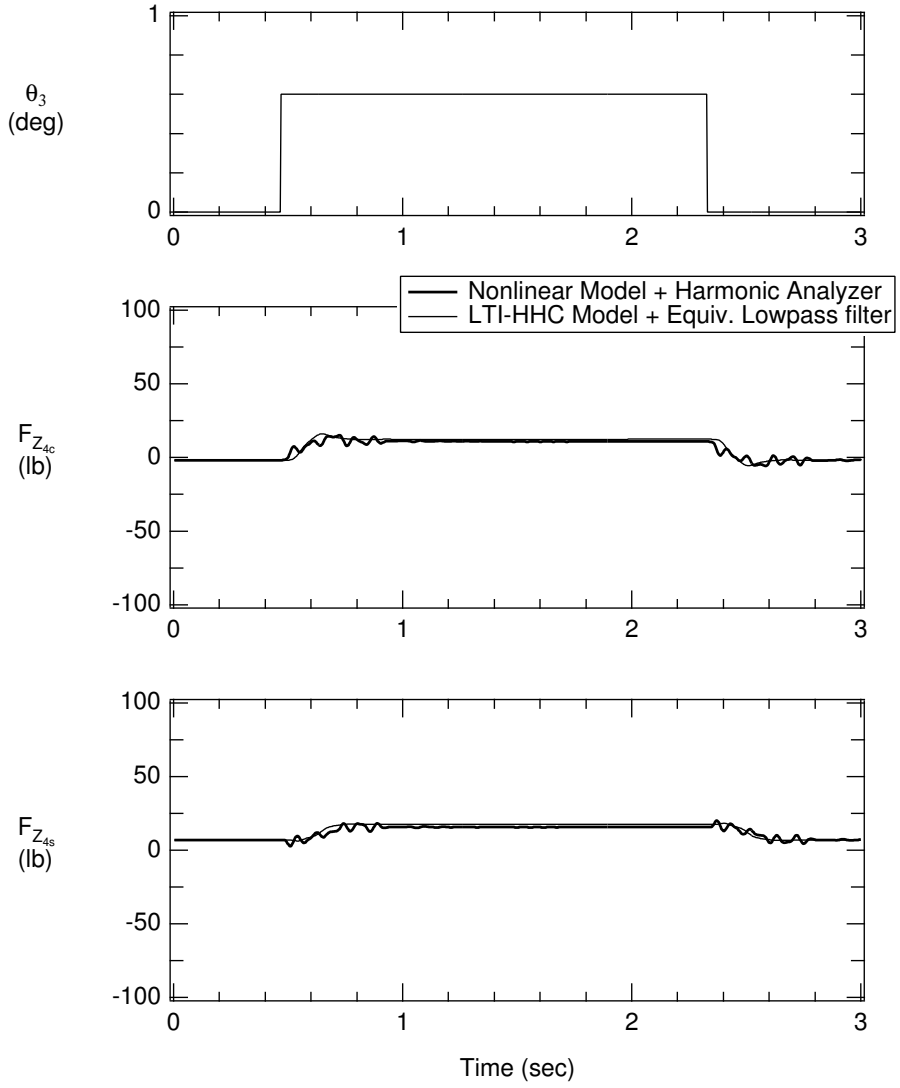

Figure 4.3: Vertical hub shear comparison; V= 40 kts, W=14,000 lb, $A_3 = 0.6^o$, $\phi_3 = 0^o$.

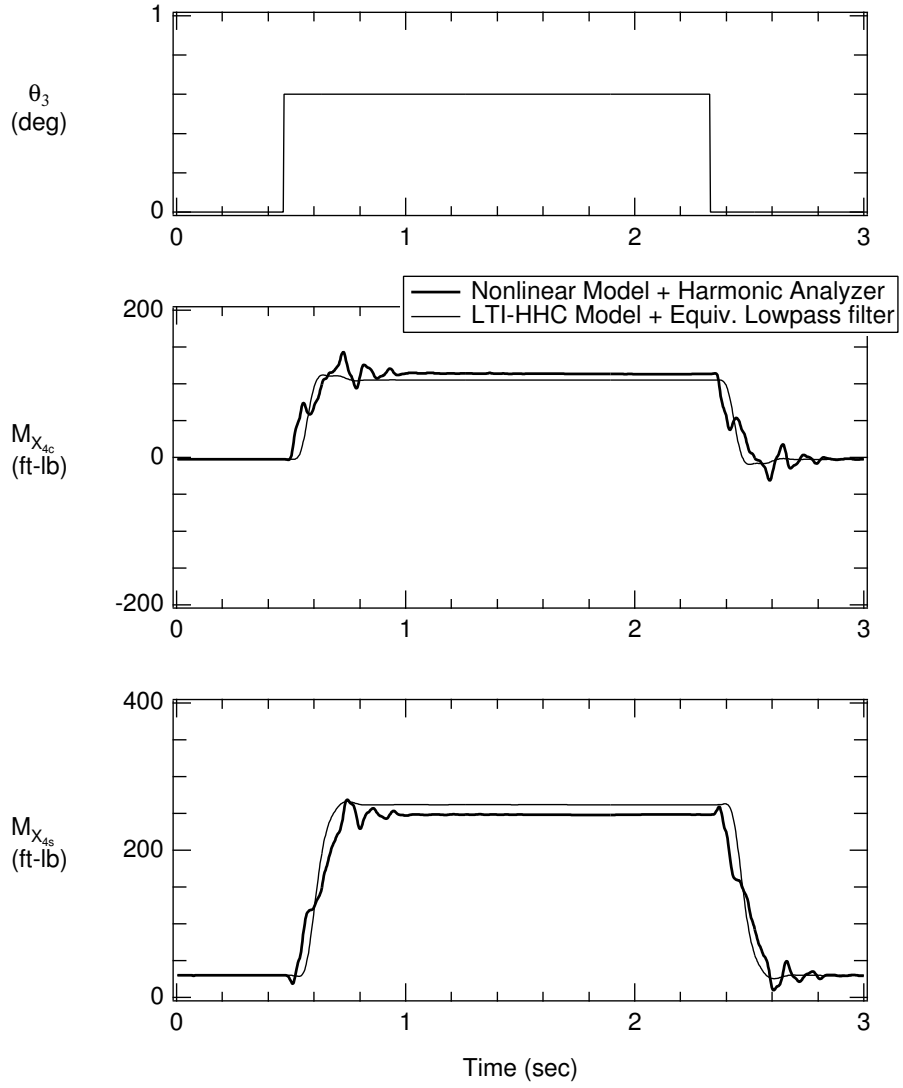

Figure 4.4: Longitudinal hub moment comparison; V= 40 kts, W=14,000 lb, $A_3 = 0.6^o$, $\phi_3 = 0^o$.

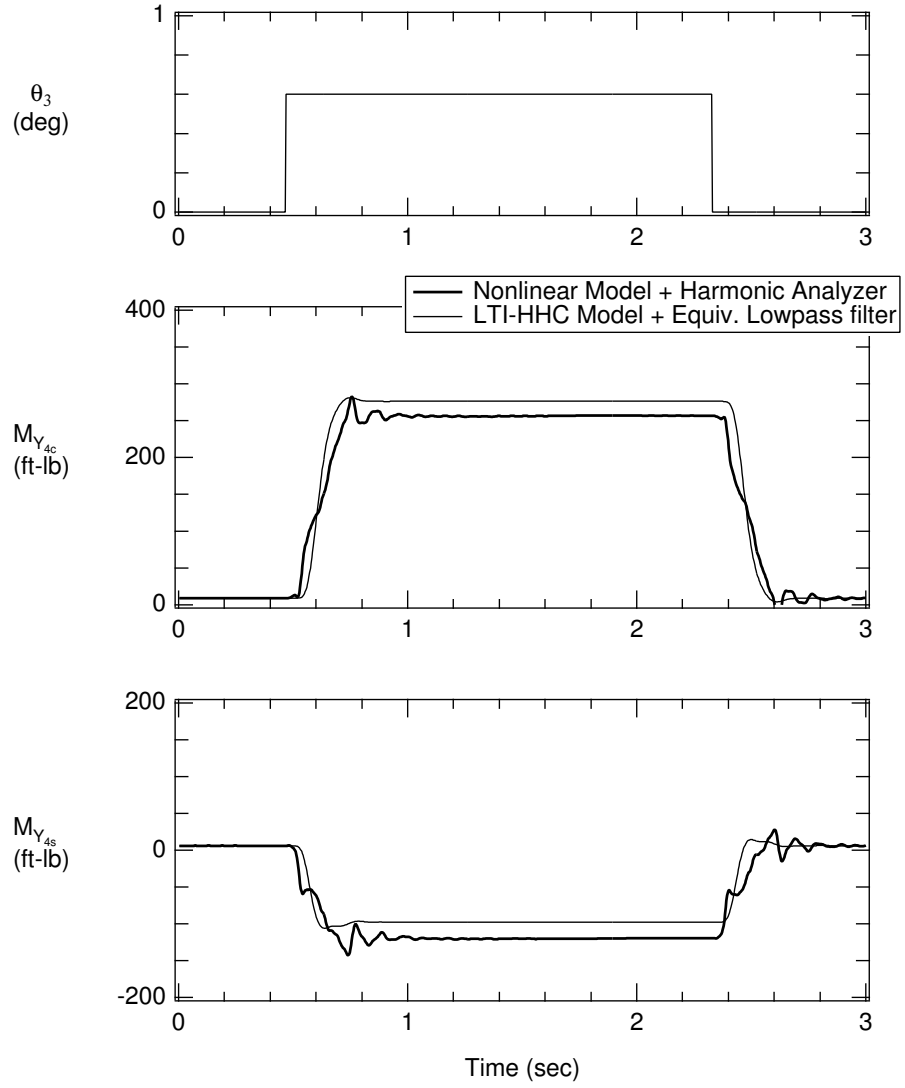

Figure 4.5: Lateral hub moment comparison; V= 40 kts, W=14,000 lb, $A_3 = 0.6^o$, $\phi_3 = 0^o$.

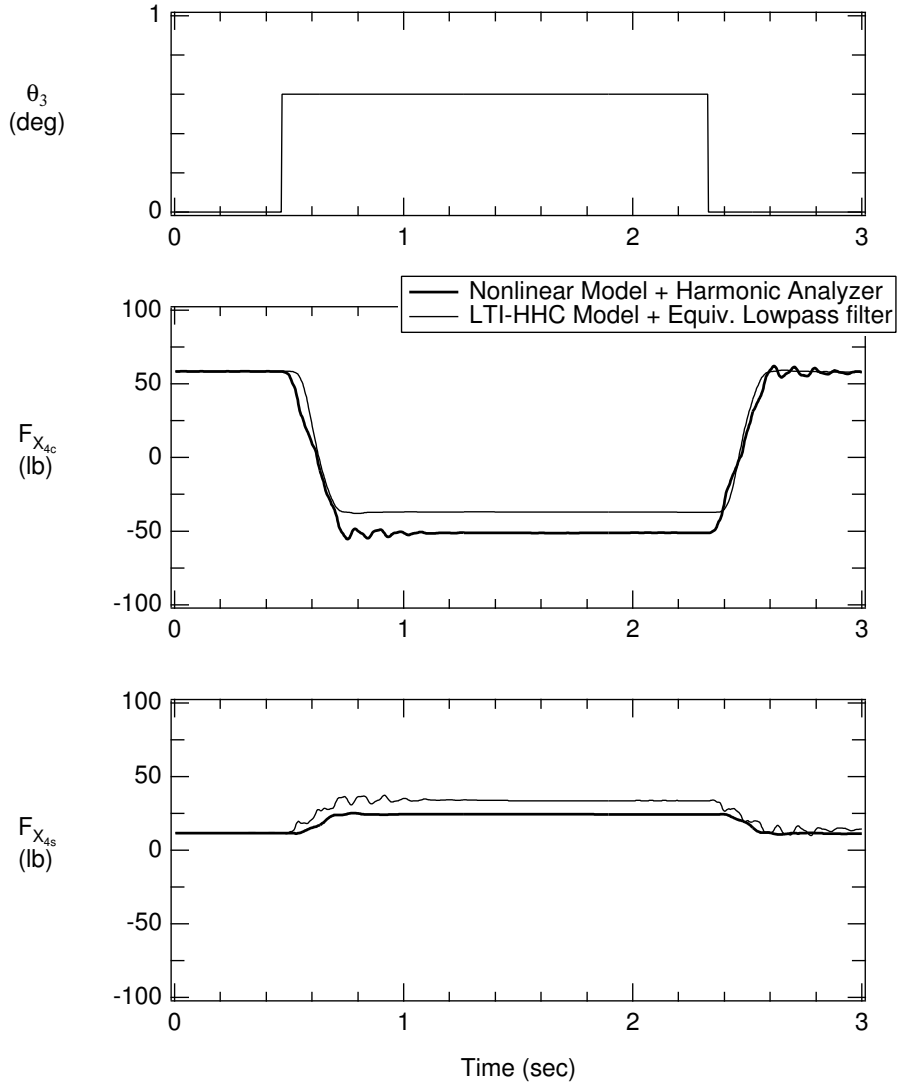

Figure 4.6: Longitudinal hub shear comparison; V= 80 kts, W=14,000 lb, $A_3 = 0.6^o$, $\phi_3 = 0^o$.

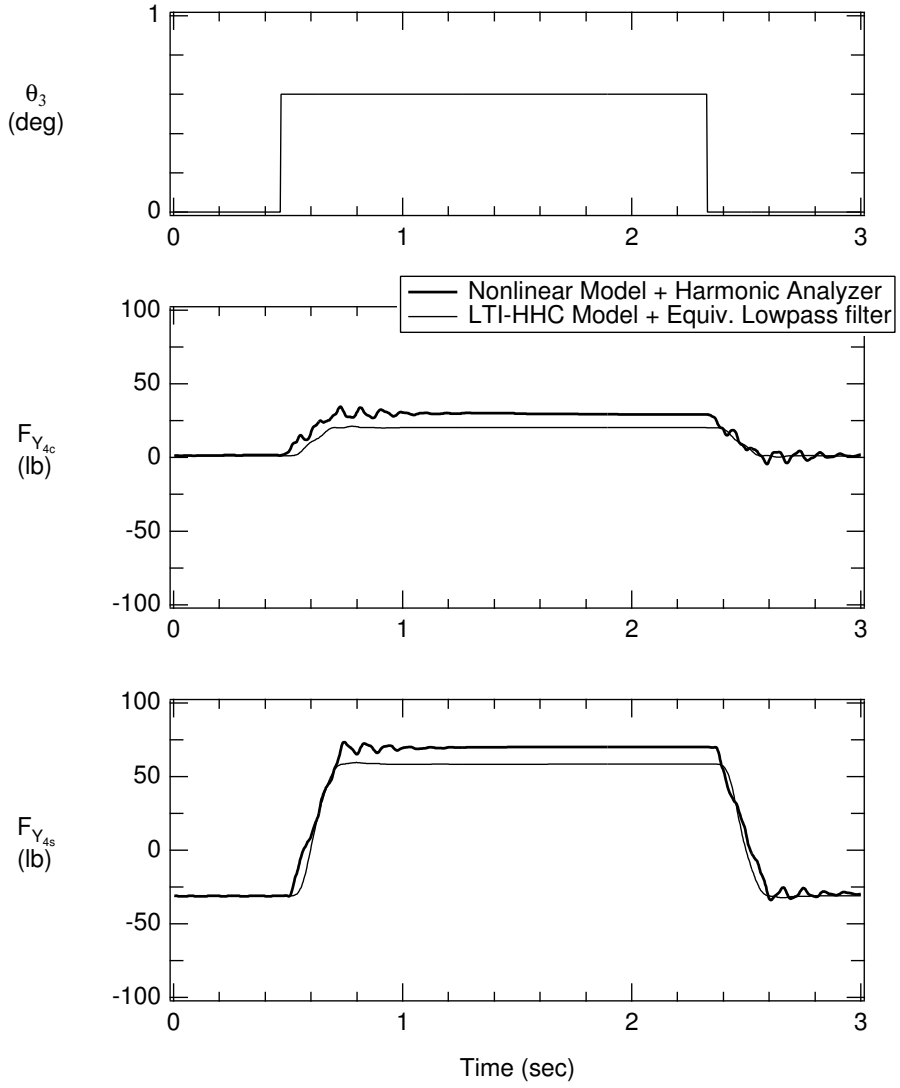

Figure 4.7: Lateral hub shear comparison; V= 80 kts, W=14,000 lb, $A_3 = 0.6^o$, $\phi_3 = 0^o$.

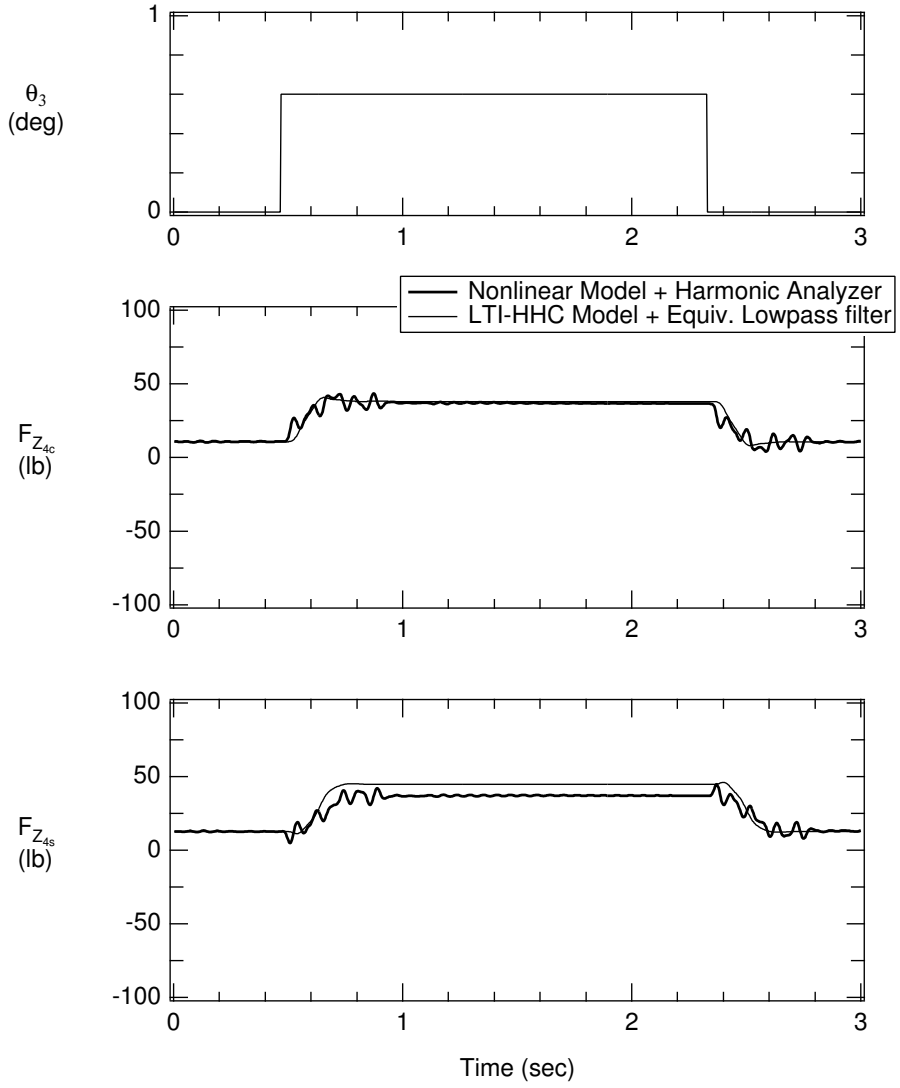

Figure 4.8: Vertical hub shear comparison; V= 80 kts, W=14,000 lb, $A_3 = 0.6^o$, $\phi_3 = 0^o$.

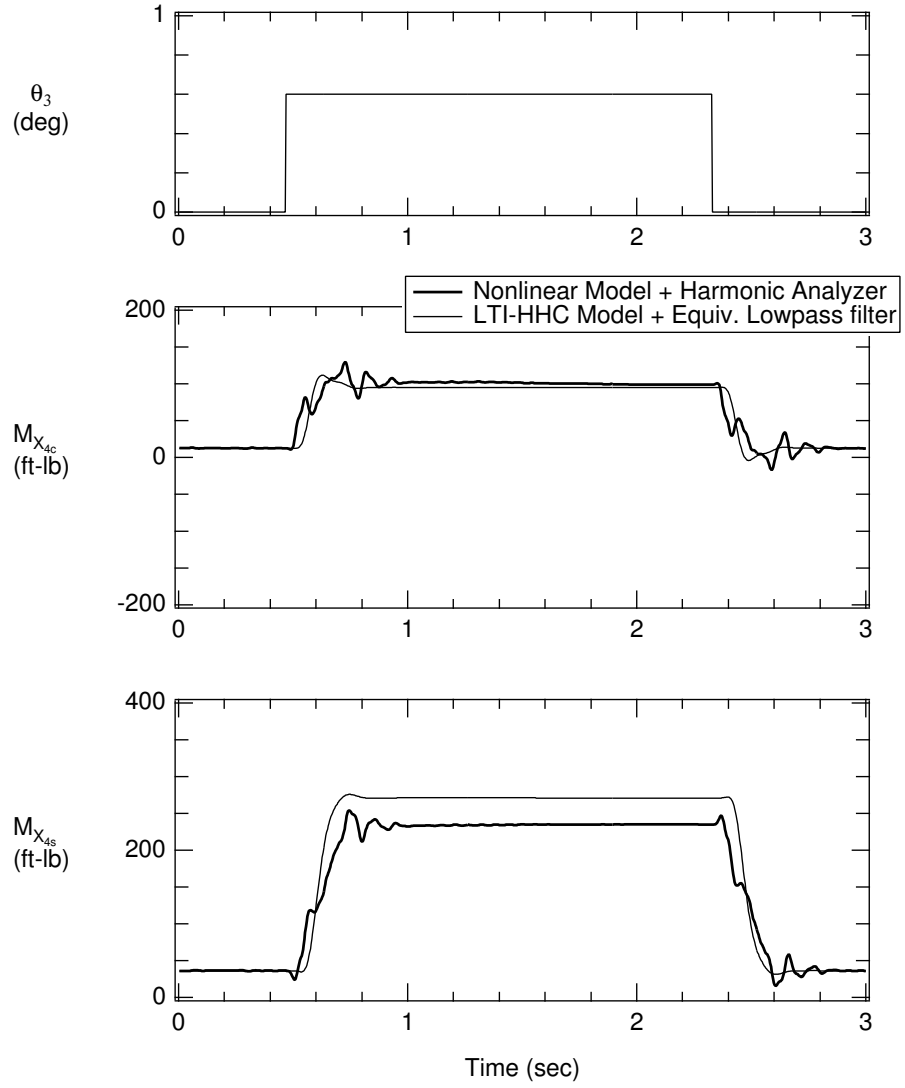

Figure 4.9: Longitudinal hub moment comparison; V= 80 kts, W=14,000 lb, $A_3 = 0.6^o$, $\phi_3 = 0^o$.

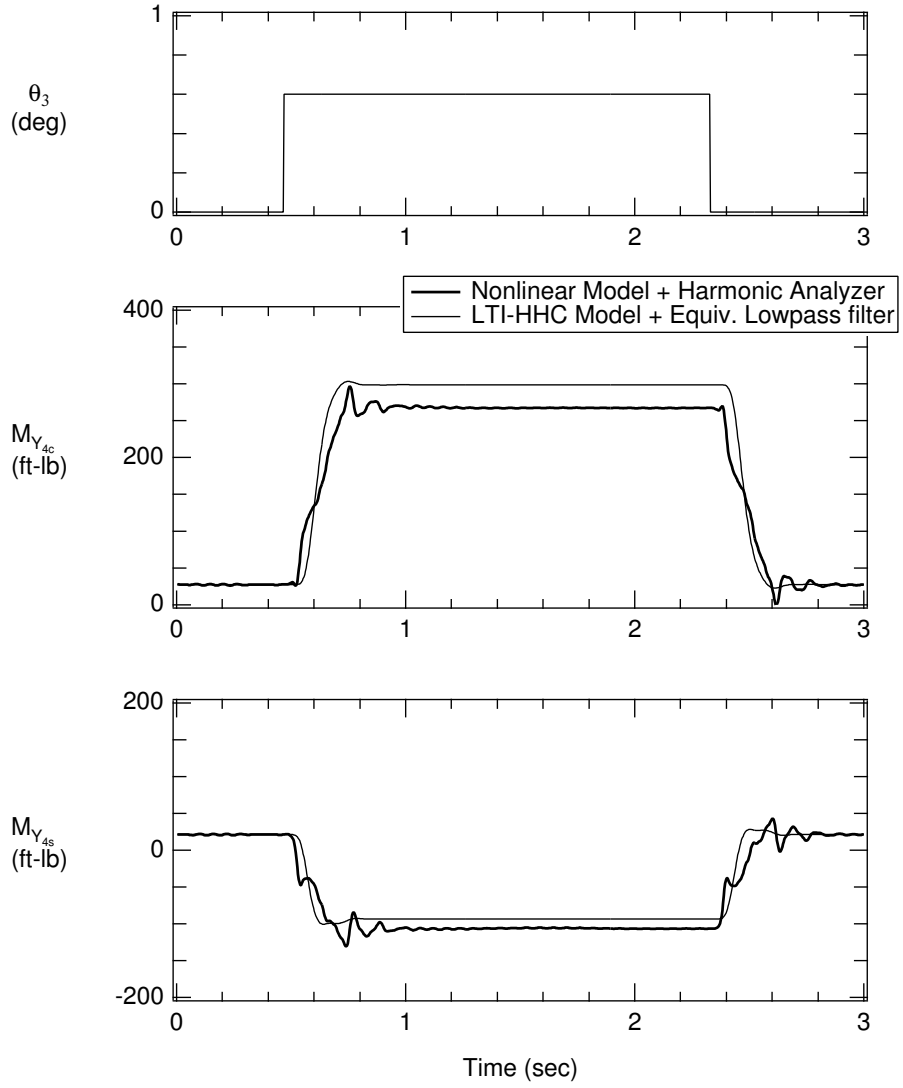

Figure 4.10: Lateral hub moment comparison; V= 80 kts, W=14,000 lb, $A_3 = 0.6^o$, $\phi_3 = 0^o$.

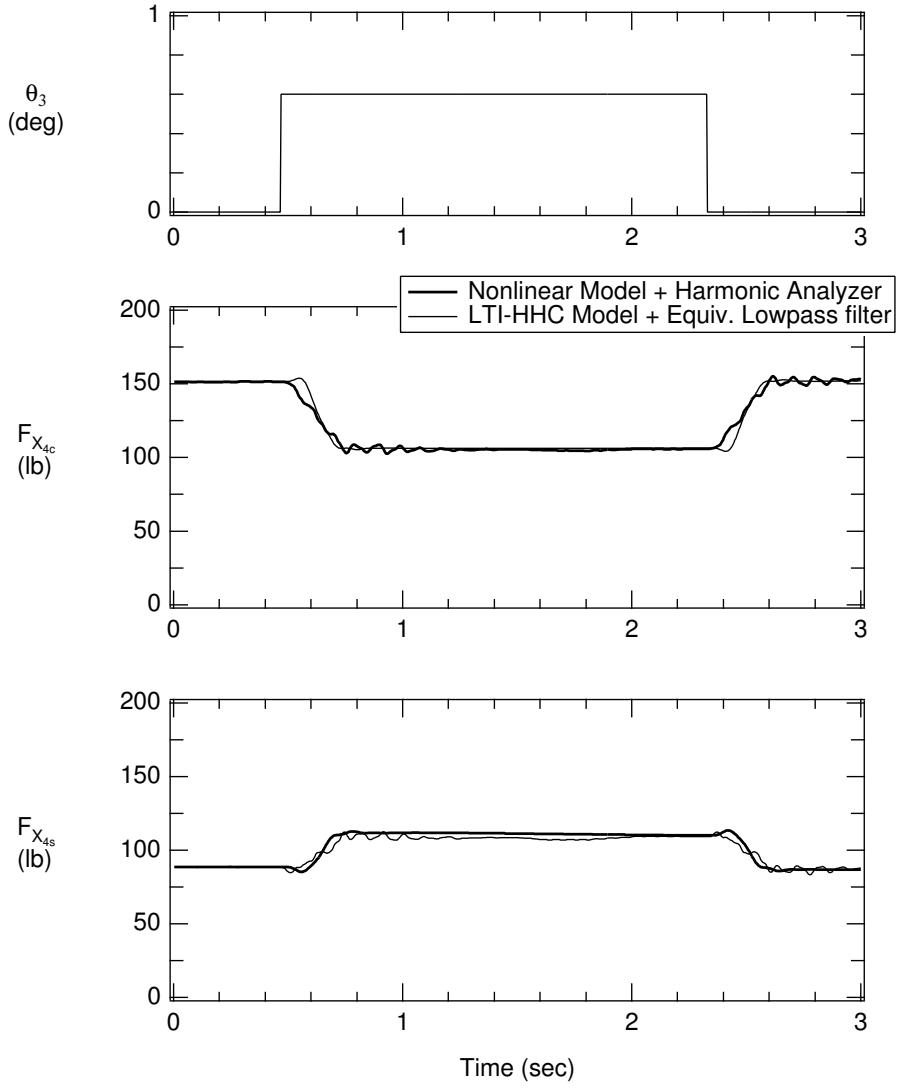

Figure 4.11: Longitudinal hub shear comparison; V= 120 kts, W=14,000 lb, $A_3 = 0.6^o$, $\phi_3 = 0^o$.

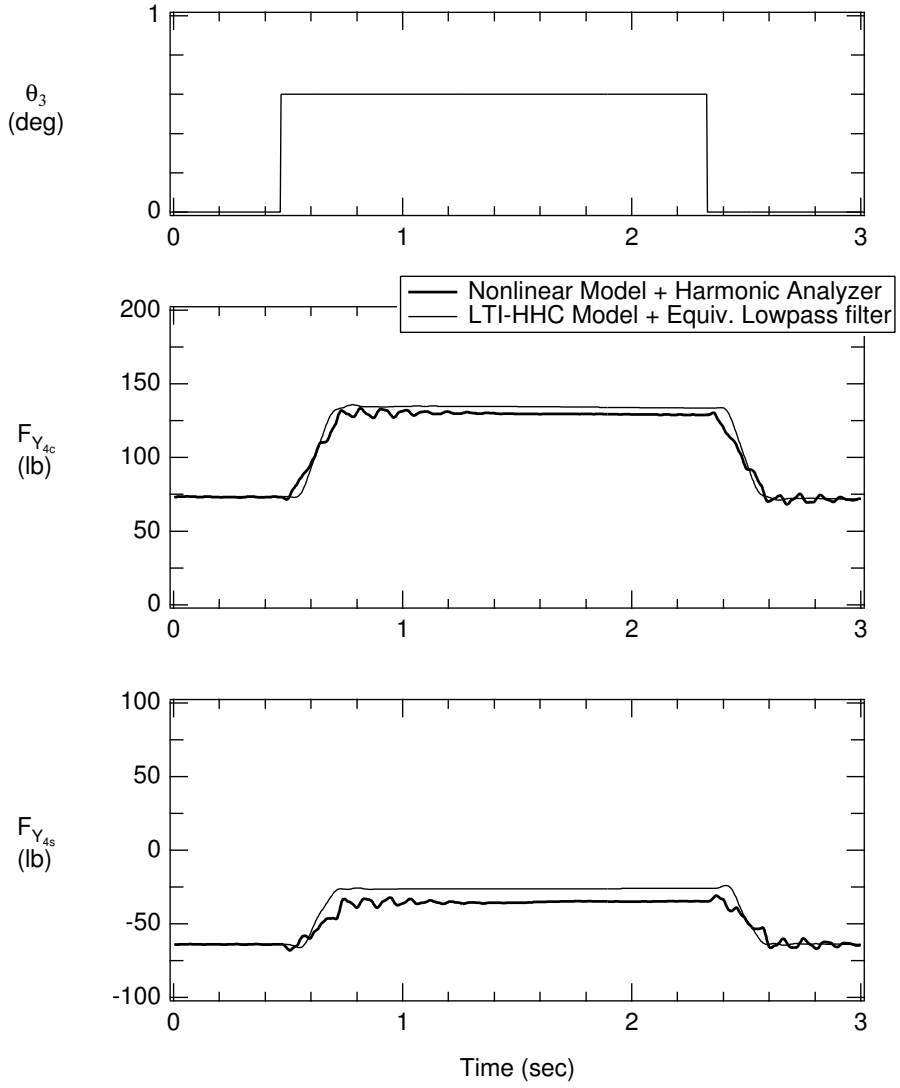

Figure 4.12: Lateral hub shear comparison; V= 120 kts, W=14,000 lb, $A_3 = 0.6^o$, $\phi_3 = 0^o$.

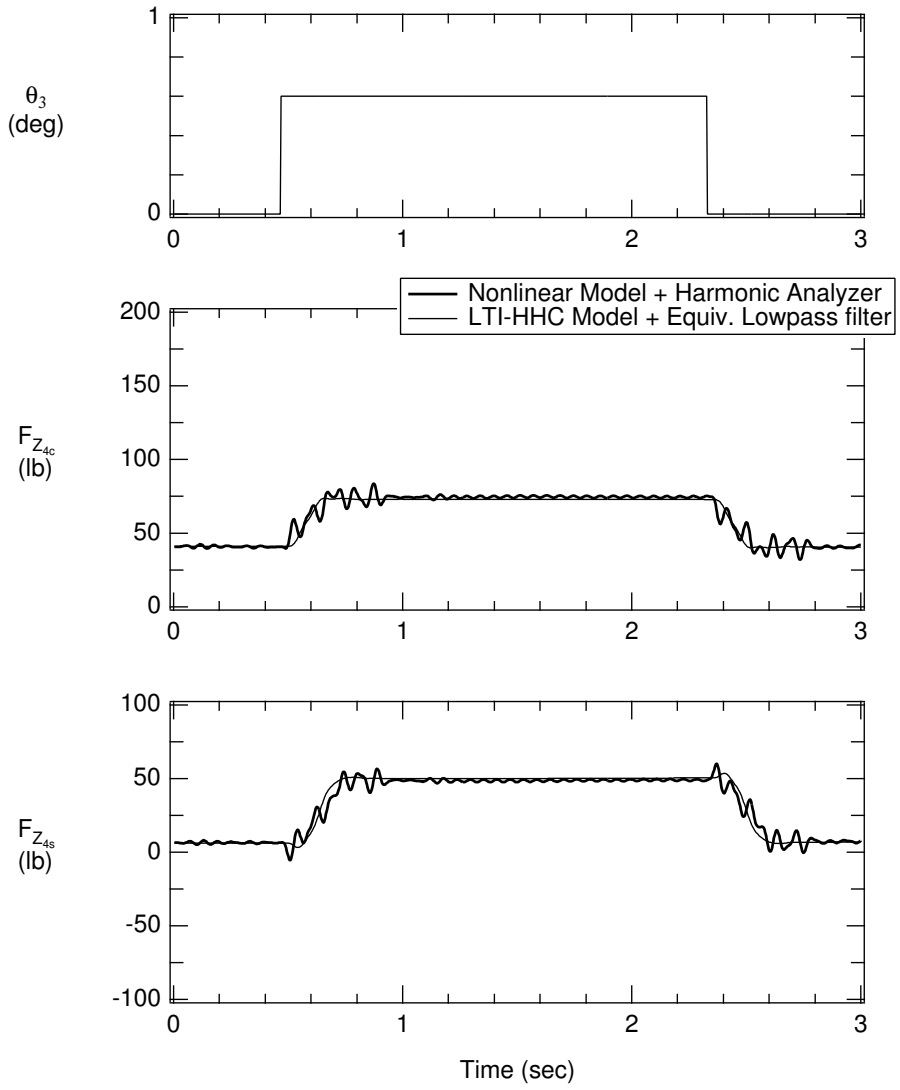

Figure 4.13: Vertical hub shear comparison; V= 120 kts, W=14,000 lb, $A_3 = 0.6^o$, $\phi_3 = 0^o$.

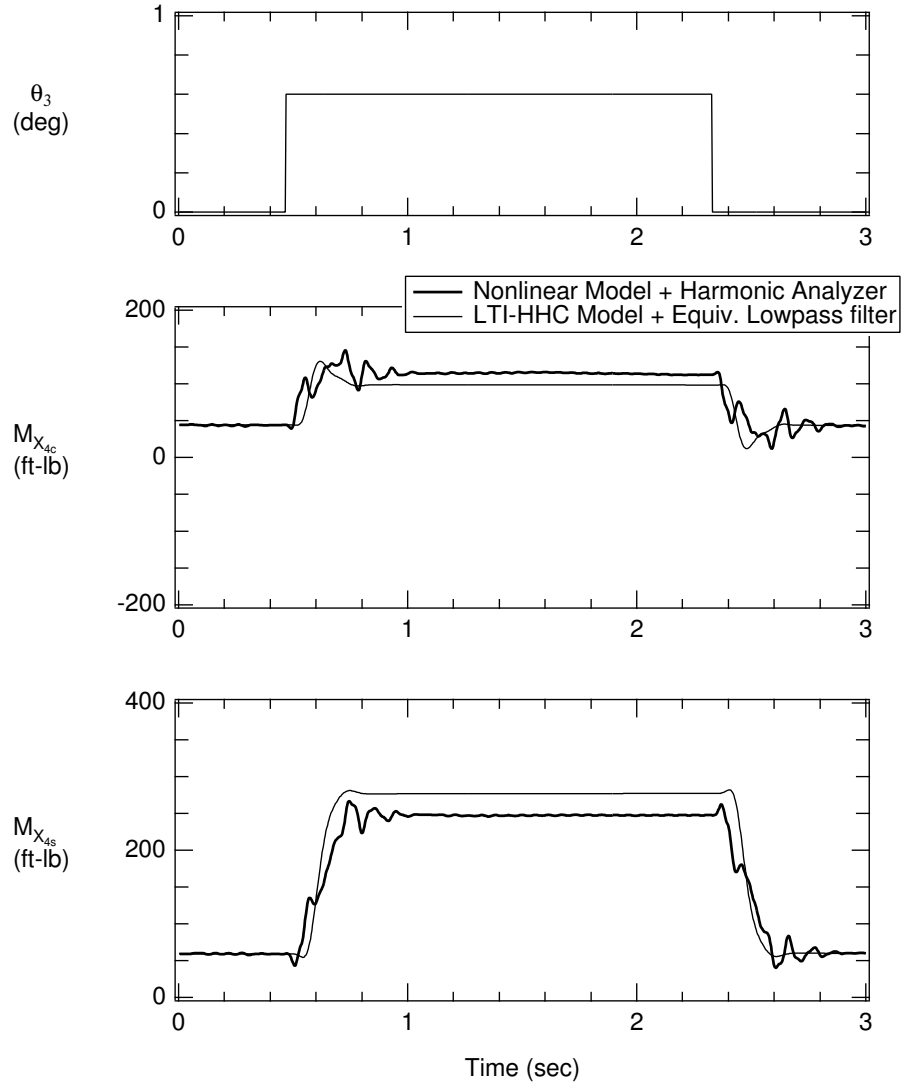

Figure 4.14: Longitudinal hub moment comparison; V= 120 kts, W=14,000 lb, $A_3 = 0.6^o$, $\phi_3 = 0^o$.

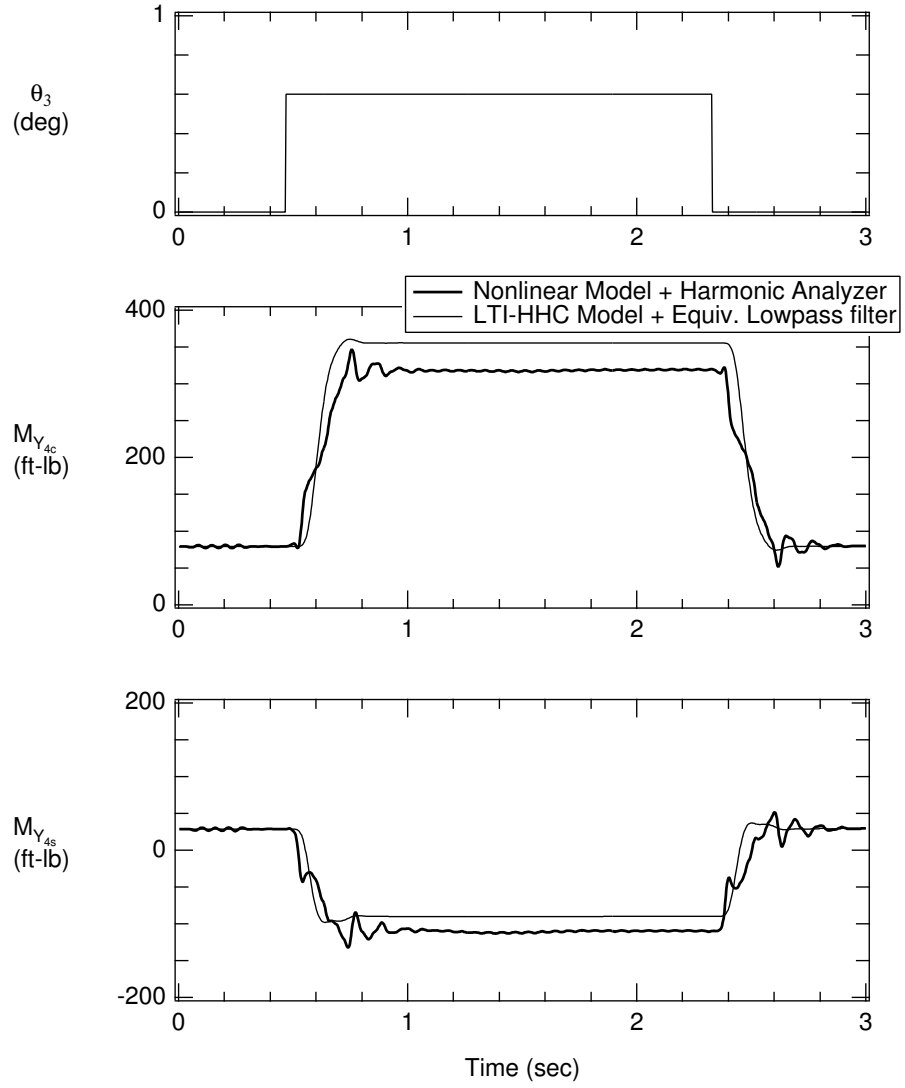

Figure 4.15: Lateral hub moment comparison; V= 120 kts, W=14,000 lb, $A_3 = 0.6^o$, $\phi_3 = 0^o$.

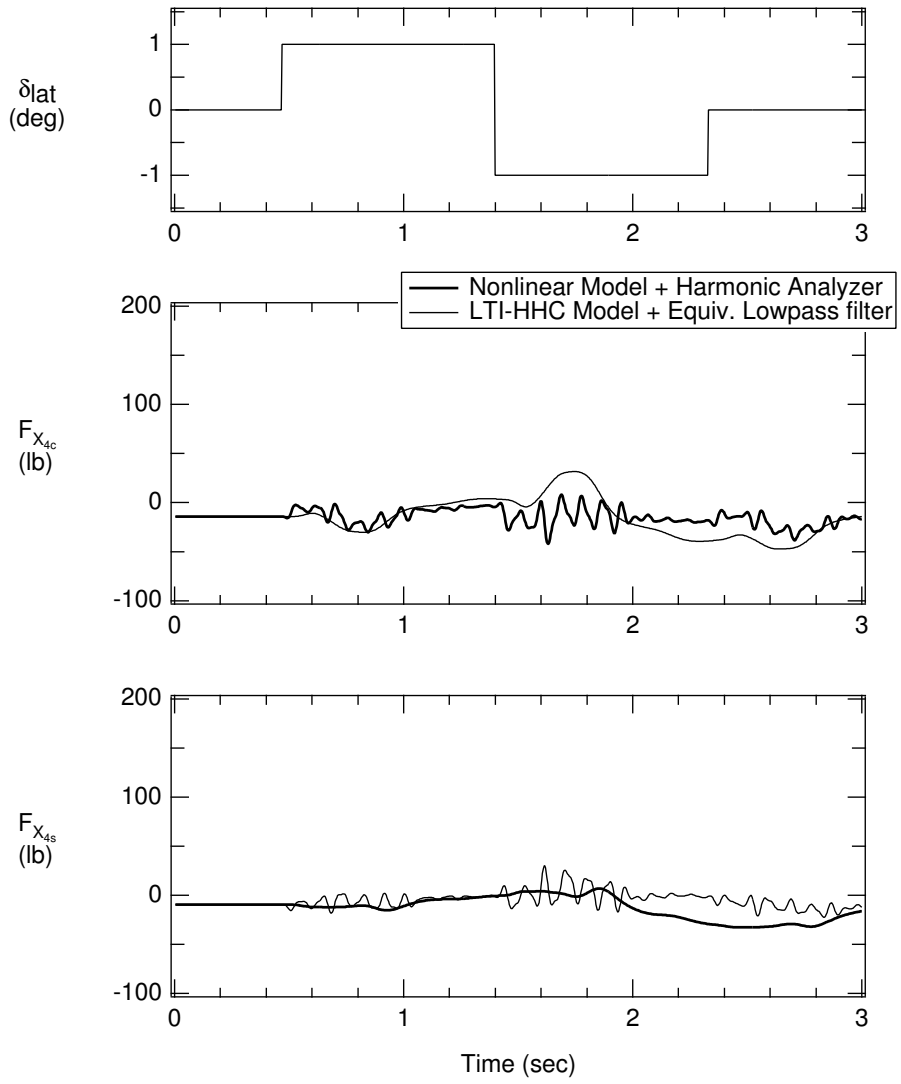

Figure 4.16: Longitudinal hub shear comparison; V= 40 kts, W=14,000 lb, 1" lateral cyclic doublet input.

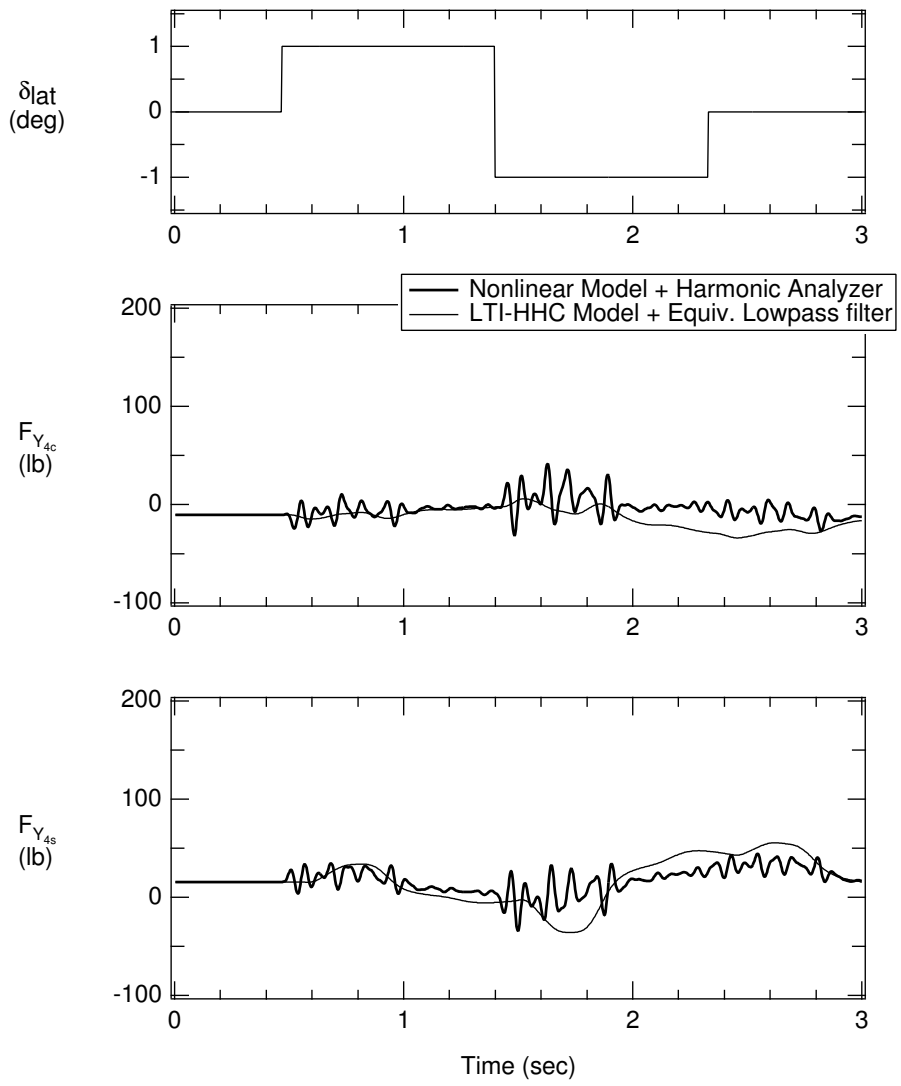

Figure 4.17: Lateral hub shear comparison; V= 40 kts, W=14,000 lb, 1" lateral cyclic doublet input.

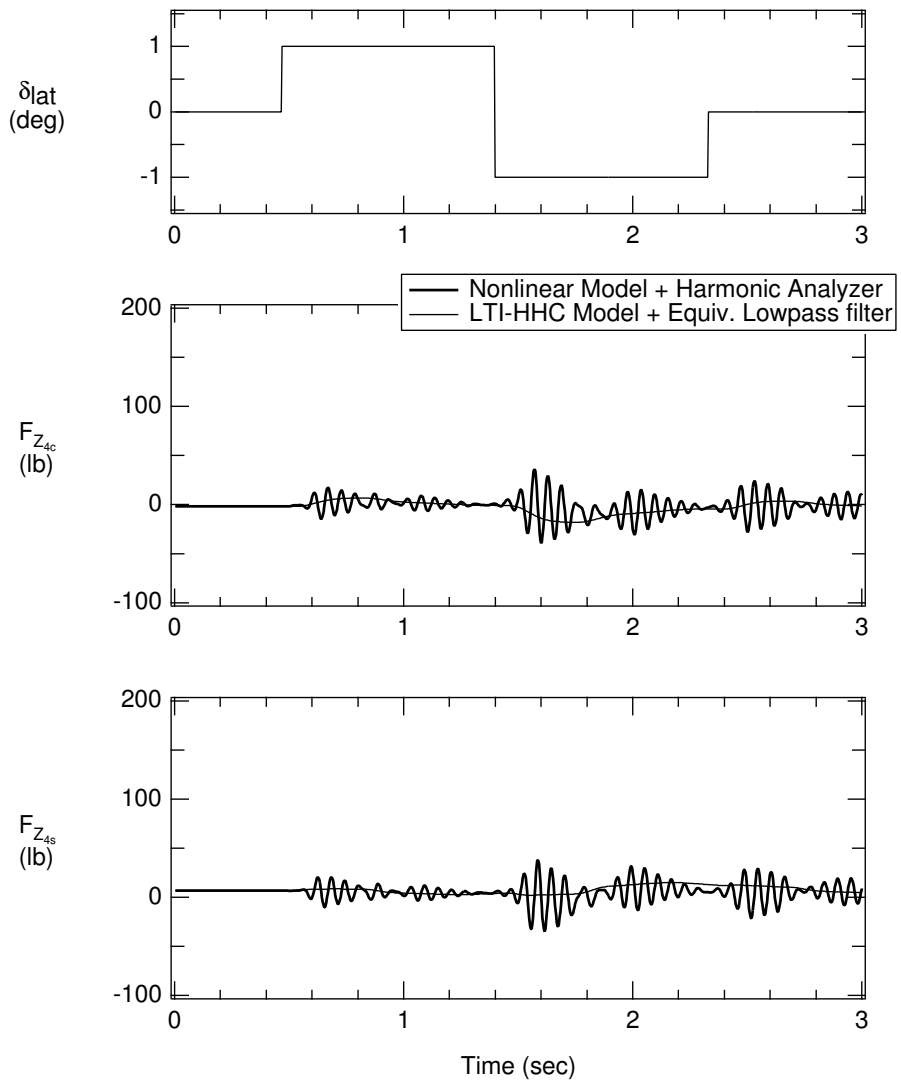

Figure 4.18: Vertical hub shear comparison; V= 40 kts, W=14,000 lb, 1" lateral cyclic doublet input.

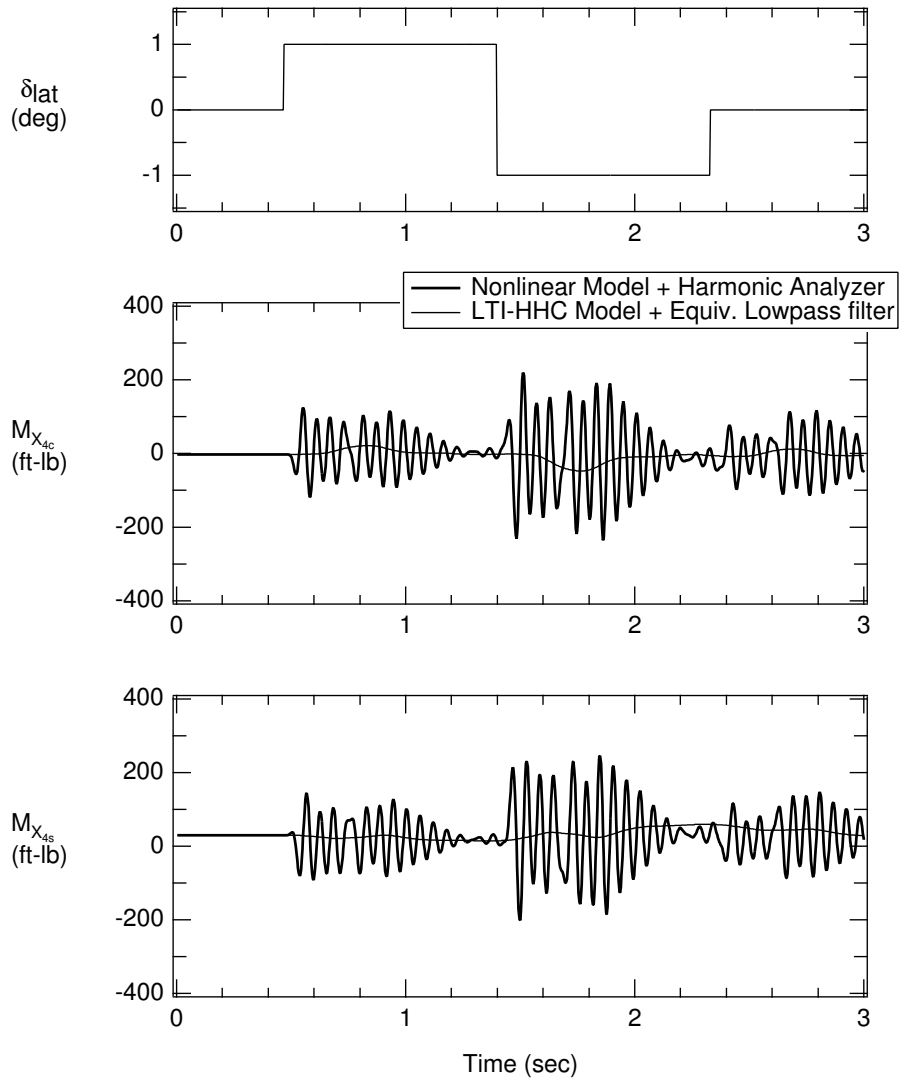

Figure 4.19: Longitudinal hub moment comparison; V= 40 kts, W=14,000 lb, 1" lateral cyclic doublet input.

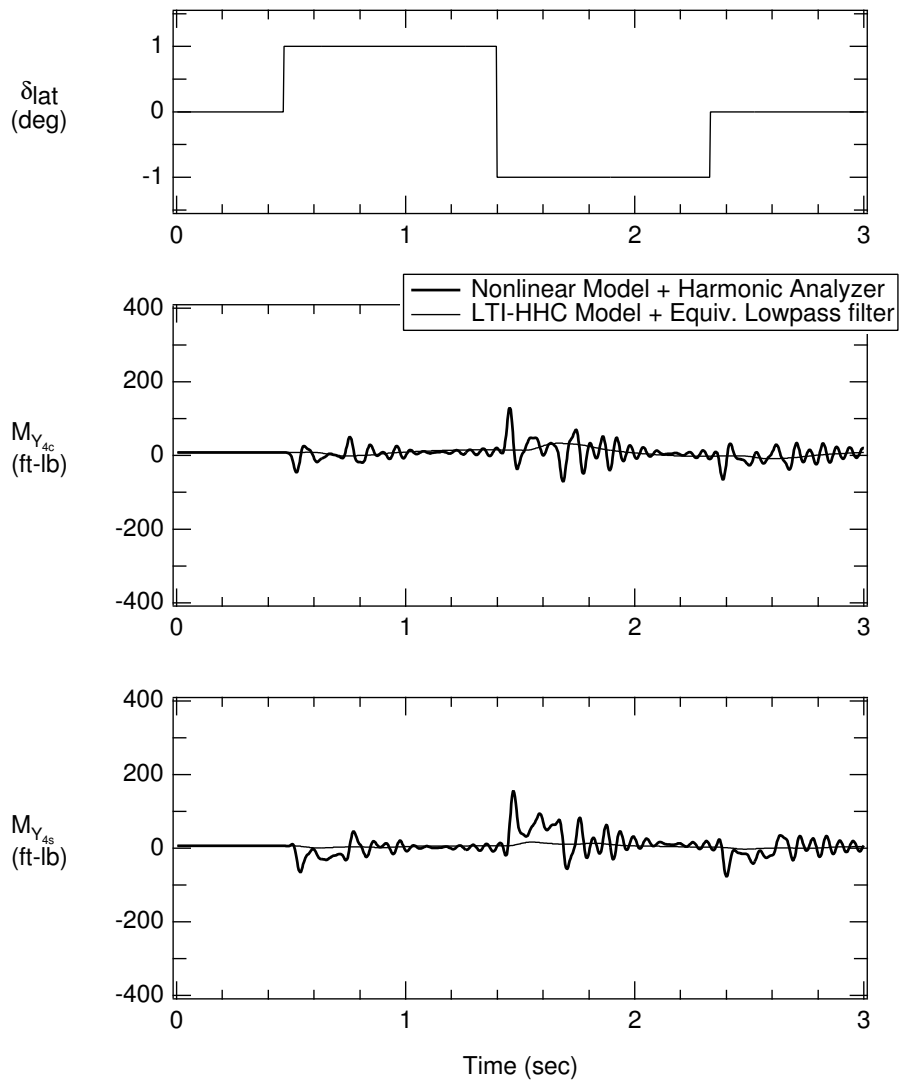

Figure 4.20: Lateral hub moment comparison; V= 40 kts, W=14,000 lb, 1" lateral cyclic doublet input.

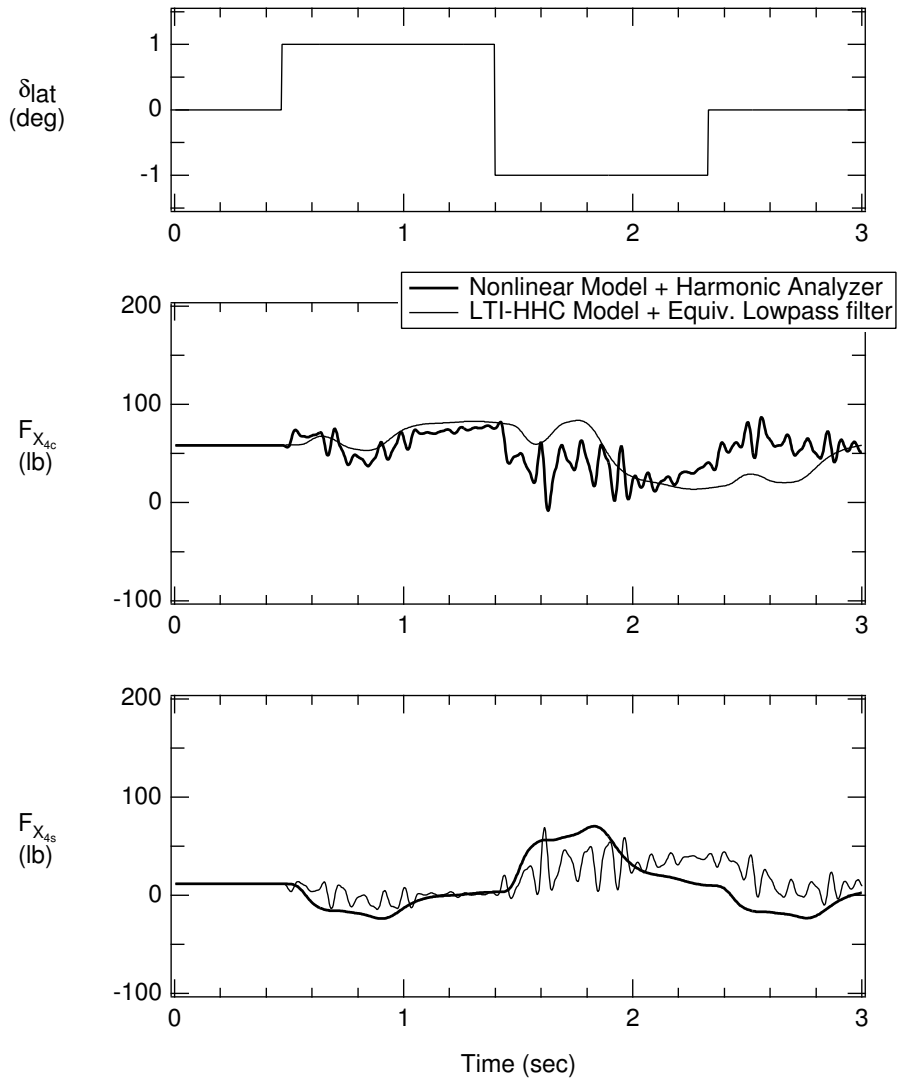

Figure 4.21: Longitudinal hub shear comparison; V= 80 kts, W=14,000 lb, 1" lateral cyclic doublet input.

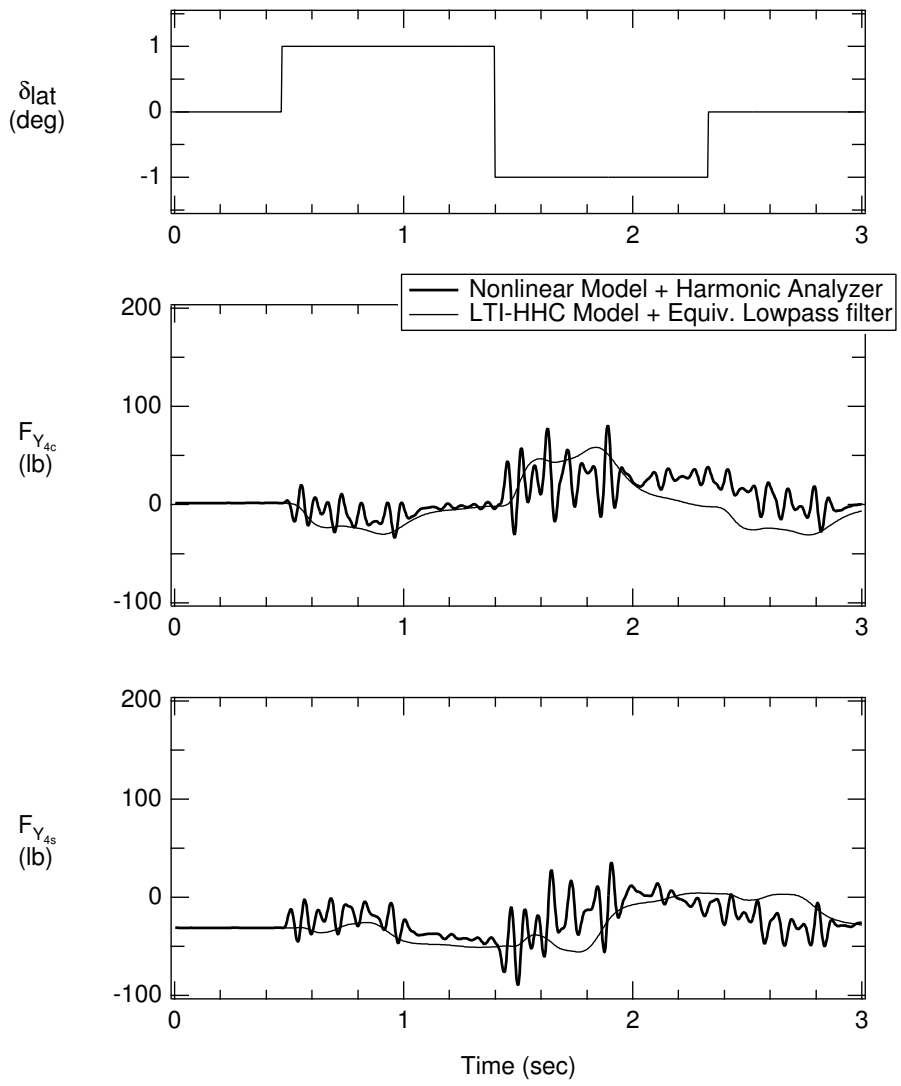

Figure 4.22: Lateral hub shear comparison; V= 80 kts, W=14,000 lb, 1" lateral cyclic doublet input.

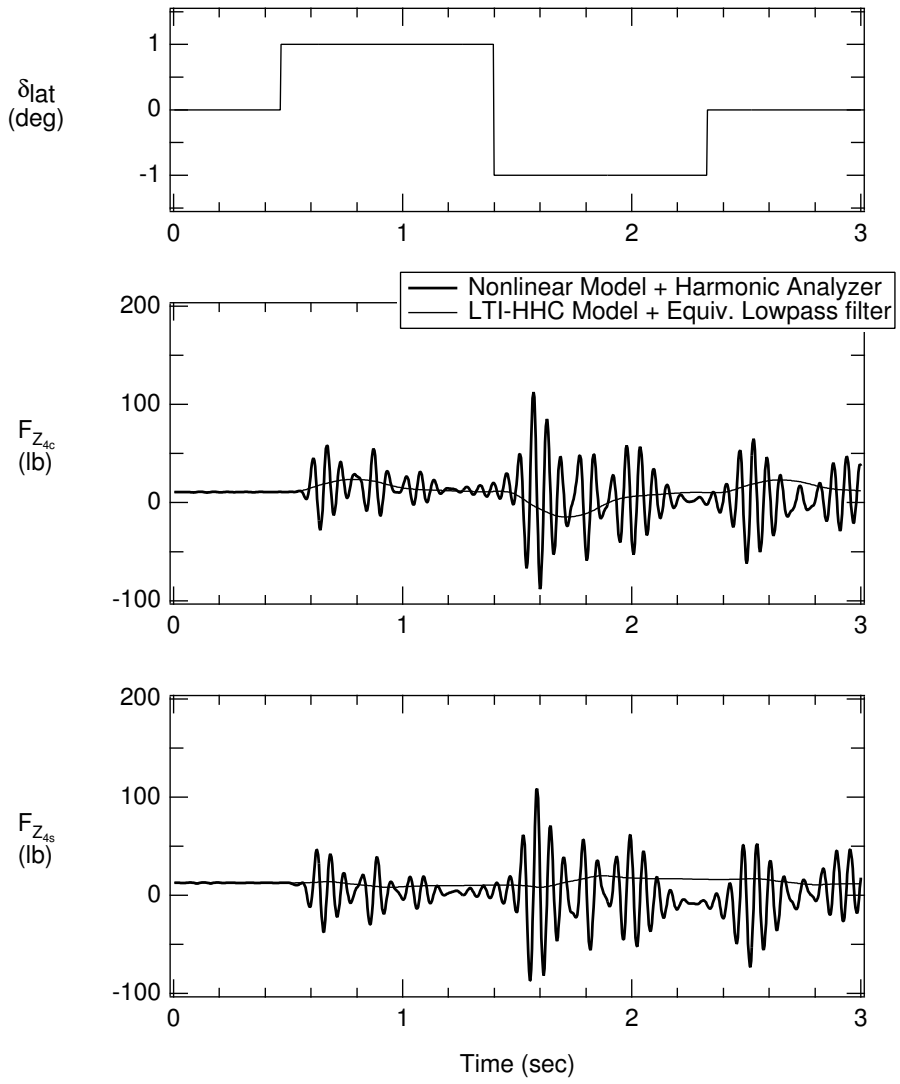

Figure 4.23: Vertical hub shear comparison; V= 80 kts, W=14,000 lb, 1" lateral cyclic doublet input.

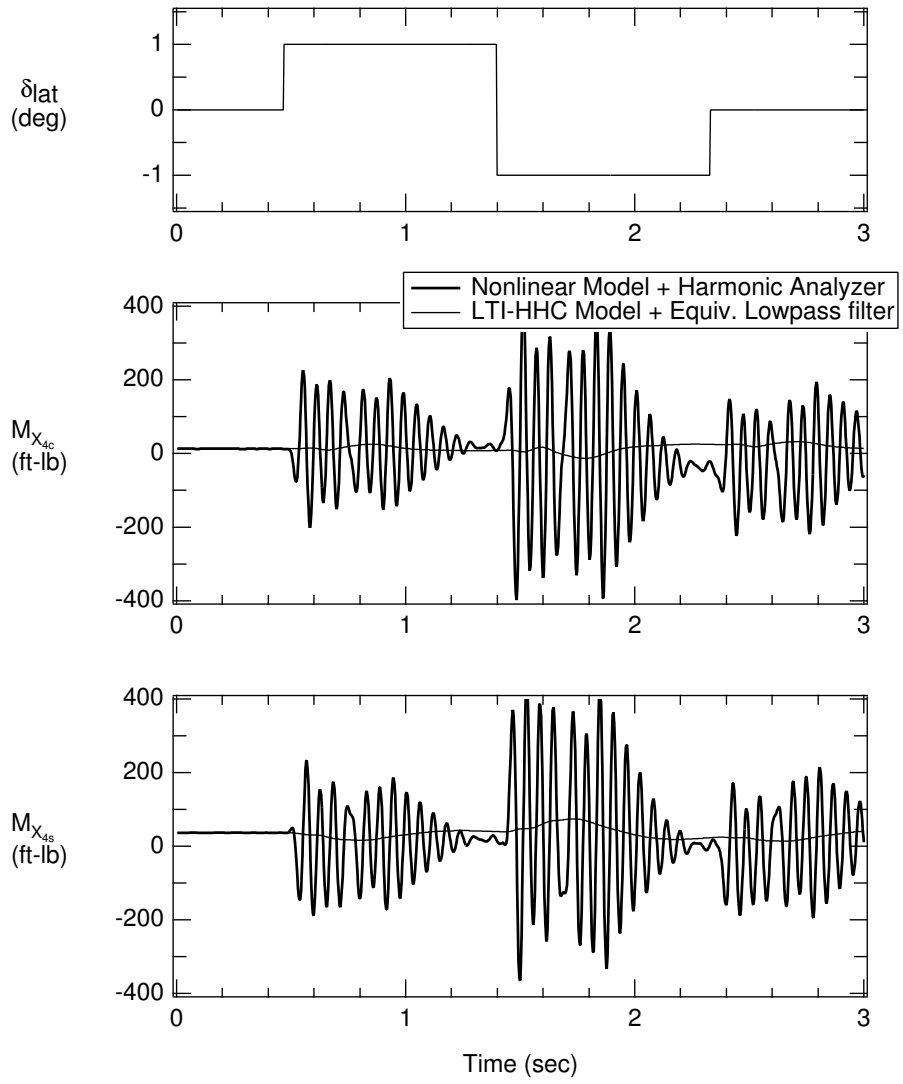

Figure 4.24: Longitudinal hub moment comparison; V= 80 kts, W=14,000 lb, 1" lateral cyclic doublet input.

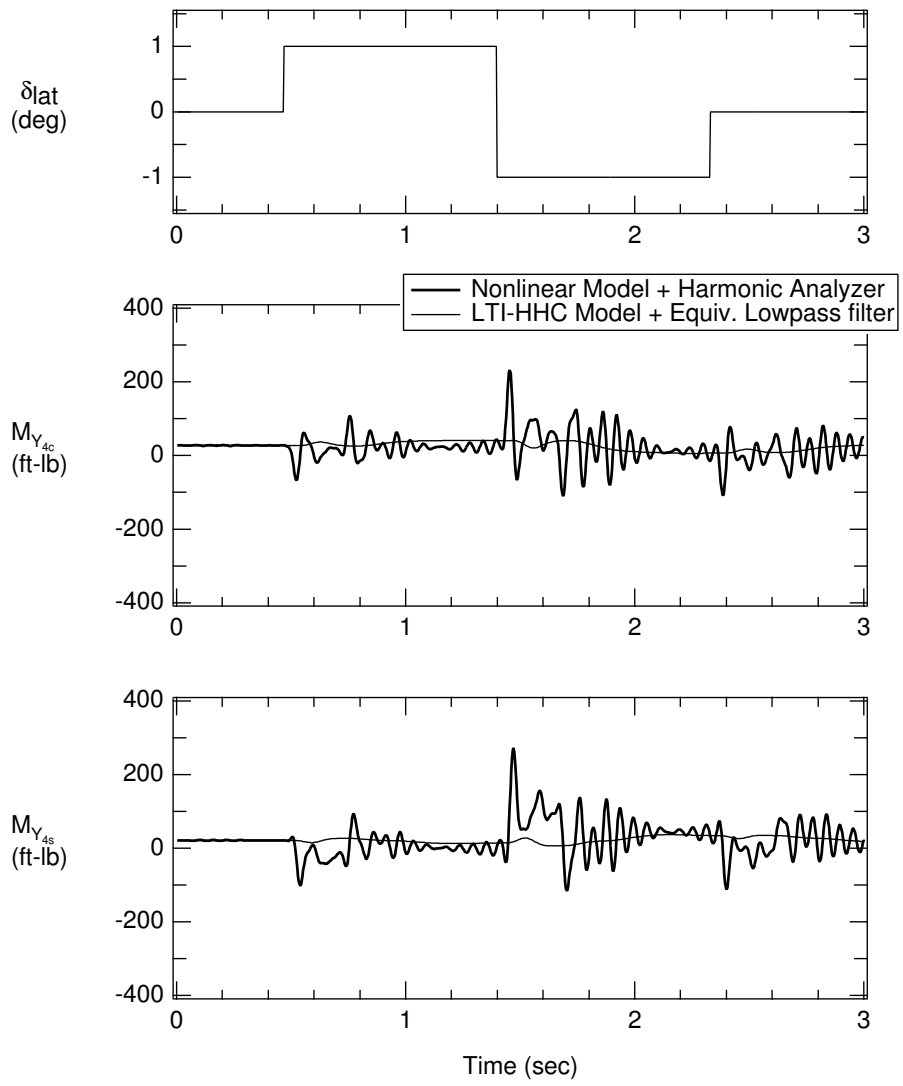

Figure 4.25: Lateral hub moment comparison; V= 80 kts, W=14,000 lb, 1" lateral cyclic doublet input.

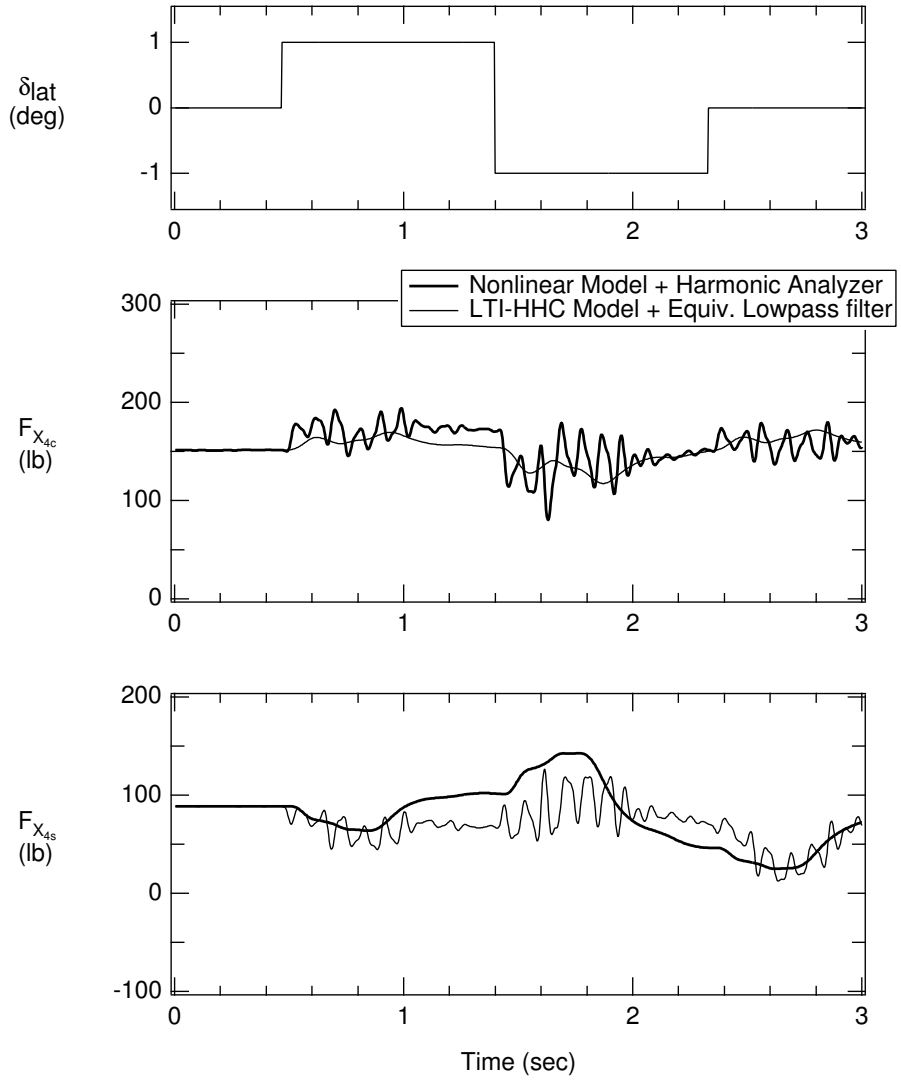

Figure 4.26: Longitudinal hub shear comparison; V= 120 kts, W=14,000 lb, 1" lateral cyclic doublet input.

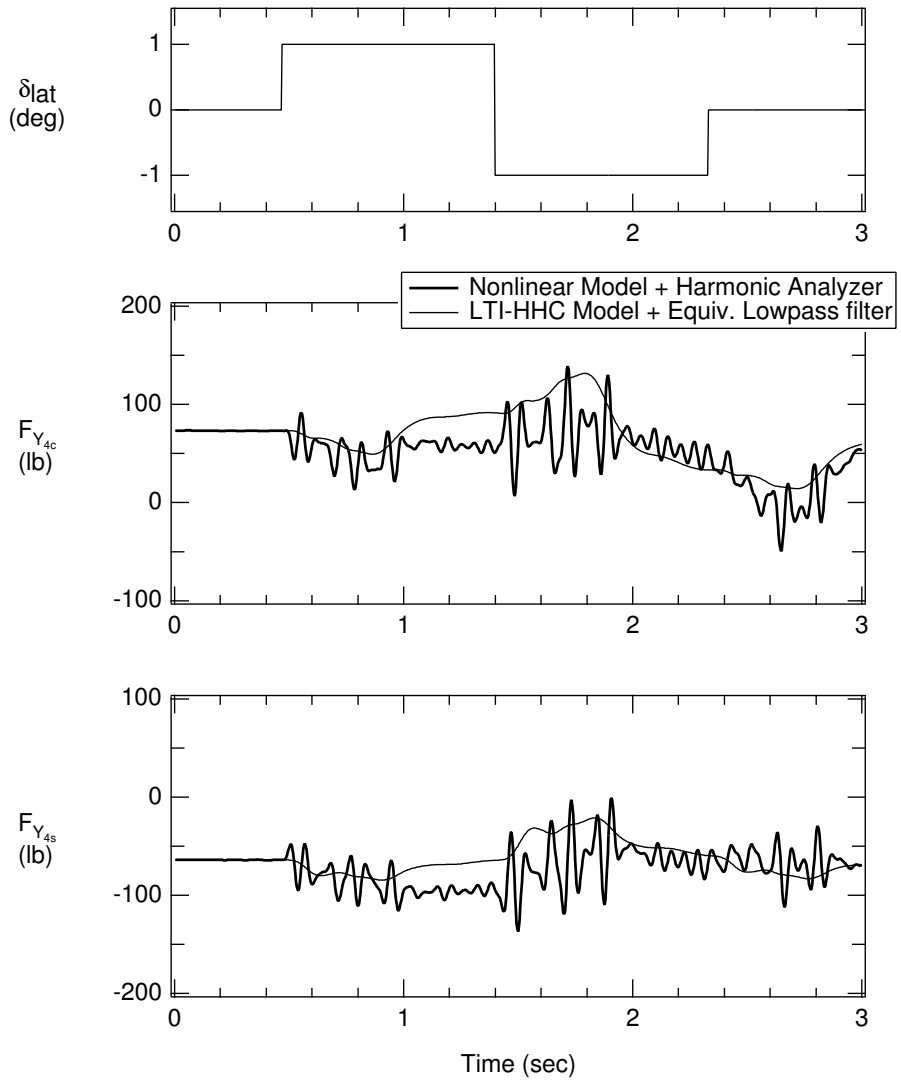

Figure 4.27: Lateral hub shear comparison; V= 120 kts, W=14,000 lb, 1" lateral cyclic doublet input.

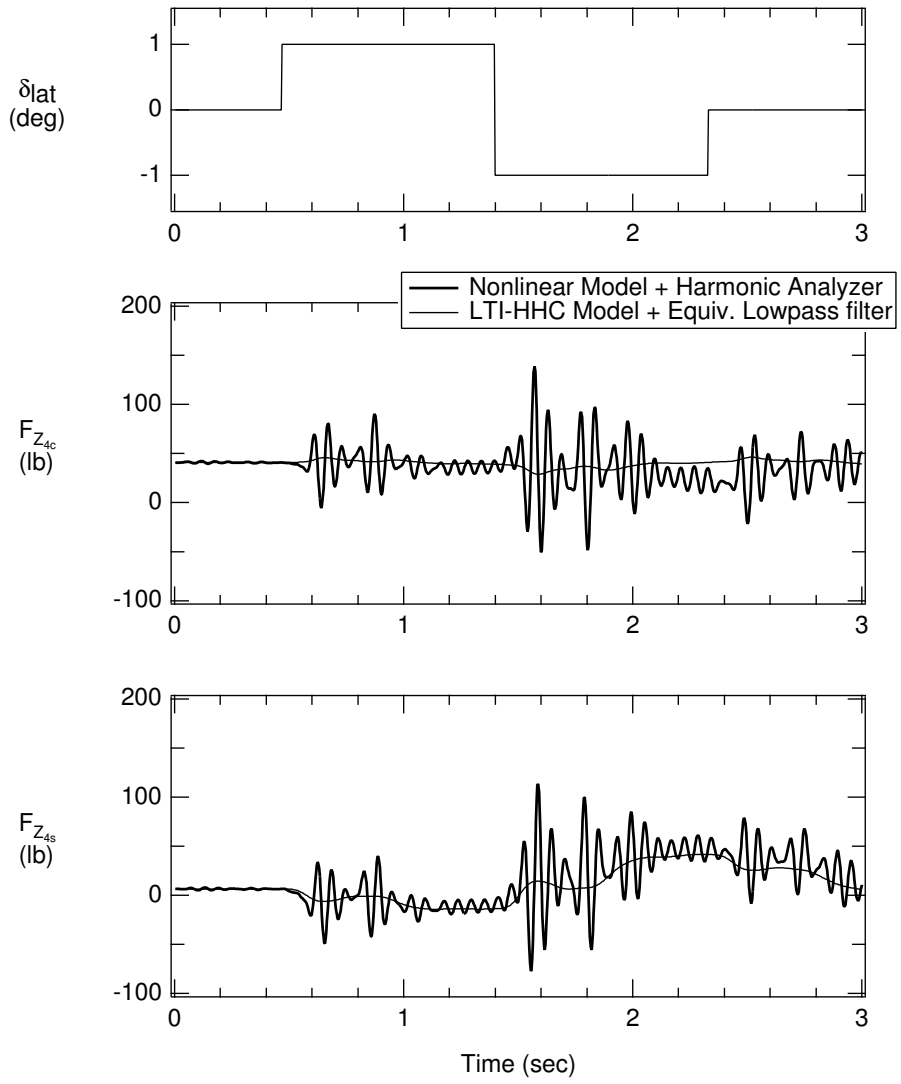

Figure 4.28: Vertical hub shear comparison; V= 120 kts, W=14,000 lb, 1" lateral cyclic doublet input.

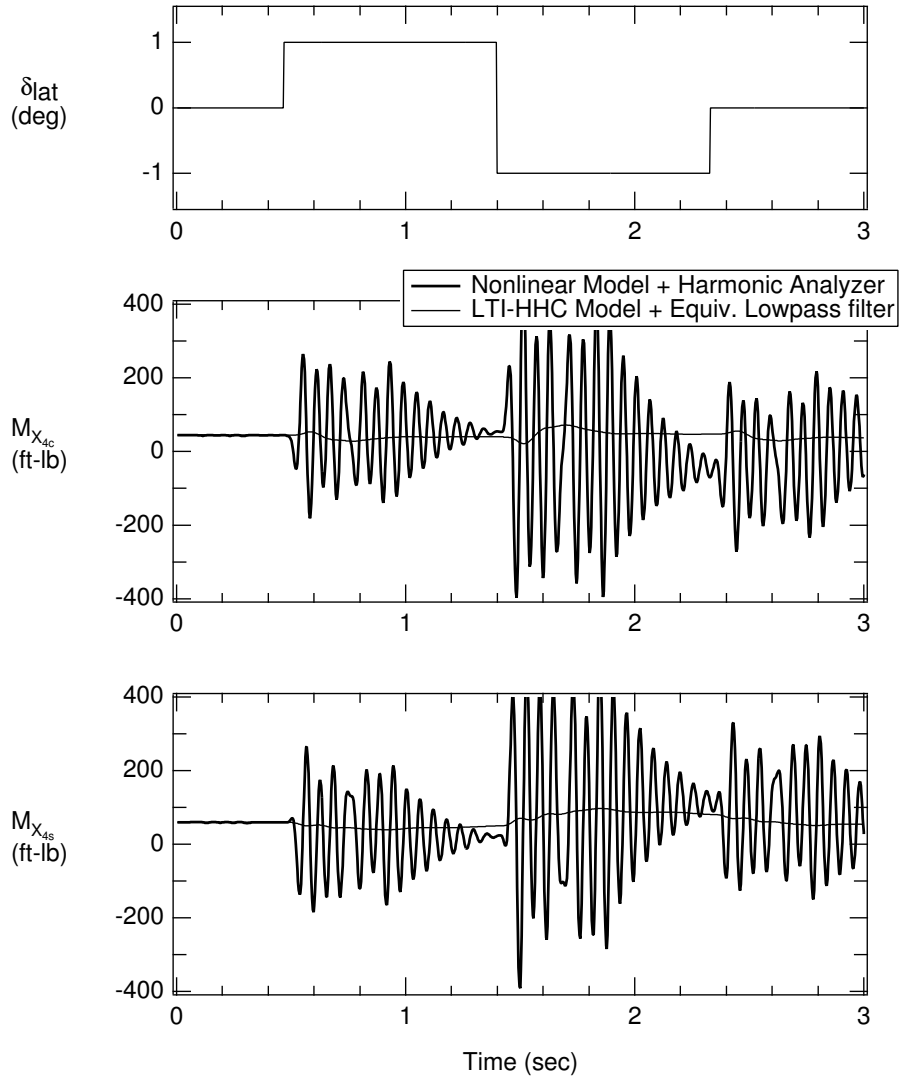

Figure 4.29: Longitudinal hub moment comparison; V= 120 kts, W=14,000 lb, 1" lateral cyclic doublet input.

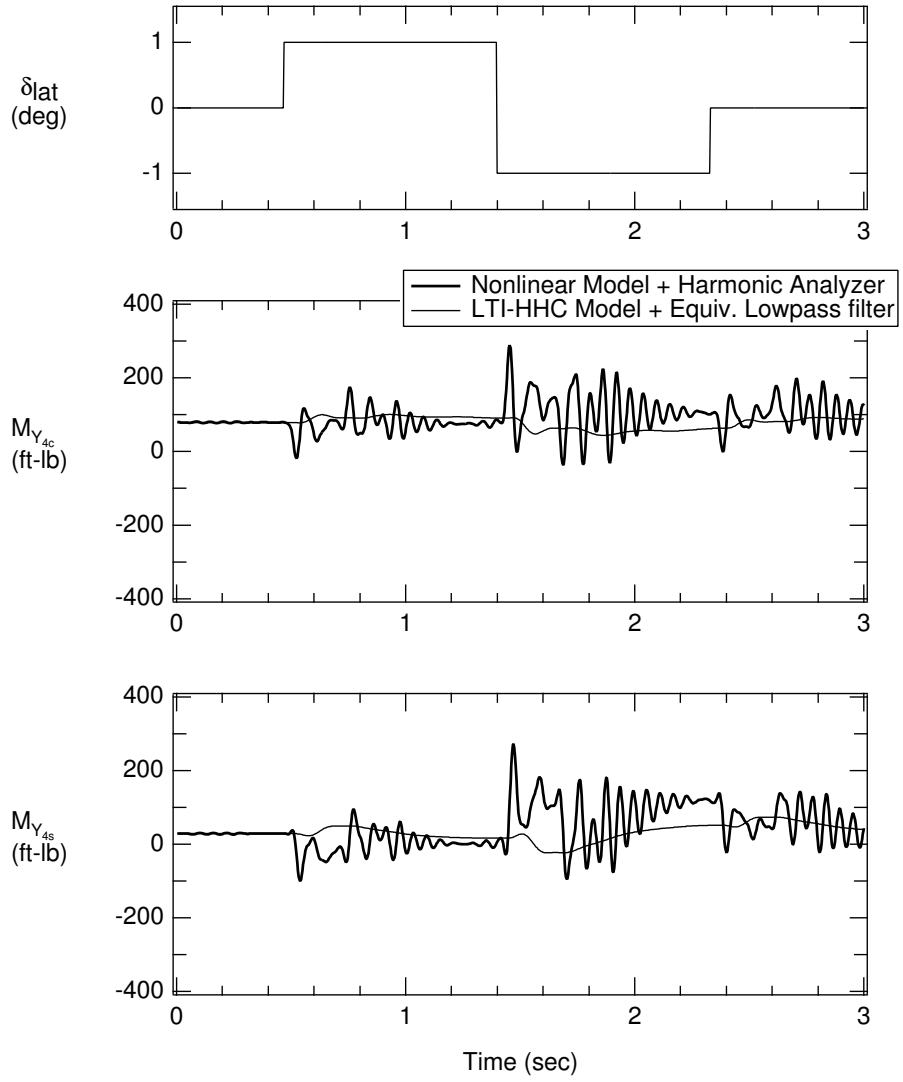

Figure 4.30: Lateral hub moment comparison; V= 120 kts, W=14,000 lb, 1" lateral cyclic doublet input.

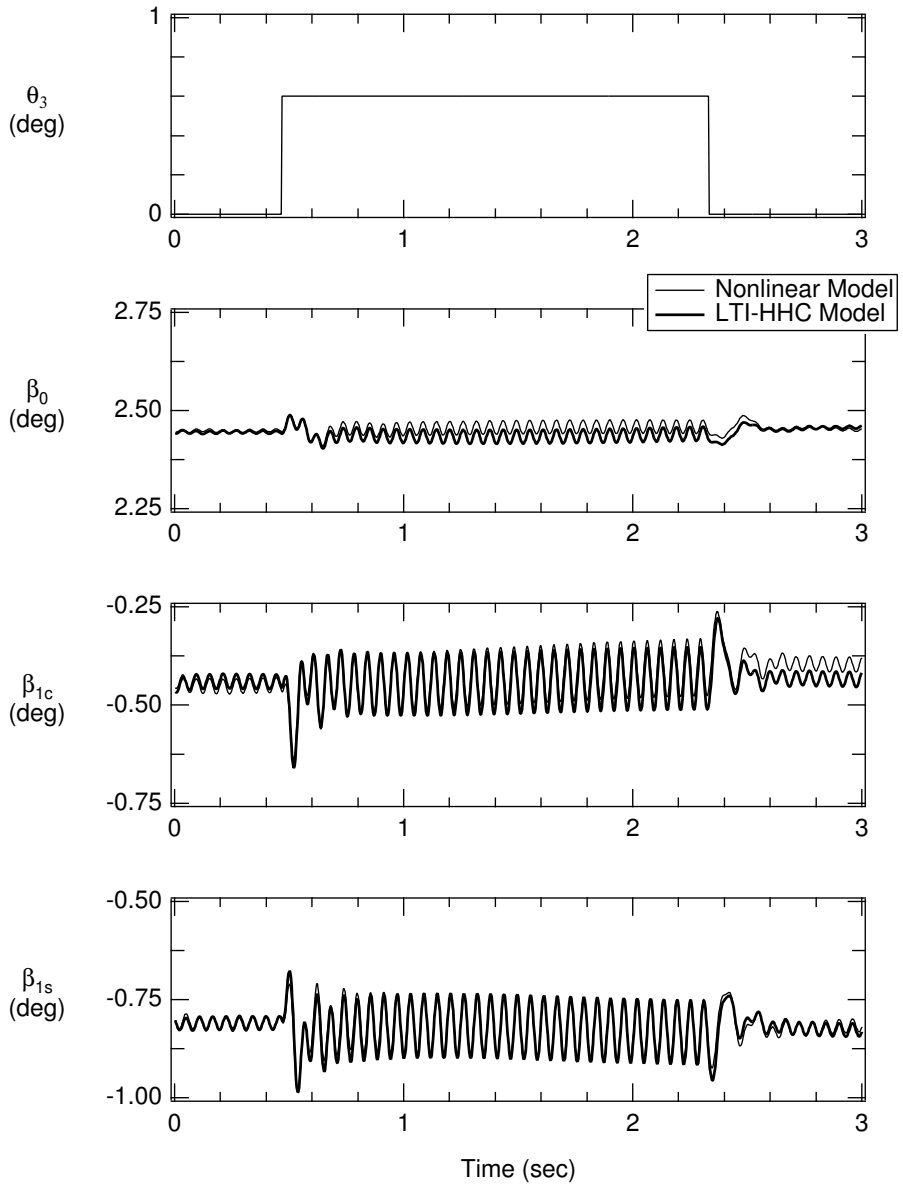

Figure 4.31: β comparison; V= 120 kts, W=14,000 lb, $A_3 = 0.6^o$, $\phi_3 = 0^o$.

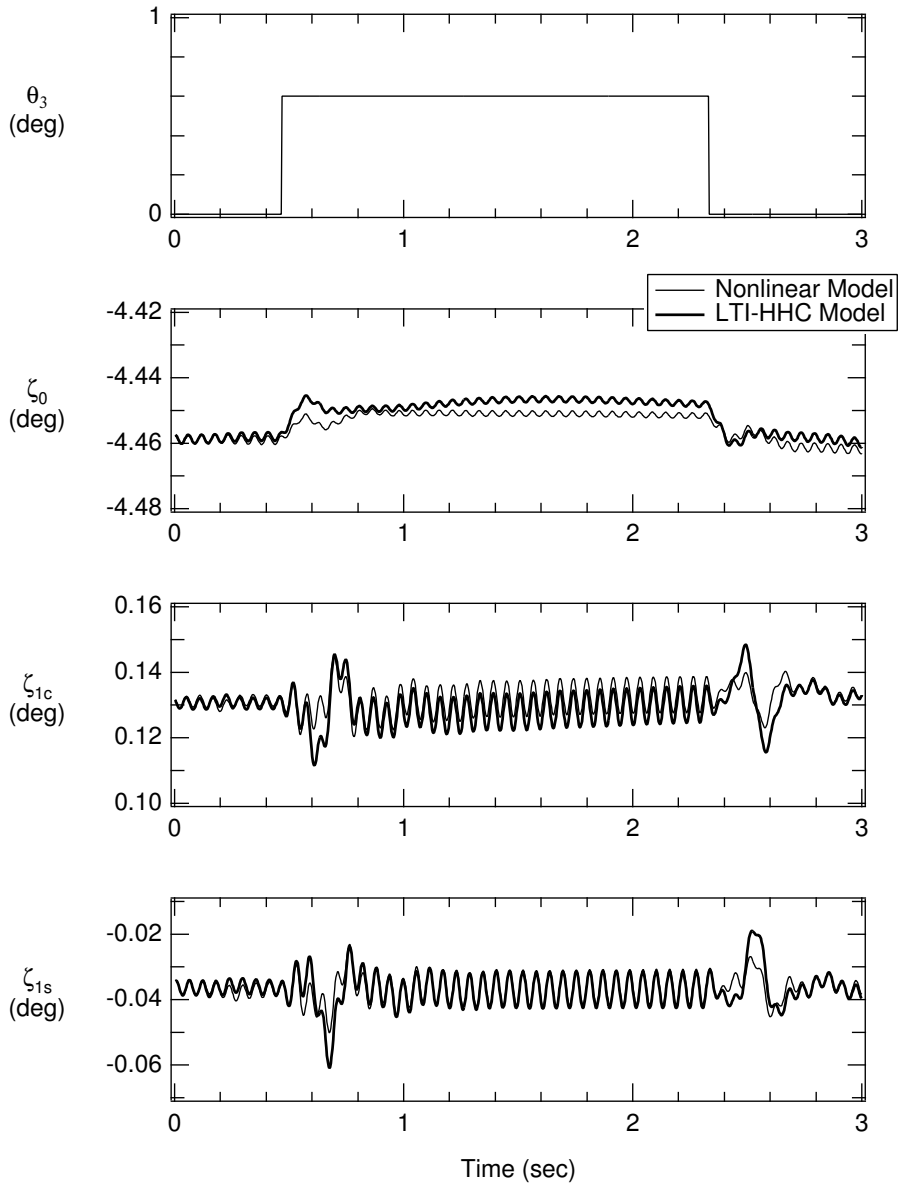

Figure 4.32: ζ comparison; V= 120 kts, W=14,000 lb, $A_3 = 0.6^o$, $\phi_3 = 0^o$.

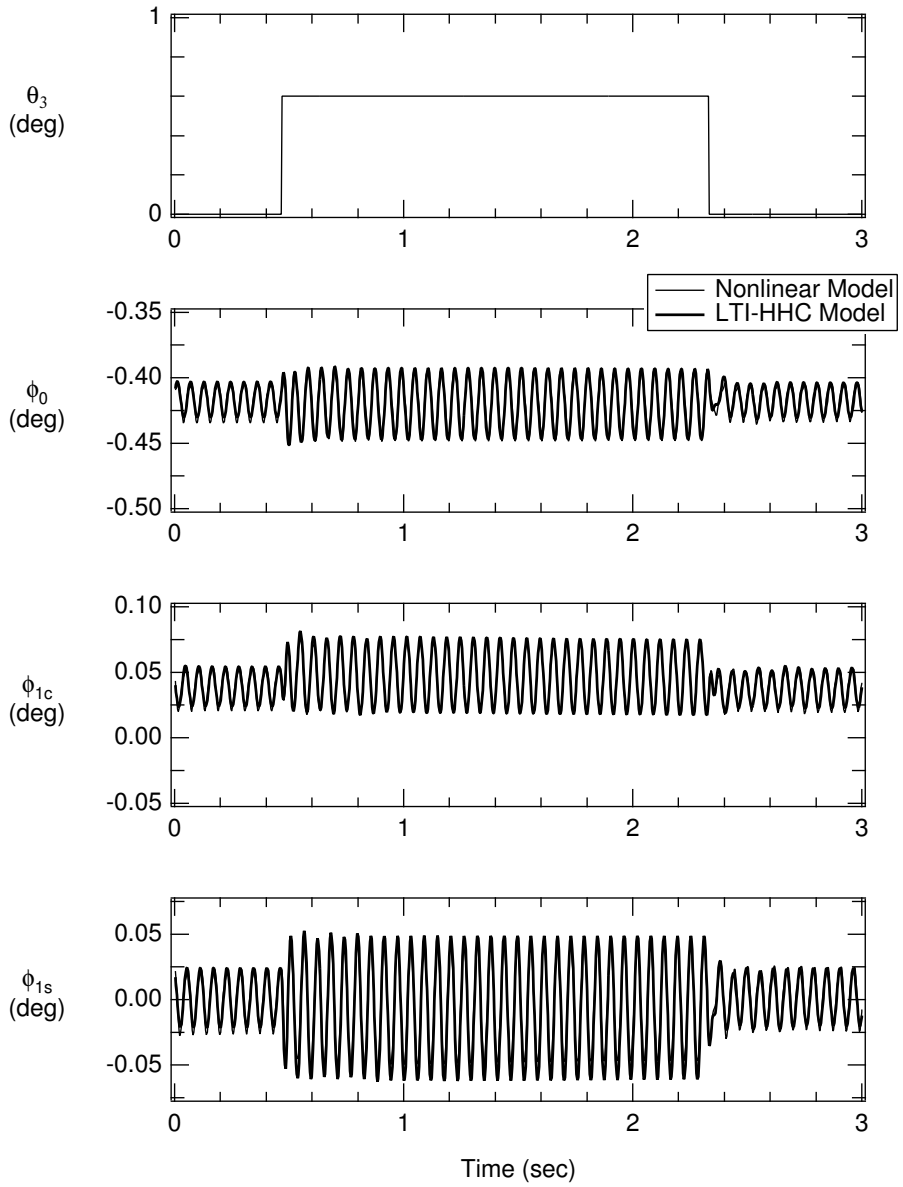

Figure 4.33: ϕ comparison; V= 120 kts, W=14,000 lb, $A_3 = 0.6^o$, $\phi_3 = 0^o$.

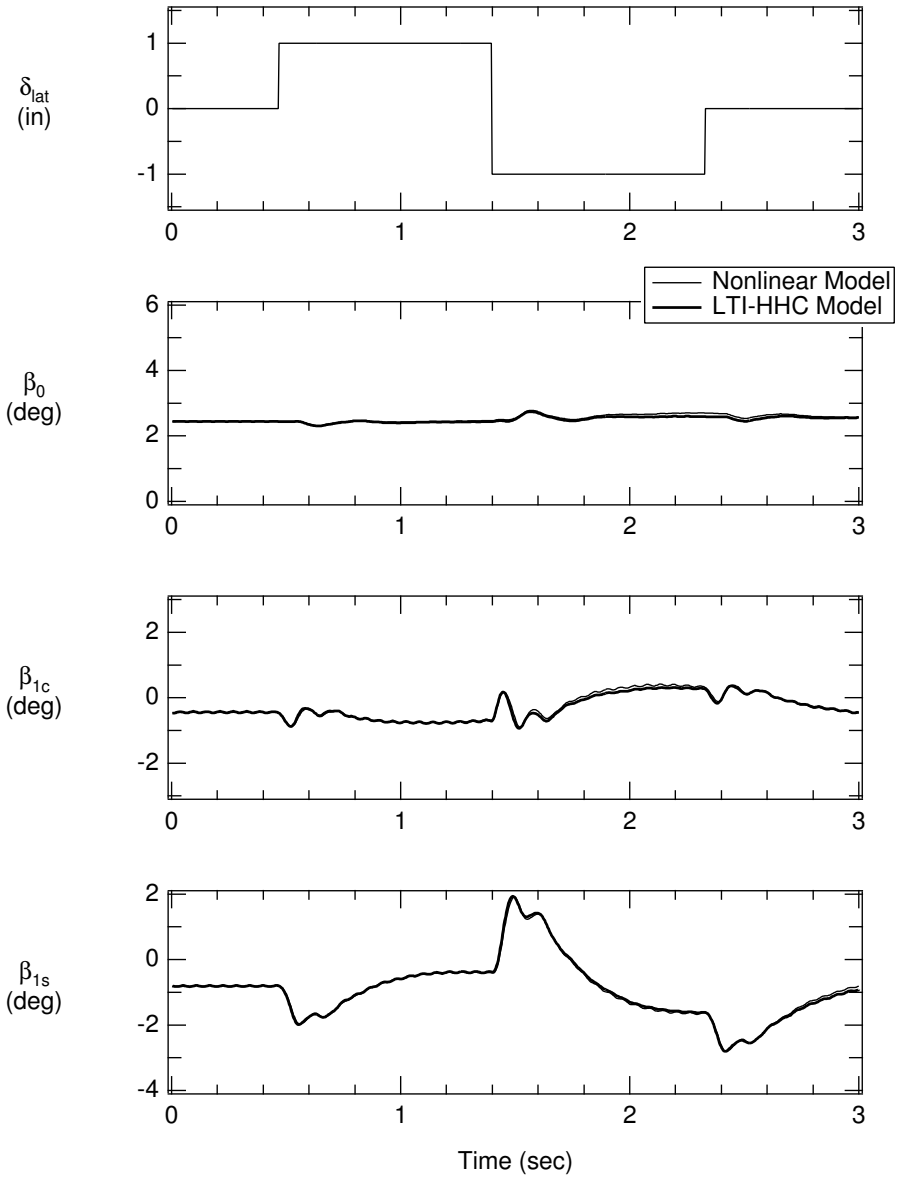

Figure 4.34: β comparison; V= 120 kts, W=14,000 lb, 1" lateral cyclic doublet input.

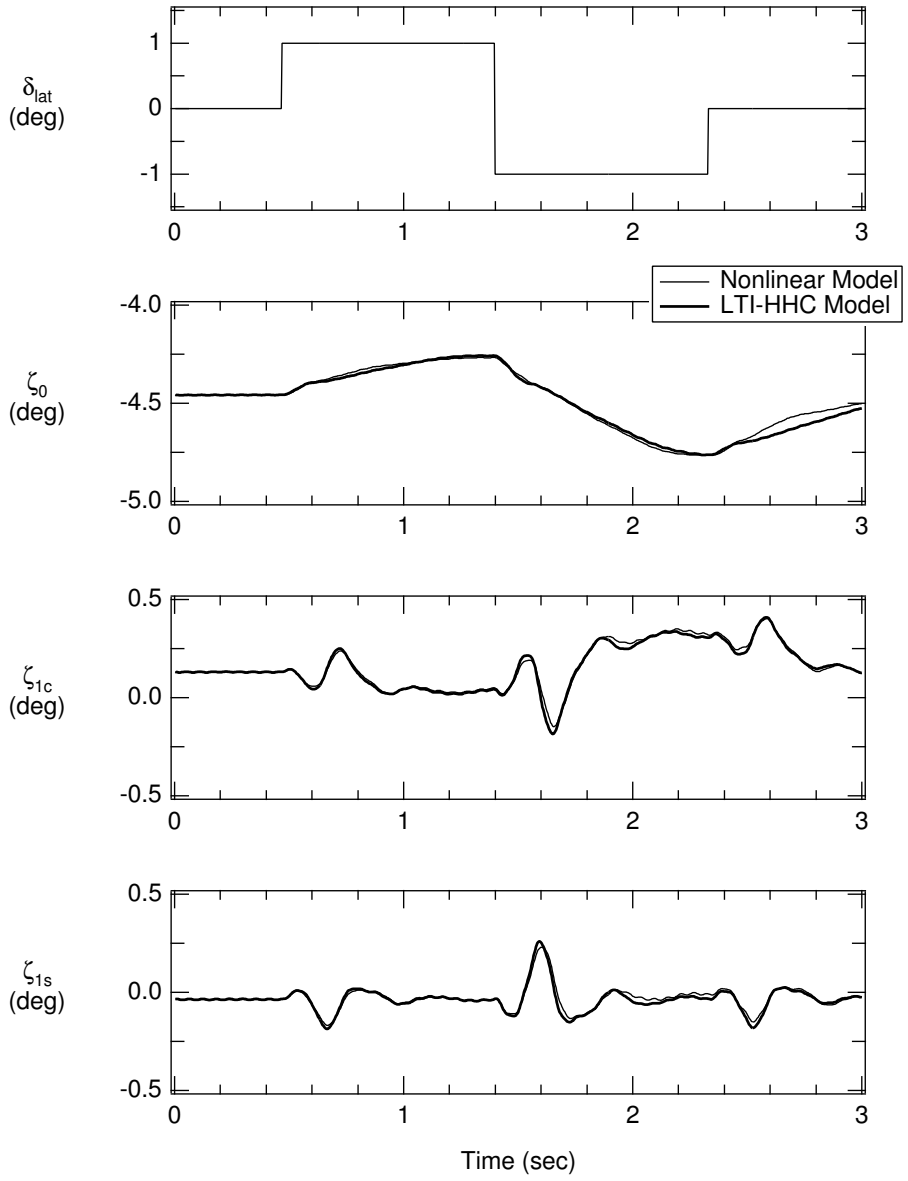

Figure 4.35: ζ comparison; V= 120 kts, W=14,000 lb, 1" lateral cyclic doublet input.

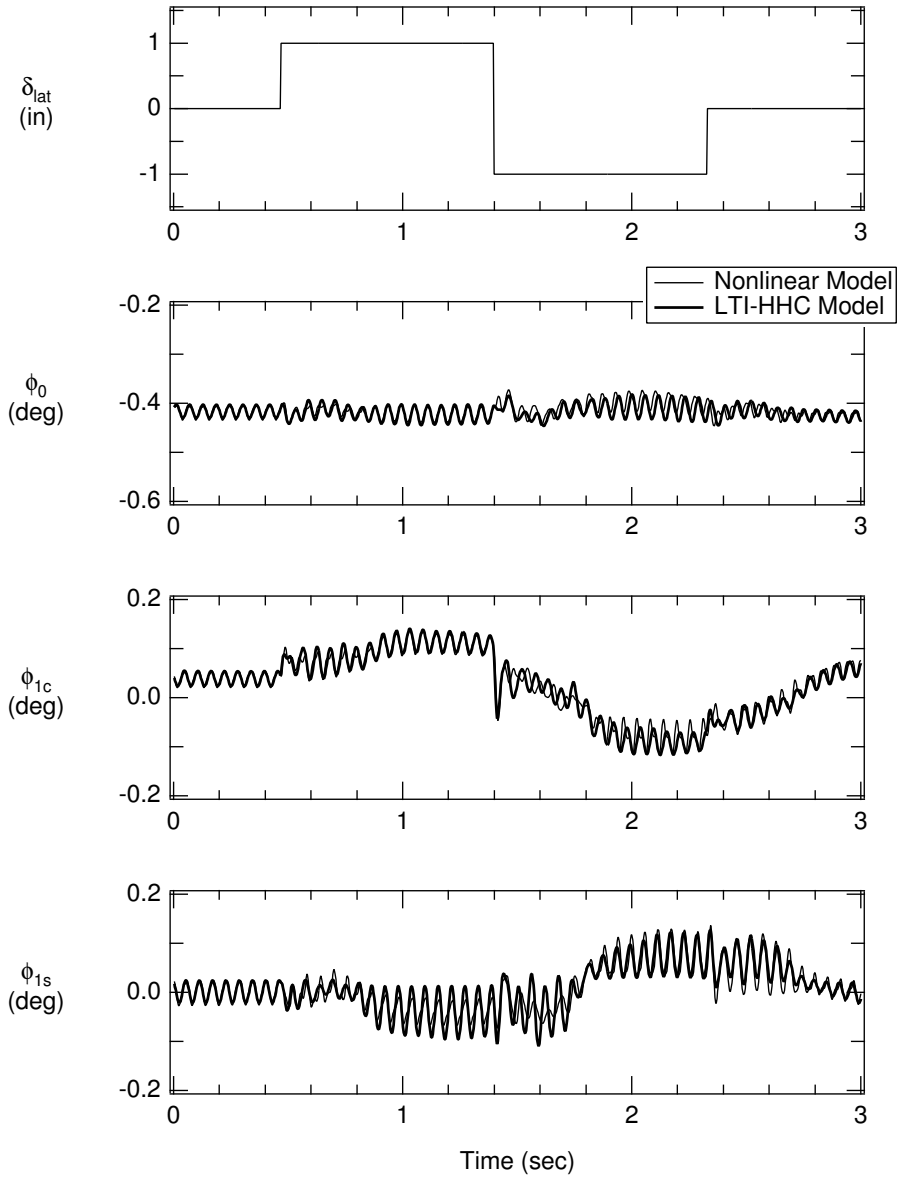

Figure 4.36: ϕ comparison; V= 120 kts, W=14,000 lb, 1" lateral cyclic doublet input.

Chapter 5

HHC and AFCS Interaction Study

A linear time-invariant state-space approximation that accurately models the coupled rotor-fuselage dynamics including the higher harmonic response of the rotor has been developed in Chapter 4. This work allows several important questions to be answered regarding the dynamic interaction between Automatic Flight Control System (AFCS) and High Harmonic Control (HHC), including the effect on handling-qualities. The key breakthrough is in the method to extract a linear time-invariant model that includes a harmonic analyzer and allows the periodicity of the helicopter response to be captured. The coupled high-order linear model provides the needed level of dynamic fidelity to permit study of AFCS and HHC interaction.

5.1 Effect of a fixed HHC input on rigid body dynamics

To understand the potential coupling between AFCS and HHC, an analysis was first performed in the open-loop system to determine whether a fixed HHC input

had any direct effect on the rigid-body dynamics. Any influence from the HHC will be indicated by the changes in the frequency response. Before proceeding with any interaction analyses, it is important to validate the baseline (HHC-off) cases of both LTI-HHC and nonlinear models by comparing their frequency responses against the flight test data.

5.1.1 Open-loop frequency response validation

In Sec. 4.4, the LTI-HHC model was validated against the nonlinear model by comparing the hub load responses over several flight configurations. It is a time domain comparison, and it is sufficient for checking the aeromechanic quantities. For flight dynamics analysis, it is more common to perform the comparison in frequency domain. Figure 5.1 shows the P/δ_{lat} frequency response comparison between the LTI model, the nonlinear model, and the flight test. Unless noted otherwise, all the results presented in this chapter have the weight of 14,000 lb at a speed of 120 kts The frequency response of the nonlinear model was obtained by performing frequency sweeps in pilot lateral stick input and recording the vehicle roll rate response time history. The P/δ_{lat} frequency response was identified by extracting the information from the time history data using CIFER® [58].

Since the LTI-HHC model is already in the linear system, its frequency response can be calculated directly from the LTI-HHC model. The Figure shows that all three cases agreed with each other in the frequency range of 2-20 rad/sec. There were some small disagreements in the frequency range of 1-2 rad/sec between the flight test result and the analytical results, but the difference is not significant. Comparing the nonlinear and LTI-HHC frequency responses, there is also a little difference, and most of the difference is in the phase curve below 2 rad/sec.

5.1.2 Effect of an optimum three/rev input on rigid body dynamics

Figure 5.2 shows the effect of a fixed HHC input on the rigid body dynamics for the nonlinear model. The fixed HHC input chosen is an optimum 3/rev input which is calculated from the optimization procedure that minimized the norm of 4/rev in-plane hub shears. The optimization procedure is similar to the one described in Sec. 2.8. This figure indicates that the optimum 3/rev input has no effect on the rigid body dynamics in the frequency range of interest. Figure 5.3 shows the same conclusion for the LTI-HHC model.

The frequency response of the nonlinear model with the optimum 3/rev input is extracted using the same method as the nonlinear baseline (HHC-off) case stated earlier. For the LTI-HHC model, one cannot simply include an optimum 3/rev input and compute the frequency response because the linear model will only respond at the same frequency as the input signal. In this case, the input signal is a 3/rev (81 rad/sec for UH-60) and it is beyond the frequency range of interest. To see the effect of the optimum 3/rev input on rigid body dynamics, one must engage the HHC loops and let the effects of the 3/rev input propagate through the HHC feedback loops.

Although the results above show that the HHC input has no effect on rigid body dynamics (or AFCS), it does not necessary mean the AFCS has no effect on the HHC. There is still a possibility that the AFCS affects vehicle vibration and indirectly affects the HHC. This closed-loop analysis is discussed in the next section.

5.2 Interaction of HHC and AFCS

A SIMULINK® simulation of the combined flight and higher harmonic control system was developed for analysis and optimization in the Control Designers Unified Interface, CONDUIT® [59]. The key elements of the simulation are illustrated in Figure 5.4, and they are:

1. Higher-order linear airframe model that provides the flight mechanics and 4/rev vibration responses to both pilot and HHC inputs.
2. Automatic Flight Control System loops based on a simple proportional-integral-derivative (PID) controller in roll, pitch, and yaw.
3. Typical actuator/sensor filter dynamics.
4. Equivalent harmonic analyzer approximates the sample window dynamics and equivalent time delay.
5. Higher harmonic controller based on fixed T-matrix feedback.
6. Zero-order-hold approximation simulates the discrete HHC update time delay.

Like the open-loop analysis, it is important to validate the closed-loop model to ensure that the linear continuous time domain model implemented in SIMULINK® is equivalent to the nonlinear multi-rate model. This can be accomplished by comparing the broken control loop response of both models.

5.2.1 Broken control loop response validation

Figure 5.5 illustrates the schematic of both linear and nonlinear simulation models. The simulation model showed in Figure 5.5a is a nonlinear multi-rate system.

Because the control system analysis was performed in the linear continuous-time domain, the entire nonlinear multi-rate system was converted to an equivalent linear continuous time system as shown in Figure 5.5b. The harmonic analyzer is now embedded within the LTI-HHC model. The effect of the sample window is modeled by an equivalent lowpass filter. The discrete HHC controller is transformed to a continuous-time domain HHC controller. The discrete HHC update (zero-order-hold) is approximated by a Padé function.

The broken control loop response is a method of studying loop stability; it allows one to determine the gain and phase stability margins. Using θ_{3c} broken control loop for instance, it is the θ_{3c} response at point B in Figure 5.5 with respect to the θ_{3c} input at point A while the 3/rev-cosine and 3/rev-sine loops are open. The flight control system is also disabled during the frequency sweep. For the purpose of the validation, six broken control loop responses (3/rev-cosine, 3/rev-sine, 4/rev-cosine, 4/rev-sine, 5/rev-cosine, 5/rev-sine) were extracted from each model, and the direct comparisons are shown in Figures 5.6-5.11. In these figures, the frequency response of the LTI-HHC model matches very well with the one from the nonlinear model in both the magnitude and phase curves for all six loops within frequency range of interest. This indicates that the linear continuous time domain model in Figure 5.5b is equivalent to the nonlinear multi-rate model in Figure 5.5a.

Although HHC input operates at 3, 4, 5/rev frequencies (or 81, 108, 135 rad/sec for UH-60 helicopter), the crossover frequency of each HHC loop is only about 1 rad/sec. The crossover frequency, the gain margin, and the phase margin of each HHC loop are tabulated in Table 5.1. Because of the high HHC input frequency, one would expect a large frequency separation between the flight control and HHC

system and assume these two systems do not interfere with each other. However, the research results show that not only do the HHC loops operate at a much lower frequency, but they are also within the frequency range of flight control system. This is another indication of potential HHC/AFCS interaction.

5.2.2 Optimization of AFCS (HHC-off)

One way to see whether the closed-loop HHC system has any effect on the AFCS or handling-qualities is to optimize the AFCS for the satisfactory (Level 1) handling-qualities with the HHC loops disengaged (Figure 5.12). Any influence introduced by closing the HHC loops will be indicated by the change in handling-qualities. The AFCS implemented in this study is based on a simple PID controller (Figure 5.13) in roll, pitch, and yaw axis. The PID controller computes individual actuator command with respect to the changes in rigid body states and pilot inputs. The actuator is a second order model (Figure 5.14) including both the position and rate saturation limits. The actuator design parameters are tabulated in Table 5.2.

First, CONDUIT® was used to optimize the PID gains of the AFCS, with the HHC loops disengaged. The PID gains were tuned to achieve satisfactory handling-qualities, based on the Aeronautical Design Standard (ADS-33E [60]), and standard control-system design specifications list below (Appendix A):

- Eigenvalue real part (EigLcG1)
- Crossover frequency (CrslnG1)
- Stability margins (StbMgG1)
- Bandwidth (BnwRoF3)

- Step response damping ratio (OvsAtH1)
- Crossover frequency (CrsMnG1)
- Eigenvalue damping ratio (EigDgG1)
- Step response rise time (RisTmG1)

CONDUIT rapidly tuned the PID gains to achieve satisfactory (Level 1) requirements with minimum over-design as shown in Figure 5.15. The optimized PID gains are tabulated in Table 5.3. Each symbol in Figure 5.15 represents the result for a particular loop and shows that all the responses lie in the light region (Level 1). For example, note that the roll bandwidth is 3 rad/sec, Figure 5.15d, which meets ADS-33E. The PID gains of the roll and yaw loops yield bandwidths in excess of the requirement in order to meet some of the other specifications. It is important to mention that this set of PID gains is not the *best* from the handling-qualities point of view. It is simply the lowest gains needed to satisfy all the design specifications while staying in the level-1 region.

5.2.3 Nominal *T*-matrix controller

Next, the T-matrix HHC loops were engaged with a nominal gain of k=1 (same in all six loops) as shown in Figure 5.16. This is referred to as the "nominal" case. With both AFCS and HHC loops closed, the CONDUIT® HQ design specifications were re-evaluated without changing the PID gains. The results are presented in Figure 5.17 which shows that the closing of the HHC loops had a negligible effect on the AFCS performance and overall handling-qualities. This indicates the lack of dynamic coupling of HHC into flight control. Therefore, no re-tuning of the AFCS was needed for the combined AFCS/HHC system. The lack of

interaction from HHC to AFCS is consistent with the earlier system identification results obtained in Sec. 5.1.2, which also showed no effect of an HHC input on the rigid-body dynamic response.

In terms of suppressing the steady state vibration level, the nominal T-matrix controller can reduce the vibration by a large amount. Figures 5.18-5.21 show the changes in the lateral and longitudinal 4/rev vibration level with respect to the HHC and pilot stick inputs for both the baseline case (HHC-off) and nominal (k=1) case. At t=0, the vehicle starts from a steady state condition, and the 4/rev vibrations are maintained at a steady level. The baseline 4/rev vibrations are tabulated in the first column of Table 5.4. At t=5 seconds, the HHC loops are engaged and the nominal T-matrix controller begins to reduce the 4/rev vibrations to a lower level. It takes approximately 2-3 seconds for the 4/rev vibrations to reach a new steady state condition where 67% of 4/rev in-plane vibrations have been reduced (Table 5.4). The large time constant of 2-3 seconds consists with the slow HHC loop dynamics stated in Sec. 5.2.1.

5.2.4 Transient vibration in maneuvering flight

While the impact of HHC on handling-qualities is negligible, there are significant vibration responses to piloted inputs in both the baseline (HHC-off) case and the nominal (k=1) case. Figures 5.18 and 5.19 show the large transient responses for a -50° roll maneuver (moderate) starting from t=12 seconds. Once the maneuver is completed, the vehicle reaches a new trim vibration level. Similar results can also be observed in Figures 5.20 and 5.21 which demonstrate the large transient responses for a 20° pitch maneuver starting from t=12 seconds.

Using $F_{X_{4C}}$ as an example, Figure 5.22 shows the $\Delta F_{X_{4C}}$ response of both

the baseline and nominal case for the same -50° roll maneuver. The symbol Δ denotes the steady state vibration of $F_{X_{4C}}$ at t=12 seconds has been removed from the figure. With the baseline case, Figure 5.22 shows that there is a maximum transient peak excitation of 150 lb above the steady state vibration level in the $F_{X_{4C}}$ channel. Note that the $F_{X_{4C}}$ steady state vibration level for the baseline case is 151 lb (Table 5.4). Therefore, this maximum transient peak excitation is roughly as same as the baseline steady state vibration level. With the nominal T-matrix controller engaged, the maximum $F_{X_{4C}}$ vibration transient increases to 163 lb, which is 9% higher than the baseline case. In other words, with the nominal T-matrix controller engaged, the transient vibration response during maneuvering flight reaches similar levels to the trim condition with HHC-off. Nevertheless, the nominal T-matrix controller is able to reduce the transient load back to lower levels faster than baseline case after the 15-second point.

The performance of the HHC system in suppressing the vibration response to piloted input is also reflected in the frequency-responses: $F_{X_{4C}}/\delta_{lat}$, $F_{X_{4S}}/\delta_{lat}$, $F_{Y_{4C}}/\delta_{lat}$, etc. The RMS, determined from the integral under the frequency-response squared functions, is a useful measure of the vibration response to the broadband pilot inputs for different HHC system designs. The spectral integration to determine the RMS is conducted up to a frequency of 3 rad/sec. The 3 rad/sec cut-off frequency corresponds to the roll command bandwidth, and it is a good estimate of the maximum closed-loop piloting frequency. Finally, the RMS levels were normalized using the baseline vibration RMS for the roll maneuver to show the relative improvement (or degradation) in vibration suppression by the HHC system.

Figure 5.23 shows the frequency response of $F_{X_{4C}}$ with respect to the lateral

piloted input. Looking at the magnitude curve, the nominal case has a small magnification effect at higher frequency range (1-3 rad/sec) and a large reduction effect below the frequency of 0.9 rad/sec. Both effects are consistent with the result shown in Figure 5.22 where there is a small increase in the transient vibration excitation and a large reduction in steady state vibration level. Because the nominal T-matrix controller is capable of suppressing the $F_{X_{4C}}/\delta_{lat}$ vibration response more than it magnifies, there is 4.1% reduction in $F_{X_{4C}}/\delta_{lat}$ channel. The small reduction of 4.1% does not seem to reflect amount of vibration suppression shown in the figure. This is because the figure is on the logarithm scale, which biases toward the lower range. When including other seven channels ($F_{X_{4S}}/\delta_{lat}$, $F_{Y_{4C}}/\delta_{lat}$, $F_{Y_{4S}}/\delta_{lat}$, $F_{X_{4C}}/\delta_{lon}$, $F_{X_{4S}}/\delta_{lon}$, $F_{Y_{4C}}/\delta_{lon}$, $F_{Y_{4S}}/\delta_{lon}$), the average vibration in maneuvering flight for a nominal case is 3.2% above the baseline case (Table 5.5). This shows that the nominal T-matrix controller is ineffective for vibration suppression during maneuvers.

5.2.5 Ideal integrator approximation

Many previous studies [6, 18–20, 22, 23, 61–64] represented the helicopter plant model in Figure 5.16 by a fixed T-matrix, which is a linear approximation of the vibration response to the HHC inputs at a steady-state condition. In other words, T-matrix corresponds to the linear state-space model at DC gain [1] to within the accuracy of the linear model extraction process. This method eliminates the need for a detailed model of the periodic helicopter dynamics. The nominal (k=1) T-matrix controller (HHC Controller in Figure 5.16) is simply a k/s diagonal compensator multiplied by the fixed-gain regulator $T^{\dagger}$. The broken-loop response

[1] DC Gain is the ratio of the *output*/*input* signal at the steady-state condition

matrix $(k/s)\ T^{\dagger}\ T$ will thus be a nearly diagonal matrix of k/s responses. This corresponds to single-input/single-output loop and without loop interactions (e.g., no response of the $3s$ loop to $3c$ transients). Assuming a nominal gain of k=1, this ideal approximation gives loop crossover frequencies of ω_c=1 rad/sec, 90° phase margin, and infinite gain margin in every loop as illustrated in Figure 5.24.

Next, the helicopter vibration model is replaced with the LTI-HHC model. The actual broken-loop response for the 3/rev-cosine loop shown in Figure 5.24 confirms that the k/s approximation is quite accurate for frequencies of up to about the 1 rad/sec crossover frequency. There is a gain offset associated with the deviation between the steady response of the nonlinear simulation (T-matrix) and the steady-state response of the linearized model. For frequencies above 1 rad/sec, there is significant deviation from the $1/s$ ideal response, especially in phase, due to the dynamics of the 4/rev vibration response relative to the simple steady-state approximation (T-matrix).

The $F_{X_{4C}}$ vibration response to a unit pulse input is shown in Figure 5.25 to be well damped. Increasing the HHC feedback gain (k=2) raises the broken-loop crossover frequency and the closed-loop HHC disturbance rejection bandwidth (Figure 5.26). There is an associated reduction in the closed-loop transient settling time, as was also concluded by Shin et al. [5]. But, there is also a magnification of the peak disturbance at frequencies above crossover (Figure 5.26), which is consistent with classical control theory and which shows up in the time-domain as well (Figure 5.25).

5.2.6 Optimized HHC controller

Analyses with CONDUIT® show that an improvement in the suppression of vibration transients during the maneuvering flight can only be achieved by increasing the HHC crossover frequency to a value that is close to the 3 rad/sec piloted bandwidth. At this increased crossover frequency, the use of the T-matrix (which is a steady-state approximation) to simulate the helicopter vibration model is unacceptable for controller optimization and analysis, and it must be replaced with the complete dynamic LTI-HHC model developed in Chapter 4. Furthermore, the simple k/s HHC controller architecture must be augmented with the addition of a second order lead-lag compensator (Figure 5.27) in each loop to add robustness and achieve the needed stability margins. The HHC feedback controller now takes the form:

$$H(s) = \left(\frac{k}{s}\right)\left(\frac{\omega_{\text{den}}^2}{\omega_{\text{num}}^2}\right)\left(\frac{s^2 + 2\zeta_{\text{num}}\omega_{\text{num}}s + \omega_{\text{num}}^2}{s^2 + 2\zeta_{\text{den}}\omega_{\text{den}}s + \omega_{\text{den}}^2}\right)\ T^{\dagger} \tag{5.1}$$

Each HHC control loop contains five design parameters, and the same controller is used for the cosine and sine loops of a particular harmonic. Thus, for the three harmonics (6 loops), there are 15 HHC feedback parameters in total.

CONDUIT® was used for HHC controller analyses and optimization. The key HHC design specifications included in the analysis were HHC loop stability margins and vibration suppression performance. Gain and phase stability margins were determined for each of the six broken HHC loops, and the vibration suppression performance are determined from the RMS value. The design metrics are list below (Appendix A):

- Eigenvalue real part (EigLcG1)
- Stability margins (StbMgG1)

- Actuator RMS value (RisAcG1)

CONDUIT® quickly minimized the sum of the normalized vibration RMS values for the four in-plane shears to both lateral and longitudinal input without sacrificing the required HHC loop stability margins. The optimum HHC feedback parameters are presented in Table 5.6. The final evaluations of these HHC design specifications are shown in Figure 5.28. Subfigures 5.28e, f, g, and h show the relative improvement/degradation in vibration suppression by the optimized HHC controller. The RMS>1 represents the vibration level has increased with respect to the baseline (HHC-off) case, the RMS<1 indicates the vibration level has reduced with respect to the baseline case, and the RMS=1 represents the vibration level is the same as the baseline case. Except for the $F_{Y_{4C}}/\delta_{lon}$ channel, the vibration levels of other channels have been reduced.

Following the previous example, Figure 5.29 shows the frequency response of $F_{X_{4C}}$ with respect to the lateral piloted input. The magnitude plot (top figure) shows that the optimized HHC controller has dramatically reduced the vibration response by 64% over broadband pilot lateral inputs. In terms of overall performance, the average vibration in maneuvering flight for the optimized HHC controller is 37% below the baseline case (Table 5.5). This is achieved by increasing the crossover frequencies to their maximum values (e.g., $\omega_c = 2.5$ rad/sec in the 3/rev-cosine loop, Table 5.7) while still maintaining adequate stability margins (Figure 5.30).

Similar conclusion can also be drawn from the time domain results. Figures 5.31-5.34 are the time history of the vibration responses with the optimized HHC controller. The vibration responses of the nominal (k=1) and baseline cases (HHC-off) are also presented in the figures. Looking at $F_{X_{4C}}/\delta_{lat}$ in Figure 5.31,

the vehicle starts from a steady state condition, and maintains at a steady 4/rev vibration level. At t=5 seconds, the HHC loops are engaged and the optimized HHC controller begins to reduce the 4/rev vibrations to a lower level. Although the optimized HHC controller has reached the same new steady-state condition as the nominal T-matrix controller, the optimized HHC controller has a much lower raise time which is directly related to the higher crossover frequency. The peak vibration in $F_{X_{4C}}/\delta_{lat}$ channel shown in Figure 5.35 is now 73 lb, or 51% below the baseline result, which again tracks the frequency-domain results of Table 5.5 closely. One can clearly see that the optimized controller has achieved performance superior to that of the baseline (HHC-off) and nominal T-matrix controller cases.

Broken-Loop Channel	ω_c (rad/sec)	Gain Margin (dB)	Phase Margin (deg)
3/rev COS	0.92	13.8	67.9
3/rev SIN	1.03	12.4	68.3
4/rev COS	1.04	13.9	61.8
4/rev SIN	0.98	14.5	64.0
5/rev COS	0.91	14.8	65.8
5/rev SIN	0.86	15.4	68.1

Table 5.1: HHC Broken-loop Stability Margins; nominal T-matrix controller.

Nature Frequency, ω, (rad/sec)	30.0
Damping Ratio, ζ,	0.8
Rate Saturation Limit (in/sec)	600.0
Upper Position Limit (in)	60.0
Lower Position Limit (in)	-60.0

Table 5.2: Second order actuator model parameters.

$K_{\dot{u}}$	0.000000
K_u	0.000000
K_v	0.000000
K_p	-0.569774
K_q	-0.765666
K_r	-0.693188
K_ϕ	-2.480360
K_θ	-3.415540
K_ψ	-2.565180
KI_ϕ	1.084240
KI_θ	0.000000
KI_ψ	0.000000

Table 5.3: Flight control system parameters.

	Baseline (HHC-off)	Nominal (k=1) T-matrix Controller	Percent Changed
$F_{X_{4C}}$ (lb)	151.6	51.4	-66.1%
$F_{X_{4S}}$ (lb)	87.8	21.7	-75.3%
$F_{Y_{4C}}$ (lb)	73.5	-3.4	-95.4%
$F_{Y_{4S}}$ (lb)	-61.3	-42.6	-30.5%
Average =			**-66.8%**

Table 5.4: Effect of fixed T-matrix on steady state vibration level.

	Nominal T-matrix (k=1)	Optimized HHC (Lead-Lag)
	Roll Maneuvering Flight	
$F_{X_{4C}}$	-4.1%	-63.8%
$F_{X_{4S}}$	1.4%	-21.3%
$F_{Y_{4C}}$	20.1%	-15.4%
$F_{Y_{4S}}$	13.6%	-67.9%
	Pitch Maneuvering Flight	
$F_{X_{4C}}$	-1.8%	-46.4%
$F_{X_{4S}}$	-59.9%	-51.1%
$F_{Y_{4C}}$	43.5%	9.7%
$F_{Y_{4S}}$	13.0%	-40.8%
Average	**3.2%**	**-37.1%**

Normalized relative to the baseline RMS

Table 5.5: Vibration RMS with respect to piloted roll and pitch inputs.

	Nominal T-matrix Controller	Optimized Lead-Lag Controller
K_{3p}	1.000	1.153
K_{4p}	1.000	1.663
K_{5p}	1.000	1.236
ω_{n3}		1.463
ω_{n4}		5.253
ω_{n5}		2.848
ζ_{n3}		2.539
ζ_{n4}		0.583
ζ_{n5}		1.246
ω_{d3}		6.900
ω_{d4}		5.627
ω_{d5}		6.787
ζ_{d3}		3.494
ζ_{d4}		1.207
ζ_{d5}		1.179

Table 5.6: HHC controller parameters.

Broken-Loop Channel	ω_c (rad/sec)	Gain Margin (dB)	Phase Margin (deg)
3/rev COS	2.46	8.2	74.6
3/rev SIN	2.71	6.0	78.6
4/rev COS	1.52	17.6	52.8
4/rev SIN	1.45	18.0	55.5
5/rev COS	1.80	6.0	99.6
5/rev SIN	1.33	6.6	102.3

Table 5.7: HHC Broken-loop Stability Margins; optimized HHC controller.

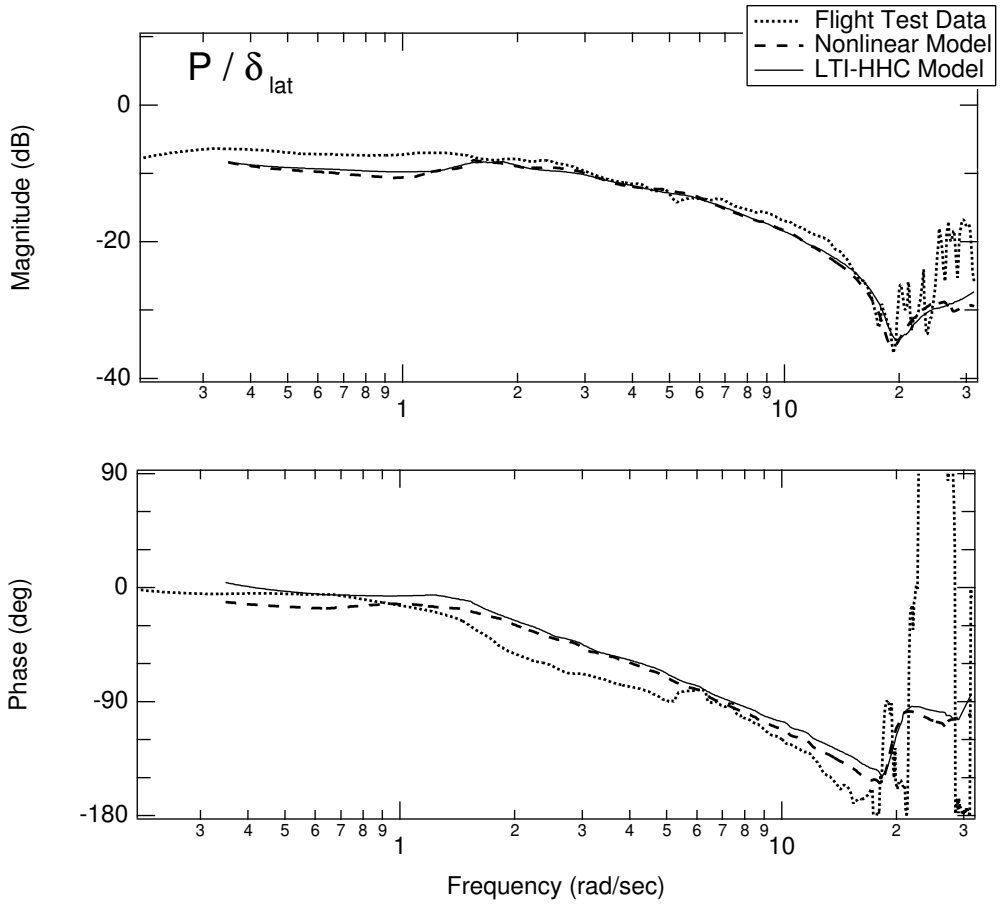

Figure 5.1: Analytic model validation, baseline (HHC-off) case.

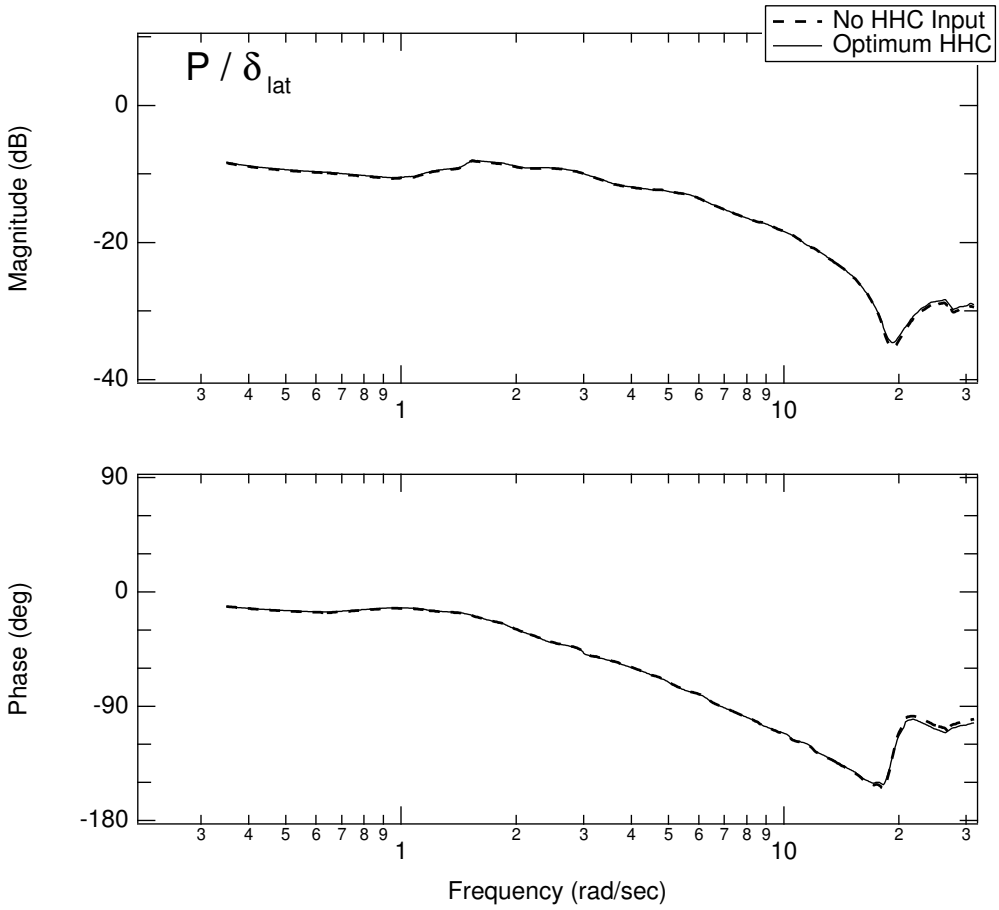

Figure 5.2: Effect of HHC input on rigid body dynamics, nonlinear model.

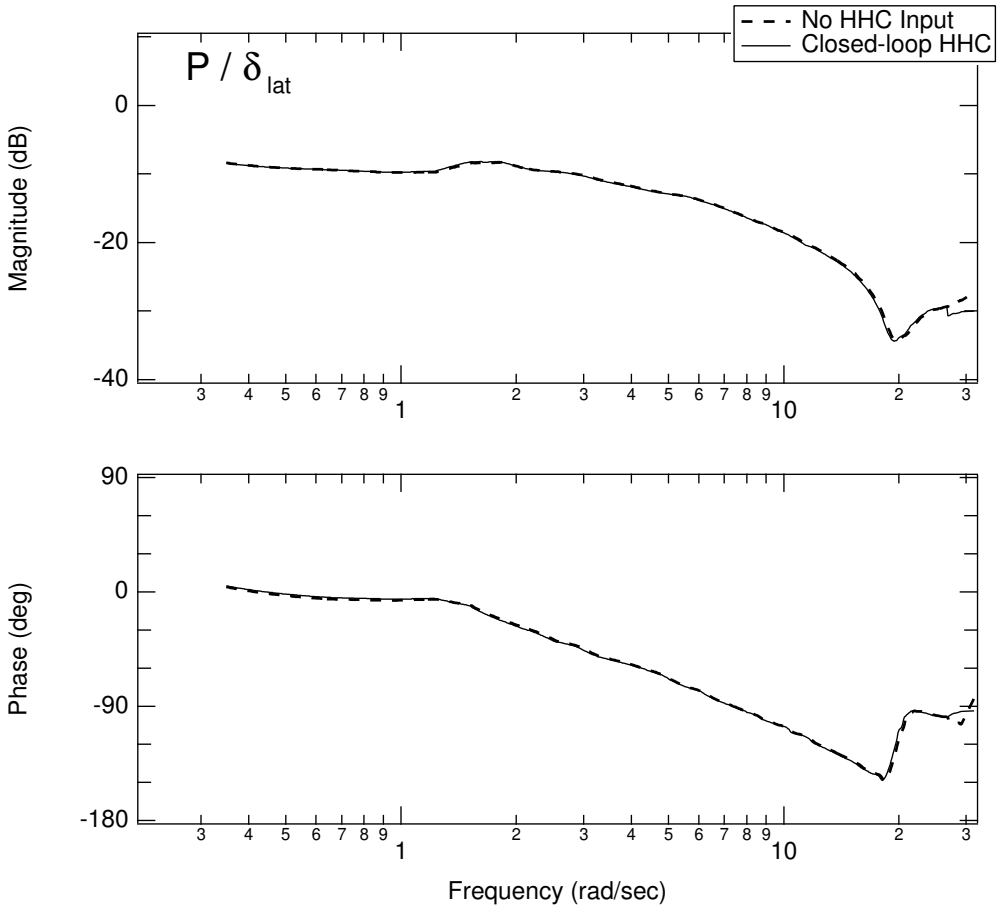

Figure 5.3: Effect of HHC input on rigid body dynamics, LTI-HHC model.

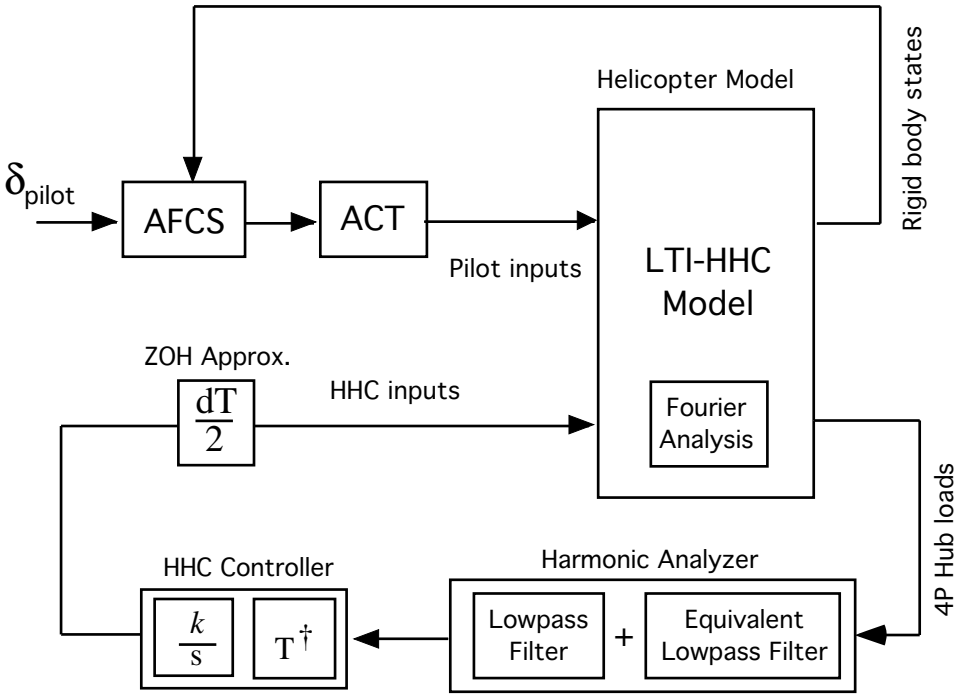

Figure 5.4: General Closed-loop HHC vibration reduction scheme.

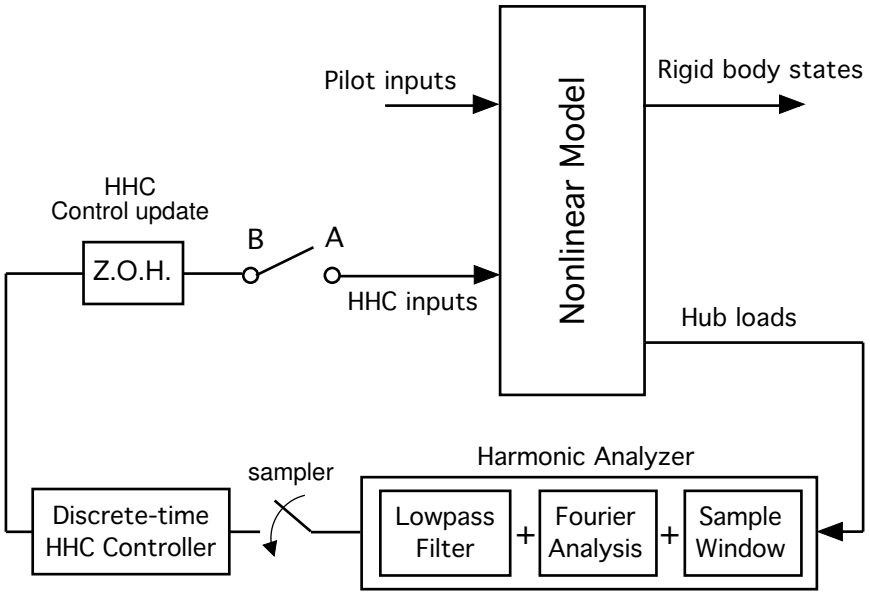

(a) Nonlinear Model (Multi-rate system)

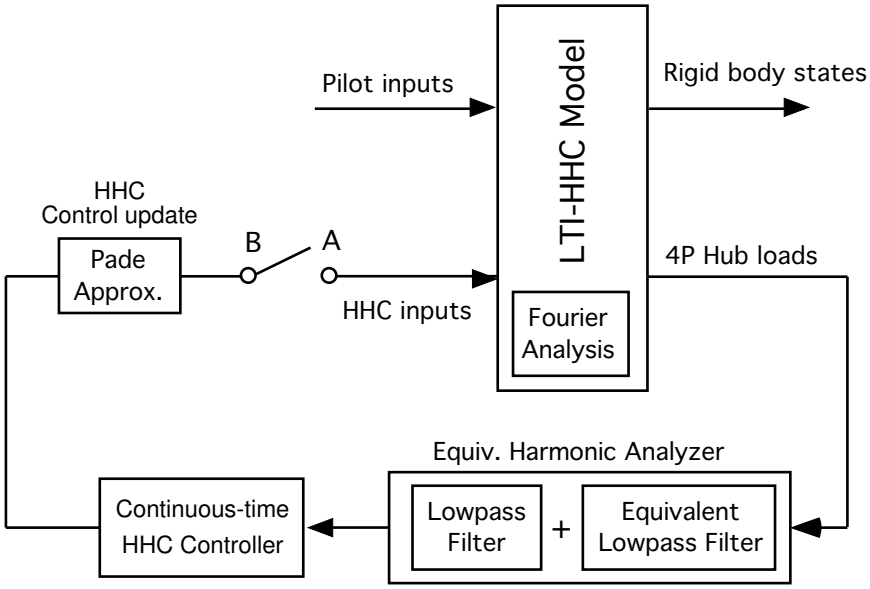

(b) LTI-HHC Model (Continuous time-domain system)

Figure 5.5: Closed-loop HHC systems comparison.

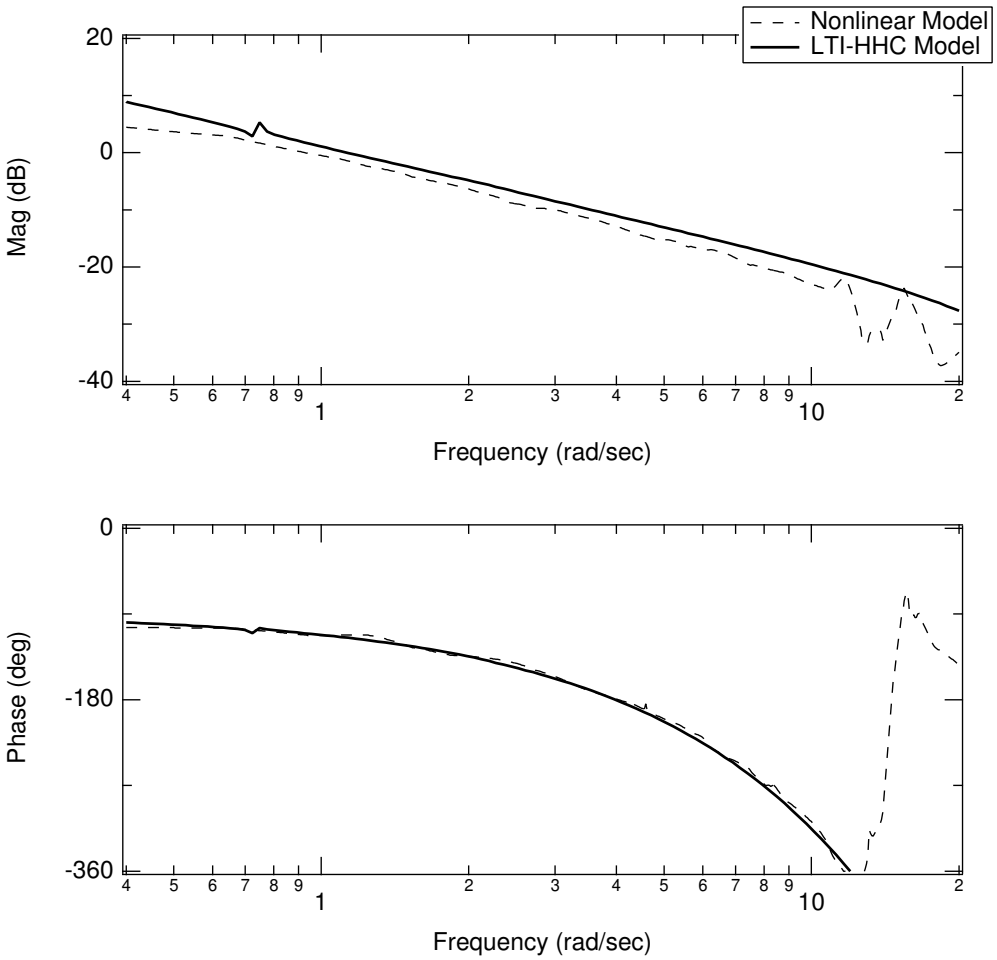

Figure 5.6: θ_{3c} Broken-loop responses comparison.

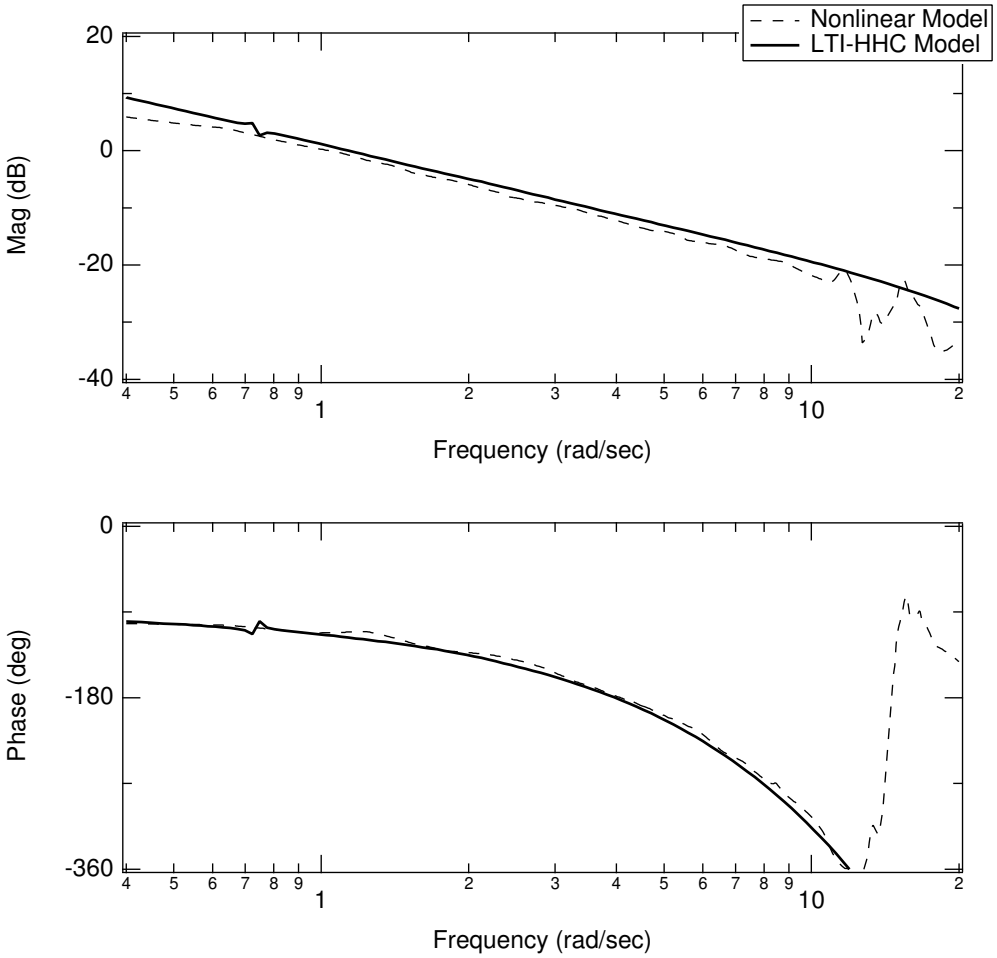

Figure 5.7: θ_{3s} Broken-loop responses comparison.

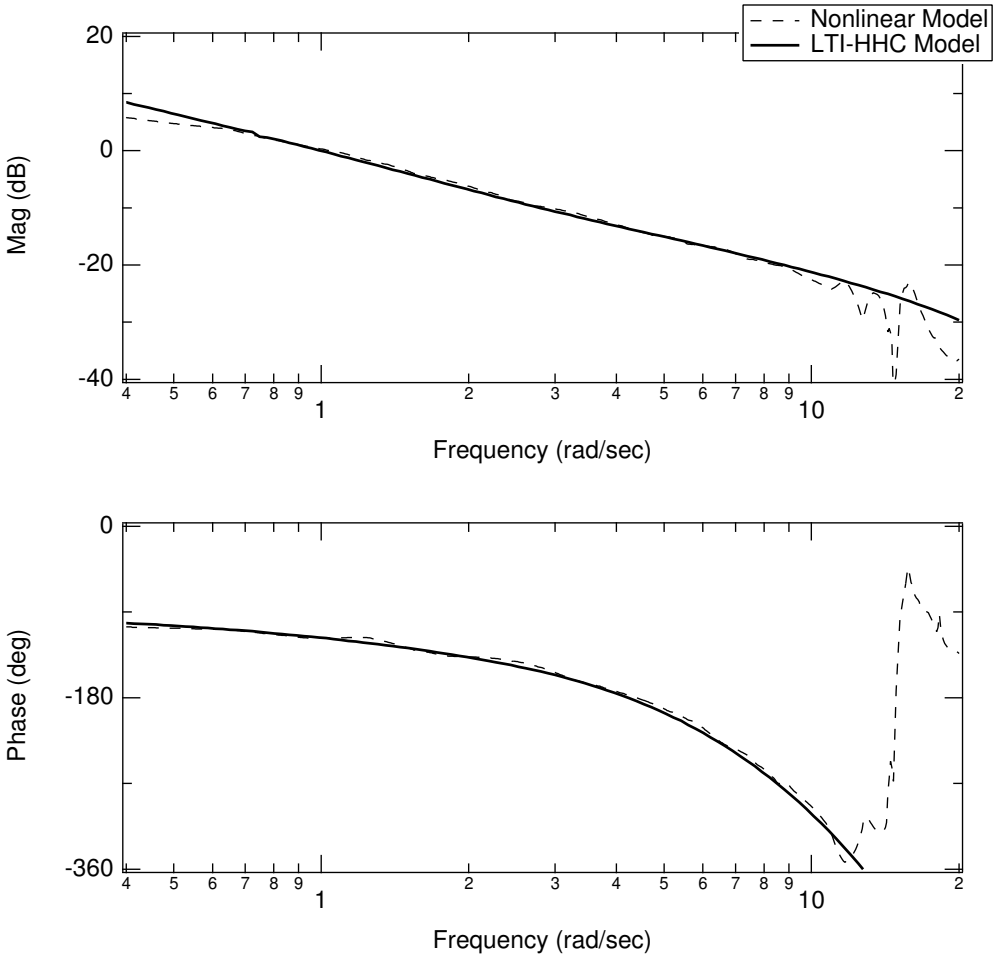

Figure 5.8: θ_{4c} Broken-loop responses comparison.

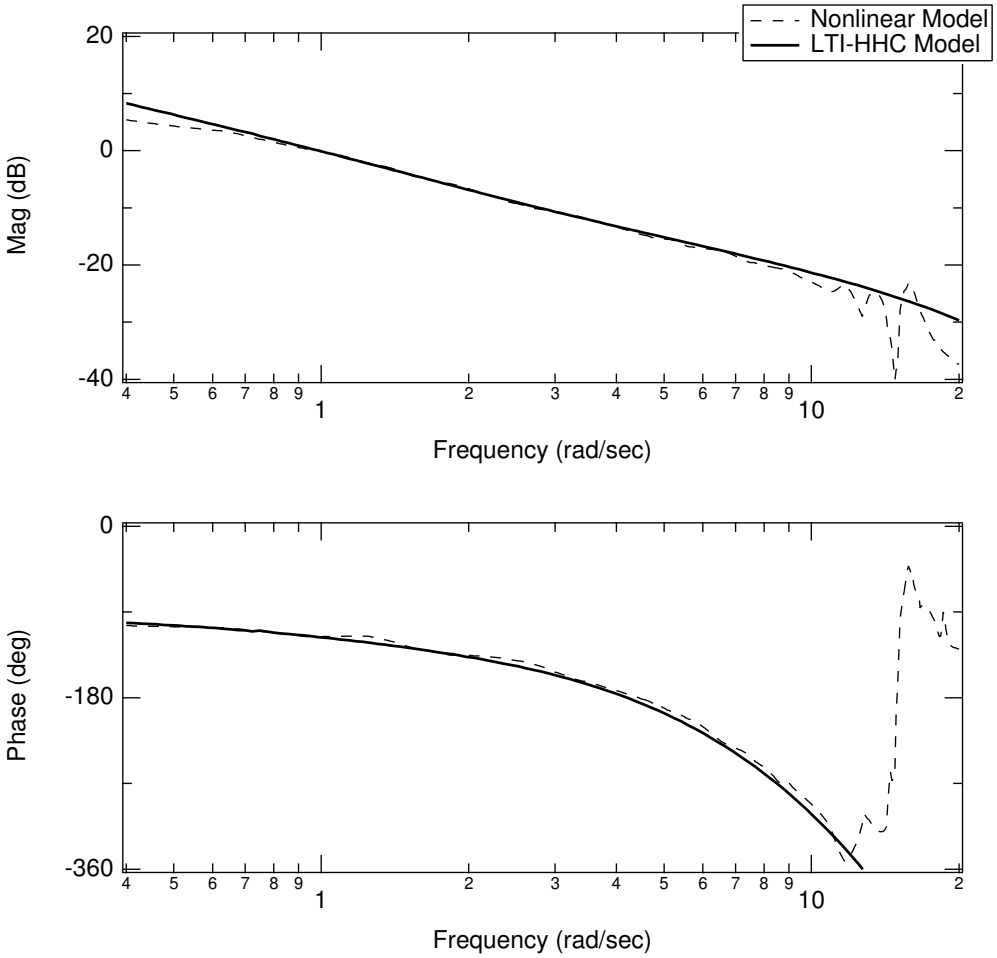

Figure 5.9: θ_{4s} Broken-loop responses comparison.

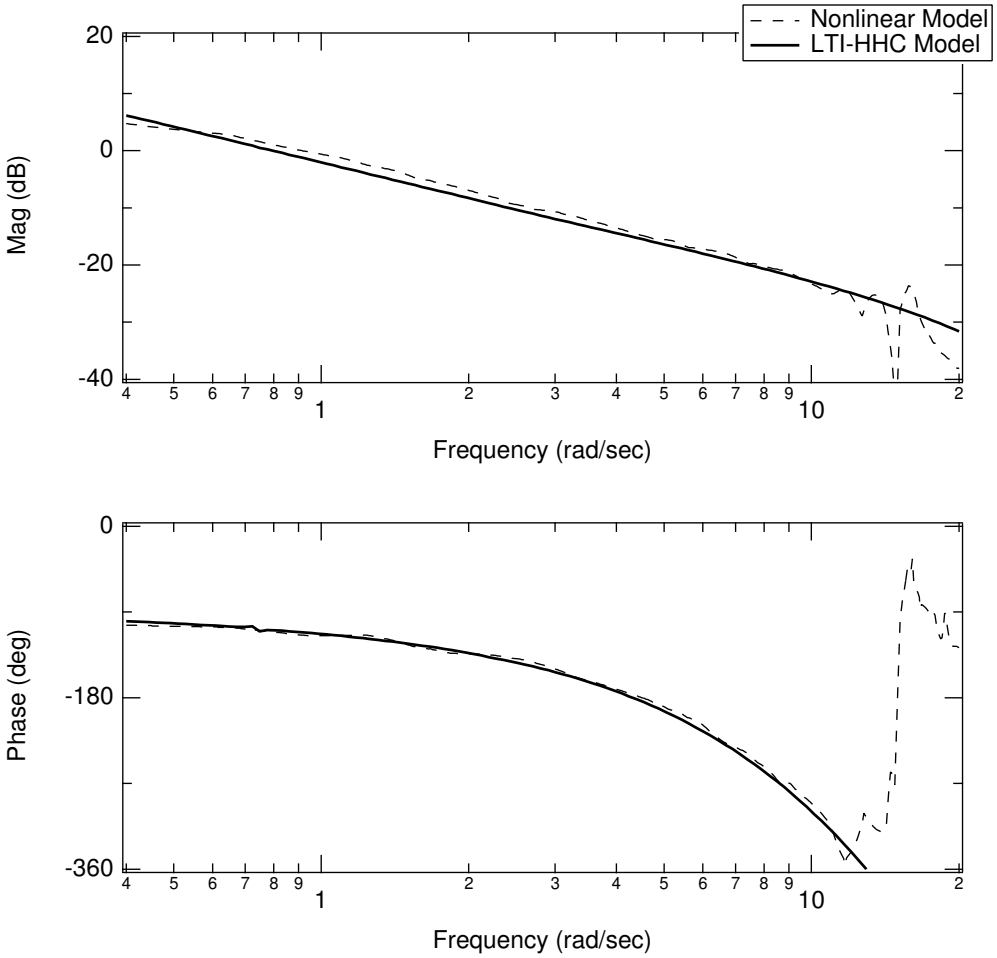

Figure 5.10: θ_{5c} Broken-loop responses comparison.

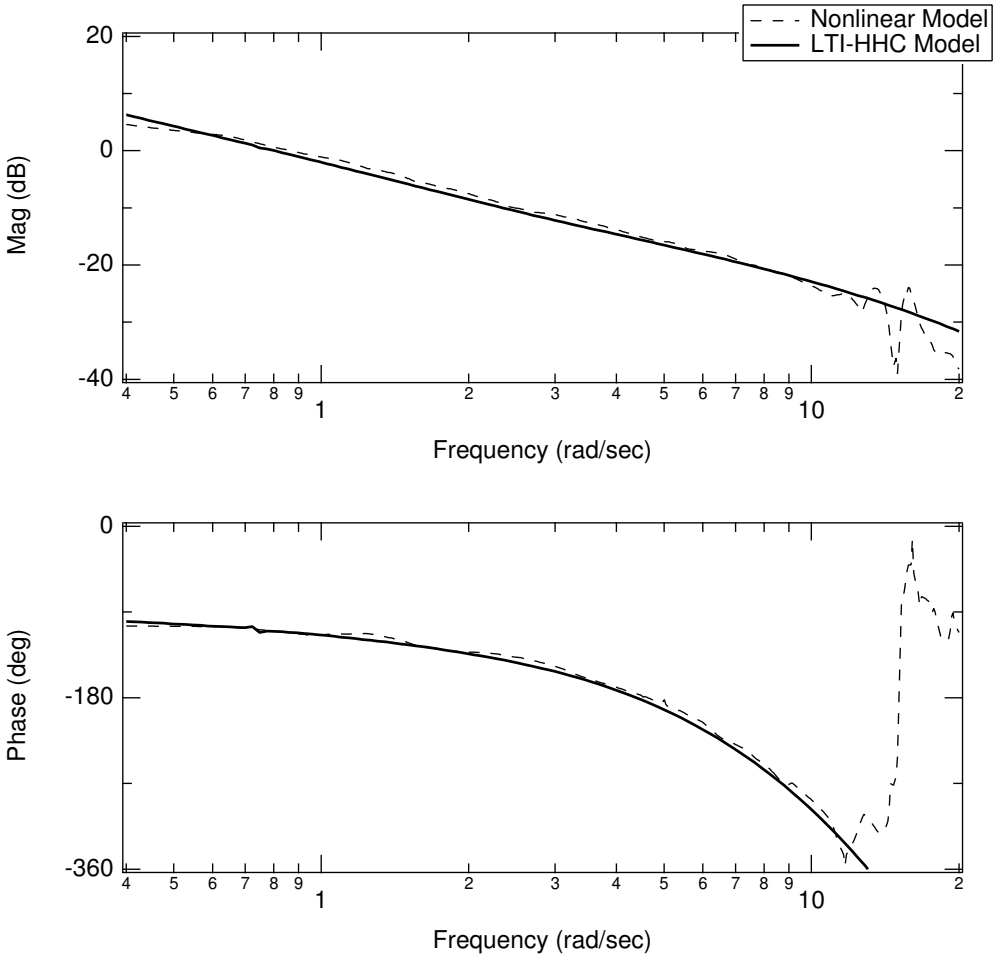

Figure 5.11: θ_{5s} Broken-loop responses comparison.

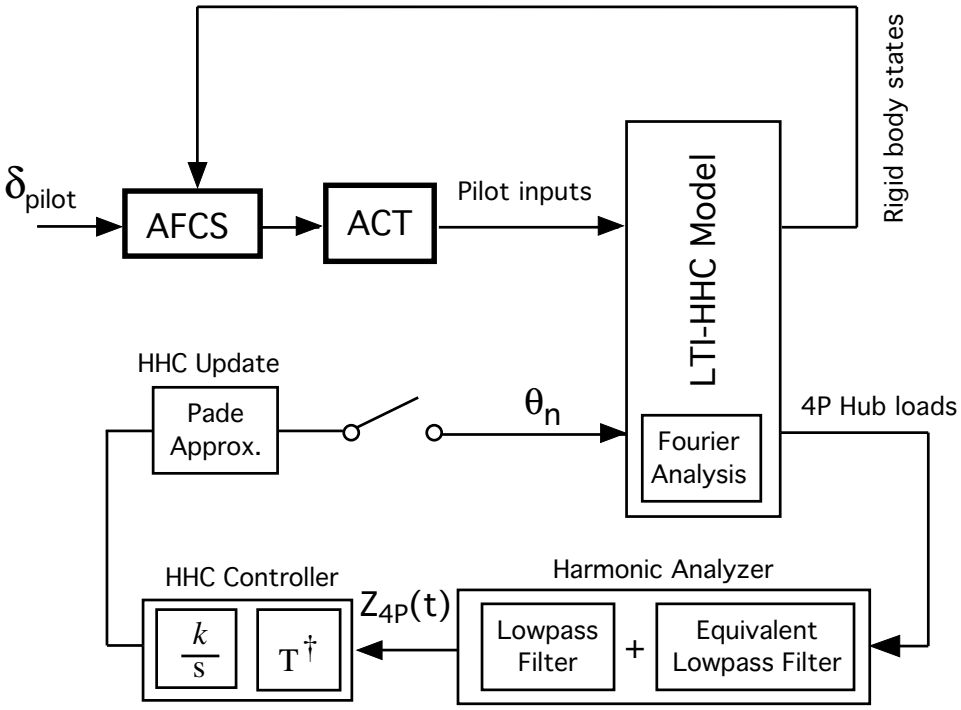

Figure 5.12: HHC vibration reduction system, HHC-loops disengaged.

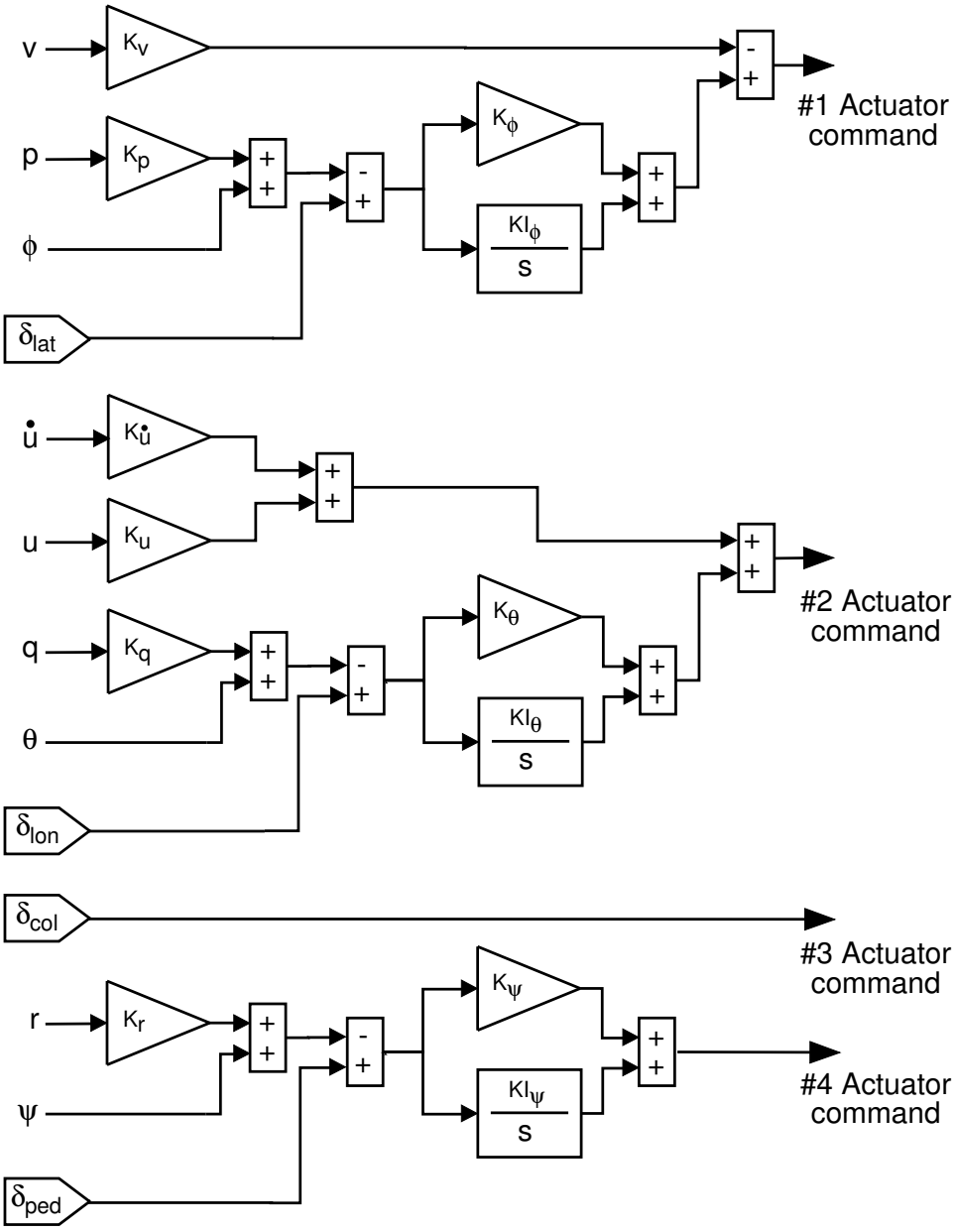

Figure 5.13: Automatic flight control system schematics.

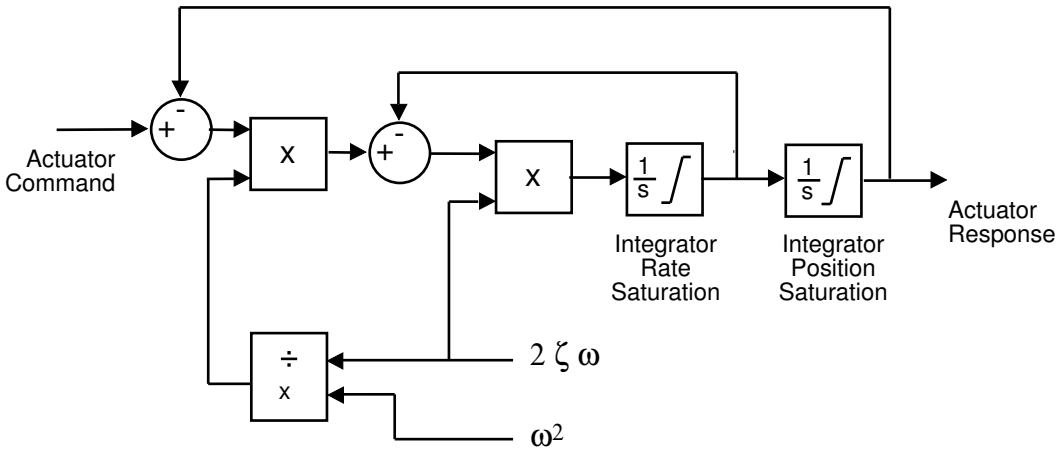

Figure 5.14: Second order actuator schematics.

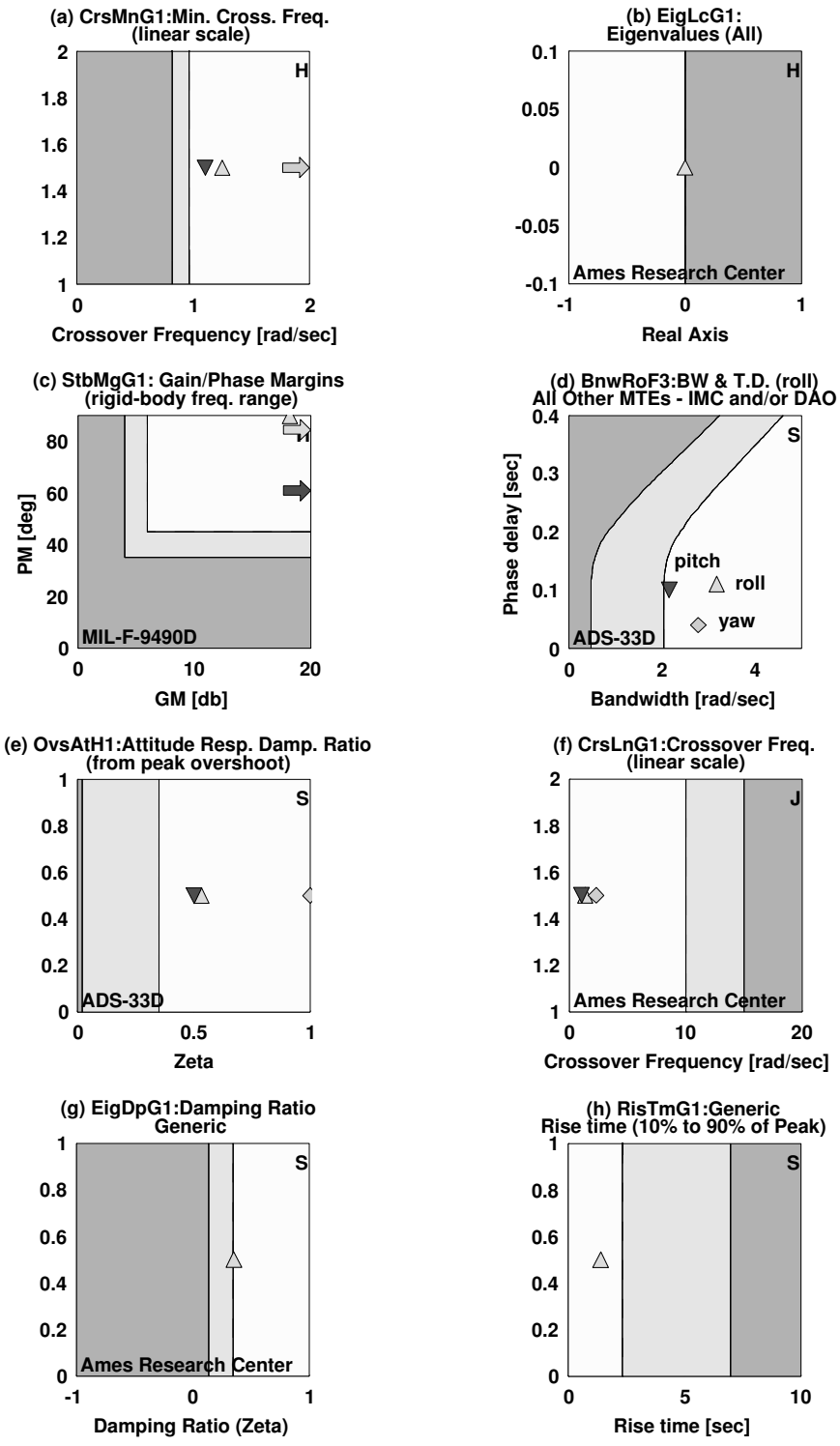

Figure 5.15: CONDUIT® handling-quality design specifications; HHC-loops disengaged.

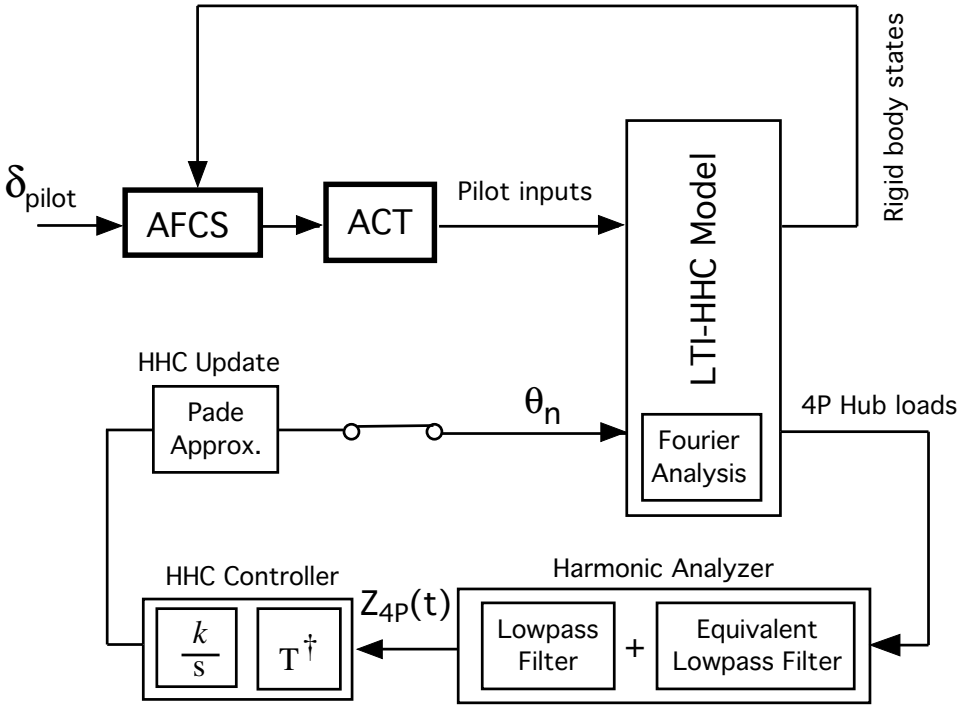

Figure 5.16: HHC vibration reduction system, HHC-loops engaged (k=1).

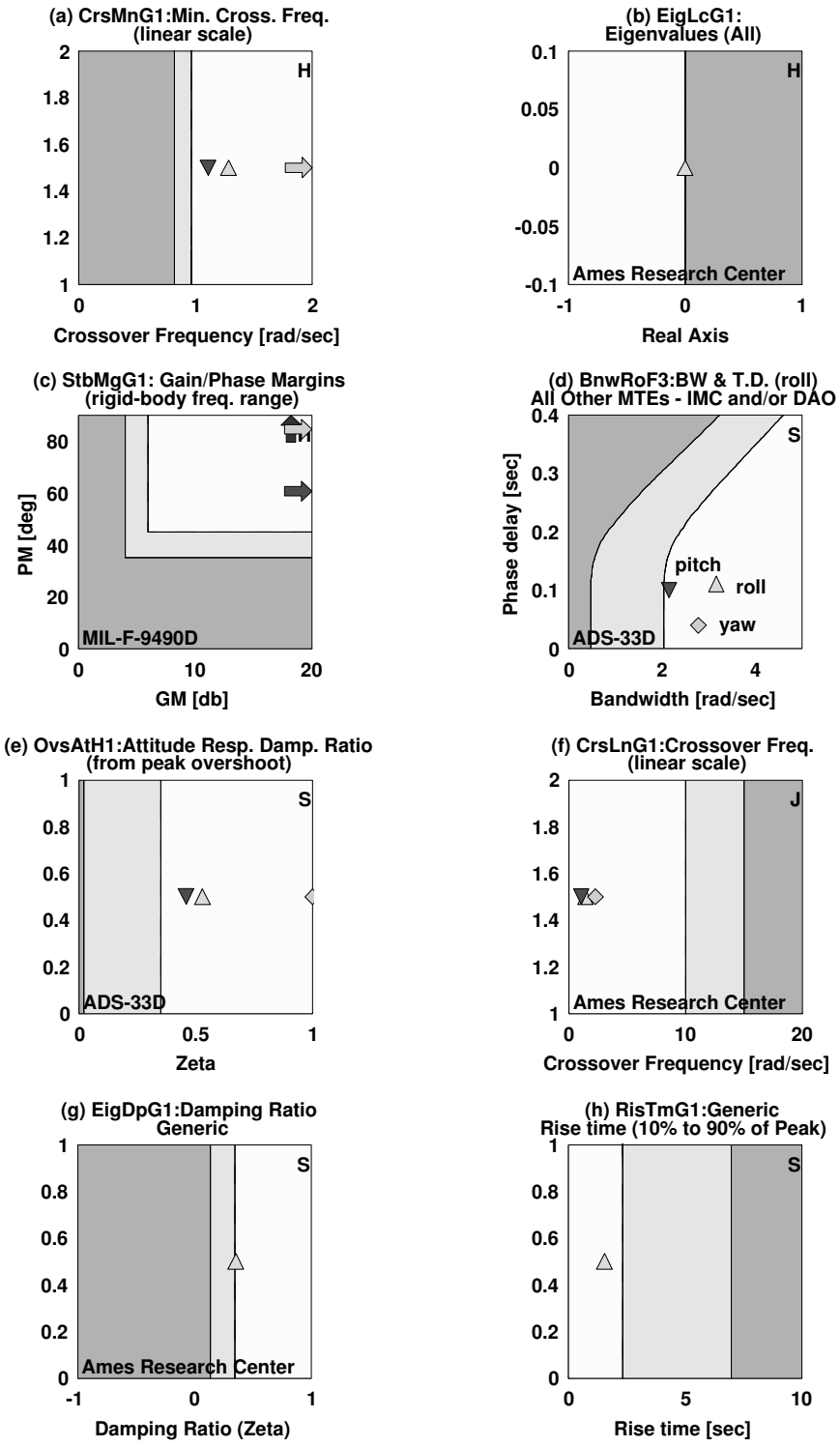

Figure 5.17: CONDUIT® handling-quality design specifications; HHC-loops engaged (k=1).

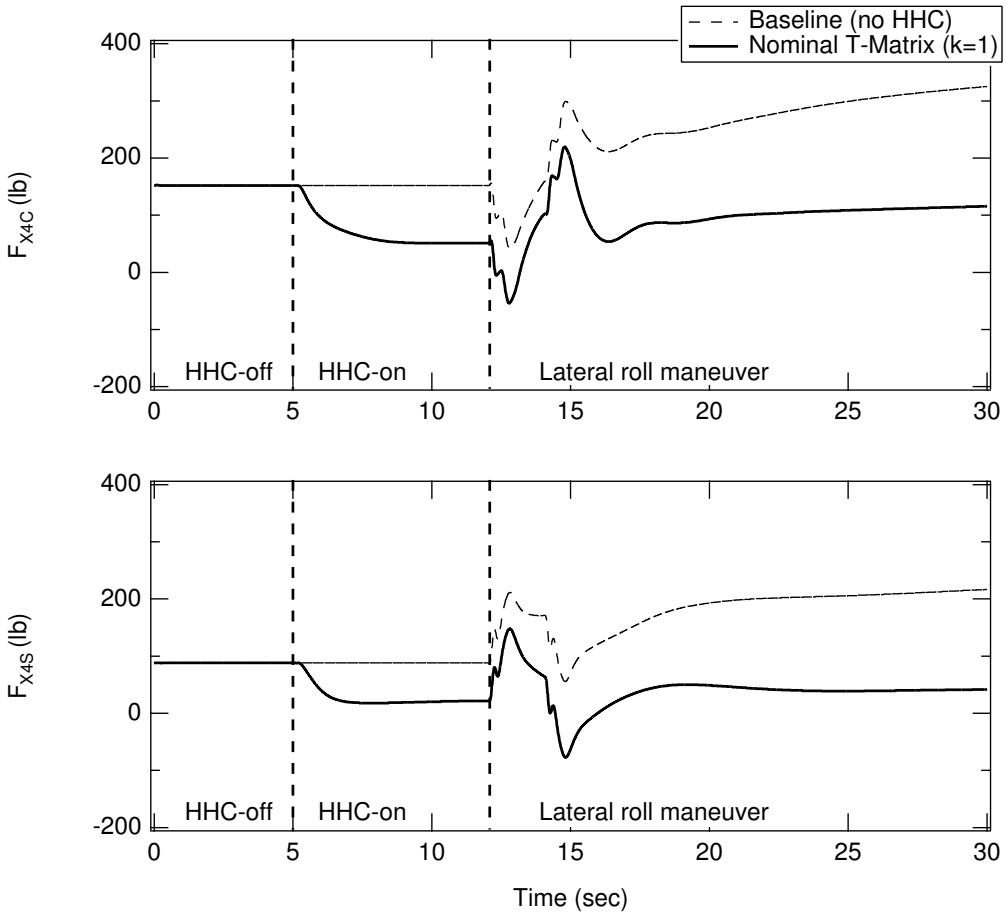

Figure 5.18: F_X vibration response in roll maneuvering flight, T-matrix controller, nominal case (k=1).

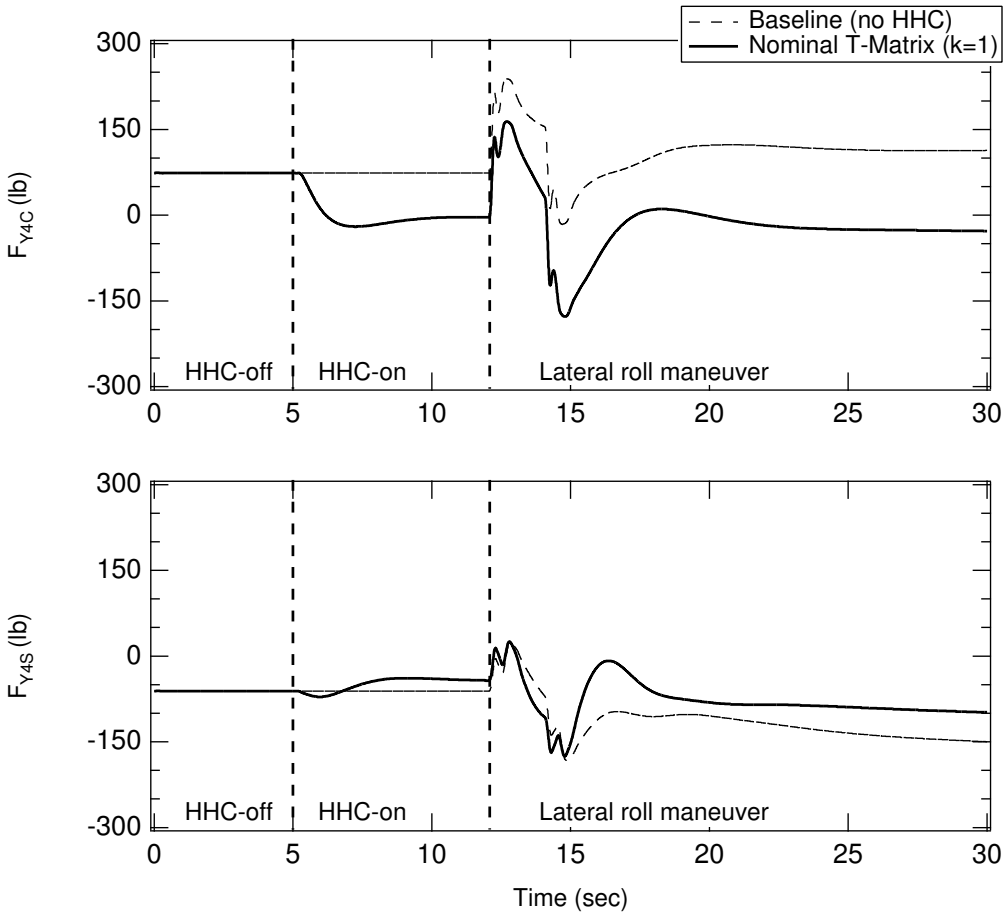

Figure 5.19: F_Y vibration response in roll maneuvering flight, T-matrix controller, nominal case (k=1).

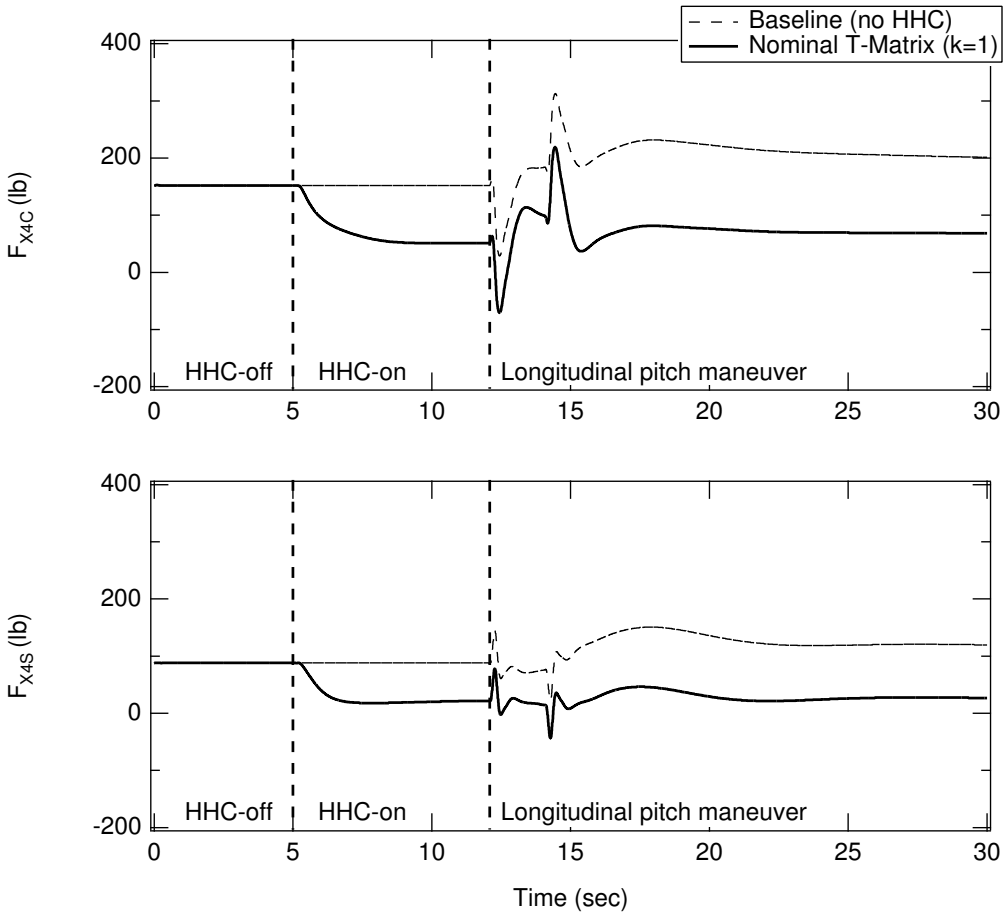

Figure 5.20: F_X vibration response in pitch maneuvering flight, T-matrix controller, nominal case (k=1).

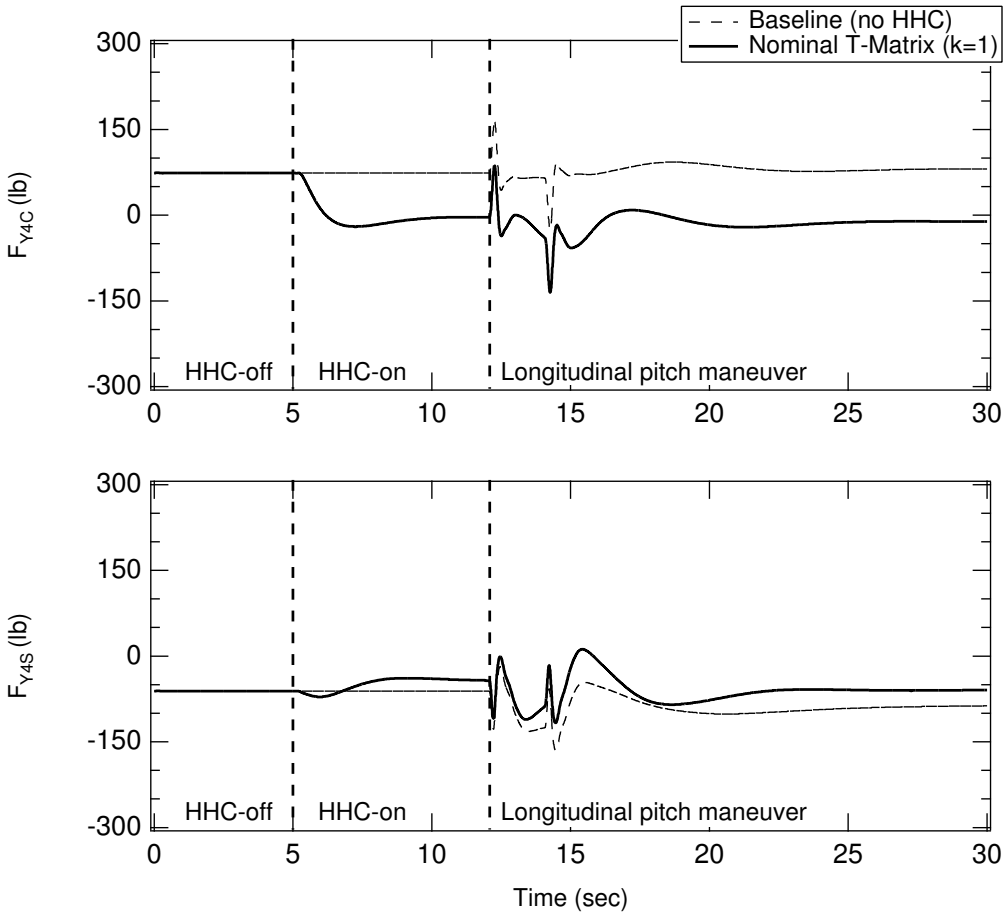

Figure 5.21: F_Y vibration response in pitch maneuvering flight, T-matrix controller, nominal case (k=1).

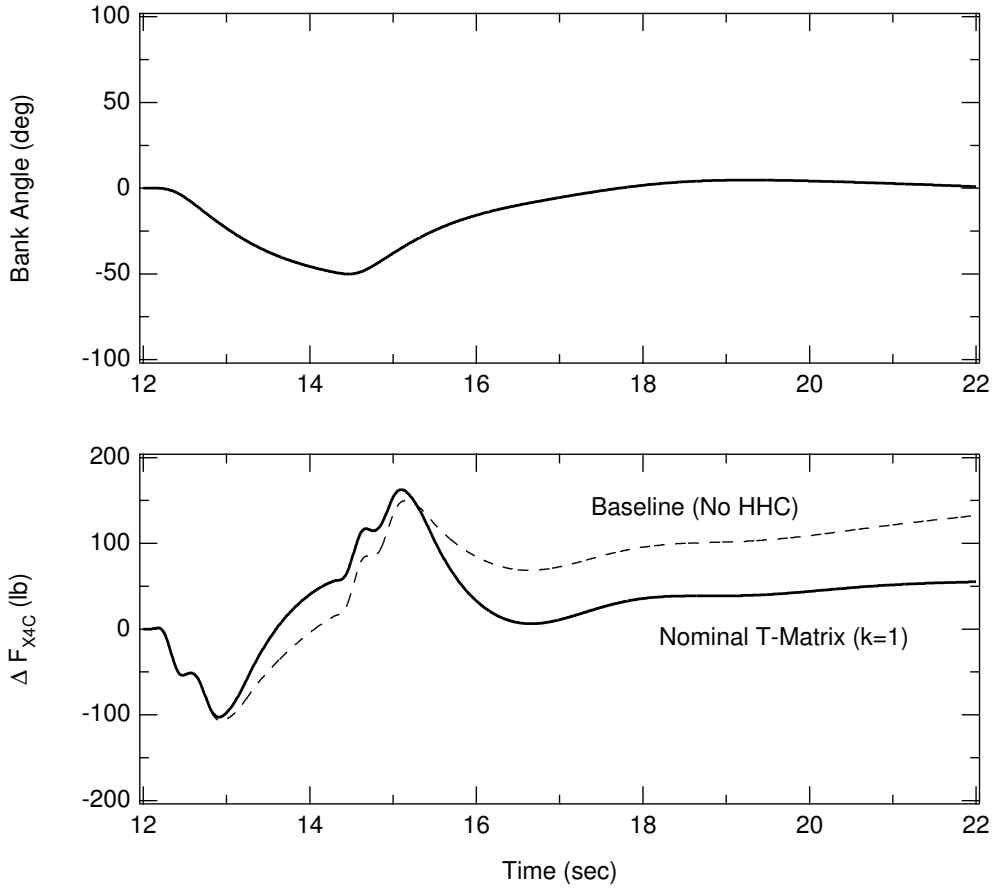

Figure 5.22: $F_{X_{4C}}$ vibration response in roll maneuvering flight, T-matrix controller, nominal case (k=1).

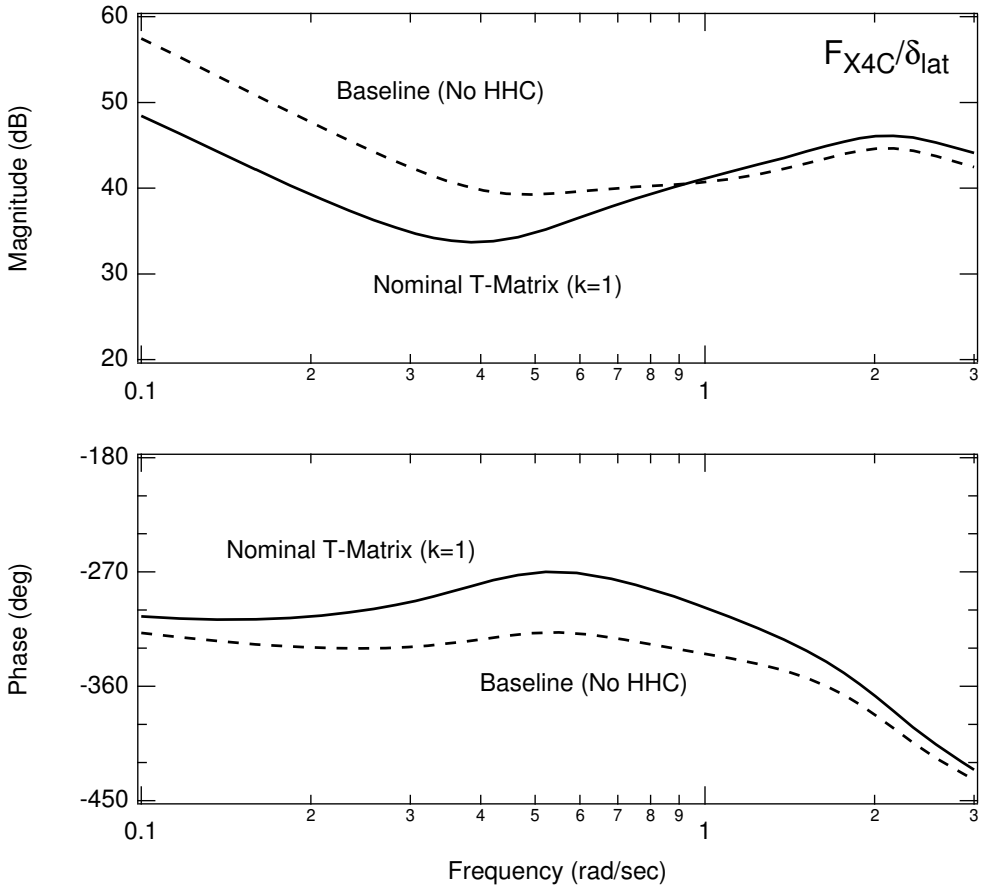

Figure 5.23: $F_{X_{4C}}$ vibration response in roll maneuvering flight, T-matrix controller, nominal case (k=1).

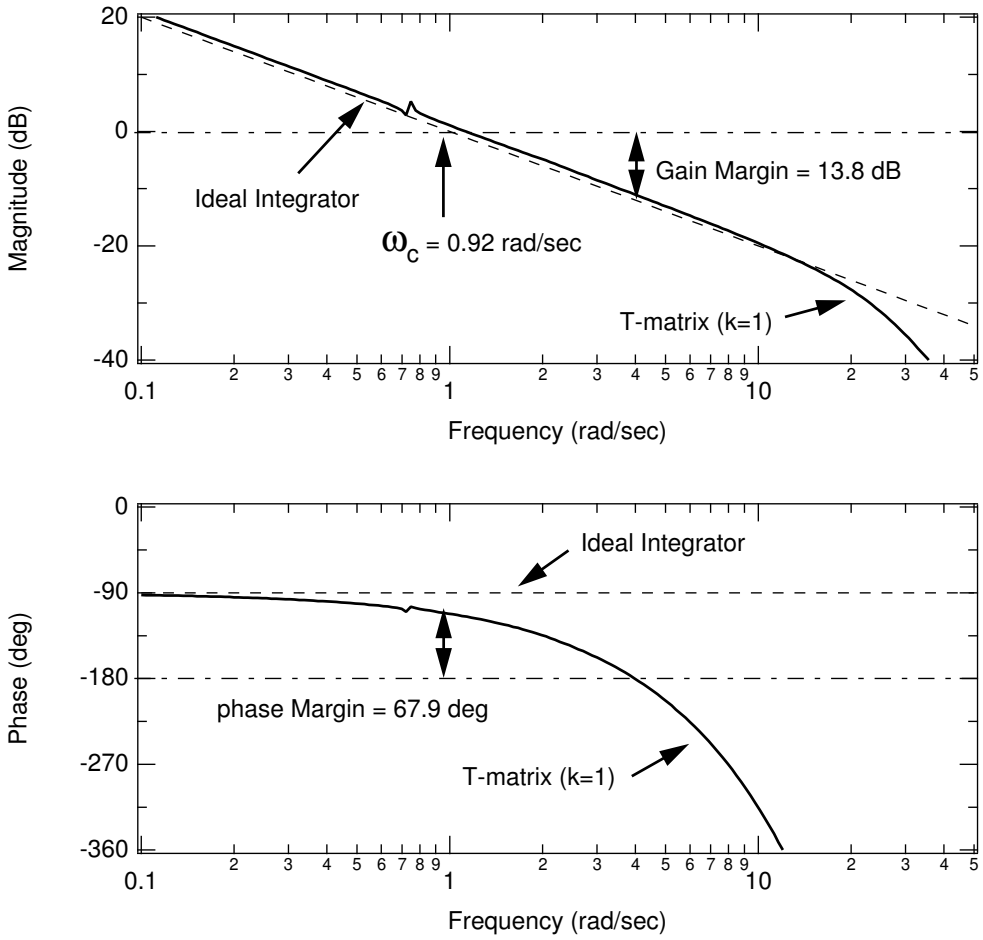

Figure 5.24: Ideal and actual broken-loop responses comparison, 3/rev-cosine loop, nominal T-matrix controller case.

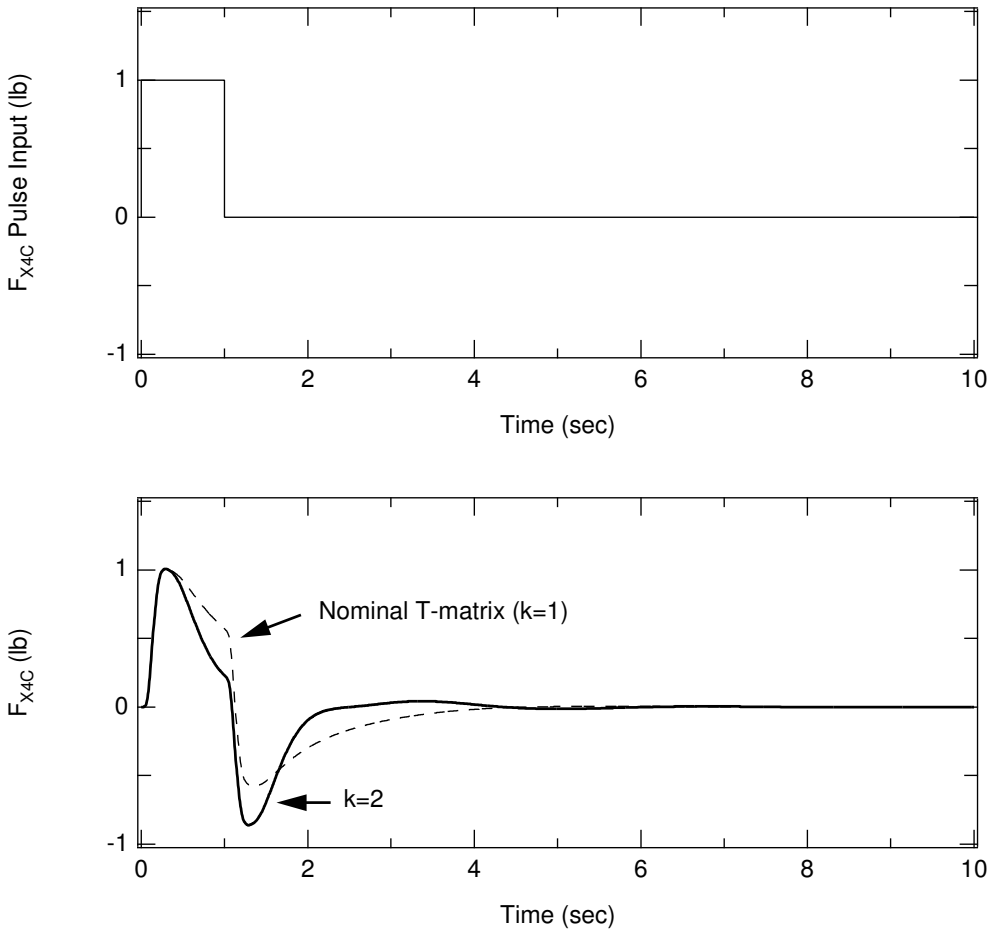

Figure 5.25: $F_{X_{4C}}$ unit pulse response; T-matrix controller, k=1 and 2.

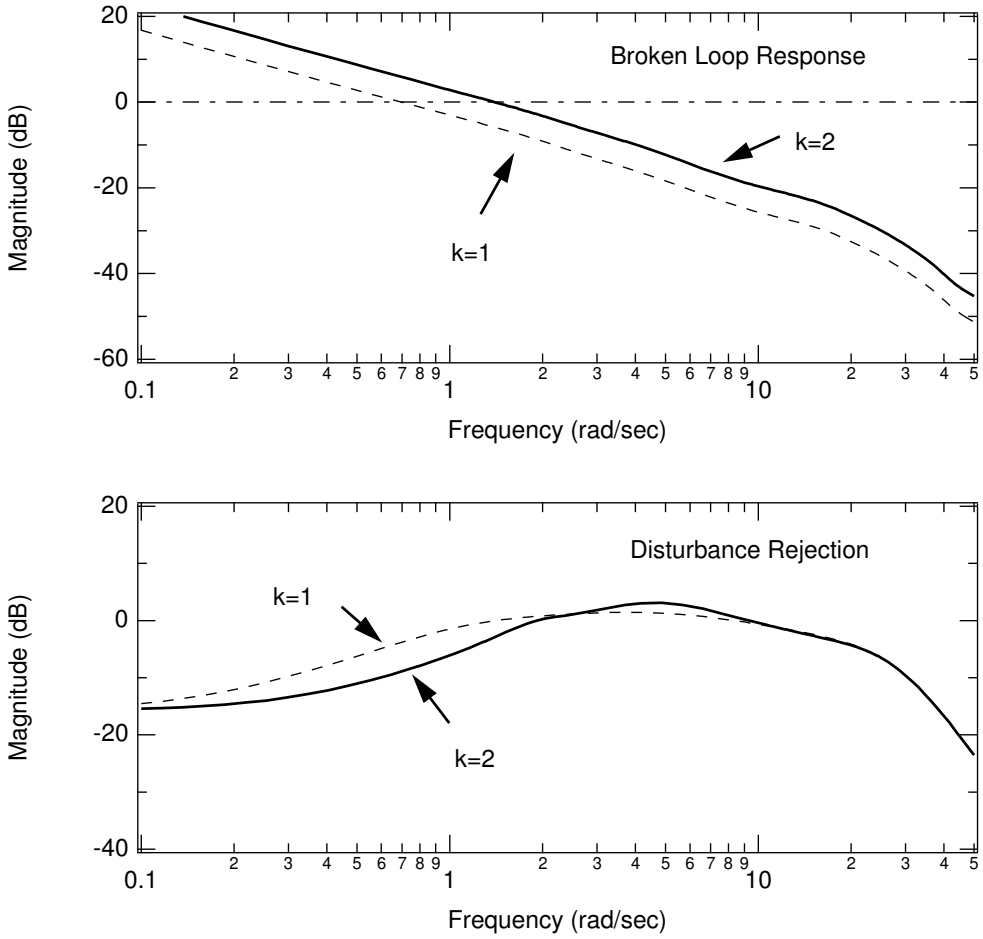

Figure 5.26: Broken-loop response of 3/rev input; T-matrix controller, k=1 and 2.

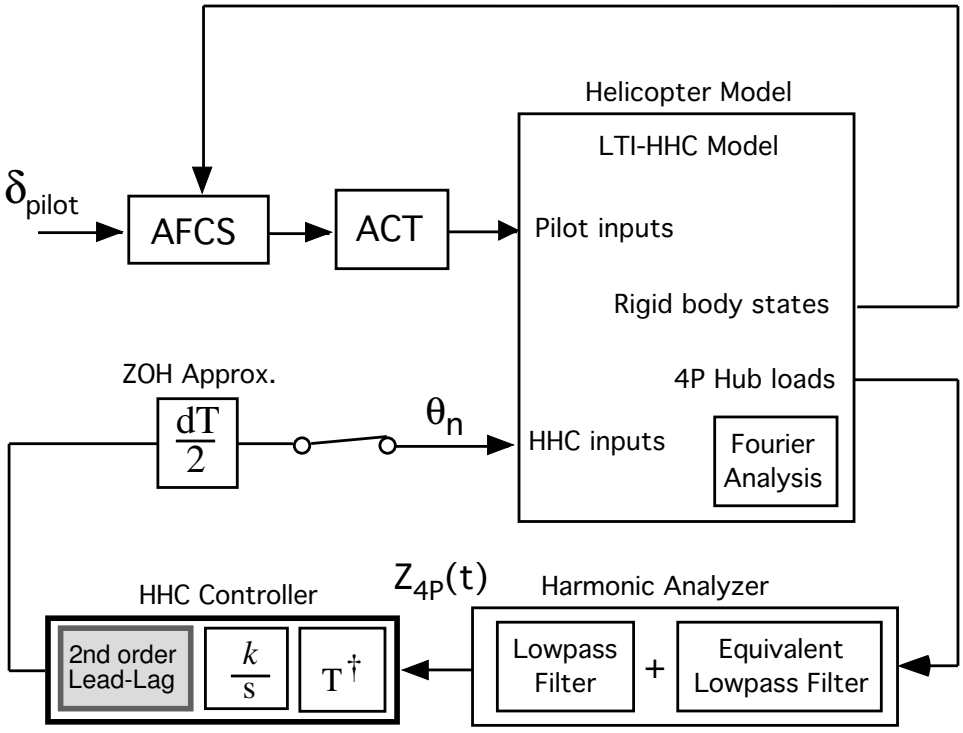

Figure 5.27: HHC vibration reduction system, HHC-loops engaged, optimized lead-lag compensator.

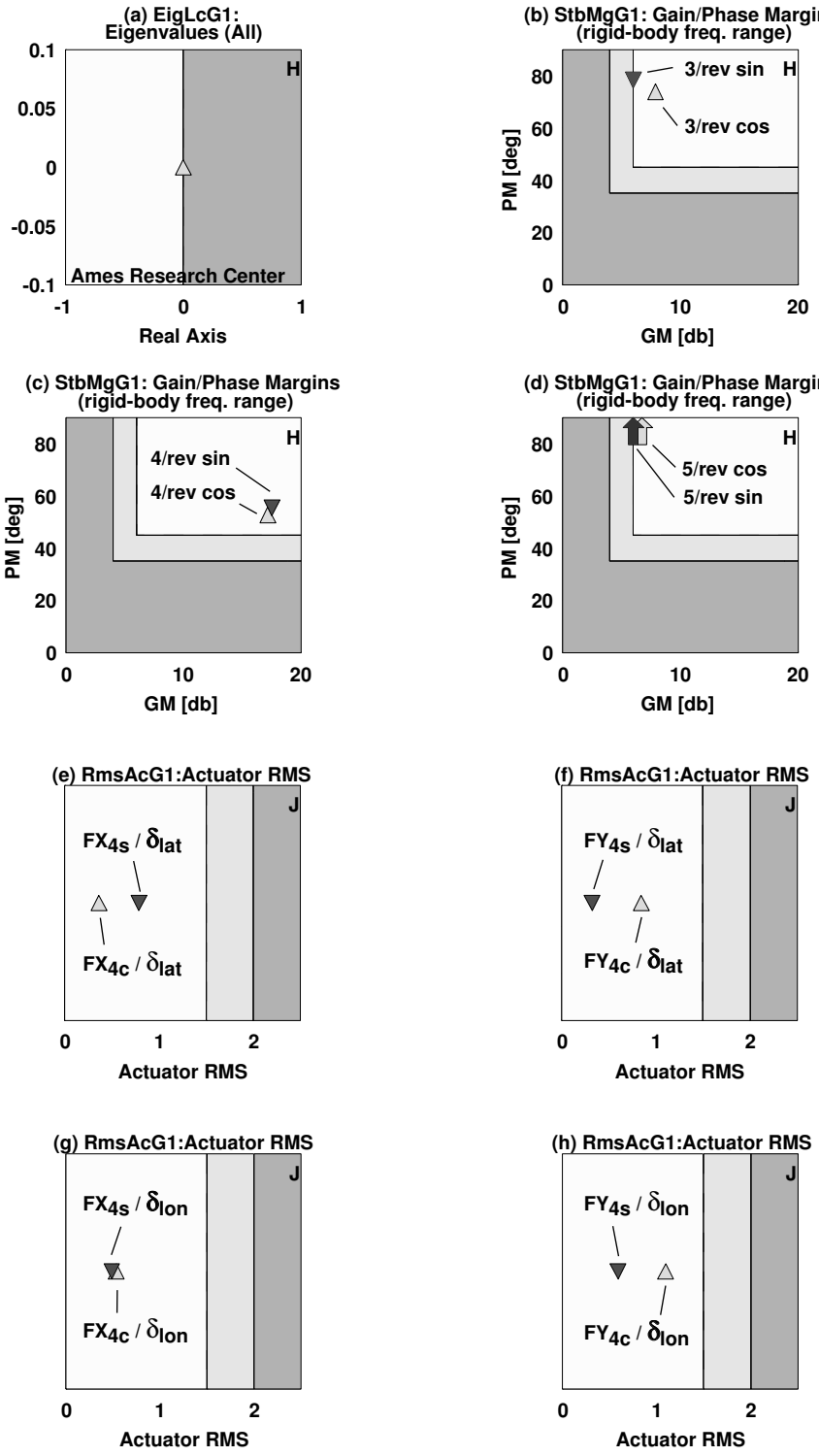

Figure 5.28: CONDUIT® HHC design specifications; HHC-loops engaged, optimized lead-lag compensator.

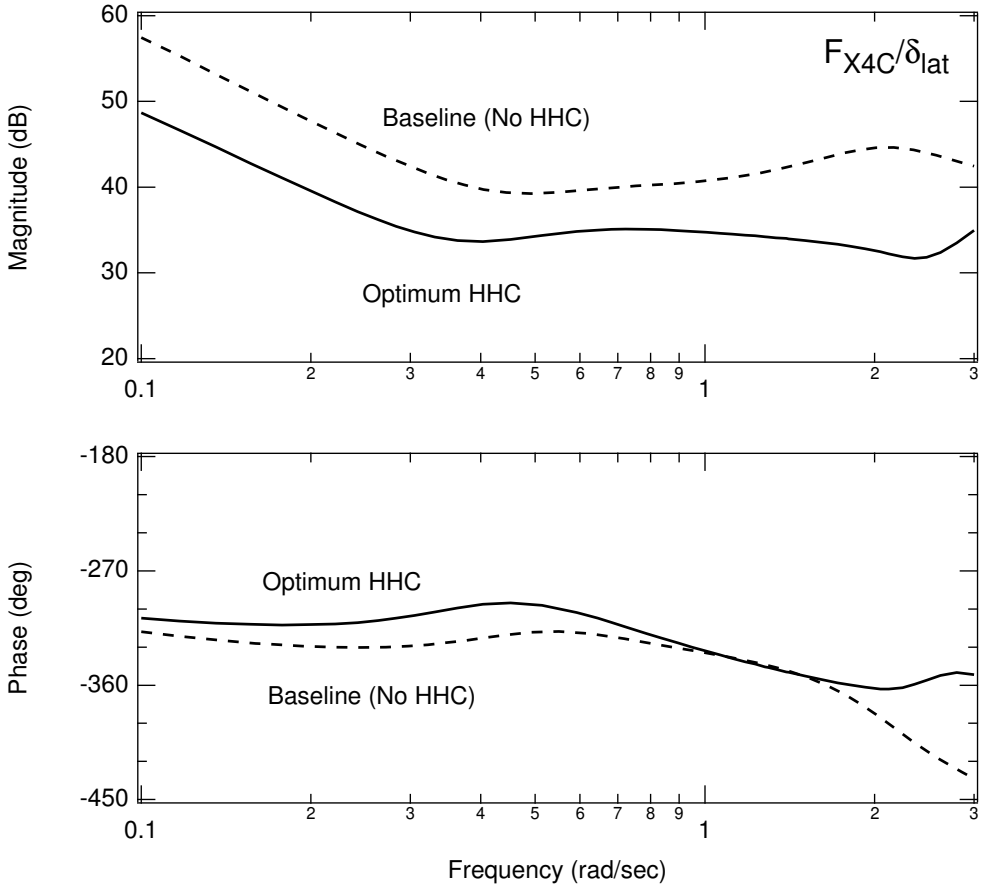

Figure 5.29: $F_{X_{4C}}$ vibration response in roll maneuvering flight, optimized lead-lag compensator.

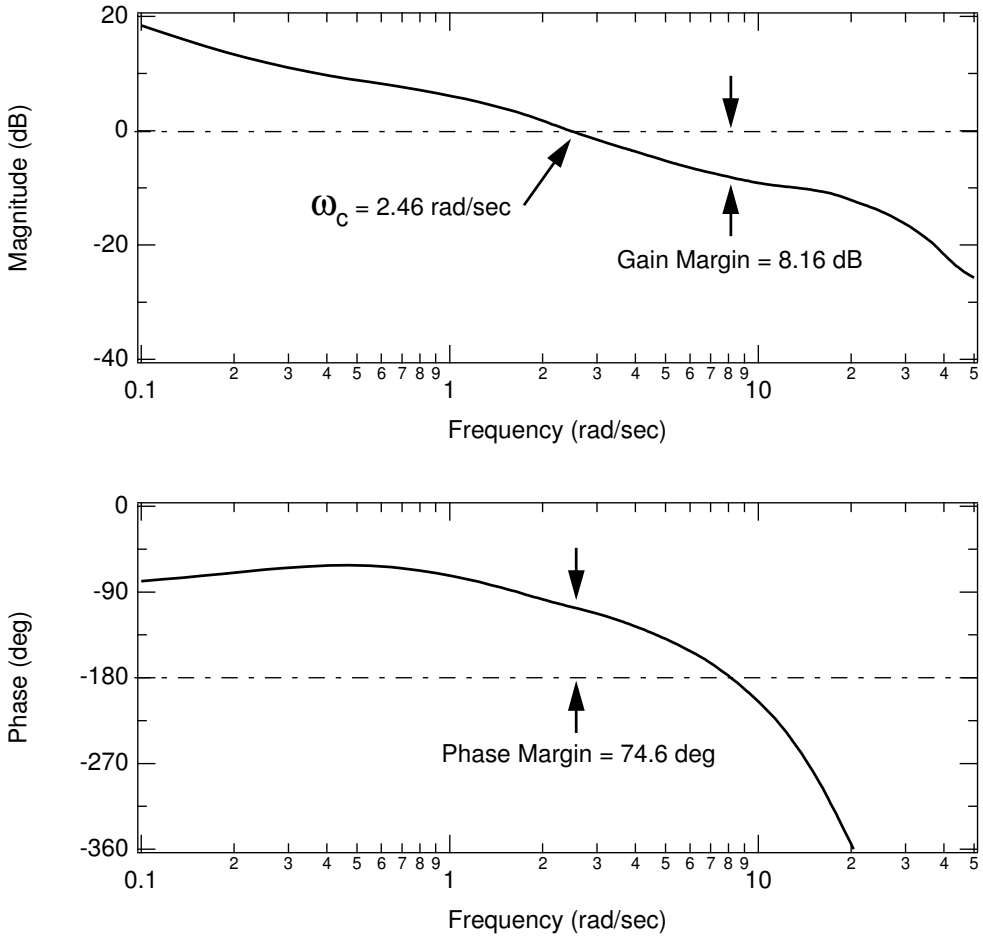

Figure 5.30: Broken-loop response of 3/rev input; optimized lead-lag compensator.

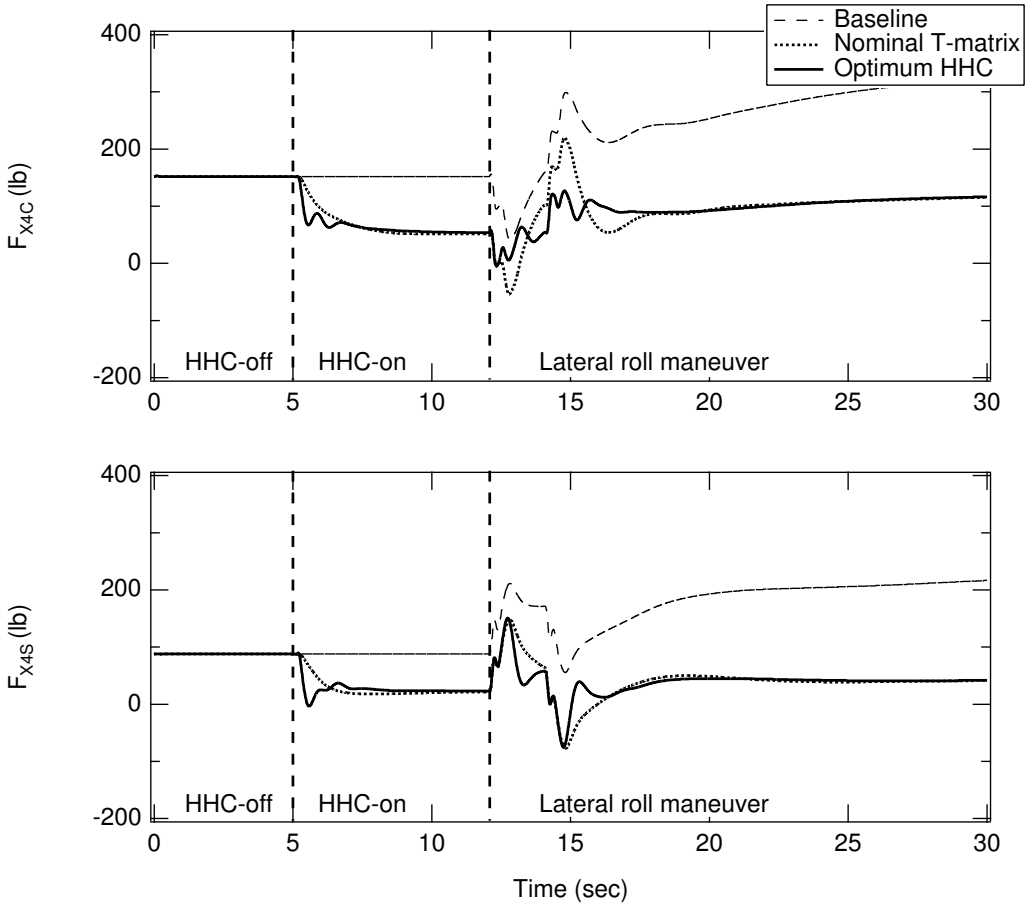

Figure 5.31: F_X vibration response in roll maneuvering flight; optimized lead-lag compensator.

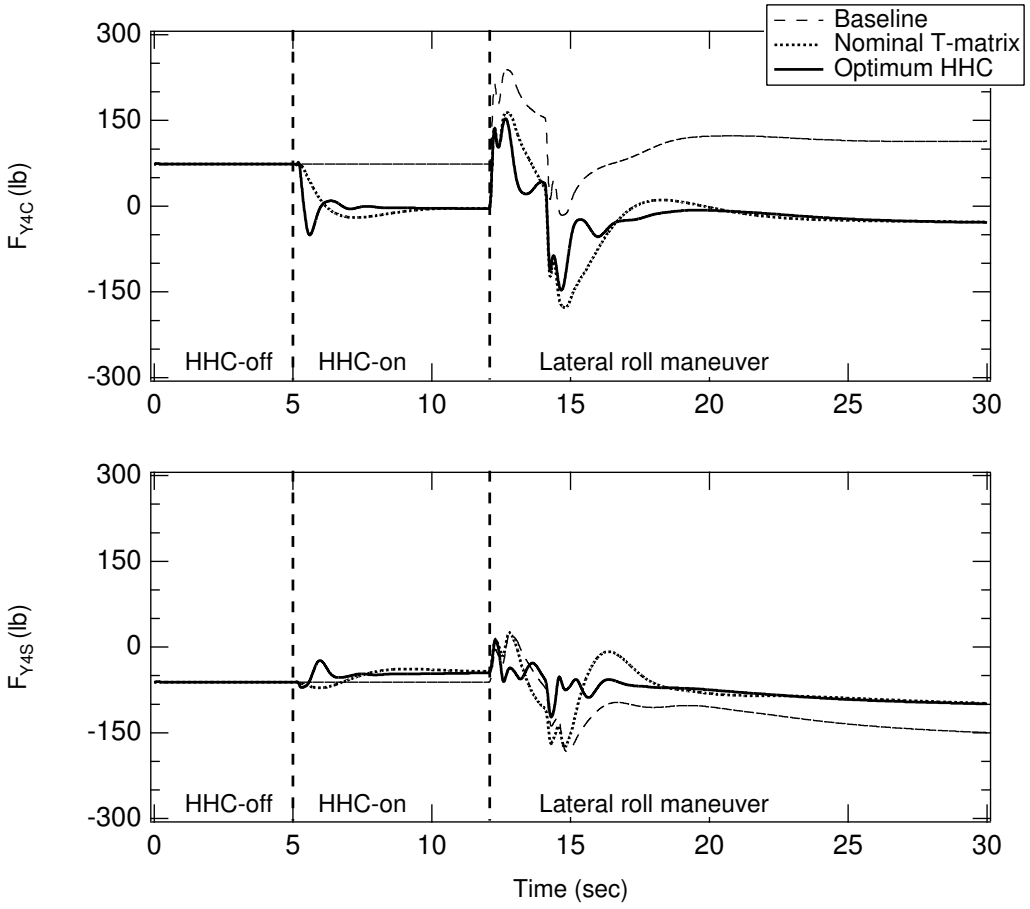

Figure 5.32: F_Y vibration response in roll maneuvering flight; optimized lead-lag compensator.

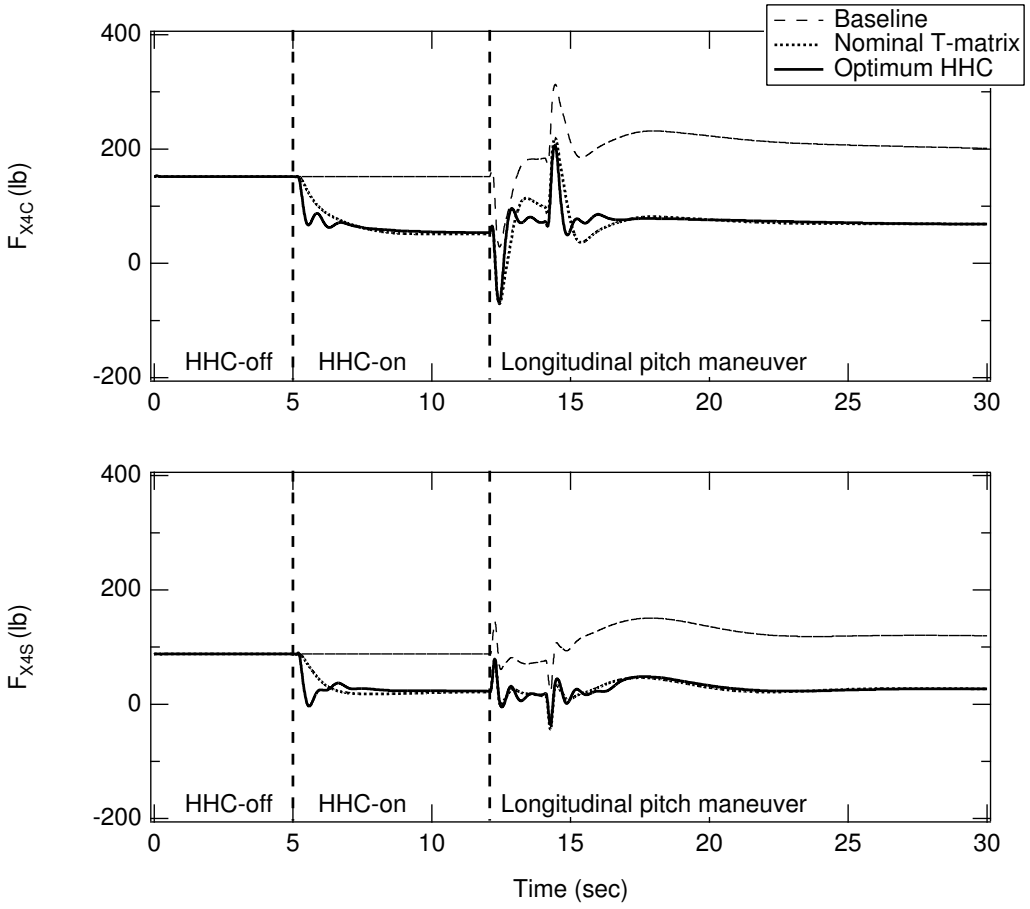

Figure 5.33: F_X vibration response in pitch maneuvering flight; optimized lead-lag compensator.

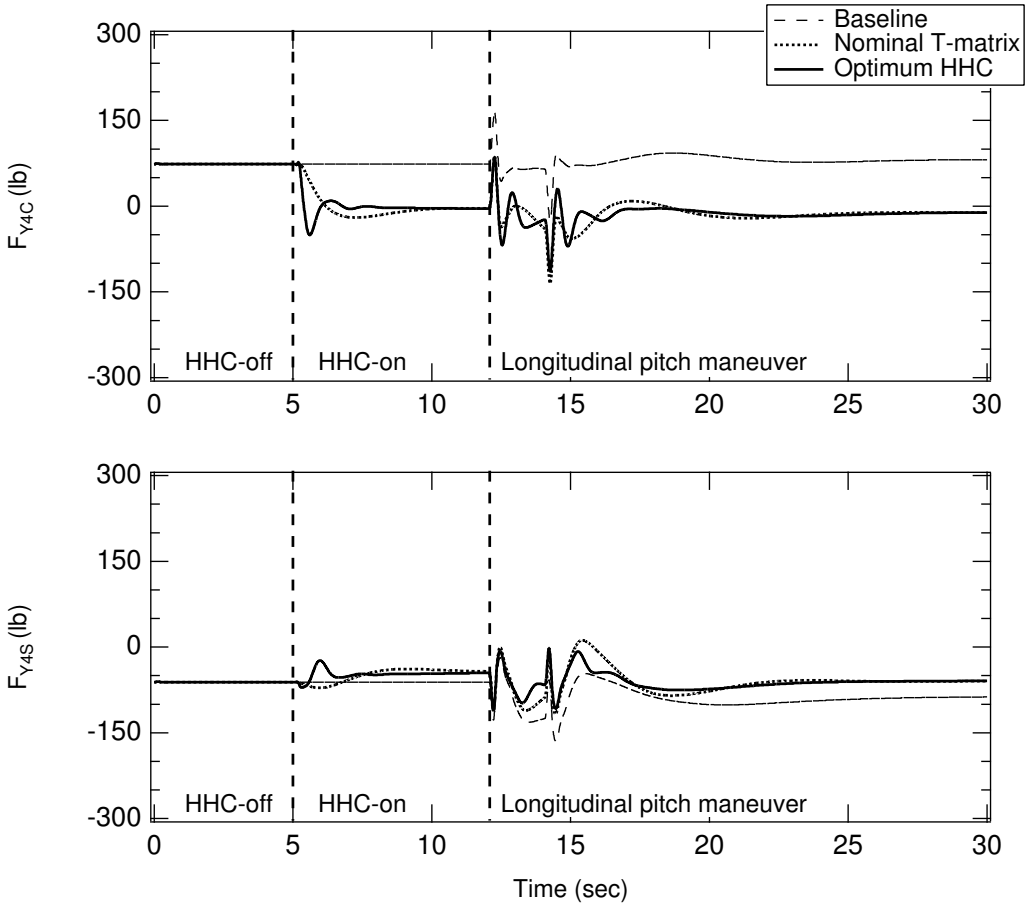

Figure 5.34: F_Y vibration response in pitch maneuvering flight; optimized lead-lag compensator.

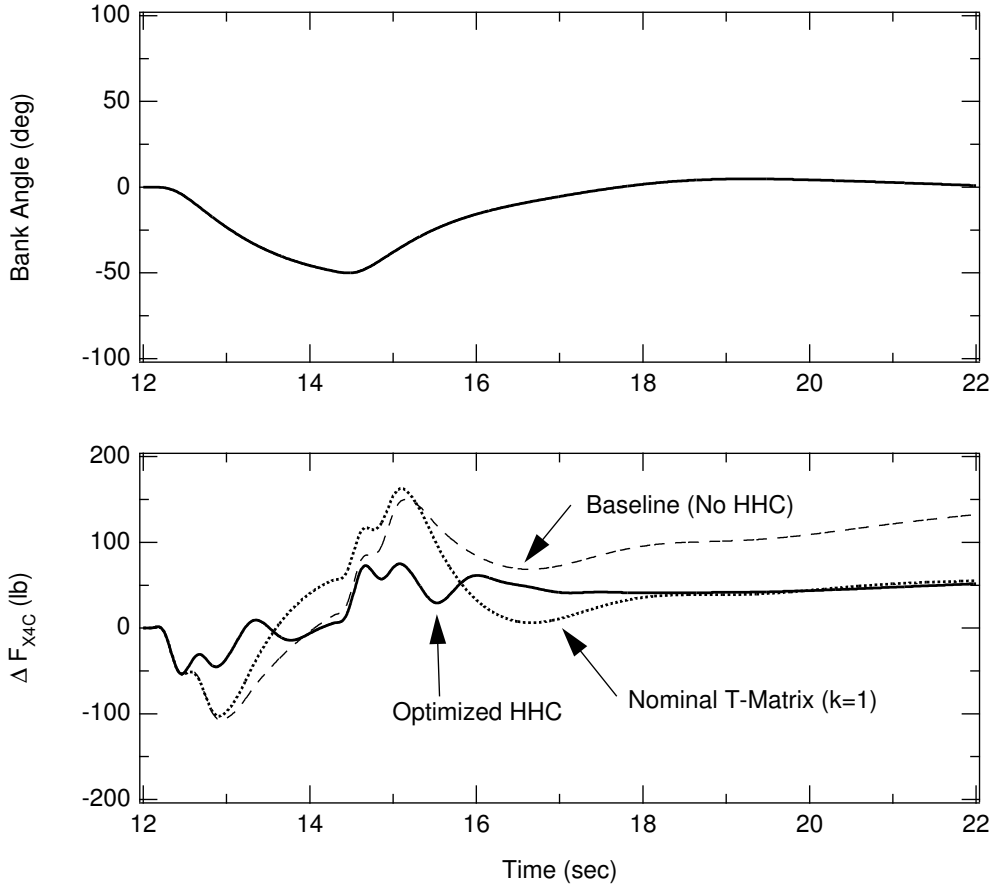

Figure 5.35: $F_{X_{4C}}$ vibration response in roll maneuvering flight; optimized lead-lag compensator.

Chapter 6

Summary and Conclusions

The increasing opportunities provided by novel sensing and actuation technologies, and the advancements in the theory and practice of flight and rotor control system open unprecedented possibilities in the constant search for low vibration levels and favorable handling qualities in modern helicopters. At the same time, however, greater care than ever must be taken to ensure that these advanced controls cooperate harmoniously and to prevent adverse dynamic interactions.

The present work makes a contribution toward this goal by developing new mathematical tools for the analysis and design of active rotor control systems, more specifically, Higher Harmonic Control (HHC) systems, and by using these tools to carry out the first systematic study of the interaction of HHC and Automatic Flight Control Systems (AFCS) available in the literature.

This chapter provides a summary of the work presented in the dissertation, details the conclusions drawn from its results, and outlines some recommendations for future work. Chapter 2 of this dissertation describes the key features of the formulation and solution techniques for the baseline helicopter simulation model used in this study. Chapter 3 provides basic information on the HHC algorithm. The extraction of a linearized, time-invariant dynamic model of the helicopter that

includes higher harmonic content is a key contribution of this dissertation, and is described in detail in Chapter 4. The other important contribution, namely, the AFCS-HHC interaction study, is presented in Chapter 5. AFCS design procedures, and basic concepts of Fourier analysis and of treatment of rotor degrees of freedom, are briefly reviewed in the Appendices.

6.1 Summary

A realistic analysis of the interaction between AFCS and HHC requires a mathematical model of the helicopter of adequate sophistication. This model must be able to provide sufficiently accurate predictions of vibratory loads in both trimmed and maneuvering flight. This model was described in Chapter 2. An existing, state-of-the-art flight dynamic simulation model was improved to allow the calculation of vibration levels both at the center of mass of the helicopter and at specific locations such as pilot and copilot seats. The results obtained with this model were successfully validated through comparisons with other simulation models and with flight test data.

A HHC system is composed of several elements, which must all be modeled in a rigorous mathematical way. This was the main topic of Chapter 3. The harmonic analyzer, which extracts the desired frequency components of the rotor vibrations, was studied first. A Fourier analysis method was described, and the effects of windowing were discussed. Then, the HHC control algorithm was presented, in the traditional T-matrix form, and validated through simulation. Finally, the issues associated with the discrete, rather than continuous, implementation of HHC were discussed.

The methodology for the extraction of a high-order, time-invariant linearized

model of the coupled rotor-fuselage system was systematically described in Chapter 4. This model included both the pilot and the HHC inputs, and both the averaged and the high frequency dynamics of the rotor states. The resulting model contains, as a subset, the more traditional linear time-invariant representation without high frequency rotor dynamics and higher harmonic controls. Therefore, the description of the methodology started with this well-known subset. The methodology to extract the remaining partitions of the state, control, and output matrices was presented next, with partitions chosen in an order that allowed the progressive introduction of the key new concepts. Chapter 4 continued with the application of the technique to a simplified rotor model, entirely formulated analytically. This model was not sufficiently sophisticated to be used in the remainder of the research. However, it was very useful to both illustrate and validate the methodology. In fact, the higher harmonics of the rotor motion and of the control inputs were explicitly accessible in the equations in analytic form. A more complete validation, performed by comparing hub loads and rotor states predicted by the linearized model and by the full nonlinear simulation, concluded the chapter.

The newly developed linearized model was then used to carry out a study of the interaction between HHC and AFCS, described in Chapter 5. First, the effect of open-loop HHC on rigid body dynamics was examined in detail, by observing the changes in the frequency responses of the helicopter to pilot inputs when the HHC controller was turned on. Then, a full closed-loop interaction study was performed. The study included a validation through simulation of the response of the helicopter with all the control loops closed, an analysis of the vibratory loads with and without HHC in both trimmed and maneuvering flight, and a discussion of the tailoring of the HHC controller to improve its performance in transient

maneuvers.

6.2 Conclusions

This section presents the main observations originating from this research, and the key conclusions of the study. The conclusions related to the new linearization procedure are presented first, followed by those concerning the AFCS/HHC interaction study.

6.2.1 Extraction of linearized, time-invariant models

1. The traditional constant coefficient linearized models of coupled rotor-fuselage dynamics, obtained through multiblade coordinate transformations followed by averaging over one rotor revolution, are not suitable for studies involving rotor vibrations, even if the control vector includes the higher harmonics typical of HHC. In fact, the averaging removes all the higher harmonics of rotor response. Such a model will capture the effects of HHC on the low frequency rigid body motion of the helicopter and of the tip path plane, but not on the N/rev vibrations.

2. The constant coefficient linearized model developed in this research, which explicitly includes states describing the high frequency rotor dynamics, does capture the vibratory loads, and the effects that HHC can have on them. The price for modeling vibrations with a linear time-invariant system, compared with a linear system with periodic coefficients, is an increase in the size of the system. On the other hand, the entire arsenal of tools of linear time-invariant system theory can now be used.

3. The validation with the full nonlinear simulation model shows that there is very good agreement between the hub loads predicted by the new LTI-HHC model and the hub loads of the nonlinear model, both for HHC inputs and pilot inputs. This suggests that a linearized model that intrinsically includes higher rotor harmonics is sufficiently accurate for full load predictions, at least for the aircraft configuration and flight conditions considered in this study. In other words, periodicity plays a far more important role than nonlinearity.

4. One limitation of the LTI-HHC model described in this dissertation is that it can model only the 4/rev components of the system and not the higher frequency components that enter the fuselage, i.e., 8/, 12/rev, etc., for the 4-bladed rotor of this study. However, this limitation can be easily overcome, by including additional harmonics in the LTI-HHC model using the same methodology as for the 4/rev states.

5. Possibly for historical reasons, the starting point for the vast majority of HHC modeling research and applications has been an update equation that links the vibration harmonics to the HHC harmonics through the T-matrix. Using instead an (A, B, C, D) state-space representation as a starting point, as done in this dissertation, leads to a much richer and informative picture. In fact, the traditional update equation is included as a subset (through a partition of the control matrix B), and the additional effects on vibrations of pilot inputs and of all the states, including aircraft rigid body, rotor, and inflow states, are now modeled explicitly. These additional effects are not included in the traditional update equations, and are usually taken into account indirectly through on-line identification and adaptation schemes.

6.2.2 HHC/AFCS interaction study

1. The closed-loop HHC system has little influence on the handling qualities characteristics of the helicopter in general, and on the behavior of the flight control system in particular, at least for the articulate rotor configuration used in this study. This conclusion is drawn on the basis of the analysis of the effects of HHC on the frequency response to pilot inputs. The effects of HHC on trim were not addressed explicitly, but the simulated free flight responses with HHC suggest that these effects are not significant.

2. Although the typical 3/, 4/, and 5/rev HHC inputs for a 4-bladed rotor are at high frequency (81, 108, and 135 rad/sec, respectively, for the helicopter used in this study), the crossover frequency of each HHC loop is only about 1 rad/sec. Because of the high HHC input frequency, one might expect a large frequency separation between the flight control and the HHC inputs, and assume that these two systems would not interfere with each other. Instead, the results clearly show that this is not the case, and that the potential for AFCS/HHC interaction does exist.

3. The vibration response to *maneuver* inputs, and not just to steady state inputs, must be considered as part of the HHC system design process. If the HHC algorithm is not properly designed, the transient vibrations in the early phases of a maneuver might even be higher than if no HHC system was present.

4. An HHC controller that improves the suppression of vibration transients turns out to have higher loop crossover frequencies. For the cases studied in this dissertation, these frequencies are of the order of 3 rad/sec. At

these frequencies, the use of the T-matrix approach to simulate the helicopter vibration model is unacceptable for controller analysis and optimization. This is because the T-matrix is simply a k/s diagonal compensator multiplied by a fixed-gain regulator, and a comparison with the more sophisticated LTI-HHC model developed in this study shows that it is inaccurate for crossover frequencies greater than about 1 rad/sec. Increasing the T-matrix controller feedback gain (k=2) does reduce the closed-loop transient settling time, but it increases the magnitude of the peak disturbance at frequencies above crossover frequency.

5. For the maneuvering flight conditions considered in this study, the optimized HHC system designed using the new linearized model reduces vibratory hub shears by 37% compared to the baseline case, and 39% compared to nominal T-matrix controller case. Therefore, the need for on-line identification and adaptation of the T-matrix is greatly reduced if not completely eliminated. This is important from a practical point of view, because of the danger that an adaptive system on board a helicopter might react in unpredictable and unwanted ways, which can clearly create safety-of-flight issues.

6.3 Future work

The research presented in this study has shown the importance of the HHC/AFCS interaction on the transient vibration suppression. However, there are some areas in which the present analysis was limited. This section suggests some areas for improvement.

1. Improve the flexible blade model, for example by adding additional blade

modes and increasing the number of blade finite elements. While the vibration results presented in this dissertation can be considered qualitatively representative, a more sophisticated model is probably needed for quantitative evaluations (e.g., for a precise quantification of the benefits of HHC).

2. For the same reason just mentioned, improve airload calculations, especially by adding non-uniform inflow and unsteady aerodynamics modeling. For the design of the HHC system, the improved models must obviously be in state-space form (not necessarily linear). For validation purposes, this characteristic is not required.

3. Further validate the vibratory hub load level predicted by the mathematical model with wind tunnel data or flight test data. Because of the large scatter, the flight test data used in this study were only adequate for a qualitative validation. Unfortunately, no other other flight test data seemed to be publicly available for a helicopter without some or all of the normal vibration suppression devices.

4. Repeat the study with a helicopter configuration with lowly damped coupled rotor/body modes, such as hingeless or bearingless rotor helicopters. The articulated rotor configuration used in this study had hydraulic lag dampers, and aeromechanic stability was never an issue.

5. Apply advanced control design theories such as H_2, H_∞ control design methods to try to achieve further improvements in vibration reduction. This may completely remove the need for adaptive T-matrices.

Appendix A

CONDUIT HQ-Window Specifications

Following are the handling-qualities specifications and control system metrics used in the AFCS optimization procedure:

(a) Eigenvalues (All) This criterion is used to ensure that all the real parts of the eigenvalues of the system are zero or negative, ensuring that all the dynamics are stable or neutrally stable. At any given iteration, the sum of unstable eigenvalues real parts or the largest stable eigenvalue is returned as the spec metric.

(b) Minimum Crossover Frequency The crossover frequency is defined as the frequency where the magnitude curve crosses 0 dB. For multiply crossing, the highest crossover frequency is returned. This specification is intended as a hard constraint to a greater than zero value of crossover frequency. Three specifications shown in figure represents the crossover frequencies of roll, pitch, and yaw broken control loops.

(c) Gain/Phase Margins The spec has very sophisticated logic for treating stable, conditionally stable, and unstable systems. It also has logic for correctly accounting for right-half plane poles and zeros. A table of margins is built for

all crossings of the 0 dB and -180 deg lines and displayed in the supporting plot. The spec returns the minimum gain and phase margin values from the table. The level 1 boundaries are taken from MIL-F-9490D. Three specifications shown in figure represents the minimum gain and phase margin values of roll, pitch, and yaw broken control loops.

(d) Bandwidth Specification The vehicle response to cockpit control force or position inputs shall meet the limits specified. It is desirable to meet this criterion for both controller force and position inputs. If the bandwidth for force inputs falls outside the specified limits, flight testing should be conducted to determine that the force feel system is not excessively sluggish.

(e) Attitude Response Damping Ratio (from peak overshoot) The calculation of the damping ratio (zeta) is from peak overshoot of the time response to a step input. ADS-33D required a minimum damping ratio of 0.35. Systems whose eigenvalues all have damping ratio of greater than 0.35 could still have excessive overshoot due to the presence of zeros in the response. This spec ensures that the end-to-end attitude response has an effective damping ratio greater than 0.35 base on the time response. An appropriate input should be used to results in a step response.

(f) Crossover Frequency The crossover frequency is defined as the frequency where the magnitude curve crosses 0 dB. For multiply crossing, the highest crossover frequency is returned. This specification is intended as an objective to minimize crossover frequency in CONDUIT phase 3 optimization.

(g) Damping ratio This specification is used to ensure damping is above the minimum value specified. This is achieved by checking the damping ratios of the eigenvalues within the range of natural frequencies specified.

(h) Rise Time (Calculated from 10% to 90% of peak response) This spec estimates rise time for first-order SISO systems by finding the peak of the time response, and calculating the time between 10% and 90% of the peak magnitude.

Appendix B

Fourier Transforms

B.1 Fourier Transform (FT)

Fourier transform can be viewed as a generalization of the Fourier series representation of a periodic function. Unlike the Fourier series which is an approximation of the source signal, Fourier transform is an direct mapping between time-domain and the frequency-domain, and it is fully reversible.

Let $f(t)$ be a continuous-time signal, its continuous Fourier transform $F(\omega)$ is defined by

$$F(\omega) = \int_{-\infty}^{\infty} f(t)\, e^{-j\omega t} \mathrm{dt}, \quad -\infty < \omega < \infty \tag{B.1}$$

where ω is the frequency variable in rad/sec. In many applications, the source signal $f(t)$ cannot be given in common function[1]; therefore, Fourier transform is often computed numerically. This numerical computation can be performed in either the continuous-time domain (continuous Fourier Transform) or the discrete-time domain (discrete-time Fourier transform).

Because a digital computer works only with discrete data, numerical compu-

[1]It is the generalized transform typically shown in Fourier transform table

tation of the Fourier transform of $f(t)$ requires discrete sample values of $f(t)$. In addition, a digital computer can compute the transform $F(\omega)$ only at discrete values of ω; therefore, discrete-time Fourier transform is often used in many applications.

B.2 Discrete-Time Fourier Transform (DTFT)

Let $f(k)$ be a sampled version of a continuous-time signal $f(t)$ with t evaluated at sample time $t = k\mathrm{T}$, where T is the sample interval.

$$f(k) \;=\; f(t)|_{t\,=\,k\mathrm{T}} \;=\; f(k\mathrm{T}),\; k \;=\; 0,\;\; \pm\,1,\;\; \pm\,2,\;\ldots \tag{B.2}$$

The Fourier transform of $f(k)$ is defined by

$$F(\Omega) \;=\; \sum_{k=-\,\infty}^{\infty} f(k)\, e^{-j\Omega k}, \qquad -\,\infty \;<\; \Omega \;<\; \infty \tag{B.3}$$

Note that DTFT is directly analogous the FT, and it is not an approximation to the FT.

The DTFT requires the calculation of the sums of Eq. (B.3) for all frequencies range. In practice, $F(\Omega)$ is usually computed only for a discrete set of frequency variable Ω, and this is accomplished by using the N-point discrete Fourier transform (N-point DFT).

$$F_n \;=\; \sum_{k\,=\,0}^{\mathrm{N}\,-\,1} \mathrm{f}(k)\, \mathrm{e}^{-\,\mathrm{j}2\pi k\mathrm{n}/\mathrm{N}}, \qquad \mathrm{n} \;=\; 0,\; 1,\ldots,\; \mathrm{N} \;-\; 1 \tag{B.4}$$

where N is a positive integer.

B.3 Fast Fourier Transform (FFT)

The computation of Eq. (B.4) can be carried out using a fast algorithm called the Fast Fourier Transforms. It is a new N-point DFT algorithm developed by Tukey

and Cooley [65] in 1965 which reduces the number of computations from something on the order of N^2 to $N \log N$. Because many special computers or add-on cards are available to perform the FFT algorithm at ultra-high speed, FFT opens the possibility of a wider use of the FT in many other areas such as the computational physics and many engineering applications. Additional information regarding to FT, DTFT, DFT, and FFT can be found in Refs. [66, 67].

Appendix C

Multi-blade Coordinate Transformation

C.1 Converting rotor equations of motion

Let the blade flapping equations of motion for a four-bladed rotor in the rotating system be

$$\ddot{\mathbf{x}}_R \;+\; C_R\,\dot{\mathbf{x}}_R \;+\; K_R\,\mathbf{x}_R \;=\; \mathbf{f}_R \tag{C.1}$$

where

$$\mathbf{x}_R \;=\; \Big[\beta_1,\ \beta_2,\ \beta_3,\ \beta_4\Big]^T \tag{C.2}$$

The matrix T_F^R is the multi-blade coordinate transformation which converts $\mathbf{x}$ from the fixed to the rotating system as follows:

$$\mathbf{x}_R \;=\; T_F^R\,\mathbf{x}_F \tag{C.3}$$

The first and the second time derivative of Eq. (C.3) are:

$$\dot{\mathbf{x}}_R \;=\; \dot{T}_F^R\,\mathbf{x}_F \;+\; T_F^R\,\dot{\mathbf{x}}_F \tag{C.4}$$

$$\ddot{\mathbf{x}}_R \;=\; \ddot{T}_F^R\,\mathbf{x}_F \;+\; 2\dot{T}_F^R\,\dot{\mathbf{x}}_F \;+\; T_F^R\,\ddot{\mathbf{x}}_F \tag{C.5}$$

Substitute Eqs. (C.4) and (C.5) into Eq. (C.1) yields

$$\begin{aligned} \ddot{T}_F^R\, \mathbf{x}_F \;\; &+ \;\; 2\dot{T}_F^R\, \dot{\mathbf{x}}_F \;+\; T_F^R\, \ddot{\mathbf{x}}_F \\ &+ \;\; C_R\, (\dot{T}_F^R\, \mathbf{x}_F \;+\; K_R\, T_F^R\, \mathbf{x}_F = \mathbf{f}_R \end{aligned} \tag{C.6}$$

Multiply T_R^F through Eq. (C.6) and re-arrange the equation, Eq. (C.6) becomes

$$\ddot{\mathbf{x}}_F \;+\; C_F \dot{\mathbf{x}}_F \;+\; K_F \mathbf{x}_F \;=\; \mathbf{f}_F \tag{C.7}$$

where

$$\mathbf{x}_F \;=\; \Big[\beta_0,\; \beta_{1c},\; \beta_{1s},\; \beta_2\Big]^T \tag{C.8}$$

$$C_F \;=\; T_R^F\, (C_R\, T_F^R \;+\; 2\dot{T}_F^R) \tag{C.9}$$

$$K_F \;=\; T_R^F\, (\ddot{T}_F^R \;+\; C_R\, \dot{T}_F^R \;+\; K_R\, T_F^R) \tag{C.10}$$

$$\mathbf{f}_F \;=\; T_R^F\, \mathbf{f}_R \tag{C.11}$$

$$T_F^R = \begin{bmatrix} 1 & \cos(\psi_1) & \sin(\psi_1) & -1 \\ 1 & \cos(\psi_2) & \sin(\psi_2) & 1 \\ 1 & \cos(\psi_3) & \sin(\psi_3) & -1 \\ 1 & \cos(\psi_4) & \sin(\psi_4) & 1 \end{bmatrix} \tag{C.12}$$

$$\dot{T}_F^R = \begin{bmatrix} 0 & -\sin(\psi) & \cos(\psi) & 0 \\ 0 & \cos(\psi) & \sin(\psi) & 0 \\ 0 & \sin(\psi) & -\cos(\psi) & 0 \\ 0 & -\cos(\psi) & -\sin(\psi) & 0 \end{bmatrix} \tag{C.13}$$

$$\ddot{T}_F^R = \begin{bmatrix} 0 & -\cos(\psi) & -\sin(\psi) & 0 \\ 0 & -\sin(\psi) & \cos(\psi) & 0 \\ 0 & \cos(\psi) & \sin(\psi) & 0 \\ 0 & \sin(\psi) & -\cos(\psi) & 0 \end{bmatrix} \tag{C.14}$$

$$T_R^F = \begin{bmatrix} 1/4 & 1/4 & 1/4 & 1/4 \\ 1/2\cos(\psi) & 1/2\sin(\psi) & -1/2\cos(\psi) & -1/2\sin(\psi) \\ 1/2\sin(\psi) & -1/2\cos(\psi) & -1/2\sin(\psi) & 1/2\cos(\psi) \\ -1/4 & 1/4 & -1/4 & 1/4 \end{bmatrix} \quad \text{(C.15)}$$

$$\dot{T}_R^F = \begin{bmatrix} 0 & 0 & 0 & 0 \\ -1/2\sin(\psi) & 1/2\cos(\psi) & 1/2\sin(\psi) & -1/2\cos(\psi) \\ 1/2\cos(\psi) & 1/2\sin(\psi) & -1/2\cos(\psi) & -1/2\sin(\psi) \\ 0 & 0 & 0 & 0 \end{bmatrix} \quad \text{(C.16)}$$

$$\ddot{T}_R^F = \begin{bmatrix} 0 & 0 & 0 & 0 \\ -1/2\cos(\psi) & -1/2\sin(\psi) & 1/2\cos(\psi) & 1/2\sin(\psi) \\ -1/2\sin(\psi) & 1/2\cos(\psi) & 1/2\sin(\psi) & -1/2\cos(\psi) \\ 0 & 0 & 0 & 0 \end{bmatrix} \quad \text{(C.17)}$$

C.2 Converting state-space representation

Let Eq. (C.18) be the state-space representation of rotor equations of motion in rotating system.

$$\dot{\mathbf{x}}_R = A_R\,\mathbf{x}_R + B_R\,\mathbf{u} \quad \text{(C.18)}$$

where A_R and B_R is the state matrix and the control matrix in the rotating system, respectively. Substituting Eqs. (C.3) and (C.4) into Eq. (C.18) yields:

$$\dot{T}_F^R\,\mathbf{x}_F + T_F^R\,\dot{\mathbf{x}}_F = A_R\,T_F^R\,\mathbf{x}_F + B_R\,\mathbf{u} \quad \text{(C.19)}$$

Multiply T_R^F through Eq. (C.19) and re-arrange the equation as:

$$\dot{\mathbf{x}}_F = A_F\,\mathbf{x}_F + B_F\,\mathbf{u} \quad \text{(C.20)}$$

where

$$A_F = T_F^F \ (A_R \ T_F^R \ - \ \dot{T}_F^R) \tag{C.21}$$

$$B_F = T_R^F \ B_R \tag{C.22}$$

BIBLIOGRAPHY

[1] Anon., "Advanced Vibration Reduction Concepts," *Dual Use Science and Technology, Projects from Fiscal Year 1999 Congressional Report*, Sikorsky Aircraft Corporation, Stratford, CT; United Technologies Research Center (UTRC), East Hartford, CT, 1999.

[2] Anon., "Enhanced Active Noise and Vibration Actuators," *Dual Use Science and Technology, Projects from Fiscal Year 1998 Congressional Report*, Sikorsky Aircraft Corporation, Stratford, CT; United Technologies Research Center (UTRC), East Hartford, CT, 1998.

[3] Friedmann, P. P. and Millott, T. A., "Vibration Reduction in Rotorcraft Using Active Control: A Comparison of Various Approaches," *Journal of Guidance, Control, and Dynamics*, Vol. 18, No. 4, July-August 1995.

[4] Teves, D., Niesl, G., Blaas, A., and Jacklin, S., "The Role of Active Control in Future Rotorcraft," *Twentyfirst European Rotorcraft Forum*, Saint Petersburg, Russia, September 1995.

[5] Shin, S. J., Cesnik, C. E. S., and Hall, S. R., "Control of Integral Twist-Actuated Helicopter Blades for Vibration Reduction," *Proceedings of the 58th Annual Forum of the American Helicopter Society*, Montreal, Canada, June 2002.

[6] Shaw, J., Albion, N., Hanker, E. J. J., and Teal, R. S., "Higher Harmonic Control: Wind Tunnel Demonstration of Fully Effective Vibratory Hub Force Suppression," *Journal of the American Helicopter Society*, Vol. 34, No. 1, 1989.

[7] Nguyen, K. Q. and Chopra, I., "Application of Higher Harmonic Control to Rotor Operating at High Speed and Thrust," *Proceedings of the 45th Annual Forum of the American Helicopter Society*, Boston, MA, 1989.

[8] Chopra, I. and McCloud III, J. L., "A Numerical Simulation Study of Open-Loop, Closed-Loop and Adaptive Multicyclic Control Systems," *Proceedings of the American Helicopter Society Northeast Region National Specialists' Meeting on Helicopter Vibration, Technology for the Jet Smooth Ride*, Hartford, CT, November 1981.

[9] Hammond, C. E., "Wind Tunnel Results Showing Rotor Vibratory Loads Reduction Using Higher Harmonic Blade Pitch," *Journal of the American Helicopter Society*, Vol. 28, No. 1, 1983.

[10] Arnold, U. T. P. and Strecker, G., "Certification, Ground and Flight Testing of an Experimental IBC System for the CH-53G Helicopter," *Proceedings of the 58th Annual Forum of the American Helicopter Society*, Montreal, Canada, June 2002.

[11] Wereley, N. M. and Hall, S. R., "Linear Control Issues in the Higher Harmonic Control for Helicopter Vibration," *Proceedings of the 45th Annual American Helicopter Society Forum*, May 1989.

[12] Stewart, W., "Second Harmonic Control in the Helicopter Rotor," Aeronautical Research Council R & M, London, 1952.

[13] Arcidiacono, P. J., "Theoretical Performance of Helicopters Having Second and Higher HArmonic Feathering Control," *Journal of the American Helicopter Society*, Vol. 6, No. 2, April 1961.

[14] Drees, J. M. and Wernicke, R. K., "An Experimental Investigation of a Second Harmonic Feathering Device on the UH-1A Helicopter," U.S. Army Transportation Research Command, TR-62-109, Fort Eustis, VA, 1961.

[15] McCloud, J. L. I., "Studies of a Large Scale Jet-Flap Rotor in the 40- by 80-Foot Wind Tunnel," *Proceedings of the American Helicopter Society Mideast Regional Symposium on Status of Testing and Modeling of V/STOL Aircraft*, October 1972.

[16] McCloud, J. L. I. and Kretz, M., "Multicyclic Jet-Flap Control for Alleviation of Helicopter Blade Stresses and Fuselage Vibration," *Proceedings of the AHS/NASA Ames Specialists Meeting on Rotorcraft Dynamics*, NASA SP-352, February 1974.

[17] McHugh, F. J. and Shaw, J., "Benefit of Higher Harmonic Blade Pitch: Vibration Reduction, Blade Load Reduction, and Performance Improvement," *Proceedings of the American Helicopter Society Mideast Regional Symposium on Rotorcraft Technology*, August 1976.

[18] McHugh, F. J. and Shaw, J., "Helicopter Vibration Reduction with Higher Harmonic Blade Pitch," *Journal of American Helicopter Society*, Vol. 23, No. 4, October 1978.

[19] Shaw, J. and Albion, N., "Active Control of the Helicopter Rotor for Vibration Reduction: A Wind Tunnel Demonstration," *Vertica*, Vol. 4, No. 1, 1980.

[20] Shaw, J. and Albion, N., "Active Control of the Helicopter Rotor for Vibration Reduction," *Journal of the American Helicopter Society*, Vol. 26, No. 3, 1981.

[21] Shaw, J., Higher Harmonic Blade Pitch Control: A System for Helicopter Vibration Reduction, Ph.D. Dissertation, Massachusetts Institute of Technology, May 1980.

[22] Molusis, J. A., Hammond, C. E., and Cline, J. H., "A Unified Approach to the Optimal Design of Adaptive and Gain Scheduled Controllers to Achieve Minimum Helicopter Rotor Vibrations," *Journal of the American Helicopter Society*, Vol. 28, No. 2, 1983.

[23] Wood, E. R., Powers, R. W., Cline, J. H., and Hammond, C. E., "On Developing and Flight Testing a Higher Harmonic Control System," *Journal of the American Helicopter Society*, Vol. 30, No. 1, January 1985.

[24] Gupta, B. P., Logan, A. H., and Wood, E. R., "Higher Harmonic Control for Rotary Wing Aircraft," *Proceedings of the AIAA/AHS/ASEE Aircraft Design Systems and Operations Meeting*, October 1984.

[25] Ham, N. D., "Helicopter Individual Blade Control Research at MIT: 1977-1985," *Vertica*, Vol. 11, No. 1/2, 1987.

[26] Ham, N. D., "Helicopter Stall Alleviation Using Individual Blade Control," *Tenth European Rotorcraft Forum*, The Hague, Netherlands, 1984.

[27] Polychroniadis, M. and Achache, M., "Higher Harmonic Control: Flight Test of an Experimental System on SA-349 Research Gazelle," *Proceedings of the*

42nd Annual Forum of the American Helicopter Society, Alexandria, VA, 1986.

[28] Achache, M. and Polychroniadis, M., "Development of an Experimental System for Active Control of Vibration on Helicopters – Development Methodology for an Airborne System," *Vertica*, Vol. 1, No. 1 and 2, 1987.

[29] Jacklin, S. A., Nguyen, K. Q., and Blaas, A., "Full-Scale Wind Tunnel Test of a Helicopter Individual Blade Control System," *American Helicopter Society 50th Annual Forum*, Washington, DC, May 1994.

[30] Jacklin, S. A., Blaas, A., Swanson, S. M., and Teves, D., "Second Test of a Helicopter Individual Blade Control System in the NASA Ames 40- by 80-foot Wind Tunnel," *Proceedings of the American Helicopter Society 2nd International Aeromechanics Specialists' Conference*, Bridgeport, CT, October 1995.

[31] Du Val, R. W. and Gupta, N. K., "A New Approach for Active Control of Rotorcraft Vibration," *Journal of the American Helicopter Society*, Vol. 26, No. 2, 1980.

[32] Wereley, N. M. and Hall, S. R., "Performance of Higher Harmonic Control Algorithms for Helicopter Vibration Reduction," *Journal of Guidance, Control, and Dynamics*, Vol. 16, No. 4, July-August 1993.

[33] Spencer, M. G., Development of a Real Time Adaptive Neural Network Controller for Active Rotorcraft Vibration Reduction, Ph.D. Dissertation, Department of Aerospace Engineering, University of Maryland, College Park, MD, 2000.

[34] Howlett, J. J., "UH-60A Black Hawk Engineering Simulation Program - Volume II - Mathematical Model," NASA CR-166309, December 1981.

[35] Zhao, X. and Curtiss, H. C., "A Linearization Model of Helicopter Dynamics Including Correlation with Flight Test," *Proceedings of the Second International Conference on Rotorcraft Basic Research*, University of Maryland, College Park, Maryland, February 1988.

[36] Chen, R. T. N. and Tischler, M. B., "The Role of Modeling and Flight Testing in Rotorcraft Parameter Identification," *Vertica*, Vol. 11, No. 4, 1987.

[37] Miller, D. G. and White, F., "A Treatment of the Impact of Rotor-Fuselage Coupling on Helicopter Handling Qualities," *Proceedings of the 43rd Annual Forum of the American Helicopter Society*, St. Louis, Missouri, May 1987.

[38] Kim, F. D., Celi, R., and Tischler, M. B., "Formulation and Validation of High-Order Linearized Models of Helicopter Flight Mechanics," *Proceedings of the 46th Annual Forum of the American Helicopter Society*, Washington, D.C., May 1990.

[39] Ballin, M. G., "Validation of a Real-Time Engineering Simulation of the UH-60A Helicopter," NASA TM-88360, 1987.

[40] Kim, F. D., Celi, R., and Tischler, M. B., "High Order State Space Simulation Models of Helicopter Flight Mechanics," *Journal of the American Helicopter Society*, Vol. 38, No. 2, October 1993.

[41] Kim, F. D., Celi, R., and Tischler, M. B., "Forward Flight Trim Calculation and Frequency Response Validation of a High-Order Helicopter Simulation Model," *Journal of Aircraft*, Vol. 30, No. 6, November-December 1993.

[42] Pitt, D. M. and Peters, D. A., "Theoretical Prediction of Dynamic Inflow Derivatives," *Vertica*, Vol. 5, No. 1, 1981.

[43] Turnour, S. R. and Celi, R., "Modeling of Flexible Blades for Helicopter Flight Dynamics Applications," *Journal of the American Helicopter Society*, Vol. 41, No. 1, January 1996.

[44] Celi, R., "Helicopter Rotor Blade Aeroelasticity in Forward Flight with an Implicit Structural Formulation," *AIAA Journal*, Vol. 30, No. 9, September 1992.

[45] Spence, A. M., A Design-Oriented Aeromechanical Analysis for Hingeless Rotor Helicopters in Straight and Turning Flight, Ph.D. Dissertation, Department of Aerospace Engineering, University of Maryland, College Park, MD, 1994.

[46] He, C.-J. and Peters, D. A., "Optimization of Rotor Blades for Combined Structural, Performance, and Aeroelastic Characteristics," *Structural Optimization*, Vol. 5, No. 1/2, December 1992.

[47] Leishman, J. G. and Q., N. K., "State Space Representation of Unsteady Airfoil Behavior," *AIAA Journal*, Vol. 28, No. 5, May 1990.

[48] Theodore, C. and Celi, R., "Flight Dynamic Simulation with Refined Aerodynamic and Flexible Blade Modeling," *Proceedings of the 56th Annual Forum of the American Helicopter Society*, Virginia Beach, VA, May 2000.

[49] Bagai, A. and Leishman, J. G., "Rotor Free-Wake Modeling using a Relaxation Technique - Including Comparisons with Experimental Data," *Pro-*

ceedings of the 50th Annual American Helicopter Society Forum, Washington D.C., May 1994.

[50] Chen, R. T. N. and Jeske, J. A., "Kinematic Properties of the Helicopter in Coordinated Turns," NASA Technical Paper 1773, April 1981.

[51] Celi, R., "Hingeless Rotor Dynamics in Coordinated Turns," *Journal of the American Helicopter Society*, Vol. 36, No. 4, October 1991.

[52] Stoer, J. and Bulirsch, R., *Introduction to Numerical Analysis*. New York: Springer-Verlag, 1980.

[53] Yang, M., Chopra, I., and Hass, D. J., "Rotor System Health Monitoring Using Coupled Rotor-Fuselage Vibration Analysis," *Proceedings of the 56th Annual Forum of the American Helicopter Society*, Virginia Beach, Virginia, May 2000.

[54] "MSC/NASTRAN Reference Manual," 1994.

[55] Vanderplaats, G. N., *Numerical Optimization Techniques for Engineering Design: With Applications*. New York, NY: McGraw-Hill, 1984.

[56] Vanderplaats, G. N., *DOT–Design Optimization Tools, User's Manual*. Goleta, CA: VMA Engineering, Inc., May 1995.

[57] Nguyen, K., Betzina, M., and Kitaplioglu, C., "Full-Scale Demonstration of Higher Harmonic Control for Noise and Vibration Reduction on the XV-15 Rotor," *Proceedings of the 56th Annual Forum of the American Helicopter Society*, Virginia Beach, Virginia, May 2000.

[58] Tischler, M. B. and Cauffman, M., "Frequency-Response Method for Rotorcraft System Identification: Flight Applications to BO-105 Coupled Rotor/Fuselage Dynamics," *Journal of the American Helicopter Society*, Vol. 37, No. 3, July 1992.

[59] Tischler, M. B., Colbourne, J. D., Morel, M. R., Biezad, D. J., Cheung, K. K., Levine, W. S., and Moldoveanu, V., "A Multidisciplinary Flight Control Development Environment and Its Application to a Helicopter," *IEEE Control Systems Magazine*, Vol. 19, No. 4, August 1999.

[60] Anon., "Handling Qualities Requirements for Military Rotorcraft: Aeronautical Design Standard-33 (ADS-33E-PRF)," US Army Aviation and Missile Command, March 2000.

[61] McCloud, J. L. I., "An Analytical Study of Multicyclic Controllable Twist Rotor," *Proceedings of the 31st Annual Forum of the American Helicopter Society*, May 1975.

[62] Molusis, J. A., "The Importance of Nonlinearity in the Higher Harmonic Control of Helicopter Vibration," *Journal of the American Helicopter Society*, Vol. 28, No. 2, 1983.

[63] McCloud, J. L. I. and Weisbrich, A. L., "Wind Tunnel Test Results of a Full-Scale Multicyclic Controllable-Twist Rotor," *Proceedings of the 34th Annual Forum of the American Helicopter Society*, May 1978.

[64] McCloud, J. L. I., "The Promise of Multicyclic Control," *Vertica*, Vol. 4, No. 1, 1980.

[65] Cooley, J. W. and Tukey, J. W., "An algorithm for the machine calculation of complex Fourier series," *Mathematics of Computation*, Vol. 19, 1965.

[66] Jury, E. I., "Analysis and synthesis of sampled-data control systems," *Communications and Electronics*, 1954.

[67] Kamen, E. W. and Heck, B., *Fundamentals of Signals and System with MATLAB*. Englewood Cliffs, NJ: Prentice Hall, 1996.